UNIVERSIDAD POLITÉCNICA DE MADRID
Escuela Técnica Superior de Ingenieros de Telecomunicación

Dual-Comb Interferometry based on Gain-Switched Semiconductor Lasers

D O C T O R A L T H E S I S

Submitted for the degree of Doctor by:

Clara Quevedo Galán
MSc in Photonics Engineering

Madrid, 2024


UNIVERSIDAD POLITÉCNICA DE MADRID
Escuela Técnica Superior de Ingenieros de Telecomunicación

Doctoral Degree in Communication Technologies and Systems

Dual-Comb Interferometry based on Gain-Switched Semiconductor Lasers

D O C T O R A L T H E S I S

Submitted for the degree of Doctor by:

Clara Quevedo Galán
MSc in Photonics Engineering

Under the supervision of:
Dr. Ignacio Esquivias Moscardó

Madrid, 2024

Title: Dual-Comb Interferometry based on Gain-Switched Semiconductor Lasers

Author: Clara Quevedo Galán

Doctoral Programme: Communication Technologies and Systems

Thesis Supervision:

Dr. Ignacio Esquivias Moscardó, Full Professor, Universidad Politécnica de Madrid (Supervisor)

External Reviewers:

Thesis Defense Committee:

Thesis Defense Date:

This thesis has been partially supported by the Ministerio de Economía y Competitividad of Spain under grant RTI2018-094118-B-C21. The international research stay has been supported by Programa Propio UPM of the Universidad Politécnica de Madrid. The author also acknowledges support from grants TED2021-131957B-100 and PID2021-1234590B-C21 funded by MCIN/AEI/10.13039/501100011033 and by the European Union NextGenerationEU/PRTR and ERDF "A way of making Europe".

There is a light that never goes out
– The Smiths

Acknowledgement

Cuando empecé mis estudios universitarios de ingeniería de *teleco* sin duda no imaginaba que algún día llegaría a ser Doctora. Si bien es cierto que es un camino largo y arduo, el aprendizaje adquirido a lo largo de esta etapa y la satisfacción personal tras haberla finalizado hacen que haya merecido la pena. Por supuesto, esto no es algo que se consiga de manera individual. Es por ello que me gustaría extender unas líneas de agradecimiento a aquellas personas que, de alguna manera u otra, han tenido algo que ver en este proceso.

El deseo de querer saber más probablemente ya lo tenga una dentro. Sin embargo, muchas veces, si no encontramos a alguien que nos permita desarrollarlo y nos guíe hacia el mundo de la investigación, es posible que nunca iniciemos ese camino. En este sentido, mi director, Ignacio Esquivias, ha tenido un papel fundamental. Ignacio, gracias por abrirme las puertas del grupo de investigación, por tu compromiso con este trabajo y por la confianza durante estos años. Ha sido una gran suerte haber contado con tu guía y haber podido aprender tanto de ti.

Me gustaría continuar con el resto de personas que conforman el grupo de investigación. Quiero hacer mención a todos los compañeros con los que he tenido el placer de coincidir en el LAB101. Y en particular, me gustaría hacer una mención especial a algunos de ellos. A José Manuel, Toni y Pablo: gracias por vuestras valiosas aportaciones a mi trabajo y por vuestra ayuda. José Manuel, de ti he aprendido la importancia del rigor en la investigación y que es necesario dedicar tiempo a comprender *bien* las cosas. Toni, me has enseñado que en la investigación también hay que *ir a la aventura*, y que es fundamental no acomodarse y tener pasión por hacer cosas nuevas. Y más allá de lo profesional, valoro mucho la confianza que hemos adquirido durante estos años. Pablo, a quien más que un compañero de trabajo considero un amigo. Gracias a ti la tesis ha tenido menos ratos de *cuánto de sufrir*. Todos vosotros contribuís a que la calidad del trabajo que se hace en el grupo y que el clima que se ha creado sean excelentes. También quiero agradecer a todos los miembros del centro de investigación al que pertenezco, el CEMDATIC, y a los *profes* fotónicos, por su acogida y trato.

Siguiendo con el ámbito de la investigación, quiero hacer una mención especial a Vicente Durán. Gracias por la confianza, ayuda, y entusiasmo y disposición para colaborar. Espero que sigamos trabajando juntos en el futuro. También quiero agradecer al Ultrafast Photonics Group de la Universidad de Chalmers, liderado por Victor Torres-Company, del cual tuve el placer de formar parte durante tres meses en una estancia de investigación. A Victor, gracias por tu disponibilidad y por darme la oportunidad de trabajar en tu grupo durante esos meses. Conocer la investigación que se realiza en otros grupos siempre es algo fructífero; pero además, hacerlo en un grupo brillante como el que dirige Victor sin duda ha sido una experiencia muy enriquecedora. Durante esos tres meses tuve la oportunidad de trabajar mano a mano con Israel Rebolledo-Salgado. Gracias Isra por todo lo que me enseñaste durante la estancia y por confiar en mí para trabajar juntos en el setup y las medidas. Gracias por todos los momentos compartidos, dentro

y fuera del laboratorio, y por abrirme las puertas de tu casa. Espero que sigamos viéndonos, ya sea en congresos, Madrid, México o Gotemburgo.

Más allá de lo profesional, esta tesis no hubiera sido posible sin el apoyo –incondicional –de mi familia. A mis padres, porque gracias a ellos he podido desarrollarme como persona y llegar a donde estoy hoy. Papá, mamá, gracias por haberme dado la oportunidad de vivir la que considero que es y será una de las mejores etapas de mi vida, la etapa universitaria. Gracias a vosotros tengo una formación muy valiosa y puedo hacer mi vida en el lugar en el que desde pequeña había querido hacerlo. Me gusta reconocerme en vosotros, y espero poder hacerlo algún día tan bien como lo habéis hecho con mis hermanos y conmigo. A Fernando y a Miguel, porque vaya suerte la de tener hermanos. Gracias por hacerme sentir siempre acompañada. Tan iguales y tan diferentes al mismo tiempo, aprendo mucho de vosotros. A mi tía Esperanza, porque aunque probablemente no entienda bien de qué va *esto de la tesis*, siempre me hace sentir su inmenso cariño. Y a Alejandro, gracias por tu punto de vista que me hace ver el bosque, por el amor, y por el apoyo que me das. Me siento afortunada de la vida que hemos construido juntos y del balance que nos aportamos el uno al otro. Sin duda, haber recorrido este *viaje* de la mano, el de haber hecho una tesis a la vez (y haberla escrito a la vez), lo ha hecho todo más sencillo: es una suerte tener a alguien que entienda lo que ello supone.

A mis amigas, a mis amigos, los de *aquí* y los de *allí*. Juntos celebramos los éxitos de cada uno y también nos acompañamos cuando lo necesitamos: gracias.

Y finalmente, a todo aquel que lea esta tesis doctoral. A los miembros del tribunal y a los revisores. Gracias por dedicar parte de vuestro tiempo en leer este trabajo.

... Y aunque en ocasiones pareciera que no: *todo pasa, y todo queda*.

Abstract

Dual-comb interferometry is a sensing technique that harnesses the unique properties of optical frequency combs. It enables to measure the complex response of a sample with unprecedented spectral resolution and precision, as multiple spectral lines simultaneously interrogate the sample. The multiheterodyne nature of the technique, which relies on the beating of two optical frequency combs with slightly different repetition rates, allows to down-convert and compress the optical information into narrow radio frequency bandwidths. Unlike traditional sensing methods, these systems do not have moving parts, and the full information of a sample can be retrieved in a single and fast acquisition using low-bandwidth electronics. Since the first demonstrations in the early 2000s, dual-comb interferometry has shown great potential for a wide range of applications, including spectroscopy, ranging, imaging, and distributed sensing.

The deployment of dual-comb systems in field applications beyond the laboratory environment demands systems that are stable, portable, and inexpensive. To meet these requirements, comb sources based on semiconductor lasers have emerged as ideal candidates due to their well-known characteristics in terms of efficiency, compactness, and cost. Furthermore, the ability to integrate these dual-comb generators into photonic chips is a crucial factor in advancing the scalability of the technology. In this thesis, a dual-comb interferometer based on semiconductor lasers is demonstrated, and its performance is evaluated for absorption spectroscopy and ranging. The selected comb generators –gain-switched lasers –are particularly appealing owing to their simplicity and frequency agility.

The motivation and novelty of this dissertation is the enhancement of the versatility of gain-switched dual-comb interferometers, achieved by extending the line spacing of the optical frequency combs to low repetition rates in the MHz and sub-MHz range. In the field of spectroscopy, the proposed system enhances the spectral resolution of existing gain-switched dual-comb spectrometers by more than two orders of magnitude. Firstly, by using two gain-switched combs driven by pulsed gain-switching signals. Then, by densifying the combs via pseudorandom phase modulation. As a result, the proposed system opens the possibility of employing gain-switched frequency combs in high-resolution spectroscopy. In the field of ranging, the use of low-repetition-rate combs results in an increase of the non-ambiguity range. The developed system allows to resolve distances on the order of tens of meters without employing disambiguation techniques. Last, in pursuit of reducing the cost of dual-comb interferometers, the suitability of software-defined radio devices as digitizers is presented and demonstrated. The novel use of these devices in the receiver end of dual-comb systems represents a significant advancement towards the development of cost-effective dual-comb technology.

Finally, in the last experimental section of this thesis, dual-comb interferometry using two microresonator-based optical frequency combs is explored. The outcomes, resulting from a three-month international research stay, successfully demonstrate the measurement of the phase profile of an interrogated sample with a system comprising two microcombs mutually-pumped by a single continuous-wave laser.

Resumen

La interferometría realizada con peines de frecuencia dual es una técnica de sensado que aprovecha la singularidad de los peines de frecuencias ópticas. Esta técnica permite medir la respuesta compleja de una muestra con alta resolución espectral y precisión, pues múltiples líneas espectrales interrogan dicha muestra de forma simultánea. La naturaleza multiheterodina de la técnica, basada en la interferencia de dos peines de frecuencias ópticas con tasas de repetición ligeramente diferentes, permite la conversión a la baja y la compresión de la información desde el dominio óptico hasta el dominio de la radiofrecuencia. A diferencia de los interferómetros tradicionales, estos sistemas no tienen partes móviles y toda la información de la muestra se puede recuperar en una sola adquisición, con tiempos de medida rápidos, y utilizando electrónica de bajo ancho de banda. Desde las primeras demostraciones a principios de los 2000, la interferometría con peines de frecuencia dual ha demostrado gran potencial para numerosas aplicaciones, entre las que se incluyen la espectroscopía, la medida de distancias, técnicas de imagen y el sensado distribuido.

El despliegue de sistemas de peine dual en aplicaciones de campo requiere de sistemas que sean estables, portátiles y cuyo coste no sea muy elevado. En este contexto, las fuentes de peines de frecuencias ópticas basadas en láseres semiconductor surgen como candidatos ideales debido a sus bien conocidas características en términos de eficiencia, compacidad y coste. Además, la capacidad de integrar estos generadores de peine dual en chips fotónicos es un factor clave para el avance en la escalabilidad de esta tecnología. En esta tesis se desarrolla un interferómetro de peine dual basado en láseres semiconductor, y se evalúa su rendimiento para espectroscopía de absorción y medida de distancias. Los generadores de peine seleccionados —láseres conmutados por ganancia —resultan particularmente atractivos debido a su sencillez y sintonización en frecuencia.

La motivación y novedad de esta tesis doctoral es el aumento de la versatilidad de los interferómetros de peine dual conmutados en ganancia a través de la reducción del espaciado de línea de los peines hasta el rango de los MHz y sub-MHz. Para aplicaciones de espectroscopía, el sistema propuesto mejora la resolución espectral de los espectrómetros de peine dual conmutados en ganancia existentes en más de dos órdenes de magnitud. Primero, utilizando dos peines conmutados en ganancia empleando señales pulsadas para la conmutación. Después, con la densificación de los peines a través de la modulación pseudoaleatoria de la fase de los pulsos ópticos. Como resultado, el sistema propuesto abre la posibilidad de emplear peines duales conmutados en ganancia en espectroscopía de alta resolución. Para aplicaciones de medida de distancias, el uso de peines de frecuencia con tasas de repetición bajas permite incrementar el rango de no ambiguedad. El sistema desarrollado permite resolver distancias del orden de decenas de metros sin emplear técnicas para romper la ambiguedad. Por último, con objeto de reducir el coste de los interferómetros de peine dual, se presenta y demuestra la idoneidad de los dispositivos de radio definida por software como digitalizadores. El uso novedoso de estos dispositivos en el extremo receptor de sistemas de peine dual representa un avance significativo hacia el desarrollo de una tecnología de bajo coste.

Finalmente, en la última sección experimental de esta tesis se explora la interferometría de peine dual utilizando dos peines de frecuencias ópticas basados en microresonadores. Los resultados, fruto de una estancia internacional de tres meses de duración, demuestran la medida del perfil de fase de una muestra interrogada con un sistema comprendido por dos peines basados en microresonadores, bombeados por un único láser de onda continua.

Contents

List of Figures

List of Tables

Abbreviations and acronyms

ADC	Analog-to-digital converter
AOM	Acousto-optic modulator
AWG	Arbitrary waveform generator
BIPM	Bureau International des Poids et Mesures
BOSA	Brillouin optical spectrum analyzer
BPD	Balanced photodetector
BPF	Band-pass filter
CMOS	Complementary metal-oxide semiconductor
CNR	Carrier-to-noise ratio
CW	Continuous wave
DAC	Digital-to-analog converter
DC	Direct current
DFB	Distributed feedback
DUT	Device under test
DVB	Digital video broadcasting
EDFA	Erbium-doped fiber amplifier
EOPM	Electro-optic phase modulator
FBG	Fiber Bragg grating
FFT	Fast Fourier transform
FM	Frequency-modulated

FMCW Frequency-modulated continuous wave

FPF Fabry-Pérot filter

FSR Free spectral range

FWHM Full width at half maximum

FWM Four-wave mixing

GC Gas cell

GFA Grupo de fotónica aplicada

GPS Global positioning system

GS Gain-switched

GVD Group velocity dispersion

HITRAN High-resolution transmission molecular absorption

IF Intermediate frequency

IM Intensity modulator

IQ In-phase and quadrature

ITU International Telecommunication Union

LEF Linewidth enhancement factor

LIDAR Light detection and ranging

LO Local oscillator

ML Master laser

MLL Mode-locked laser

MLS Maximum length sequence

NIST National Institute for Standards and Technology

OFC Optical frequency comb

PM Phase modulator

PPG Pulse pattern generator

PRBS Pseudorandom binary sequence

RF Radio frequency

RMS Root mean square

SDR Software-defined radio

SL Slave laser

SMF Single-mode fiber

SNR Signal-to-noise ratio

VCSEL Vertical cavity surface emitting laser

WDM Wavelength-division multiplexing

Chapter 1

Introduction

This chapter aims to provide context for the present doctoral thesis. First, the motivation for the research line pursued is outlined. Next, an overview of the background of the research group where the thesis has been developed is provided, along with brief insights into the state-of-the-art of dual-comb interferometers based on gain-switched optical frequency combs at the time the thesis began. Finally, the objectives and structure of the thesis are detailed.

1.1 Motivation

The first demonstration of stimulated light emission by a semiconductor laser was reported in 1962 by three research groups: Robert Hall's group at General Electric Research Labs, Marshall Nathan's group at IBM Watson Research Labs, and Ted Quist's group at the Massachusetts Institute of Technology Lincoln Labs. This demonstration represents one of the major milestones in modern physics, as semiconductor lasers are now integral to numerous systems that are essential for contemporary life. After years of research, semiconductor lasers have enabled the generation of coherent light with devices that operate at room temperature, exhibit high wall-plug efficiency, and have progressively decreased in cost and size. Currently, these devices are mass-produced using a wide range of materials and structures, and can emit laser light across a spectral range from ultraviolet to mid-infrared. They are found in many systems, including optical communication systems, where semiconductor lasers serve as transmitters enabling global interconnection and data center interconnection; consumer electronics; sensing systems; materials processing; and medical applications, among others.

Functioning as a set of multiple coherent laser emitters with equally-spaced emission wavelengths distributed over a certain bandwidth, optical frequency combs (OFCs) have revolutionized many fields, such as metrology and spectroscopy, over the past twenty years. OFCs enable the generation of coherent multi-wavelength spectra from a single laser emitter, whose time-domain emission corresponds to a train of phase-locked short pulses featuring a specific periodicity. Over the years, the generation of OFCs has been demonstrated using various techniques and devices. In particular, semiconductor lasers offer a pathway towards simple, compact, and cost-effective comb sources.

In addition to the already mentioned advantages of semiconductor lasers, they can be integrated into photonic circuits. In recent years, integrated photonic circuits have emerged as a key-enabling technology for the next generation. This growth is driven by factors such as the increasing demand for transmission capacity and speed in current networks, as well as the emergence of new technologies based on light emission and detection, which are to be included in compact systems for applications such as mapping or high-resolution sensing. The evolution of integrated photonics aims to integrate various devices (such as laser sources, modulators, passive components, and detectors) manufactured from different materials (as silicon or indium phosphide) onto a single chip, allowing for the creation of complex on-chip photonic systems. Consequently, the development of photonic technologies using devices that can be integrated on a chip, such as semiconductor lasers and, in particular, comb sources based on these lasers, significantly contributes to the advancement of this transformative technology, providing solutions to address current needs.

This thesis is focused on the development of an interferometric system based on two OFCs generated by semiconductor lasers, for applications such as gas sensing and distance measurement. Aiming to develop a simple and inexpensive system that can potentially be integrated, gain switching of laser diodes is selected as the technique for the generation of the two combs. Moreover, this technique also provides flexibility in the selection of the repetition rate of the generated combs and can benefit from the use of low-cost electronics for the generation of the electrical signals involved. Compared to mature systems serving the same purpose, such as tunable diode laser spectrometers for gas sensing or time-of-flight light detection and ranging (LIDAR) systems for measuring distances, dual-comb interferometers benefit from their multi-wavelength nature. By simultaneously interrogating the sample or target with multiple wavelengths, dual-comb interferometers achieve improved spectral resolution for gas sensing measurements and enhanced precision for distance measurements. In addition, the interferometric information is down-converted from the optical domain to the radio frequency (RF) domain, and can be retrieved in a single and fast acquisition using a setup without moving parts and low-bandwidth detectors and digitizers. Finally, the targeted applications align with current demands, such as the development of environmental pollution monitoring systems to quantify the increasing emission of pollutant gases into the atmosphere or the development of miniaturized mapping systems to be included in augmented reality systems, personal health devices, or unmanned vehicles.

1.2 Antecedents and context

The present doctoral thesis has been carried out in the Applied Photonics Group (GFA, by its acronym in Spanish) of the CEMDATIC (*Centro de Materiales y Dispositivos para las TIC*) - Universidad Politécnica de Madrid. The group has a long research trajectory, focused during the last thirty years on the theoretical and experimental study of semiconductor lasers and their applications.

This thesis begins in the context of a national project, through a contract for the training of research fellows[1]. This project, the LIDERA project, coordinated by the GFA together with researchers from the Institute of Physics of Cantabria, was granted in 2018. The goal of the project was the study and development of advanced LIDAR systems based on OFCs, coherent technologies, and chaotic signals. And more specifically, the objective of the thesis, as defined in the LIDERA project and fully aligned with the results achieved during the course of the thesis, was the development of remote sensing systems for gases and ranging using dual OFCs generated by semiconductor lasers. The LIDERA project emerged as a continuation of a previous national project held by the research group, which was jointly coordinated with Institute of Physics of Cantabria and researchers from the University of the Balearic Islands. This project was devoted to the research on the generation of OFCs with semiconductor lasers. As a result of this earlier project, Alejandro Rosado completed his Ph.D. thesis on the experimental and theoretical study of OFCs generated by gain switching of semiconductor lasers. Conducted within the GFA, that thesis enabled the group to acquire extensive knowledge about the dynamics of semiconductor lasers subjected to gain switching and external optical injection. In addition to the experimental generation of gain-switched (GS) combs, a rate equation model for the numerical simulation of these combs was developed. This model has been used during this thesis for the simulation of two mutually-coherent GS OFCs.

Given the expertise of the group in GS OFCs, the topic of this thesis –which in basic aspects is focused on exploring applications where the use of these combs might offer advantages over existing systems –was a natural evolution of the research line. By the time this thesis started, the research group had made four scientific contributions related to the experimental generation and numerical simulation of GS OFCs, featuring different repetition rates and using various electrical excitation signals (sine waves and trains of pulses). In relation to existing publications on this topic, pioneered by the first demonstration of a GS OFC by P. Anandarajah et al. [1] as detailed in the review of the state of the art in Chapter 2, the works of the GFA focused on the underlying physics of GS combs, which were rather unexplored at that time. These investigations resulted in useful guidelines for the generation of combs with specific characteristics, beneficial for various applications.

[1]After 18 months of this contract, the thesis was continued through a contract as an Assistant Professor at *Escuela Técnica Superior de Ingenieros de Telecomunicación* of *Universidad Politécnica de Madrid*, without altering the objectives of the thesis defined in the national project.

Since the first demonstration of a GS comb in 2009, several contributions have been made regarding the potential of systems based on a single OFC, primarily in the field of optical communications. These applications involve the generation of combs with high repetition rates of several gigahertz to be included in multi-carrier systems as an alternative to the use of multiple laser transmitters. In parallel, in 2008, the potential of using systems based on the interference of two mutually-coherent OFCs [2] was demonstrated as a powerful sensing technique that enabled mapping information contained in the optical frequency range to the RF domain. The potential of this technique, known as dual-comb interferometry, is enhanced when the employed combs exhibit low repetition rates and broad bandwidths, as these characteristics allow to perform measurements with a high spectral resolution extracting the information from a wide spectral range. The use of a pair of GS combs for dual-comb interferometry was first reported in 2016 by the research group led by P. Acedo from Universidad Carlos III de Madrid. They demonstrated the retrieval of an absorption line of hydrogen cyanide in gaseous state in the 1.5 μm range [3], [4]. Prior to this thesis, these two works carried out by the group of P. Acedo were the only publications on systems based on dual GS combs. This gap in the research topic presented an exciting opportunity to further explore these systems. In this regard, the research line followed in this work is oriented towards the impact of reducing the repetition rate of the combs employed for dual-comb interferometric measurements. The investigated approaches open the possibility of measuring narrow spectral features (spectral widths of hundreds of MHz) or increasing the non-ambiguity range of ranging measurements using semiconductor-based dual-comb systems.

1.3 Objetives

The primary objective of this thesis is the development of a dual-comb system based on OFCs generated by gain switching of semiconductor lasers for gas sensing and distance measurement applications. The use of low-repetition-rate OFCs is proposed, given their benefits for the targeted applications: improvement of the spectral resolution in spectroscopic measurements and extension of the maximum distance that can be measured without ambiguity in ranging applications. This main goal has been pursued through the following specific objectives:

- Optimization of the spectral characteristics of low-repetition-rate GS OFCs for their use in gas sensing and ranging applications.
- Reduction of the line spacing of GS OFCs through advanced techniques: external electro-optic densification.
- Implementation of a gas sensing system based on two GS combs that improves the spectral resolution of similar state-of-the-art systems.
- Implementation of a ranging system based on two GS combs exhibiting low repetition rates for the extension of the non-ambiguity range.

Additionally, the exploration of microcomb generation and the development of a microcomb-based dual-comb sensing system were proposed as objectives for the three-month international research stay.

1.4 Structure of the thesis

Next to this introductory chapter, the dissertation is structured as follows:

- Chapter 2: Optical frequency combs. In this chapter, a comprehensive review of the fundamentals underlying OFCs is provided, with particular emphasis on the gain-switching technique for generating frequency combs using laser diodes. A historical perspective and an overview of the state of the art are also provided. In addition, alternative techniques for generating combs are discussed.

- Chapter 3: Dual-comb interferometry. In this chapter, the fundamentals of dual-comb interferometry are presented, and the main considerations for the design and implementation of a dual-comb interferometer are outlined. The use of dual-comb interferometers for molecular spectroscopy and ranging is discussed, and contributions in these areas using GS combs and other related sources are reviewed.

- Chapter 4: High-resolution dual-comb spectroscopy with gain-switched combs. In this chapter, an experimental demonstration of a dual-comb spectrometer with a spectral resolution of 100 MHz is presented. The resolution of 100 MHz is achieved through pulsed gain switching of laser diodes. An optimization of the spectral characteristics of the combs is first detailed, and the influence of the driving parameters of the lasers on the performance of the combs is studied. Then, using two of these combs, an absorption line of hydrogen cyanide gas is measured. Finally, the use of a software-defined radio at the receiver end of the spectrometer is proposed as an inexpensive digitizer.

- Chapter 5: Improving the resolution of gain-switched dual-comb spectrometers. In this chapter, different strategies for decreasing the line spacing of GS combs are explored. Through the electro-optic modulation of two GS combs, two mutually-coherent densified combs with a repetition rate in the few megahertz range are experimentally generated and used for dual-comb interferometry measurements.

- Chapter 6: Dual-comb ranging with gain-switched combs. This chapter is devoted to the experimental demonstration of a dual-comb ranging system using GS OFCs. The measurement of open-path distances by means of the analysis of the interferometric information resulting from the interference of two 100-MHz GS combs is demonstrated. The extension of the non-ambiguity range by means of the densification of the two combs is explored, and proof-of-concept measurements are presented.

- Chapter 7: Exploring other dual-comb interferometers. In this last experimental chapter, the results from an international research stay at the Ultrafast Photonics group of Chalmers University of Technology in Gothenburg (Sweden) are presented. The Ultrafast Photonics group, led by Professor Victor Torres-Company, has a proven track record in microcomb research. From the work developed alongside Israel Rebolledo-Salgado, a dual-comb interferometer based on microcombs is demonstrated. The performance of the system is verified by successfully retrieving the phase of a programmed optical filter.

- Chapter 8: Conclusions and outlook. In this last chapter, the main conclusions extracted from the dissertation are outlined. Also, future lines are proposed.

Chapter 2

Optical frequency combs

Optical frequency combs are laser sources that act as rulers of light, capable of measuring optical frequencies with unprecedented precision. Their discovery more than twenty years ago marked a revolution in the field of metrology, recognized in 2005 with the awarding of half of the Nobel Prize in Physics to Theodor W. Hänsch and John L. Hall for their significant contribution to precision spectroscopy. Since then, the generation, control, and application of frequency combs constitutes a relevant research field in photonics, attracting the attention of a large scientific community. In the last decade, the advent of photonic integrated circuits has enabled the integration of these light sources. Current technology allows to obtain comb sources in millimeter or micrometer-sized chips with outstanding power consumption performances. The wide range of applications of these light sources, combined with their miniaturization, has paved the way for significant advancements towards including comb generators in real-world systems, such as high-capacity optical transmitters, light detection and ranging, spectroscopy systems, and microwave photonics.

This chapter is devoted to the description of optical frequency combs. The fundamentals of optical frequency combs are first explained, along with a historical perspective. Next, the main technique used in this dissertation for the generation of frequency combs is detailed: gain switching of semiconductor lasers. In addition to the fundamentals of the technique, contributions related to gain-switched optical frequency combs based on discrete components as well as integrated systems are reviewed. Other comb generation techniques based on semiconductor lasers are also presented, outlining their most important aspects and some relevant demonstrations. Finally, a description of optical frequency combs based on Kerr microresonators is provided.

2.1 Fundamentals of optical frequency combs

An optical frequency comb (OFC) is a coherent light source whose spectrum consists of equally spaced, discrete, frequency lines. In the time domain, this spectrum corresponds to a train of phase-correlated optical pulses.

The first sources for generating OFCs were femtosecond mode-locked lasers (MLLs). In an MLL, an optical pulse circulates within an optical cavity, and on every round trip an attenuated version of the optical pulse leaves the cavity through a partially reflective mirror. The output of the laser is a train of coherent ultra-short optical pulses with carrier frequency ν_c modulated by a periodic envelope $A(t) = A(t+T)$, where the period $T = (2L)/v_g$ is defined by the group velocity of the pulses within the cavity, v_g, and by the length of the cavity, L. Such train of pulses corresponds to a broad optical spectrum composed by frequency tones that are evenly spaced $f_R = 1/T$. The spectral width of the comb is related to the temporal width of the optical pulses.

Due to dispersion in the cavity, the group velocity at which $A(t)$ propagates and the phase velocity of the carrier wave are different. Consequently, the generated optical pulses undergo a constant phase slip of the carrier wave with respect to the pulse envelope, $\Delta\phi$. In the frequency domain, this slip introduces a frequency shift in the comb spectrum by the carrier-envelope offset frequency, f_{CEO}. As a result, the positions of the comb lines are not an exact multiple of the repetition frequency, but an offset must be taken into account. Accordingly, the frequencies of the comb lines can be written as [5]

$$\nu_m = f_{CEO} + m f_R \tag{2.1}$$

where m is a positive integer in the order of $10^5 - 10^6$ for typical MLLs.

The potential of OFCs is summarized in this simple equation (Eq. (2.1)). If the values of f_{CEO} and f_R are known, it is possible to define any comb line ν_m in terms of two radio frequencies. As a consequence, the OFC acts as a highly precise optical ruler and provides a direct link between radio frequencies and optical frequencies. The time and frequency domain pictures of a typical MLL comb are illustrated in Fig. 2.1.

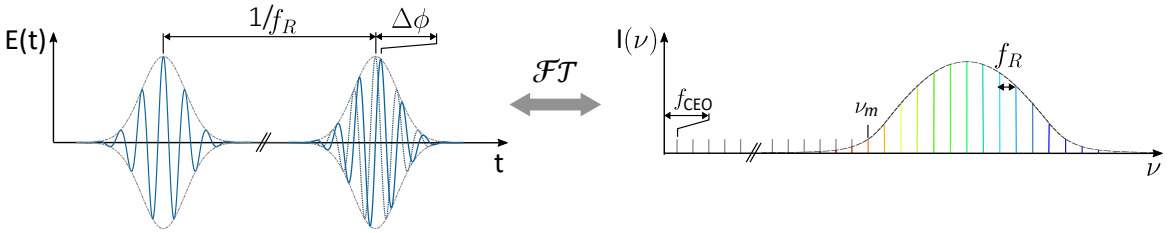

Figure 2.1: Illustration of an OFC in time and frequency domains.

In this thesis, without loss of generality, it is more convenient to number the comb lines relative to a reference optical mode, denoted ν_0, as

$$\nu_n = \nu_0 + n f_R \tag{2.2}$$

where n is a positive integer, with $n = 0$ corresponding to ν_0, the first (lowest-frequency) comb line that has sufficient optical power.

The complex representation of the optical field of an ideal frequency comb can be then described with the following equation

$$E(t) = \sum_{n=0}^{N-1} A_n e^{-j(2\pi\nu_n t + \phi_n)}, \tag{2.3}$$

with A_n, ν_n, and ϕ_n being the amplitude, frequency, and phase of the n^{th} comb line, and N representing the total number of comb teeth.

The history of OFCs is closely tied to the field of frequency metrology. Frequency is the physical quantity that can be measured with highest accuracy. It is measured by counting the number of cycles over a specific time interval, and the accuracy of the measurement depends on the clockwork that counts the cycles [5]. In 1967 the *Boureau International des Poids et Measures* (BIPM) redefined the second, the unit of time of the International System. It was defined from the frequency of a hyperfine transition of the cesium-133 atom, which oscillates at 9 192 631 770 Hz. This definition is still valid today; however, the development of optical atomic clocks, in which OFCs serve as clockworks, may likely result in a forthcoming redefinition of the second, based on an optical frequency standard rather than on a microwave standard. This redefinition, projected by the BIPM for 2030 [6], will result in a significant improvement in accuracy over current atomic clocks, as it allows for a finer division of the second.

Prior to the advent of OFCs, the measurement of absolute optical frequencies was a complex process. It involved heterodyning the optical frequency of a stabilized laser and the optical frequency of the targeted transition, followed by down-conversion frequency chains to bring the generated beat note into the bandwidth of a fast photodetector. This beat note, which was in the microwave range, could then be calibrated against a cesium clock. However, these measurements required long, complex, and bulky frequency-conversion chains, which were specifically designed to measure a single optical frequency. The development of the OFC represented a revolutionary milestone, as it permitted to replace these complex frequency chains by a single laser source [7].

OFCs are the result of research efforts in various fields: laser stabilization, ultrafast lasers, and nonlinear optics [8]. The starting point of this journey dates back to 1978, with the publication by Theodor W. Hänsch's group at Standford of an impressive work that demonstrated the generation of an OFC from a picosecond mode-locked dye laser to measure the 3s-4d transition of the sodium atom [9]. However, the bandwidth of these combs was not wide enough to determine the offset frequency, preventing their use for absolute frequency measurements. In the early 1990s, femtosecond Ti:sapphire lasers became commercially available. The possibility of having one of these solid-state lasers in a laboratory facilitated the progress in the generation of ultra-short pulses, allowing significant advancements in the field. As a result, in 1997, Hänsch proposed a self-referenced OFC synthesizer capable of producing a ruler of light with known, equidistant frequencies, and described the self-referencing technique to determine the carrier-envelope offset frequency. This technique, illustrated in Fig. 2.2, is based on the generation of an octave-spanning (frequency doubling) comb. A spectral line with index m of the OFC is frequency doubled and then interfered with the $2m$ line, in a configuration widely known as $f-2f$ interferometer. The beating of these two frequency lines provides f_{CEO}: $2\nu_m - \nu_{2m} = 2mf_R + 2f_{CEO} - 2mf_R - f_{CEO} = f_{CEO}$. In addition, other important contributions such as the demonstration of the equal spacing of the lines of a frequency comb [10] or the realization of precision spectroscopy measurements using a femtosecond laser [11] were made at that time.

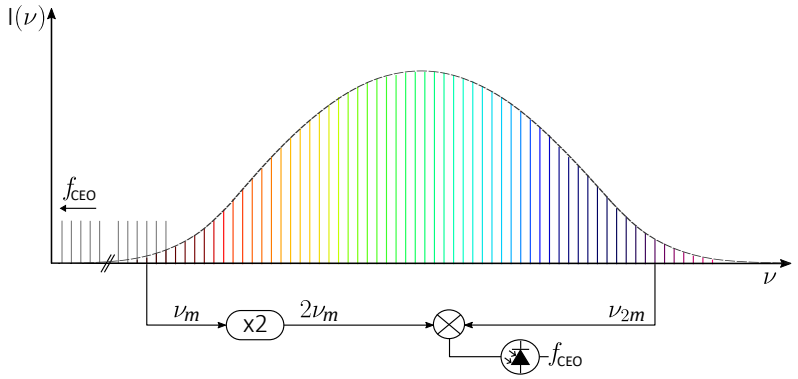

Figure 2.2: Illustration of an $f-2f$ interferometer based on an octave-spanning optical frequency comb that enables to measure the carrier-envelope offset frequency and therefore to perform absolute frequency measurements.

During those years, two researchers from the Joint Institute for Laboratory Astrophysics, John L. Hall and Steven Cundiff, visited Hänsch's laboratory at the Max Planck Institute of Quantum Optics in Garching, Germany. Motivated by the achievements of the Garching group, they decided to pursue research in this direction. The "competition" between the two groups accelerated the results. At that moment, although femtosecond OFCs were broader than those obtained with the picosecond counterpart, it was still necessary to incorporate some frequency-conversion stages in the systems used to measure absolute optical frequencies. This changed with the advent of nonlinear optics in the late 1990s. At CLEO (Conference of Lasers and Electro-Optics) 1999, researchers from Bell Labs presented a new type of fibers, microstructured fibers, capable of broadening the

spectrum of femtosecond Ti:sapphire lasers without the need for frequency multipliers or dividers [12]. The emergence of these fibers marked a significant turning point. Soon after, in the early 2000s, Hall's group in Boulder and Hänsch's group in Garching published the first works demonstrating the generation of octave-spanning self-referenced combs expanded by means of these novel fibers [13]–[15]. This path culminated in 2005 with the awarding of half of the Nobel Prize to Hänsch and Hall for their contributions to precision spectroscopy. From then to the present day, OFCs remain an active and continuously evolving area of research. In addition, commercial comb synthesizers, such as those developed by Menlo Systems (originally a spin-off company of the Garching group) are available nowadays.

Since then, the versatility of OFCs has been expanded to a variety of applications [7]. Likewise, the number of sources or techniques for generating combs has also increased. The performance of the generated OFCs, in terms of spectral coverage and line spacing, varies depending on the technique employed, and their suitability for specific applications accordingly differs. OFCs with large line spacings (from a few GHz up to hundreds of GHz) are used, for instance, in optical communications, acting as transmitters in wavelength-division multiplexing (WDM) systems. In such systems, continuous-wave (CW) laser sources used to generate optical carriers at different wavelengths are replaced by a single OFC. They are also employed as microwave generators, since the detection of the OFC in a photodetector with a bandwidth adjusted to the comb repetition frequency generates a sinusoidal RF signal that shows a high stability, provided that the comb is stabilized. Also, for the calibration of astronomical spectrographs. These instruments, typically used in the search for exoplanets or in cosmology studies, experience drifts that can mask the true signal. The continuous calibration of the spectrograph using an OFC with known frequency positions allows to correct these drifts and enhances the performance of the measurements. On the other hand, OFCs with low line spacings (below 1 GHz) are of particular interest for such applications in which the spectral resolution is a key factor. Molecular spectroscopy is one of these applications, in which the use of OFCs (especially in dual-comb configuration) is widespread. The resolution of the measurement improves as the comb spacing is reduced. For ranging, the use of these combs is also beneficial, since the maximum distance that can be measured without ambiguity (non-ambiguity range) is inversely proportional to the repetition rate of the optical pulses.

Finally, although the research on OFCs based on discrete components continues growing, their integration on different platforms such as III-V semiconductors, silicon nitride (Si_3N_4), and lithium niobate ($LiNbO_3$), among others, is gaining increasing relevance in recent years [16]. The miniaturization of comb generators shows a promising prospect, as it enables the development of comb-based systems that feature lower cost and higher energy efficiency than their discrete counterparts. These advancements facilitate their widespread use in field-deployable applications.

2.2 Optical frequency combs generated by gain-switched laser diodes

OFCs based on semiconductor lasers have garnered significant attention from the scientific community in recent years, as they offer simple, cost-effective, and easily integrable comb sources. In particular, gain-switched laser diodes have proven effective for the generation of frequency combs. They combine the advantages of semiconductor lasers and the advantages of the generation technique itself. Moreover, the generated combs are reproducible and stable over time under fixed operating conditions (current and temperature). One of their main advantages is the tunability of the modulation frequency, yielding frequency-agile combs whose line spacing can be easily changed. The tuning range of the modulation frequency covers from ∼10 GHz (limited by the modulation bandwidth of the laser diode) to frequencies below 100 MHz, as it will be discussed in this thesis. Therefore, the generated OFCs can address a wide range of applications: high-frequency OFCs are of interest for applications such as optical communications or RF signal synthesis, while low-frequency OFCs are useful for spectroscopy or ranging applications, to cite a few.

The tunability of the repetition rate of GS combs is a great advantage over techniques where the line spacing is fixed. This is the case, for example, of microcombs, where the line spacing is also generally limited to high repetition rates (from tens of GHz), as the generation of low-repetition-rate OFCs involves long optical cavities. In addition, they can operate in different spectral regions, since the center wavelength of GS combs corresponds to the laser emission wavelength. Although most of the demonstrations have been carried out in the C-band, there have also been demonstrations at 2 μm [17]. This center wavelength can be slightly tuned by changing the laser driving current and/or the laser operating temperature, being this tuning range limited to 1 or 2 nm. Regarding the limitations, the main one is the low power of the generated combs. When the laser intensity is modulated, the duty cycle of the pulsed optical signal at the laser output is usually below 50%, a quantity that deteriorates as the modulation frequency is reduced. Therefore, the average optical power is generally low, and the power per comb line (obtained as the ratio of the average power to the number of comb lines) is dramatically reduced as the number of comb lines is increased. Finally, it should be noted that GS combs have modest bandwidths (currently up to values in the order of a hundred GHz without post-broadening techniques) compared to those obtained with other comb generators such as mode-locked lasers or microcombs, where OFCs with spectral widths of tens of THz (or even octave-spanning bandwidths in the case of microcombs [18]) are obtained.

2.2.1 Introduction to gain switching

Gain switching is a well-established method for generating picosecond optical pulses in semiconductor lasers, with its origins dating back to the 1980s [19]–[21]. This technique is based on the modulation of the electric current that drives the laser utilizing the superposition of a direct bias current (DC) and an alternating RF current (AC). This RF current is usually a sinusoidal signal. Both currents, DC and AC, are combined using a bias-tee element, which includes an inductance in the low-frequency port to block the AC component and a capacitor in the high-frequency port to block the DC bias component entering into the RF source. By conveniently configuring the driving current (bias + RF), a train of optical pulses is generated at the output of the laser, with a repetition frequency imposed by the frequency of the alternating current. A typical setup for obtaining gain-switched optical pulses in a laser diode is shown in Fig. 2.3.

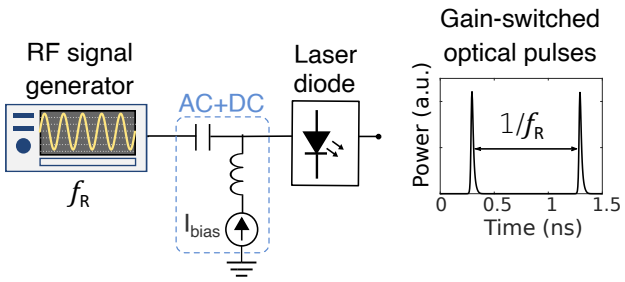

Figure 2.3: Typical experimental setup for the generation of gain-switched optical pulses. The appropriate modulation of the laser diode with the superposition of an RF signal and a bias current results in a train of short optical pulses emitted by the laser.

To understand the gain-switching technique, it is convenient to analyze the dynamic response of a semiconductor laser by means of a rate equation model [22], [23], which describes the variation of carriers and photons in the active region of the laser and the evolution of the optical phase. Considering single-mode emission and assuming spatial uniformity in the laser cavity, the expressions of the rate equations for the carrier density, $N(t)$, the photon density, $S(t)$, and the optical phase, $\phi(t)$, can be written as

$$\frac{dN(t)}{dt} = \frac{I(t)}{qV_{act}} - [R_{sp}(N) + R_{nr}(N)] - \frac{v_g g(N) S(t)}{1 + \varepsilon S(t)}, \tag{2.4}$$

$$\frac{dS(t)}{dt} = \frac{\Gamma v_g g(N)}{1 + \varepsilon S(t)} S(t) - \frac{S(t)}{\tau_p} + \Gamma \beta_{sp} R_{sp}(N), \tag{2.5}$$

$$\frac{d\phi(t)}{dt} = \frac{\alpha}{2}\left(\Gamma v_g g(N) - \frac{1}{\tau_p}\right), \tag{2.6}$$

where $I(t)$ is the injected current, q is the electron charge, V_{act} is the volume of the laser active region, $R_{sp}(N)$ is the spontaneous recombination rate, $R_{nr}(N)$ is the nonradiative recombination rate, v_g is the group velocity in the laser medium, $g(N)$ is the optical

gain, ε is the nonlinear gain coefficient (which accounts for the saturation of the optical gain that occurs for high photon densities), τ_p is the photon lifetime, β_{sp} accounts for the spontaneous emission coupled into the lasing mode, Γ is the confinement factor of the optical mode in the active region, and α is the linewidth enhancement factor (LEF). Noise sources and thermal effects have not been considered in Eqs. (2.4) to (2.6). For a detailed description of the noise and the changes of the emission frequency of the laser due to temperature variations, the reader is referred to [24].

Eq. (2.4) represents the change in the carrier density when current is injected into the laser diode (first term), counteracted by the depletion of carriers due to spontaneous or nonradiative (second term), and stimulated (third term) recombination. R_{sp} describes the recombination of an electron of the conduction band with a hole of the valence band, a process that results in the spontaneous generation of a photon, while R_{nr} accounts for recombination processes that does not contribute to the generation of a photon, such as recombination at defects, surfaces, and Auger recombination. It is common to assume linearity between these recombination rates and the carrier density using the carrier lifetime, τ_c, as $R_{sp} + R_{nr} = N/\tau_c$. Furthermore, according to their dependence with the carrier density, they can be expressed as a polynomial in N

$$R_{sp} + R_{nr} = AN + BN^2 + CN^3, \tag{2.7}$$

where $R_{sp} \sim BN^2$, and $R_{nr} \sim (AN + CN^3)$. A, B and C being the linear, bimolecular and Auger recombination coefficients, respectively.

Eq. (2.5) describes the evolution of the photons, generated via stimulated (first term) and spontaneous (third term) emission. The decay rate of the photon density (second term) is expressed in terms of τ_p, defined as

$$\tau_p = \frac{1}{v_g(\alpha_m + \alpha_i)}, \tag{2.8}$$

with α_m and α_i being the mirror loss and internal loss coefficients of the cavity, respectively.

The optical gain, $g(N)$, can be described with a linear dependence with the carrier density

$$g(N) = \frac{dg}{dN}(N - N_{tr}), \tag{2.9}$$

with $\frac{dg}{dN}$ being the differential gain and N_{tr} the transparency value of the carrier density.

Finally, Eq. (2.6) describes the variation of the optical phase related to changes in the carrier density, and hence in the optical gain. This occurs due to the variation induced in the refractive index of the laser active region as a consequence of variations in the carrier density. In addition, the α parameter or LEF, also known as Henry factor after Charles H. Henry [25], is introduced in the equation. This parameter, which is essential

for describing a laser diode, describes how the complex refractive index is influenced by changes in the carrier density

$$\alpha = -\frac{dn/dN}{dn_i/dN} = -\frac{4\pi}{\lambda}\frac{dn/dN}{dg/dN}, \tag{2.10}$$

where n and n_i are the real and imaginary parts of the refractive index, respectively, and λ is the emission wavelength.

For a laser diode to operate under gain-switching conditions, the electric current supplied to the laser must be abruptly varied from a value near or below its threshold current to a value well above threshold. The nonlinear response of the laser diode when it is subjected to a sudden change in the injection current leads to different effects that determine the characteristics of the generated optical signal. First, in the turn-on process, the laser initially undergoes a transient regime. This process is illustrated in Fig. 2.4 (a), which is a simulation showing the evolution of the carrier density (blue trace) and the optical power (orange trace) of a laser diode in response to a current step (black trace). It must be mentioned that the results shown in Fig. 2.4 have been generated using a simulation model that numerically solves the rate equations described above (Eq. (2.4), Eq. (2.5), Eq. (2.6)). The model[1] used is the one developed in [24]. This model will be the one used throughout all the simulations performed in this thesis, sometimes with certain modifications that will be conveniently detailed. The laser used in the simulations is a discrete-mode laser, described by the parameters used in [24]. These parameters were extracted, as detailed in [24], from [26] and from experimental measurements. They are summarized in Table 2.1 for the ease of the reader.

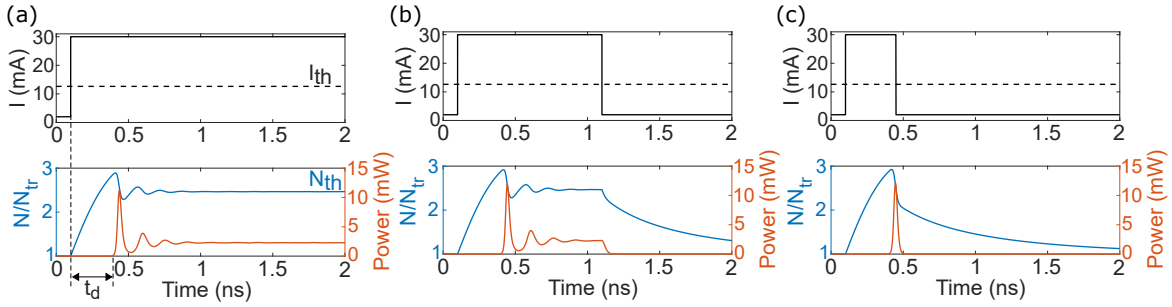

Figure 2.4: (a) Numerical simulation of the turn-on process of a laser when an ideal current step is injected into the laser. The injected electric current is depicted in the top panel, while the evolution of the carrier density normalized to N_{tr} (blue) and the optical power (orange) is included in the lower panel. (b) Numerical simulation showing the response of the carriers and the photon density of the discrete-mode laser to a current pulse having a duration of 1.09 ns. (c) Emission of a gain-switched pulse when the duration of the current pulse injected into the laser is decreased to 440 ps.

[1]The model includes stochastic noise terms that are not included in the rate equations described in this text. A detailed description of the noise treatment can be found in [24]. In addition, in the simulations carried out during this thesis, temperature-dependent frequency shifts are not considered.

Symbol	Value	Units
V_{act}	$1.53 \cdot 10^{-17}$	m^3
Γ	0.06	-
N_{tr}	$1.3 \cdot 10^{24}$	m^{-3}
B	$1.5 \cdot 10^{-16}$	m^3s^{-1}
dg/dN	$4.38 \cdot 10^{-20}$	m^2
τ_p	2.17	ps
A	$2.8 \cdot 10^{8}$	s^{-1}
C	$9 \cdot 10^{-41}$	m^6s^{-1}
β_{sp}	$5.3 \cdot 10^{-6}$	-
η_f	0.17	-
ε	$1.97 \cdot 10^{-23}$	m^3
α	3	-

Table 2.1: Internal parameters of the discrete-mode laser used in the numerical simulations [24].

As a result of the injection of electrons, the carrier density of the laser starts to increase, and, eventually, it reaches its threshold value (N_{th}). After this moment, the photon density starts to rise. The time elapsed between the application of electric current and the onset of the optical pulse emission is known as turn-on delay (t_d). The turn-on delay can be derived from the rate equation of the carriers [27], and can be written as follows

$$t_d = \tau_c \ln \frac{I_{on} - I_{off}}{I_{on} - I_{th}}, \quad I_{off} < I_{th} < I_{on} \tag{2.11}$$

where I_{off}, I_{on} and I_{th} are the initial, final and threshold current of the laser, respectively. In the simulation shown in Fig. 2.4, $I_{off} = 2$ mA and $I_{on} = 30$ mA. The threshold current, obtained from the simulated power-current characteristic, is $I_{th} = 12.6$ mA. These values lead to a turn-on delay $t_d \sim 200$ ps.

Then, after the photon density starts to grow, both the carrier density and the photon density experience damped oscillations until they reach steady state. These oscillations, known as relaxation oscillations, are the result of the different dynamic response of carriers and photons. At the conditions of Fig. 2.4, the frequency of the relaxation oscillations is ∼6.25 GHz. In order to generate short gain-switched optical pulses, it is necessary to configure the modulation current in such a way that the laser diode is turned off before the second peak of the relaxation oscillations occurs. Fig. 2.4 (b) shows the carrier density and the output power when an ideal current pulse of 1.09 ns is applied to the laser. In this case, the electrical pulse is not short enough to prevent the relaxation oscillations. In Fig. 2.4 (c) the duration of the electrical pulse is decreased to 440 ps, and the laser switches off before the appearance of the second spike of the relaxation oscillations, resulting in the emission of an optical pulse. It is in this situation when the laser is effectively emitting gain-switched pulses.

In addition to the turn-on delay and the relaxation oscillations, there are other effects resulting from the abrupt modulation of a laser diode that condition the properties of the generated optical pulses, such as frequency chirp. Frequency chirp ($\delta\nu$) is a frequency modulation that arises from the intensity modulation of the laser. It is related to instantaneous changes of the optical phase, in the form $\delta\nu(t) = \frac{1}{2\pi}\frac{d\phi(t)}{dt}$. Due to the already mentioned variations of the refractive index of the laser medium as a consequence of changes of the carrier density, the optical phase changes. These changes translate into shifts of the emission frequency of the laser and the resulting optical spectrum experiences broadening.

Frequency chirp is often expressed in terms of the optical power at the output of the laser, $P(t)$. The optical power at the output of one facet of the laser can be expressed in terms of the photon density [28] as

$$P(t) = \frac{V_{act}\eta_f h\nu_0}{2\Gamma\tau_p} S(t), \tag{2.12}$$

where η_f is the total differential quantum efficiency including laser to fiber coupling, h is the Planck constant, and ν_0 is the emission frequency. Then, using Eq. (2.12) and the rate equations for the photon density and the optical phase (Eq. (2.5) and Eq. (2.6), respectively), the frequency chirp can be approximated as

$$\delta\nu(t) = \frac{\alpha}{4\pi}\left(\frac{1}{P(t)}\frac{dP(t)}{dt} + \frac{2\Gamma\varepsilon}{V_{act}\eta_f h\nu_0}P(t)\right). \tag{2.13}$$

The first term of Eq. (2.13), commonly referred to as dynamic chirp, originates from rapid carrier variations that occur during the laser transient regime. The second term is an adiabatic component that occurs when the laser operates in steady state regime, and it is linked to the saturation of the optical gain. There is also a contribution to the adiabatic chirp term related to thermal effects, not included in this formulation.

In gain-switching operation, the optical pulses are mainly affected by dynamic chirp, since the laser is not allowed to reach steady state. Since chirp is inherent to laser modulation, the generated optical pulses deviate from being Fourier-transform limited pulses, which can be detrimental for some applications. However, in the context of gain-switched combs, a higher dynamic chirp can be beneficial since it results in an enhancement of the spectral width of the combs [24], [29].

Gain switching and optical injection

In addition to the already mentioned characteristics, gain-switched pulses suffer from timing jitter, i.e., temporal fluctuations that affect the periodicity of the pulses. The nature of this timing jitter is related to the pulse generation mechanism, and it is attributed to random fluctuations in the spontaneously emitted photons during the turn-on process of the laser, causing differences in the turn-on delays of subsequent pulses. Although this is an inherent process in the generation of gain-switched pulses,

some strategies such as external optical injection of the modulated laser by a second laser have demonstrated to significantly reduce it [30], [31]. Furthermore, not only timing jitter but also side mode suppression ratio or frequency chirp can be improved through external optical injection [32].

The typical configuration used to implement external injection locking is the so-called master-slave configuration, shown in Fig. 2.5. The master laser (ML), which operates in CW, injects its light through an optical circulator into the slave laser (SL), which is under gain-switching operation. It is crucial for the SL not to have a built-in optical isolator in order to enable external optical injection. As a consequence of injection, the SL switches on from stimulated emission photons injected in its cavity by the master, thereby reducing random fluctuations in the photon density that affect the quality of the generated optical pulses. Additionally, the ML transfers its optical properties, such as its linewidth, to the SL.

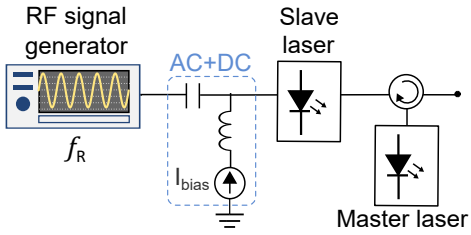

Figure 2.5: Typical experimental setup for the generation of gain-switched optical pulses with external optical injection. This configuration is widely known in the literature as master-slave configuration. The master laser injects its CW light into the gain-switched slave laser by means of an optical circulator, provided that the slave laser does not incorporate an optical isolator at its output.

If a laser diode is optically injected, the rate equation model introduced before needs to be modified, since the injected photon density, the phase of the injected photons, and the emission wavelength of the ML have to be included.

Frequency detuning ($\delta\nu'$) is defined as the frequency difference between the emission wavelength of the ML and the SL, both in CW and operating at threshold current. This parameter, together with the injected power, determine the locking conditions, i.e., only under certain power and detuning conditions the slave is injected and operates in a stable locking region. Under external optical injection, the rate equations for the photons and phase can be described by the expressions below [24]

$$\frac{dS(t)}{dt} = \frac{\Gamma v_g g(N)}{1+\varepsilon S(t)} S(t) - \frac{S(t)}{\tau_p} + \Gamma \beta_{sp} R_{sp} + 2k_c \sqrt{S(t) S_{inj}(t)} \cos(\phi(t) - \phi_{inj}(t) - 2\pi\delta\nu' t), \tag{2.14}$$

$$\frac{d\phi(t)}{dt} = \frac{\alpha}{2}\left(\Gamma v_g g(N) - \frac{1}{\tau_p}\right) - k_c \sqrt{S_{inj}(t)/S(t)} \sin(\phi(t) - \phi_{inj}(t) - 2\pi\delta\nu' t), \tag{2.15}$$

where k_c denotes the coupling coefficient, and S_{inj} and ϕ_{inj} represent the injected photon density and the phase of the injected photons, respectively.

In the case of simulations involving the use of injection in this text, two rate equation systems will be solved. A rate equation system for the SL, defined by Eq. (2.4), Eq. (2.14), and Eq. (2.15), and a rate equation system for the ML, defined by Eq. (2.4), Eq. (2.5), and Eq. (2.6).

2.2.2 Gain-switched optical frequency combs

Gain switching as a technique to generate short optical pulses has been discussed so far. However, to generate a GS OFC, it is essential that the optical phase is preserved from pulse to pulse. It is only when coherence between the generated optical pulses is maintained that an OFC with defined spectral tones is obtained [33]. Conversely, an incoherent spectrum without discernible tones results when pulse-to-pulse phase coherence is lost. As will be discussed throughout this section, the optical phase is preserved from pulse to pulse if the optical pulses emitted by the laser are not completely extinguished between consecutive periods. For high repetition rates, this condition can typically be met in absence of optical injection. However, for low repetition rates, the optical pulses are typically extinguished between periods due to the longer repetition periods associated with these frequencies. In such cases, optical injection provides coherence to the generated optical pulses, enabling the formation of coherent optical spectra.

This thesis is focused on the generation of GS combs with low repetition rates and their application in gas sensing and ranging. The generation of low-repetition-rate GS combs with optimized spectral characteristics for these applications is based on the findings of the research group reported prior to this thesis. These findings offered insights into the underlying physics of OFC generation by gain switching of semiconductor lasers and a comprehensive analysis of the generation of GS combs, providing guidelines for selecting appropriate gain-switching conditions to achieve combs with specific characteristics at both high and low repetition rates. These contributions included the study of the impact of gain-switching conditions on combs generated at high and low frequencies by means of systematic experimental analyses [34], the development of a numerical model for simulating GS combs at different repetition rates [24], and the investigation of the generation of combs with repetition rates in the order of hundreds of MHz using pulsed excitation [35].

Due to the different generation mechanisms involved, the most relevant aspects behind the generation of GS combs at high and low frequencies based on the three aforementioned works are discussed below. The discussion is supported by numerical simulations. The figures of merit used for the evaluation of the frequency combs obtained in this section, which are widely adopted in the literature, are the 10-dB bandwidth and the carrier-to-noise ratio (CNR). Additionally, and particularly when it comes to the application of OFCs to spectroscopy in this dissertation, a figure of merit dedicated to assessing the power uniformity of the comb lines, the spectral flatness, will be considered.

- The **bandwidth at 10 dB** (Δf_{10dB}) is defined as the bandwidth comprised between the two most separated comb lines whose intensity is ten times lower than the highest-intensity comb line.
- The **CNR** is defined as the average value of the ratio between the intensities of the comb lines within Δf_{10dB} and the noise level.
- The **spectral flatness** (SF) is defined as the ratio of the geometric mean to the arithmetic mean of the comb power spectrum. This intuitive figure of merit, which is commonly used in digital signal processing for characterizing audio spectra, has a value of 1 for a completely flat spectrum and a value close to 0 for spectra with a large amplitude variation of the harmonics.

$$SF = \frac{\sqrt[N]{\prod_{n=0}^{N-1} |A_n|^2}}{\frac{\sum_{n=0}^{N-1} |A_n|^2}{N}}, \tag{2.16}$$

where $|A_n|^2$ represents the amplitude of each comb line in the electrical or optical power spectrum, and n is a positive integer representing the harmonic index or comb line index, with N being the total number of harmonics.

High-repetition-rate gain-switched optical frequency combs

In this document, the term high repetition rate is defined as those frequencies that are around or above the frequency of the relaxation oscillations of the laser diode, a range typically comprised between 5 GHz and 10 GHz. The upper limit is determined by the modulation bandwidth of the laser, while the lower limit is set by the frequency of the relaxation oscillations of the device. The generation of GS OFCs in edge-emitting lasers was first investigated for a limited frequency range around the frequency of the relaxation oscillations using fixed gain-switching conditions (bias current and RF amplitude). It was revealed that the complete extinction of the optical pulses between periods (occurring at low frequency with respect to the relaxation oscillations) resulted in incoherent optical spectra [36].

To illustrate these situations, the generation of GS combs at repetition rates below and above the relaxation oscillations frequency is shown in Fig. 2.6. This figure corresponds to simulations in which the previously used discrete-mode laser is gain switched using a sinusoidal current whose expression is

$$I(t) = I_{bias} + \frac{2\sqrt{2}V_{RF}}{Z_0 + Z_l} \sin(2\pi f_R t), \tag{2.17}$$

where I_{bias} is the bias current, V_{RF} is the root-mean-square (RMS) voltage of the RF signal applied to a 50 Ω load, $Z_0 = 50$ Ω is the impedance of the RF signal generator, and Z_l is the impedance of the laser diode, also around 50 Ω due to the package series resistance. The bias current and the RF signal voltage are respectively set to I_{bias}=$2I_{th}$, and V_{RF}=1 V, for both simulation scenarios. This configuration leads to off and on

currents I_{off}= 4.3 mA, I_{on}= 46.2 mA. Fig. 2.6 (a) illustrates the temporal profiles (electric current, normalized carrier density, and output power) corresponding to a modulation frequency of f_{down}= 4 GHz, which is below the frequency of the relaxation oscillations at the specified driving conditions (∼6 GHz). In this scenario, the output optical power is extremely low between consecutive pulses, resulting in an incoherent optical spectrum, as shown in Fig. 2.6 (b). Fig. 2.6 (c) depicts the temporal profiles corresponding to a higher modulation frequency, f_{up}= 7 GHz. As the laser pulses are not utterly extinguished between periods, they remain phase-coherent, as reflected in the resulting optical spectrum (Fig. 2.6 (d)).

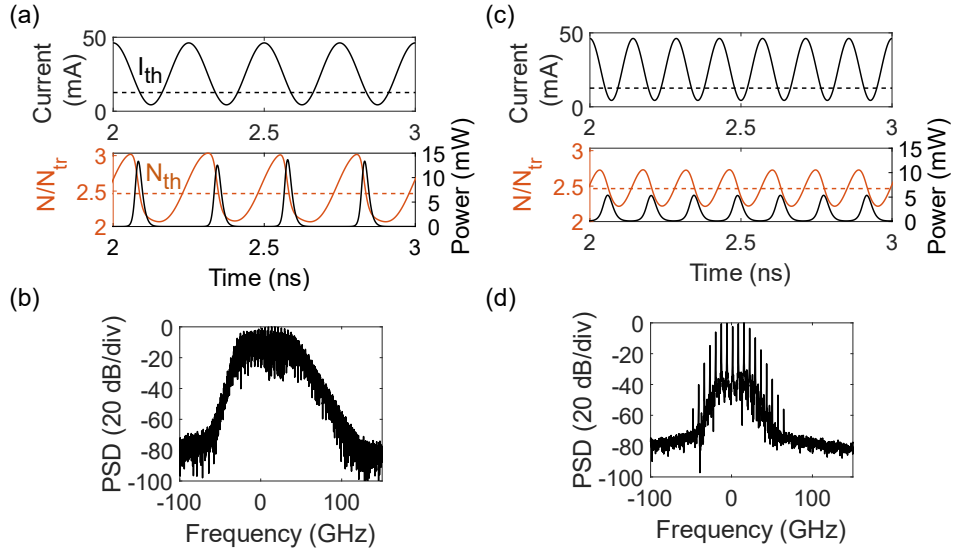

Figure 2.6: Numerical simulations of GS OFCs without external optical injection. Temporal profiles and normalized optical spectrum corresponding to a gain-switching frequency: (a), (b) below the frequency of the relaxation oscillations (f_{down}= 4 GHz), and (c), (d) above the frequency of the relaxation oscillations (f_{up}= 7 GHz).

The dependence of gain-switching conditions on the generated combs was investigated by A. Rosado et al. through experimental [34] and numerical [24] analysis. The experimental analysis involved two representative edge-emitting lasers, a discrete-mode laser and a distributed feedback (DFB) laser. The numerical analysis was conducted using a discrete-mode laser. These works showed that the characteristics of the combs strongly depend on the gain-switching conditions rather than on the internal parameters of the employed lasers, since they behaved similarly when switched. These works explored, for a repetition rate of 5 GHz and using sinusoidal modulation, the evolution of CNR, Δf_{10dB}, and their product (CNR·Δf_{10dB}) with I_{bias} and V_{RF}. Different representative regions were observed:

- A region corresponding to the direct modulation of the laser.

Here, the modulation current $I(t)$ (Eq. (2.17)) has a small excursion and it is always above the threshold current of the laser. As a result, the laser output power is capable of following the sinusoidal variation of $I(t)$ and in the optical spectrum only a few lines

appear around the carrier, corresponding to the amplitude and frequency modulation of the laser. The simulated temporal profiles corresponding to this scenario representing $I(t)$, the normalized carrier density, and the output optical power are depicted in Fig. 2.7 (a), (b), and (c), respectively. The resulting optical spectrum is shown in panel (d). As it can be seen, the obtained spectrum is characterized by a few tones with high CNR but low Δf_{10dB}. For this simulation, I_{bias}= 34 mA, V_{RF}= 0.1 V, and f_R= 5 GHz (resulting in I_{off}= 31.9 mA and I_{on}= 36.1 mA).

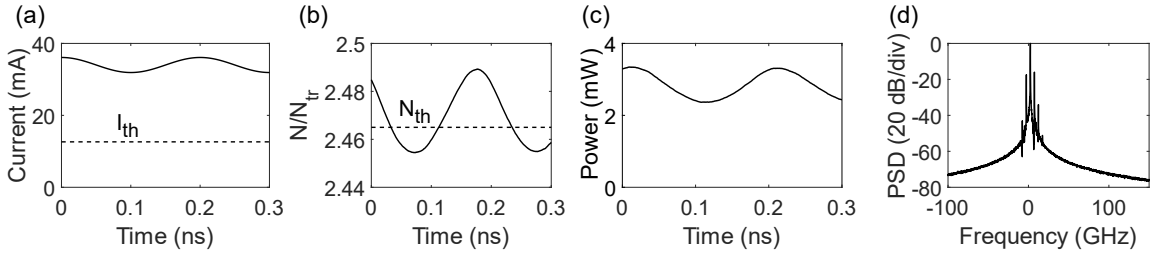

Figure 2.7: Numerical simulation of the direct modulation of the discrete-mode laser, i.e., the laser is well above threshold during the whole modulation period. (a) 5-GHz sinusoidal current that drives the laser diode. (b) Evolution of the normalized carrier density. (c) Emitted optical power. (d) Normalized optical spectrum.

- A gain-switching region in which $I(t)$ has an amplitude excursion high enough to extinguish the optical pulses between periods.

In this region, every time a new pulse emerges, the spontaneous emission contribution exceeds the stimulated emission and there is a loss of coherence between consecutive pulses. The results of a simulation corresponding to this situation are shown in Fig. 2.8. For this simulation, I_{bias}= 34 mA, V_{RF}= 1.8 V, and f_R= 5 GHz (resulting in I_{off}= -3.7 mA and I_{on}= 71.7 mA). As it can be seen in panel (b), there is a large carrier variation. This abrupt carrier density swing results in a high dynamic chirp (see panel (c), orange trace), causing the broadening of the optical spectrum. The fluctuations observed in the chirp before switch-on are attributed to the predominance of spontaneous emission photons in the formation of the optical pulses. In this scenario, the obtained optical spectrum features high Δf_{10dB} but poor CNR (see Fig. 2.8 (d)).

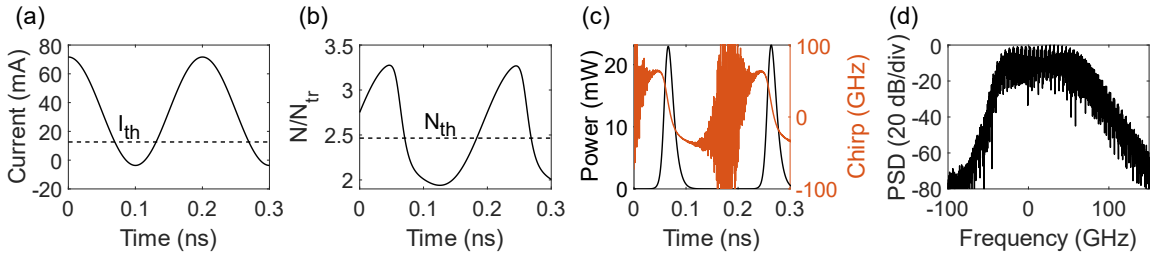

Figure 2.8: Numerical simulation of 5-GHz sinusoidal gain switching of a discrete-mode laser resulting in the generation of an incoherent GS OFC. External optical injection is not considered. (a) Temporal profile of the current injected into the laser. (b) Normalized carrier density. (c) Emitted optical pulses (black) and frequency chirp. (d) Optical spectrum.

- A region in which $I(t)$ allows the laser to operate in gain switching emitting optical pulses that are not completely extinguished between periods, preserving pulse-to-pulse coherence.

This process involves adjusting I_{bias} and the amplitude of the RF current ensuring that cavity photons are not entirely depleted between periods, allowing for the generation of new pulses from a major contribution of stimulated emission photons. For a constant I_{bias}, the increase of V_{RF} results in the generation of optical pulses that progressively deviate from the sinusoidal character that corresponds to the direct modulation of the laser. Moreover, as V_{RF} increases, in addition to the amplitude modulation, a frequency modulation associated with the change of carriers is induced. A large carrier variation results in high dynamic chirp and broad spectra. In this region, maximum modulation efficiency is achieved when the modulation frequency is close to the frequency of the relaxation oscillations (which varies with I_{bias}), and the obtained comb spectra exhibit higher spectral widths compared to those attained for higher values of I_{bias}. Therefore, Δf_{10dB} increases with V_{RF} but also depends on I_{bias}, finding an optimum value for an I_{bias} that maximizes the modulation efficiency. A simulated example corresponding to this scenario is shown in Fig. 2.9, obtained for I_{bias}= 34 mA, V_{RF}= 1.1 V, and f_R= 5 GHz (resulting in I_{off}= 10.9 mA and I_{on}= 57 mA). In these driving conditions, coherent optical pulses leave the laser cavity. As well as in Fig. 2.8 (c), frequency chirp is in phase with the carrier density but out of phase with respect to the optical pulses. As a result, in addition to its role in the spectral broadening of GS combs, frequency chirp also contributes to their spectral flatness. The typical asymmetry of these OFCs is compensated for by the different levels of power associated with each frequency component. For f_R=5 GHz the optimum reported GS OFC featured a CNR around 40 dB with Δf_{10dB} of 60 GHz [34].

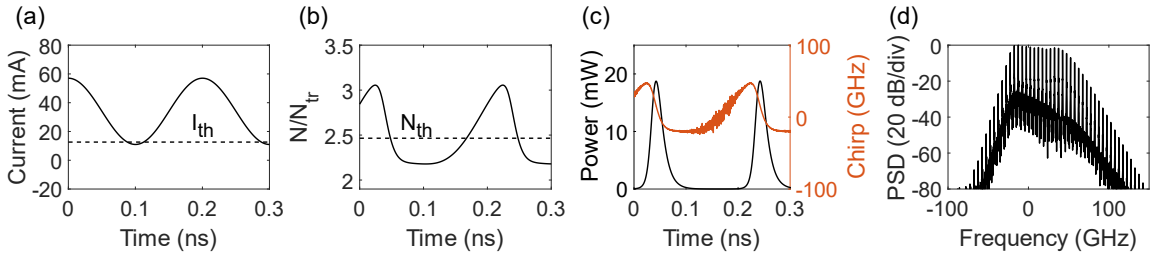

Figure 2.9: Numerical simulation of 5-GHz sinusoidal gain switching of a discrete-mode laser resulting in the generation of a coherent GS OFC. External optical injection is not considered. (a) Electric current driving the laser diode.(b) Evolution of the normalized carrier density. (c) Optical pulses and frequency chirp. (d) Obtained normalized optical spectrum showing defined comb teeth evenly spaced by 5 GHz.

Regarding the role of external optical injection, it is known that it can transform an incoherent comb such as the one displayed in Fig. 2.8 (d) into a high-quality comb with well-defined tones. The reason under this is that gain-switched pulses that initially emerged from spontaneous emission in the absence of injection, now turn on from the photons of the master laser. However, for this to occur, the ML emission must lie within the bandwidth of the GS comb and the power level must be such that the number of

stimulated photons of the ML injected into the SL exceeds the number of spontaneous photons of the slave. The detuning level with respect to the original SL frequency determines the power to be injected to achieve locking. For higher detuning values, the injected power has to be increased. Moreover, for a fixed detuning, as the injected power increases, the comb bandwidth is reduced since the chirp decreases. Also, a higher injected power leads to an increase of CNR and comb asymmetry. A useful guide for selecting optimal injection conditions depending on the detuning and the injected power can be found in the maps developed in [24] from experimental measurements and simulations. Finally, optical injection can as well degrade the quality of GS combs showing good spectral characteristics in absence of injection, such as the one shown in Fig. 2.9. External optical injection in such combs lead to complex dynamics and multiple-period combs can be obtained due to the competition between the stimulated emission photons of the slave laser and the master laser occurring in the turn-on process of gain-switched pulses [24], [34].

Low-repetition-rate gain-switched optical frequency combs

Low repetition rate is referred to in this document as those frequencies that are well below the laser relaxation oscillations, frequencies $\leq$1 GHz, to establish a criterion. This is the frequency range of interest for the applications studied in this thesis. Gain-switching conditions to obtain OFCs within this frequency range using sinusoidal modulation signals are very limited [35]. Moreover, the obtained GS OFCs are spectrally narrow (Δf_{10dB} typically below 30 GHz) and usually display suppressed tones. Indeed, it was not until pulsed excitation was used that flat and broad GS OFCs at low repetition rates could be obtained [35].

Obtaining low-repetition-rate combs with sinusoidal modulation has been explored experimentally [34] and numerically [24] for frequencies of hundreds of MHz (500 MHz and 200 MHz, respectively). At these frequencies, the off-time between pulses is long enough for the photons existing within the laser cavity to deplete, resulting in incoherent spectra. However, under certain conditions it is possible to obtain sinusoidal GS combs without injection. These conditions lie in keeping the modulation current $I(t)$ always above the threshold current of the laser. Although in these conditions the laser is not strictly operating in gain-switching regime because it is not actually switched off, the obtained spectra are recognized in the literature as GS OFCs [3], [4], [34]. The mechanism underlying the generation of this type of combs is different from that present in high-frequency modulation. In the high-frequency case, the rapid carrier variation during laser turn-on results in a high dynamic chirp that causes the spectrum to broaden. In the case of low-frequency modulation using sinusoidal excitation, there is no such abrupt change of carriers, but carriers are able to follow the gain variation and maintain a sinusoidal profile. This can be observed in the graphs shown in Fig. 2.10, which corresponds to a simulation of sinusoidal gain switching of a discrete-mode laser at 500 MHz. For this simulation, I_{bias}= 60 mA and V_{RF}= 1.5 V (I_{off}= 19.7 mA and I_{on}= 100.3 mA, with I_{off} being always above I_{th}). In this case, the dominating type of chirp is adiabatic chirp. As depicted in Fig. 2.10 (c) (orange trace), chirp has a frequency variation of $\sim$12 GHz and hence a narrow spectrum is attained (see panel (d)).

Furthermore, chirp is in phase with the optical power and so the obtained spectrum is asymmetrical, since lower frequencies are associated to lower power values.

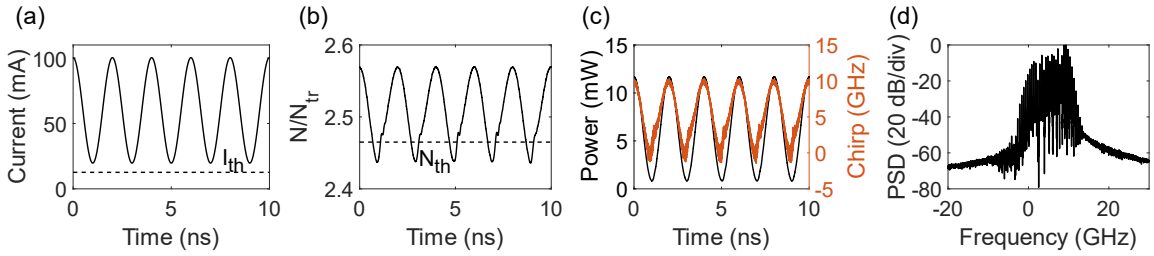

Figure 2.10: Numerical simulation of a 500 MHz coherent OFC obtained by sinusoidal gain switching of a discrete-mode laser. (a) Evolution of the sinusoidal electric current, which is always above threshold. (b) Normalized carrier density. (c) Evolution of the emitted optical power (black), which follows a sinusoidal profile and is in phase with the frequency chirp (orange). (d) Resulting normalized optical spectrum.

Despite the fact that spectral broadening is in this case dominated by adiabatic chirp, the evolution of the comb characteristics with gain-switching conditions is identical to that discussed for high-frequency GS OFCs. For $I(t)$ currents with low amplitude excursion which are, in addition, always above threshold, a few amplitude-modulation tones are obtained. Then, increasing V_{RF} induces frequency modulation and yields spectra with a larger number of tones exhibiting good CNR. However, these combs exhibit poor flatness and tone suppression due to frequency modulation. Finally, further increasing V_{RF} leads to a value of $I(t)$ that turns off the laser and causes the optical pulses to lose coherence.

The generation of broad GS combs (Δf_{10dB} on the order of ∼100 GHz) with repetition frequencies of hundreds of MHz became possible by replacing sinusoidal excitation with pulsed excitation. Pulsed modulation has been commonly used since the early days of gain switching for the generation of optical pulses; however, the first time its use was reported for the generation of GS combs was in a research work conducted by our group [35]. The train of current pulses used to modulate the laser, $I(t)$, is now defined from off and on currents, which are related to I_{bias} and V_{RF} [35] as follows

$$I_{off} = I_{bias} - \frac{4V_{RF}}{Z_0 + Z_l} d_{cycle}, \tag{2.18}$$

$$I_{on} = I_{off} + \frac{4V_{RF}}{Z_0 + Z_l}, \tag{2.19}$$

d_{cycle} being the duty cycle of the electrical pulse train, calculated as $d_{cycle} = f_R \tau_{pulse}$, where τ_{pulse} is the duration of the electrical pulses. As already mentioned, $I(t)$ is a signal composed by an alternating current and a direct current, coupled together with a bias-tee. Because of the capacitor of the bias-tee, I_{off} is calculated as the bias current minus the DC component of the RF signal.

The use of electrical pulses with short rise times allows the laser to turn on abruptly and results in a rapid and large carrier variation. Consequently, as in the case of high-frequency combs, dynamic chirp now dominates as the mechanism causing the spectral broadening of OFCs. Additionally, the electrical pulse duration must be configured to excite only the first peak of the laser relaxation oscillations, thus ensuring the emission of short-duration optical pulses. This electrical pulse duration typically takes values between 100 ps and 200 ps. For a fixed value of I_{bias} and V_{RF}, increasing the duration of the electrical pulses results in higher comb bandwidths up to a certain pulse duration, beyond which the spectrum degrades due to the excitation of the second spike of the relaxation oscillations. Also, because τ_{pulse} is short compared to the period of the electrical signal, the laser is completely switched off between successive pulses. Accordingly, the generation of low-repetition-rate pulsed GS combs requires the use of optical injection. Regarding the modulation current, it must be properly configured (by means of adjusting I_{bias} and V_{RF}) to attain values of I_{off} below the threshold current of the laser, and values of I_{on} well above it. The dependence of the modulation amplitude on Δf_{10dB} follows the same trend as that of high-frequency GS combs. As in the case of sinusoidal modulation at high repetition rates, the carriers experience faster growth and higher excursion as the modulation amplitude increases.

A simulation of the generation of a 500-MHz GS comb under pulsed excitation without and with external optical injection is shown in Fig. 2.11. The electrical pulses, shown in panel (a), are configured to have low and high values of I_{off}= 5 mA and I_{on}= 50 mA, respectively, and a temporal width of τ_{pulse}= 150 ps. With this modulation current and without performing injection locking, the incoherent and broad spectrum shown in Fig. 2.11 (b) is obtained. It features a Δf_{10dB} of 98 GHz. Panel (c) depicts a narrower region of this spectrum, allowing to check the absence of resolved comb lines. Then, the OFC is externally injected to provide coherence for consecutive optical pulses. The conventional approach involves adjusting the master laser wavelength so that injection is performed in the spectral region where the comb displays the lowest power. This compensates for the asymmetry of the comb, resulting in a flattened injected spectrum. In Fig. 2.11 (b), this region corresponds to the blue side of the spectrum, indicating higher frequencies. The laser used as ML is a discrete-mode laser with the same internal parameters as the slave laser (Table 2.1), except for the β_{sp} parameter, which has been reduced from $5.3{\cdot}10^{-6}$ to $5.3{\cdot}10^{-9}$ for a better noise performance. The injection power is set to 0.5 mW and the detuning, $\delta\nu'$, to 40 GHz. The master-slave coupling coefficient is $k_c = 4.23{\cdot}10^{10}$ s^{-1} [24]. The dynamics of the carriers and the optical pulses obtained when the SL is optically injected, along with the chirp, are depicted in panels (d) and (e), respectively. Upon the application of the electrical pulse, the carriers exhibit a rapid rise, followed by a subsequent decrease due to recombination for optical pulse formation. Then, they experience an exponential drop according to the extinction of the electrical pulse. The optical pulse has a full width at half maximum (FWHM) of $\sim$30 ps and a maximum power of 14.5 mW. The dominant dynamic chirp shows a frequency amplitude around 52 GHz within the pulse width. The optical spectrum of the injected comb, illustrated in Fig. 2.11 (f), exhibits a Δf_{10dB} of 66 GHz and a CNR of approximately 40 dB (see inset of panel (f)).

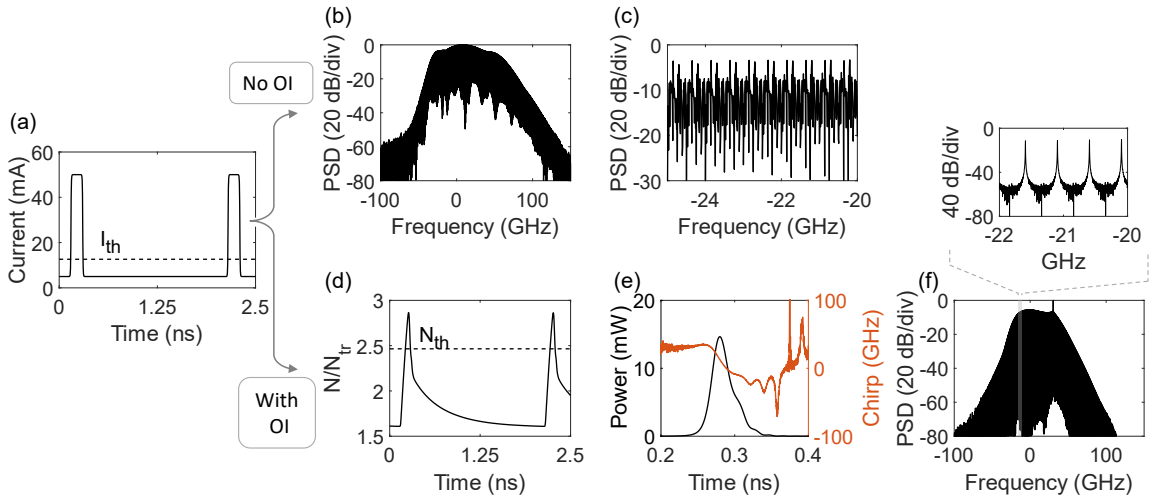

Figure 2.11: Numerical simulations on the generation of GS OFCs with a repetition rate of 500 MHz using pulsed electrical excitation. (a) Train of pulses driving the discrete-mode laser. (b) Incoherent optical spectrum resulting from gain switching of the laser diode at the conditions described in the main text and (c) zoomed view of it (d) Evolution of the carrier density, (e) optical power (black) and frequency chirp (orange) when the previous comb is optically injected. (f) Coherent 500-MHz optical spectrum obtained by pulsed gain switching and external optical injection.

Low-repetition-rate GS combs exhibit good characteristics down to repetition frequencies in the order of tens of MHz. Below these frequencies, the obtained duty cycles are very low (below 0.5%). Consequently, the average optical power and the power per comb line are poor. Nonetheless, as it will be detailed later in the experimental results, other strategies can be followed to alleviate this problem. Other than that, the spectral flatness is very good, making these OFCs a valuable choice for applications such as spectroscopy. Furthermore, their modest bandwidth proves sufficiently broad for the measurement of individual absorption lines.

Historical review of gain-switched optical frequency combs

The first GS OFC was demonstrated in 2009 by P. Anandarajah et al. [1]. In their work, the authors experimentally obtained an OFC from a GS discrete-mode laser. The generated comb, included in Fig. 2.12, featured 7 spectral lines within a 10-dB bandwidth, with a line spacing of 10.7 GHz. They demonstrated the feasibility of using the generated GS OFC as a transmitter in an optical communications system, proving the suitability of these comb generators for optical communications (frequency range 5-10 GHz), featuring a simple and robust implementation, and with a tunable line spacing within the mentioned frequency range. In 2011, the same group extended their previous results and demonstrated the feasibility of generating a 10.7-GHz GS OFC with a DFB laser when it was optically injected [37]. A few years later, they reported the generation of a GS comb with a non-injected DFB [36]. This work is of particular significance as it first disclosed that, for the generation of a GS comb without optical injection, it is necessary for the modulation frequency to be close to or to exceed the frequency of the laser relaxation oscillations.

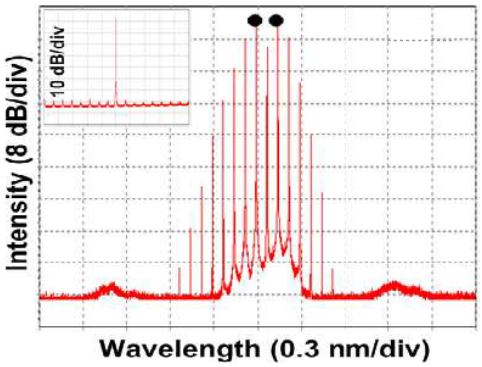

Figure 2.12: First experimental demonstration of a GS OFC obtained from a discrete-mode laser gain switched at a frequency of 10.7 GHz using the superposition of a direct bias current and a sinusoidal signal. Figure taken from [1].

There have been several demonstrations showing the convenient use of GS combs as robust transmitters in WDM optical networks using advanced modulation formats [38]–[40] and coherent reception [41]. These approaches based on frequency-stable phase-correlated optical carriers allow to increase the transmission capacity and to simplify digital signal processing. Besides the use of GS OFCs on the transmission side, it has also been proved that the use of a GS comb in reception as a multi-tone local oscillator allows the simultaneous demodulation of multiple channels [42].

In addition to the feasibility of using GS combs for optical communications, their viability for other applications was also early demonstrated. In 2012, the group led by P. Acedo demonstrated a microwave signal synthesizer based on a GS comb [43]. The GS OFC was generated by modulating a discrete-mode laser with a 10-GHz sinusoidal signal. The generated comb was afterwards phase modulated in order to improve its flatness. The sub-THz signal synthesis was achieved by filtering two comb tones with two tunable bandpass filters and beating the tones in a photodetector. The output of the free-space photodetector, after being coupled to an antenna, was measured in an electrical spectrum analyzer, showing a 120-GHz tone whose linewidth was below the spectral resolution of the measurement instrument (<10 Hz). In a subsequent work, the use of optical injection locking to filter the two comb lines resulted in an improvement of the performance of the synthesizer in terms of linewidth, side-mode-suppression ratio, and stability [44].

Regarding the laser sources used to generate GS combs, in addition to the aforementioned edge-emitting laser diodes like DFB and discrete-mode lasers, vertical cavity surface-emitting lasers (VCSELs) have also shown excellent performance. Á. R. Criado et al. reported for the first time a GS comb generator based on a VCSEL [45]. The resulting comb, obtained under sinusoidal modulation at 4.2 GHz, featured a spectral bandwidth of 84 GHz (13 lines) within 3 dB. In addition to their reduced power consumption and cost-effective manufacturing, these sources show interesting polarization dynamics, as they can emit two linearly polarized transverse modes with orthogonal polarizations. This opened up the possibility of generating two frequency combs with orthogonal polarizations from a single laser cavity, as experimentally demonstrated in [46], where

the authors obtained an overall comb composed by two orthogonal sub-combs with repetition rates of 5 GHz and a bandwidth at 10 dB of ∼100 GHz. One of the generated sub-combs, the one with orthogonal polarization with respect to the overall comb, exhibited lower power. This was overcome by the use of external optical injection, allowing the generation of two sub-combs with the same optical power under specific injection conditions [47]. The impact of the injection conditions on the generated sub-combs was further investigated in a study [48] that provided a comprehensive theoretical analysis, supported by numerical simulations, for both linearly and elliptically polarized injection conditions. In addition, under certain conditions, an expanded comb was obtained.

The expansion of GS combs was explored soon after their first demonstration, in an attempt to achieve bandwidths comparable to those obtained with other techniques. In [37], the authors demonstrated the nonlinear expansion of a 10.7-GHz GS comb initially formed by eight tones in a 3-dB bandwidth. The expanded comb, shown in Fig. 2.13, featured 50 spectral lines in a 3-dB bandwidth of 535 GHz.

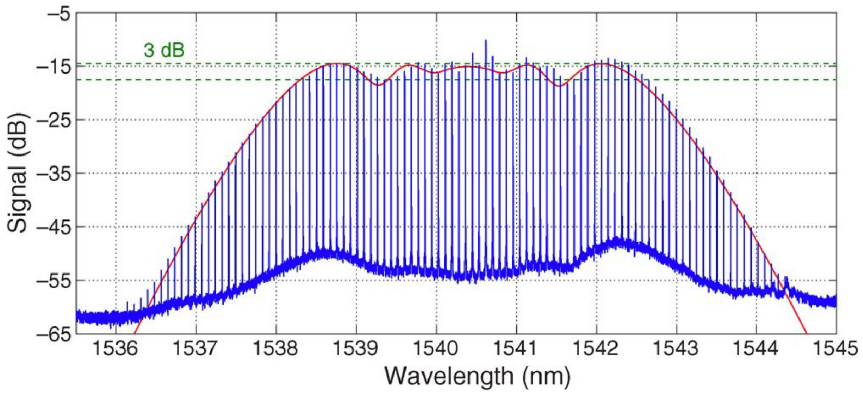

Figure 2.13: Nonlinear expansion of a GS comb, featuring an expansion factor of 6.25. The configuration for the nonlinear expansion of the comb comprises two dispersion compensating fiber sections and a highly nonlinear optical fiber section, enabling the compression of the gain-switched pulses. Figure extracted from [37].

The use of cascaded electro-optic modulators is also a widespread method for frequency comb expansion. These expansion setups consist of one or more electro-optic phase modulators (EOPMs) modulated at the gain-switching frequency [49], [50] or multiples of it [51]. An intensity modulator can also be introduced to optimize the flatness of the comb. The comb bandwidth is increased by a factor of ∼2 after each phase modulator. This approach affords photonic integrability and superior comb flatness compared to nonlinear methods, albeit at the expense of increased complexity and cost.

Besides these expansion methods, it is also possible to spectrally overlap multiple combs. In the case of not using external optical injection, several GS OFCs can be partially overlapped, and a semiconductor optical amplifier can be used to phase-correlate the comb tones [52]. When using optical injection from a single-mode master laser, two injected combs can be combined [51] in a simpler setup. Finally, a recent proposal showed the highest expansion achieved so far in GS OFCs [53]. This proposal was based

on injection locking multiple modes of a Fabry-Pérot laser diode under gain-switching operation using a GS comb as master. Two configurations were presented: a first one achieving a lower bandwidth and better flatness, and a second one in which flatness was compromised in exchange for a high expansion factor of 10. Both configurations were based on a master-slave architecture in which the slave laser was a gain-switched Fabry-Pérot laser, and the master laser was a gain-switched DFB laser. Both lasers, SL and ML, were switched at the same frequency, 6.25 GHz. The experimental setups of both approaches and their operation principles are shown in Fig. 2.14. In the first approach, two comb lines of the master comb simultaneously injected two GS Fabry-Pérot modes. The resulting OFC, formed by the combination of the two GS Fabry-Pérot modes, showed coherence since the two Fabry-Pérot modes were injected by two lines of a coherent OFC. Then, this comb was further expanded by means of an EOPM modulated at a multiple of the comb repetition rate (12.5 GHz). After the phase modulation stage, the initial OFC was expanded by a factor of ∼4, from a bandwidth (within 5 dB) of 81.25 GHz to 337.5 GHz. However, the bandwidth of the master comb imposed a limit on the number of Fabry-Pérot modes that could be injected. The second approach enabled to increase the bandwidth of the master comb, allowing more than two Fabry-Pérot modes to be simultaneously injected. This approach involved using two demultiplexers, through which the master comb was passed before injecting the Fabry-Pérot OFC. In the first demultiplexer, one line of the master comb was amplified, while the rest of the comb lines remained unaffected. This modified comb was then inserted into the second demultiplexer, configured to amplify an additional comb line. The two demultiplexers were configured to amplify two comb lines with a frequency spacing equal to the mode spacing of the Fabry-Pérot slave laser. Additionally, the strong injection in the second demultiplexer triggered four-wave mixing, generating new spectral components. As a result, instead of injecting only two Fabry-Pérot modes, six modes could be injected using six demultiplexed comb lines of the master OFC, resulting in a broad, expanded comb.

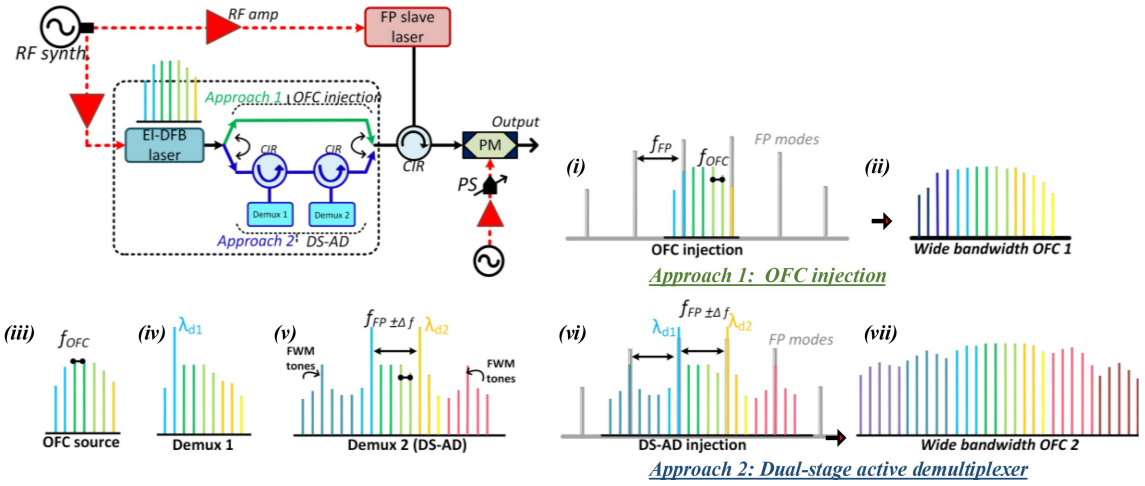

Figure 2.14: Expansion of a GS comb based on injection locking of multiple modes of a GS Fabry-Pérot laser diode acting as slave laser. Two approaches, described in the main text, are illustrated. Figure extracted from [53].

Concerning low repetition rates, GS OFCs with repetition frequencies $\leq$1 GHz have proven beneficial for applications where low line spacing is desired, such as spectroscopy. In these applications, the resolution of the measurement is determined by the line spacing, i.e., a better spectral resolution is achieved with a lower line spacing. The first demonstration of a GS comb with a repetition rate well below the laser relaxation oscillations was devoted to the realization of molecular spectroscopy in the 1.5 μm region [3]. Through the generation of two 1-GHz OFCs, obtained by sinusoidal gain switching of two discrete-mode lasers externally injected by the same master laser, an absorption line of hydrogen cyanide was measured. The technique used, widely known as dual-comb spectroscopy, will be discussed in depth in Chapter 3. The resolution of the measurement was improved by a factor of 2 in a subsequent work by the same group [4], in which, in addition to the absorption profile, information on the phase was retrieved. Later in 2019, Rosado et al. demonstrated that replacing the sinusoidal gain-switching signals by trains of short electrical pulses and external optical injection allowed to further decrease the repetition rate of GS combs and to improve their spectral characteristics [35]. By employing two of these GS OFCs, dual-comb interferometry is demonstrated in this thesis. Finally, other waveforms, such as sawtooth or sinc waveforms, have been also explored as gain-switching signals for the generation of low-repetition-rate combs [54]. The experimental analyses revealed that pulsed excitation yielded the superior performance for comb generation.

- **Integrated gain-switched optical frequency combs**

The integration of GS comb sources constitutes a recent research field. Discrete off-the-shelf laser diodes already offer advantages in terms of cost and size compared to other OFC generators, however, their integration yields a substantial improvement in both aspects. In addition, it enhances the feasibility of employing OFCs in real-world applications.

There are different mechanisms for the integration of photonic devices. Monolithic integration relies on the use of a single substrate onto which other materials are grown or deposited. In the case of GS combs, the substrates are III-V semiconductors, direct band gap compounds that enable the fabrication of active devices. In contrast, hybrid and heterogeneous integration involve the combination of different materials, such as III-V semiconductors and Si_3N_4 [55]. Hybrid integration entails connecting two already fabricated chips, generally in the packaging process. On the other hand, in heterogeneous integration, different material technologies are combined usually before packaging. This can be achieved through various techniques such as transfer-printing or epitaxial growth. For GS OFCs, indium phosphide (InP) is the photonic integration platform used for the fabrication of the laser diodes. For technologies such as InP, Si_3N_4 or silicon on insulator (SOI), there are different foundries dedicated to each technology, offering reliable manufacturing processes. These foundries offer libraries of basic photonic components that allow users to design complex systems from mature building blocks.

One of the first demonstrations of an integrated GS OFC was published by J.K. Alexander et al. in 2016 [56]. The authors reported a monolithically-integrated GS comb with optical injection, being the master and slave lasers integrated within the same device. The device consisted in a three-section laser composed by two Fabry-Pérot lasers having a shared slotted reflector to achieve single-mode operation for the ML and the SL. The overall size of the device was 2 mm, comprising the gain section of the master laser (800 μm), a mirror (756 μm), and the gain section of the slave laser (756 μm). It was fabricated using five AlGaInAs quantum wells on an n-doped InP substrate. The device was characterized in CW, showing single-mode emission when both lasers were switched on, and a tuning range of approximately 10 nm was achieved in discrete steps of 3.2 nm, corresponding to different lasing modes of the Fabry-Pérot lasers. The generation of an OFC with a line spacing of 4 GHz was demonstrated, featuring 5 lines within Δf_{10dB} when the ML was not switched on and doubling this bandwidth when optical injection was performed, as depicted in Fig. 2.15. That spectral width enhancement was attributed to the increased modulation bandwidth resulting from injection, as the frequency of relaxation oscillations increased.

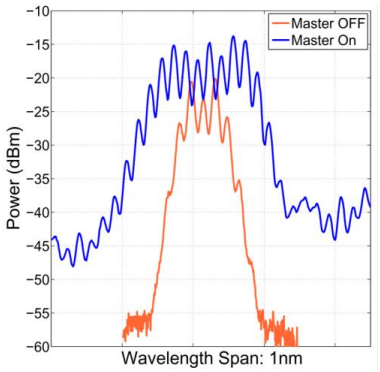

Figure 2.15: GS OFC based on a monolithically integrated three-section laser. From [56].

In a later work by a different group, M.D. Gutierrez et al. demonstrated the generation of an integrated OFC, with and without optical injection, with a repetition rate tunability from 6.25 GHz to 10 GHz [57]. The comb generator was similar to the one presented in [56], including an additional reflector at the end of the master laser, favoring emission in a single direction and allowing for higher optical injection efficiency. The viability of such combs was also proved for optical communication systems using advanced modulation formats [58]. Part of the same research group recently presented an integrated comb source based on two DFB lasers mutually injected by a four-section distributed Bragg reflector (DBR) laser. The device was fabricated by a foundry in a multi-project wafer run using InP generic platform [59]. The DFB lasers were designed so that their spectra partially overlapped under gain-switching operation. In addition, thermal heaters were attached to these lasers to allow for independent thermal wavelength tunability. The ML consisted of gain and phase sections sandwiched between two DBRs (rear and front). A block diagram of the comb source is shown in Fig. 2.16 (a). It includes the possibility of also injecting the two SLs by an external laser. The slave lasers showed good performance under static and gain-switching conditions. On the other hand, the integrated ML showed poor performance in terms of output optical power and its emission wavelength did not match the wavelength of the slave lasers, resulting invalid for mutual injection locking of both SLs. However, it remains a good proof-of-concept device that can be improved in a further fabrication run. The demonstration of the mutually-injected system was achieved using an external non-integrated tunable master laser. As a result, an expanded coherent OFC composed by two 6.25-GHz GS combs was obtained, featuring a 10-dB bandwidth of 256.25 GHz and showing very good

performance in terms of phase correlation (12-15 Hz, comparable to the RF source used). Also, the tunability of the repetition rate between 6.25 GHz and 12.5 GHz was proved. The obtained optical spectrum at a f_R of 6.25 GHz can be seen in Fig. 2.16 (b).

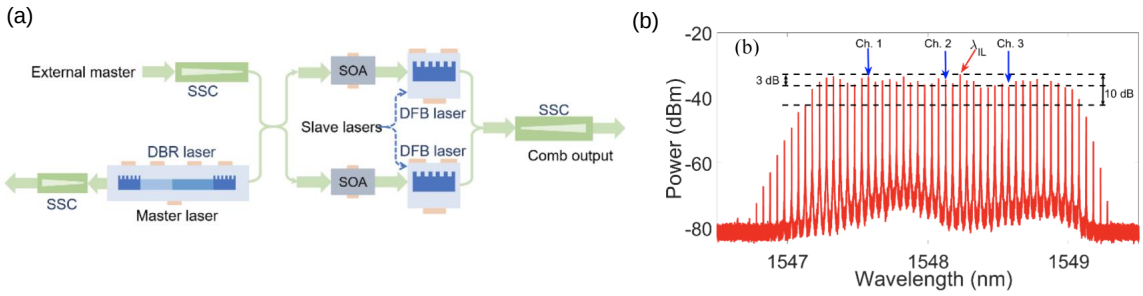

Figure 2.16: (a) Integrated GS OFC generator comprising two DFB lasers that operate as SLs and a DBR laser acting as ML. The device was fabricated in a multi-project wafer run using InP generic integration platform. (b) Resulting 6.25-GHz GS OFC, obtained from partially overlapping two individual comb spectra from the two SLs, and performing optical injection with an external (non-integrated) laser in the overlapped region. (a) and (b) taken from [59].

Finally, regarding hybrid approaches, a GS comb source based on an integrated DFB laser butt-coupled to a Si_3N_4 microring resonator was recently demonstrated [60]. In their proposal, the authors performed gain switching to the DFB laser to generate an OFC. The resonator acted as an optical filter, selecting one of the comb lines and reflecting it back towards the DFB laser, which was self-injected by the filtered comb line. The DFB laser without optical injection, at the used modulation frequency (variable between 5.55 GHz and 8.7 GHz), generated a coherent comb whose optical pulses did not completely extinguish, which is essential for self-injection locking. Injection was shown to improve the spectral width, the CNR, and the linewidth of the comb tones. As a result, in the self-injection locking state, the generated comb showed 12 comb lines evenly spaced 6.5 GHz with an excellent CNR of 40 dB. The linewidth of the comb tones decreased ∼10 times under optical injection, reaching a value of 615 kHz. Also, phase correlation of the generated OFC was proved, with the beat tone of two comb lines having a linewidth of 50 Hz.

In conclusion, despite the fact that the first demonstration was published in 2016, it is in recent years that a greater number of contributions are being reported. The reason for this is that, though InP chip fabrication is expensive, the presence of foundries that currently provide photonic circuit design kits based on the aforementioned building blocks has allowed open access to fabrication to those researchers who did not have the means to do it in their laboratories. In addition, manufacturing processes are gradually becoming more stable and mature. Finally, although most of the contributions made so far have been based on monolithic architectures the trend goes towards hybridization or heterogeneous manufacturing, permitting the development of more complex systems combining active and passive devices and benefiting from the advantages and performance of each technology.

2.3 Other optical frequency comb generators

In addition to gain-switched laser diodes, there are other reliable comb sources based on semiconductor lasers, such as mode-locked laser diodes and electro-optic frequency combs driven by laser diodes. These techniques, together with microresonator-based OFCs, are detailed in the following section.

2.3.1 Mode-locked semiconductor lasers

Mode-locked lasers, which have already been mentioned as the first OFC sources, are lasers that emit phase-locked ultra-short pulses. Mode-locking technique can be used to generate pulsed light not only in dye, solid-state, and fiber lasers, but also in semiconductor lasers. In a laser cavity, one or more longitudinal modes oscillate at certain frequencies. In the absence of mode-locking mechanisms, the phases of each longitudinal mode fluctuate independently and the interference of the longitudinal modes results in the emission of CW light whose intensity randomly varies around the average intensity value and tends to a constant value for a high number of longitudinal modes within the cavity. Fig. 2.17 (a) illustrates the interference of three longitudinal modes with the same amplitude (depicted in blue, orange, and green) whose phases are not locked, resulting in continuous light exhibiting random intensity fluctuations (black trace). On the contrary, if the laser is mode-locked, a fixed phase relationship is set between the longitudinal modes of the cavity so that their interference results in the formation of short-duration light pulses with a periodicity defined by the cavity length, as shown in Fig. 2.17 (b). The pulse width is fixed by the cavity dispersion and the spectral width of the semiconductor optical gain.

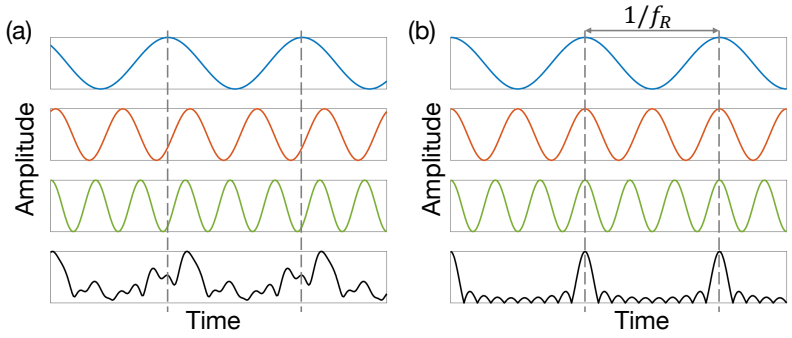

Figure 2.17: Illustration of the mode-locking mechanism in a laser. (a) The interference of three longitudinal modes in absence of phase-locking mechanisms results in the generation of a continuous wave signal (black) that varies in a random manner around its average value. (b) The implementation of a phase-locking mechanism results in the constructive interference of the modes at specific frequencies related to the cavity length.

There are different mode-locking mechanisms, classified as active, passive, and hybrid [61]. Active mode-locking consists in modulating either the gain or the losses of a laser at a repetition rate matching the mode spacing or a harmonic of it. As a result, the modulation sidebands of each mode will couple to adjacent cavity modes, leading to the locking of their phases. It is usually implemented by driving the laser with a modulation signal composed by the superposition of DC and AC currents or by adding in the laser cavity an intensity, phase, or acousto-optic modulator driven by an AC signal. On the other hand, passive mode-locking does not involve the use of modulation signals. Instead, a material exhibiting a nonlinear response to the light intensity is placed within the cavity, being this material usually a saturable absorber. The response of a saturable absorber depends on the intensity of the light impinging on it, such that when high-intensity light reaches the material, the absorption of the material saturates and the cavity losses are reduced. Most of the time, the cavity losses are greater than the gain, and the laser is turned off. However, when the light intensity is sufficiently high, the absorption saturates and the gain exceeds the losses for a short time. In this time interval, a short light pulse is formed, and its width depends on the recovery time of the saturable absorber. This process repeats every round trip, resulting in the amplification of high-intensity pulses and attenuation or absorption of low-intensity light. Passive mode-locking enables the generation of shorter pulses than those obtained by active mode-locking but they exhibit higher timing jitter. Finally, hybrid mode-locking combines both active and passive approaches by using a passively mode-locked laser and an AC signal to modulate the saturable absorber injection current or the gain section at a frequency equal to the frequency spacing of the optical modes. This allows for the synchronization or stabilization of the repetition rate to an external source [16]. The generated pulses can benefit from the shortening effect of passive mode-locking and the lower timing jitter of actively mode-locked lasers.

OFCs generated with mode-locked semiconductor lasers feature fixed and high repetition rates, typically ranging from a few GHz to hundreds of GHz. As for the pulse durations, they range from ∼300 fs, obtained with passive and hybrid mode-locking methods, to a few ps, obtained with active mode-locked lasers. As a method to decrease the repetition rate, architectures involving external cavities have been reported, also improving the phase noise properties of the generated combs [62]. Mode-locked semiconductor lasers allow obtaining comb sources that can be developed on-chip through monolithic, hybrid or heterogeneous integration. Demonstrations with various devices across different spectral regions, from the visible to the mid-infrared, can be found in the literature [16]. Currently, one of the most promising proposals are quantum-dot and quantum-dash mode-locked lasers, given their advantageous optical properties, including broad optical gain, low laser thresholds, and high tolerance to growth defects [63]. Regarding their application, several demonstrations validate these comb sources for high-capacity WDM systems [64], [65], since their repetition rates aligns with grid specifications set by the International Telecommunication Union (ITU) [66]. Additionally, they show promise in other applications such as ranging, where fast measurement rates of up to 500 MHz have been achieved using two slightly detuned 50-GHz quantum-dash mode-locked lasers [67].

2.3.2 Electro-optic frequency combs

Electro-optic frequency combs are generated by the external modulation of a CW laser source using a single o various electro-optic modulators driven by RF signals. These modulators are based on the electro-optic effect, a phenomenon that induces a change in the refractive index of a material in response to an applied electric field. This change in the refractive index results in the modification of the phase of the field propagating in the material. The most common configuration for generating electro-optic combs is to use a phase modulator or a combination of phase and intensity modulators.

The optical field at the output of a phase modulator driven by a sinusoidal signal at a modulation frequency f_m can be written as

$$E_{pm}(t) = E_{in}(t)e^{j\phi(t)} = E_{in}e^{j2\pi\nu_c t}e^{j\beta\sin(2\pi f_m t)}, \tag{2.20}$$

where $E_{in}(t)$ is the input optical field, with its corresponding amplitude E_{in} and carrier frequency ν_c, $\phi(t)$ is the phase imparted in the input field, and β is the modulation index. The phase change depends on the modulation index β. The modulation index is defined as $\beta = \pi V_m/V_\pi$, where V_m is the amplitude of the modulation signal and V_π is the half-wave voltage of the modulator, a parameter that determines the required voltage to achieve a phase change of π rad.

Using the Jacobi-Anger expansion, Eq. (2.20) can be written as

$$E_{pm}(t) = E_{in}e^{j2\pi\nu_c t}\sum_{n=-\infty}^{\infty} J_n(\beta)e^{j2\pi n f_m t}, \tag{2.21}$$

J_n being Bessel functions of the first kind.

The frequency domain counterpart of Eq. (2.21) can be obtained by means of the Fourier transform, and results in

$$E_{pm}(f) = E_{in}\sum_{n=-\infty}^{\infty} J_n(\beta)\delta(f-\nu_c-nf_m), \tag{2.22}$$

where $\delta(f)$ represents the Dirac delta function. Eq. (2.22) corresponds to a spectrum composed of sidebands around the carrier frequency, with a frequency spacing set by the frequency of the modulation signal. The amplitudes of the comb lines follow the Bessel functions of the first kind. As a result, the combs obtained using a single phase modulator have suppressed tones and their flatness is poor.

To improve the flatness of electro-optic OFCs, more complex architectures are typically used. The replacement of a single modulator by a dual-drive Mach-Zehnder modulator [68] or the use of setups involving a tandem of intensity and phase modulators [69], [70] are common approaches. The combination of intensity modulators driven at the appropriate conditions to carve flat-topped optical pulses and phase modulators to transfer a (quasi-) quadratic phase to the generated combs have proven the generation

of flat combs [71], as the temporal shape of the pulses is transferred to the shape of the spectrum [72]. The maximum attainable line spacing is limited by the optical bandwidth of the modulator. Commercial electro-optic modulators commonly display modulation bandwidths up to 40 GHz.

With regard to the bandwidth of electro-optic combs, the number of generated lines depends on the modulation index and increases almost linearly with it [73]. Then, low V_π values are desirable for electro-optic modulators, as well as the capability to handle high RF powers. However, commercial discrete lithium niobate modulators show typical values of V_π ranging from ∼2 V for low frequencies and up to 11 V or more for frequencies of tens of GHz [74]. The maximum RF power handled by these devices is usually around 30 dBm, which corresponds to a RMS voltage of 7 V in 50 Ω. Therefore, the number of lines that can be generated with a single phase modulator is not very high as this would require modulation signals with very high powers that cannot be handled by standard commercial devices. To address this limitation, several phase modulators are usually placed in cascade to expand the generated comb. The effective modulation index corresponds to the sum of the modulation indices of each phase modulator. These architectures require the use of phase shifters to ensure the phase alignment of the signals driving each modulator (see Fig. 2.18, which is a representation of an electro-optic frequency comb source consisting of three phase modulators for comb expansion followed by an intensity modulator to flatten the spectrum). The expansion of electro-optic combs with cascaded phase modulators leads, however, to high insertion losses due to the use of several modulators and increases the complexity of the experimental setup. In addition to this method, if combs with larger bandwidths are required, nonlinear expansion techniques can be used [75]–[77].

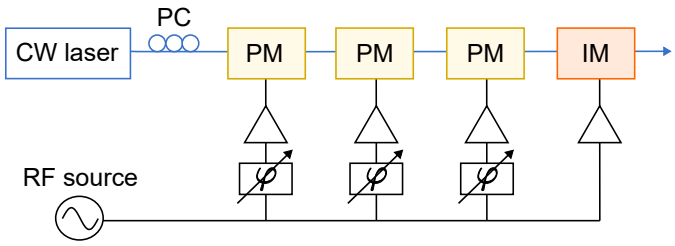

Figure 2.18: Illustration of an electro-optic frequency comb generator, based on the use of cascaded phase and intensity modulators. A CW laser is phase modulated by three cascaded EOPMs. The resulting spectrum is flattened by means of an electro-optic intensity modulator. All the modulators are driven by the same RF source and phase shifters are used to align the RF driving signals. A polarization controller (PC) aligns the states of polarization.

Electro-optic frequency combs have proven very useful for a wide variety of applications. This is due to the tunability of their line spacing, which can be easily adjusted by varying the frequency of the RF signal driving the modulators. A wide tuning range can be achieved, spanning from values below the MHz up to ∼10 GHz, with the upper limit dictated by the bandwidth of the modulators. Among the applications requiring OFCs with low repetition rates, contributions related to interferometry and spectroscopy [78], sensing [79], [80], and ranging [81] have been reported, to cite a few.

With respect to applications in which high repetition rates are needed, demonstrations in multiple areas such as optical communications, arbitrary waveform generation or microwave signal synthesis have been published. A detailed review article developed by V. Torres-Company and A. Weiner covers this subject [74].

Electro-optic combs also allow for their integration in photonic circuits, and fully integrated comb sources have been reported. In 2018, the first monolithic InP electro-optic comb generator was published [82], incorporating an integrated DBR laser, a Mach-Zehnder modulator followed by two cascaded phase modulators, and a semiconductor optical amplifier to boost the optical signal. The comb source showed a demonstrated tunability range from 4 GHz to 10 GHz, with 28 comb lines within 5 dB achieved at 4 GHz, and 11 lines achieved at the highest repetition rate.

Moreover, recent advancements in the development of an integration platform based on lithium niobate on insulator have significantly enhanced the prospects for on-chip electro-optic combs. It has opened up the possibility of generating on-chip electro-optic combs with superior modulation efficiencies, low losses, high modulation bandwidths, and low V_π values. Some works have demonstrated the generation of flat OFCs with integrated electro-optic devices developed on the aforementioned platform using external (non-integrated) CW laser sources [83]. A recent contribution by M. Yu et al. [84] introduced a fully integrated electro-optic comb generator, consisting of a DFB laser edge-coupled to a lithium niobate chip. This chip (scheme of the setup and picture of the comb generator shown in Fig. 2.19 (a) and (b), respectively) included an amplitude modulator for generating flat-topped optical pulses, a phase modulator to induce a quadratic phase profile in the optical pulses, and a dispersive medium to compress the optical pulses, enabling the generation of frequency-agile and flat OFCs with an on-chip pulse duration of 8 ps. Both modulators exhibited high optical bandwidths (45 GHz for the amplitude modulator and 30 GHz for the phase modulator) and state-of-the-art V_π values, allowing for the generation of a 10.075-GHz OFC having a 10-dB bandwidth of $\sim$740 GHz with a modulation index of 11.2π rad (RF power of 38 dBm limited by the available RF amplifiers, not by the power handling capacity of the chip). A 30.135-GHz comb was also demonstrated, and both combs showed excellent flatness. Wavelength tunability was also proved, and pulse compression (up to 500 fs) based on an integrated lithium niobate chirped Bragg grating included in the device was reported. This research work illustrates the potential of hybrid and heterogeneously integrated comb generators combining III-V materials for the laser source and the lithium niobate platform for electro-optic devices, allowing for the generation of OFCs with outstanding properties catering to a diverse range of applications.

Finally, besides generating electro-optic frequency combs with the described single-pass architectures, there are other proposals that involve multiple passes of the signal through the modulators, allowing for the generation of a higher number of spectral lines [85]. Ring resonators modulated with an RF signal whose frequency matches a harmonic of the free spectral range of the cavity are commonly used. Although this proposals provide less flexibility in tuning the repetition frequency, combs with broad bandwidths can be generated using a CW laser source and a single resonator. The CW light that enters the

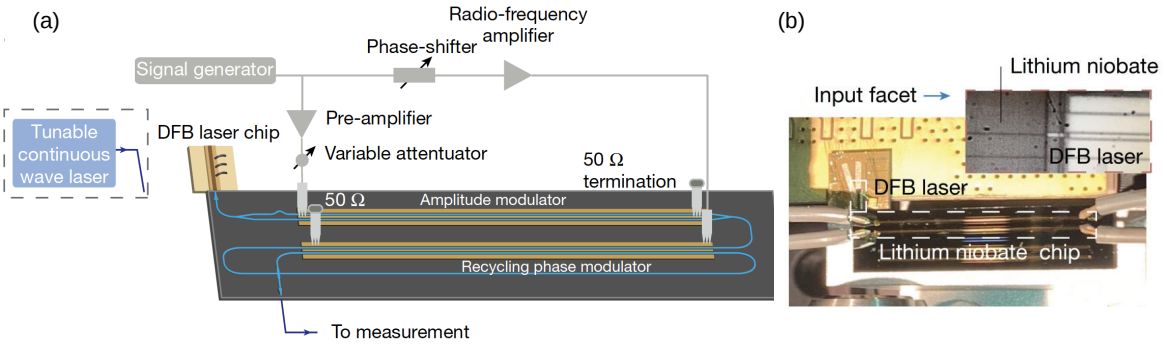

Figure 2.19: (a) Integrated electro-optic frequency comb generator based on lithium-niobate intensity and phase modulators. A DFB laser is butt-coupled to the photonic chip, providing the CW source for the generation of a 10.075-GHz OFC. (b) Picture of the device. (a) and (b) taken from [84].

resonator is modulated, resulting in the generation of sidebands that recirculate within the cavity, a process that leads to a cascaded generation of sidebands, i.e., comb lines. The generation of spectral lines is based on second-order nonlinear processes. With an integrated lithium niobate ring resonator, the generation of an electro-optic OFC with a bandwidth exceeding 80 nm (more than 900 equally spaced lines at ∼10 GHz) was demonstrated, using a pump power of 2 mW [86]. To conclude with, for further details on the generation and applications of electro-optic OFCs, the reader can be referred to [73], [87], which are excellent review articles.

2.3.3 Microcombs

Microcombs are defined in this document as OFCs generated in a microresonator fabricated in a material exhibiting third-order nonlinearity ($\chi^{(3)}$) pumped by a CW laser coupled to the resonator [88]. They are also referred to in the literature as Kerr combs. As a result of third-order nonlinearity, equally-spaced optical sidebands are generated around the pump frequency via four-wave mixing (FWM). The microresonators used to generate microcombs are passive devices made of a nonlinear dielectric material. The light coupled into these micrometer-sized resonators is strongly confined due to the higher index of the material of the core of the waveguide compared to that of the cladding. The coupling of light into the resonator and subsequent extraction are typically achieved through a waveguide via evanescent coupling (see Fig. 2.20).

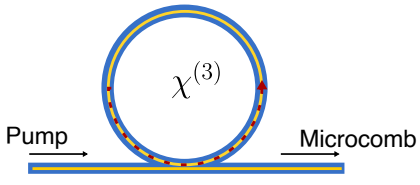

Figure 2.20: Sketch of a $\chi^{(3)}$ microresonator used for the generation of a microcomb.

As in mode-locked lasers, the resonant frequencies or cavity modes are defined by the round-trip time of the cavity, which in this case is $T_{res} = L/v_g$, where L is the length of the resonator and v_g is the group velocity. The spacing between adjacent resonant frequencies, the free spectral range (FSR), is equal to the inverse of the round-trip time, FSR $= 1/T_{res}$. Common parameters to describe a resonator are the width of the resonances, the finesse, and the quality factor of the resonator:

- The linewidth of the resonances, $\Delta\nu_{res}$, is determined by the cavity losses, which include the internal losses of the resonator and the coupling losses.
- The finesse, $\mathcal{F}$, is given by the ratio of the linewidth of the resonances to the FSR, $\mathcal{F} = \Delta\nu_{res}/\text{FSR}$. Sharp resonances are assessed with high finesse values.
- The quality factor or Q-factor, Q_{res}, indicates the losses in the cavity. In terms of energy, it is defined as 2π times the ratio of the energy stored in the cavity to the energy dissipated per oscillation cycle. Equivalently, in terms of resonance bandwidth, it is described as the ratio of the resonance center frequency ω_0 and the linewidth of the resonance as $Q_{res} = \frac{\omega_0}{\Delta\nu_{res}}$. It is an essential figure of merit of a resonator. High Q-factors, in the order of 1 million, are needed for efficient microcomb generation.

Microcomb generation is based on phase-matched FWM, a third-order nonlinear process that involves the interaction of four optical fields through an energy and momentum conservative process

$$\omega_1 + \omega_2 = \omega_3 + \omega_4, \tag{2.23}$$

$$\Delta\beta = \beta(\omega_1) + \beta(\omega_2) - \beta(\omega_3) - \beta(\omega_4), \tag{2.24}$$

where ω_i, with $i = (1, 2, 3, 4)$, denotes the angular frequency ($\omega_i = 2\pi\nu_i$) of the interacting waves, and $\beta(\omega_i)$ is the frequency-dependent propagation constant.

FWM can be non-degenerate, when it involves the interaction of four waves having four different frequencies, and degenerate, when the interacting fields have the same frequency ($\omega_1 = \omega_2$). The first lines of a microcomb originate from a degenerate FWM process, as a result of the increase of power within the resonator when the pump laser is tuned into a cavity resonance. On a fundamental level, two photons with the same frequency (the pump frequency) are annihilated and create idler and signal photons. Then, following the generation of initial sidebands through degenerate FWM, new sidebands are created through cascaded FWM processes (degenerate and non-degenerate), leading to the formation of the comb. In addition, for the generation of the comb lines to be efficient, FWM needs to be phase-matched ($\Delta\beta = 0$), i.e. the pump and the generated waves need to interfere constructively. As a result, the new generated sidebands are symmetrically located around the pump frequency. Phase-matched FWM is also known in the literature as modulation instability.

The formation of a microcomb stems from a balance between the cavity losses and parametric amplification on one hand, and between dispersion and Kerr nonlinearity on the other hand. Due to dispersion, the resonances of the microresonator deviate from their FSR. Since the sidebands are generated symmetrically around the pump, dispersion imposes a limit on the maximum achievable comb bandwidth. However, dispersion is not the only process that perturbs the positions of the cavity resonances, and the displacement of the cavity resonances can be compensated by shifts of the resonances associated to Kerr nonlinearity.

Phase-matched FWM, which triggers the generation of the microcomb, is easily achieved when the microresonator exhibits anomalous group velocity dispersion (GVD) in the frequency range of interest [89]. Anomalous GVD is characterized by a negative GVD parameter ($\beta_2<0$) and therefore a positive dispersion parameter ($D>0$). In a waveguide exhibiting anomalous GVD, the high-frequency components travel faster than the low-frequency components. Consequently, in a microresonator exhibiting anomalous dispersion, the cavity resonances deviate from being equally spaced and the spacing between modes increases with ascending frequency. The generation of an OFC in a microresonator operating in the anomalous dispersion regime is illustrated in Fig. 2.21. The figure depicts the distribution of the resonances of the microresonator, and the resonance with index $n=0$ corresponds to the pumped resonance. The resonances affected by anomalous GVD are represented in the figure in gray, while the ideal position of the resonances evenly spaced by the FSR of the resonator are represented with dashed red lines.

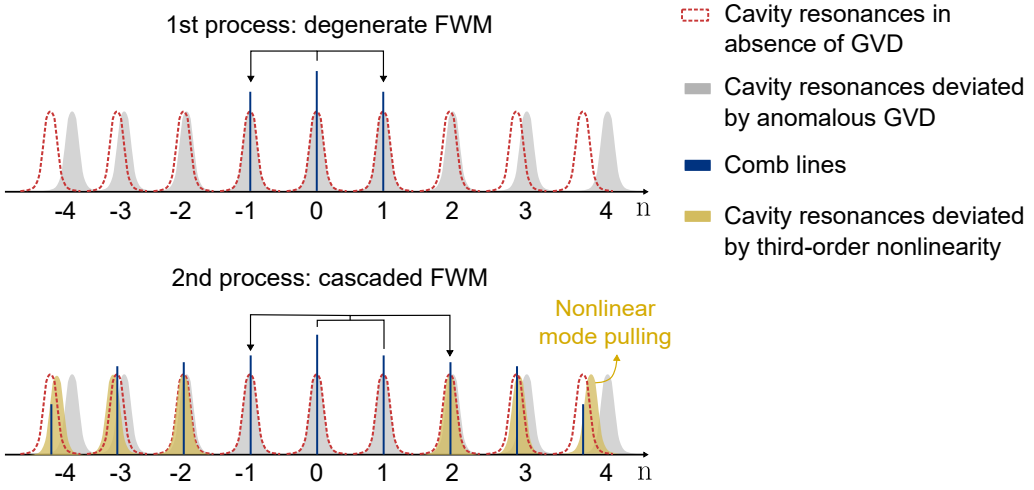

Figure 2.21: Formation process of a microcomb in a microresonator exhibiting anomalous GVD. The cavity resonances are denoted by an index n, with $n=0$ corresponding to the resonance in which the pump is coupled. The first comb lines are created through degenerate FWM. After this, additional sidebands are generated by means of cascaded FWM. The deviation of the FSR of the cavity modes due to dispersion is compensated by the Kerr effect, allowing to extend the comb bandwidth.

First, the pump laser is coupled into the microresonator and is tuned into one of the resonances of the cavity. As the pump laser moves towards and across the cavity resonance, the intracavity power increases. When a specific amount of power is coupled, nonlinear processes are triggered and the first comb lines are created around the pump through degenerate FWM. Subsequently, the rest of comb lines are generated by means of cascaded FWM. As a consequence of the intracavity power increase, other third-order nonlinear processes such as self-phase modulation and cross-phase modulation arise, which also affect the position of the resonances [90]: the deviation of the resonances due to anomalous GVD is counteracted by means of self-phase modulation and cross-phase modulation, which pull the resonances towards lower frequency positions. The resonances affected by nonlinear pulling effects are represented in the figure in yellow. Furthermore, as a consequence of the temperature increase, the cavity length and the refractive index slightly change. This variation also causes the frequency of the resonances to decrease as the temperature increases.

The generation of a Kerr OFC was first reported in 2007 by Del'Haye et al. [91]. In their demonstration, they obtained a microcomb from a silica toroidal microresonator exhibiting a quality factor Q_{res}>10^8 and a threshold for parametric interactions about 50 μW. By pumping a 75-μm-diameter microresonator with a CW power of 130 mW at 1550 nm, the authors generated a frequency comb with a bandwidth extended over 500 nm (64.1 THz) and a line spacing defined by the FSR of the resonator of 873 GHz. They also reported the generation of combs with lower repetition rates (around 375 GHz), obtained with devices showing larger diameters. This publication paved the way towards the miniaturization of comb generators by harnessing the Kerr effect within micrometer cavities to obtain OFC spectra with large line spacings and bandwidths that can extend over an octave without utilizing post-broadening techniques. Since then, microcomb generation has emerged as a relevant and ongoing area of research. Nonetheless, these combs suffered from noise and they did not correspond to pulses in the time domain.

Dissipative cavity soliton generation in microresonators

In 2013, K. Saha et al. [92] reported the generation of coherent and periodic optical pulses in a Si_3N_4 microresonator, caused by nonlinear interactions within the externally, CW-pumped resonator. Later in 2014, T. Herr et al. [93] identified the generation of such a phase-locked train of pulses as a result of the formation of temporal dissipative cavity solitons within the microresonator, in a work that certainly changed the paradigm in microcomb generation. In their publication, the authors experimentally demonstrated the formation of stable solitons in a magnesium fluoride (MgF_2) microresonator, assisted with numerical and analytical results.

A dissipative cavity soliton is a temporal structure that can propagate in a nonlinear cavity for an infinite amount of time without suffering any deformation. The existence of the soliton relies on the aforementioned balance between GVD and Kerr nonlinearity, and between gain (associated to parametric amplification) and cavity losses. By pumping a high-Q microresonator with a certain power and a specific detuning with respect to a cavity resonance, it is possible to reach a soliton regime in which a single soliton

stably circulates within the cavity. At each round-trip, part of the energy "escapes" from the cavity, forming a train of coherent optical pulses at the output. The phases of the generated optical pulses are locked to the phase of the pump laser. In the frequency domain, such train of pulses corresponds to a frequency comb with high-coherence properties. To reach the soliton regime, the pump laser is swept from a blue-detuned position with respect to one of the cavity resonances towards a red-detuned position. During this scan, the cavity field transits through different states for different detuning values until single soliton regime is achieved [93]. First, when the threshold for parametric interactions is exceeded, modulation instability occurs as in the case of FWM-based (in absence of dissipative solitons) microcombs. Then, chaotic and multiple-soliton states are experienced until a single soliton is achieved. The formation of a single soliton corresponds to the pump laser being effectively red-detuned from the pumped resonance. Temporal dynamics of microcombs are described by the Lugiato-Lefever equation [94], an externally-driven nonlinear Schödinger equation. Dissipative solitons on top of a CW component are a stable solution of this equation [90].

Soon after the demonstration of dissipative solitons in microresonators exhibiting anomalous dispersion, also known as bright solitons, the generation of phase-locked Kerr combs in a microresonator with normal GVD was reported [95]. The localized structures observed in these devices are known as dark solitons or platicons as, in contrast to bright solitons, they are characterized by a notch in the CW background. A sketch illustrating the formation of bright and dark solitons in a microresonator (top) and their typical spectral shapes (bottom) is included in Fig. 2.22 (a) and (b), respectively.

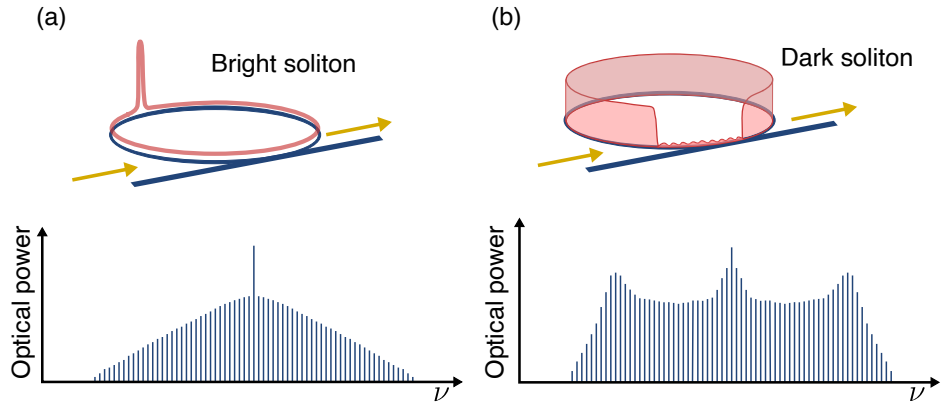

Figure 2.22: Sketch of a (a) bright and a (b) dark soliton in an optical microresonator and illustration of their typical spectra.

The generation of microcombs in the normal dispersion regime is typically achieved through the local modification of the dispersion [96]. In a device exhibiting global normal GVD, anomalous dispersion can be locally induced at specific frequencies. In such frequencies, the condition of phase-matching of FWM can be fulfilled and the formation of the comb can be initiated. The possibility of initiating a microcomb in the normal dispersion regime offered significant benefits since most materials used to generate microcombs exhibit normal GVD dispersion in the visible and near infrared

[97]. As a consequence, the generation of normal-dispersion microcombs alleviates the need for dispersion engineering required to obtain microresonators exhibiting anomalous dispersion. Moreover, the conversion efficiency attained with these combs, defined as the power transferred from the pump to the new generated lines, is higher than that obtained with bright-soliton OFCs [98]. This characteristic enhances the flatness of the generated comb, as the power difference between the pump and the rest of the lines is reduced, which can be advantageous for some applications such as optical communications or spectroscopy.

One of the techniques employed to generate microcombs in the normal dispersion regime is the use of coupled cavities. In this approach, the interaction between modes of the two coupled cavities is leveraged to induce local anomalous dispersion. In a work presented by Xue et al. [99], they proposed the use of two coupled cavities (main and auxiliary) of similar radii. In the auxiliary cavity, a microheater was included in order to slightly shift the position of the auxiliary resonances as a consequence of the refractive index change with temperature. Through the microheater, they demonstrated the ability to control the region where mode coupling occurs, therefore gaining control and reliability over the generation of the microcomb. In addition, the use of coupled-cavity systems has also proven beneficial for the generation of microcombs exhibiting anomalous dispersion [100]. In their work, Helgason et al. reported the generation of an anomalous-GVD microcomb featuring unprecedented conversion efficiencies (up to 54%) using a coupled-cavity system formed by two cavities with very dissimilar radii. The microcomb was generated using the conventional method of tuning the pump laser across one of the main cavity resonances, until reaching a red-detuned position where a single soliton circulated within the cavity. Then, bringing the auxiliary resonance closer to the main resonance via microheaters induced mode coupling, causing the main resonance to red shift. As a result of such frequency shift, the pump was centered around the main resonance while maintaining a single-soliton state. This allowed to achieve a higher conversion efficiency due to the increased power coupled into the resonator. This configuration of two dissimilar coupled cavities will be used later in Chapter 7 for the generation of two OFCs in the normal dispersion regime.

Finally, over last years, the research community has made significant progress toward achieving a better understanding of microcomb generation, as well as in their manipulation and control, both in anomalous and normal dispersion regimes. The reader is referred to the review by A. Pasquazi et al. [88] for further insights into this matter. Furthermore, the generation of dissipative cavity solitons in Kerr microresonators has been demonstrated on various platforms [101]. Among them, Si_3N_4 has stood out for several reasons. First, microresonators based on Si_3N_4 waveguides with silica cladding are fabricated with CMOS-compatible techniques, mature processes that potentially allow for mass fabrication of these devices. Also, Si_3N_4 has a large transparency window that covers from the visible to the mid-infrared (400 nm - 3700 nm), exhibits high $\chi^{(3)}$ nonlinearity, and does not suffer from two-photon absorption. Other materials such as lithium niobate have proven to be interesting for the generation and manipulation of the Kerr comb on the same chip [102], exploiting $\chi^{(3)}$ nonlinearity for OFC generation and $\chi^{(2)}$ nonlinearity for its manipulation (filtering, electro-optic modulation). Regarding

the use of microcombs, they have proven to be well suited for a variety of applications [103]. Because of their repetition rate range (from tens to hundreds of GHz) and their extremely broad bandwidths, they are especially useful for applications such as optical clocks [104], optical communications [105], or for the calibration of astronomical spectrographs [106].

Chapter 3

Dual-comb interferometry

The multiheterodyne interference of two optical frequency combs with slightly different repetition rates has demonstrated to overcome the limitations of traditional interferometers. The technique, widely known as dual-comb interferometry, emerged in the early 2000s in the search for new applications of frequency combs. It enables the direct mapping of optical frequency information to the radio frequency domain, exploiting the unique properties of optical frequency combs. Dual-comb interferometry enables the retrieval of interferometric information in a single acquisition with a setup that contains no moving parts, achieving unprecedented acquisition speeds and spectral resolutions.

This chapter focuses on the description and comprehensive analysis of dual-comb interferometry. First, the fundamental principles of the technique and its implementation are discussed. Subsequently, practical implications are considered, including the structure of the down-converted electrical spectrum and the trade-off between spectral resolution and measurement speed. Following this, the generation of gain-switched dual frequency combs is detailed, with the assistance of numerical simulations. Finally, the use of dual-comb interferometers for applications such as molecular spectroscopy or ranging is discussed.

3.1 Fundamentals of dual-comb interferometry

Dual-comb interferometry is a technique based on the multiheterodyne beating of two OFCs. It enables the translation of the complex (amplitude and phase) response of a device or sample from the optical domain to the electrical domain, in a single and rapid interrogation, with high spectral resolution, and using radio frequency electronics.

The main antecedent of dual-comb interferometry is Michelson-based Fourier transform spectroscopy. This widely used spectroscopic technique is based on the characterization of a sample using a system fundamentally composed of a Michelson interferometer, illustrated in Fig. 3.1.

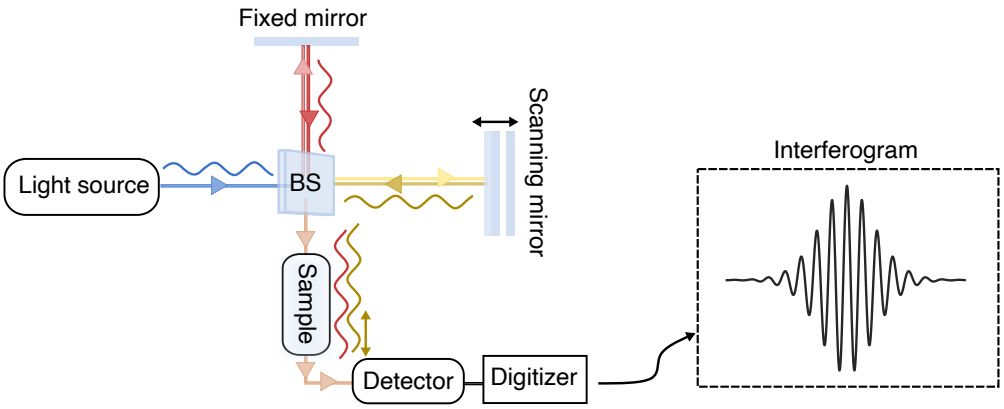

Figure 3.1: Illustration of a Michelson-based Fourier transform interferometer. The interference of two beams as a function of a varying optical path difference induced by a scanning mirror is measured. The recorded signal is known as interferogram. BS: beam-splitter.

The interferometer is illuminated by a light source. A broadband, incoherent, light source has been traditionally used for this purpose. In the interferometer, a beam splitter divides the input beam into two branches. One of the branches contains a mirror set to a fixed position. The second arm of the interferometer includes a scanning mirror, which induces changes in the path length traversed by the optical field in this second branch. Considering an ideal splitting ratio of 50:50, the optical fields in the two arms of the interferometer can be written as

$$E_1(t) = \frac{E_0(\nu)}{2} e^{-j2\pi\nu t}, \tag{3.1}$$

$$E_2(t) = \frac{E_0(\nu)}{2} e^{-j(2\pi\nu t - \Delta\phi)}, \tag{3.2}$$

where $E_0(\nu)$ is the amplitude of the optical field as a function of the optical frequency ν, and $\Delta\phi$ is the phase change induced in the arm containing the scanning mirror. This phase change can be expressed in terms of the optical path difference δ as $\Delta\phi = 2\pi\tilde{\nu}\delta$,

with $\tilde{\nu}$ being the wavenumber[1].

Then, the two beams from the two arms are combined and finally interfere in a detector. Through the movement of the scanning mirror, the optical path difference of the two combined signals is varied. Consequently, the interference pattern between the two beams changes as a function of the optical path difference. The resulting interference wave is known as interferogram, and its expression is given by

$$I(\delta) \propto [E_1(t) + E_2(t)][E_1(t) + E_2(t)]^* = \frac{|E_0(\nu)|^2}{2}\Big[1 + \cos(2\pi\tilde{\nu}\delta)\Big], \tag{3.3}$$

where * represents the complex conjugate and $|E_0(\nu)|^2$, the squared magnitude of $E_0(\nu)$, denotes the intensity of the optical field. In the case of monochromatic light, the interferogram presents interference maxima and minima. The Fourier transform of the interferogram yields a spectrum that contains the response of the sample across different frequencies. The sample can be interrogated by either the optical beam from one path or by the combined beams.

The spectral resolution of the measurement, which refers to the capability of the interferometer to resolve two closely spaced frequency components, is limited by the maximum scanning range of the movable mirror. To distinguish between two frequency components spaced by $\Delta\tilde{\nu}$, a complete period of the beat frequency of these two components must be scanned, in order for the two signals to become in phase [107]. As illustrated in Eq. (3.3), after zero path difference, the two signals will first interfere destructively at $\delta = \Delta\tilde{\nu}^{-1}/2$. Then, at $\delta = \Delta\tilde{\nu}^{-1}$ they will be in phase, resulting in constructive interference. Therefore, a higher spectral resolution requires a higher retardation of one of the optical beams (or, in other words, a longer scanning range). On the other hand, the minimum time step of the scanning mirror determines the bandwidth of the measurement. The acquisition speed of the interferometer is set by the speed of the mirror and the total scanning time.

The advent of OFCs made it possible to replace the incoherent white source by a coherent source composed of many evenly-spaced frequencies, allowing to improve the signal-to-noise ratio (SNR) [108]. However, despite the higher brightness of the light source, these systems were still limited by the scanning mirror. The mirror not only adds complexity, but also prevents the system from having a fast acquisition speed, since the velocity of the mirror is typically on the order of 1 cm per second. At this scanning speed, a measurement time on the order of tens of seconds would be required to achieve a spectral resolution of 1 GHz. The replacement of the scanning mirror by a second OFC featuring a slightly different repetition rate, in a configuration widely known as dual-comb interferometer, has enabled to surpass the performance of Michelson-based Fourier transform interferometers. Dual-comb interferometry allows to improve the acquisition speed of Michelson interferometers by several orders of magnitude, enabling high-resolution measurements using a compact setup without moving elements.

[1]The wavenumber ($\tilde{\nu} = 1/\lambda$, with λ being the wavelength in vacuum) is used here to write the final expression more compactly.

Dual-comb technique was proposed and experimentally demonstrated in 2001 by Lee et al. to perform time-domain optical coherence tomography [109]. One year later, in 2002, S. Schiller reported a theoretical analysis and described the time and frequency domain fundamentals of dual-comb systems [110]. The technique is based on the generation of two OFCs with slightly different repetition frequencies, f_{R1} and f_{R2}, where f_{R2} can be expressed as

$$f_{R2} = f_{R1} + \delta f_R, \tag{3.4}$$

with $\delta f_R << f_{R1}, f_{R2}$ being the repetition frequency difference.

As a result, the optical frequencies of the two involved combs, ν_{1n} and ν_{2m}, can be written as

$$\nu_{1n} = \nu_{01} + n f_{R1}, \tag{3.5}$$

$$\nu_{2m} = \nu_{02} + m f_{R2} = \nu_{02} + m(f_{R1} + \delta f_R), \tag{3.6}$$

ν_{01} and ν_{02} being the lowest-frequency comb line of OFCs 1 and 2, respectively, and n and m being positive integer numbers. In the literature, the two OFCs used in a dual-comb system are often referred to as dual frequency combs.

The two OFCs are combined and then mixed on a photodetector. In the photodetector, a multiheterodyne beating process occurs, in which each comb line of one comb beats with the lines of the second comb. As a result, a down-converted frequency comb is obtained, with a line spacing that corresponds to the repetition frequency difference of the two OFCs, δf_R. The down-converted frequency comb is a compressed version of the original optical spectrum, and the optical information is effectively translated into the RF domain. This compression process is quantified by the compression factor, defined as the ratio of f_{R1} and δf_R ($C = f_{R1}/\delta f_R$). Fig. 3.2 illustrates the down-conversion process of two OFCs from optical frequencies to radio frequencies. In the figure, the amplitude information of a sample interrogated by the two OFCs is translated from the optical to the RF domain.

In the Michelson-based Fourier transform interferometer the down-conversion process was achieved by means of the scanning mirror, as it is the element which induces the phase shift between the two interfering waves. Due to the typical scanning velocities of these mirrors, the optical frequencies are down-converted to the audio range [108]. In dual-comb interferometry, the down-conversion process is achieved and controlled by means of the repetition rate difference of the combs. As it will be detailed later, to prevent spectral overlap in the down-conversion process, an appropriate compression factor must be chosen. Typical values of the compression factor lie within the range of 10^4 to 10^6. Consequently, opto-electronic conversion becomes feasible using a low-bandwidth photodetector, and the resulting signal can be digitized using equipment operating at electrical frequencies.

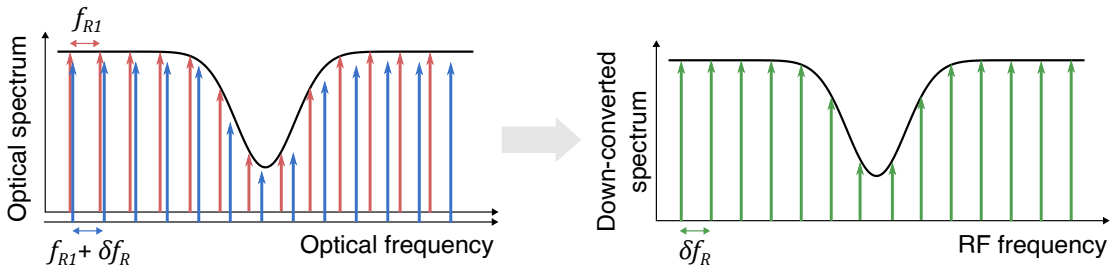

Figure 3.2: Frequency-domain picture of the basic principle of the dual-comb technique. The beating of two OFCs with repetition rates f_{R1} and f_{R2}= f_{R1} + δf_R generates a down-converted spectrum with a line spacing of δf_R. The response of a sample interrogated by the optical combs can be recovered from the analysis of the down-converted spectrum.

In the time domain, an interferogram is obtained from the interference on the photodetector of the two trains of optical pulses with slightly different periodicity. The two trains of optical pulses sample each other with relative timing increments of δT_R, and a maximum of interference is obtained when two optical pulses from the two OFCs arrive at the photodetector in phase. The temporal increments between each consecutive pair of pulses is given by

$$\delta T_R = \frac{1}{f_{R1}} - \frac{1}{f_{R2}} = \frac{\delta f_R}{f_{R1}(f_{R1} + \delta f_R)} \approx \frac{1}{C f_{R1}}. \tag{3.7}$$

The time-domain picture of dual-comb interferometry is illustrated in Fig. 3.3.

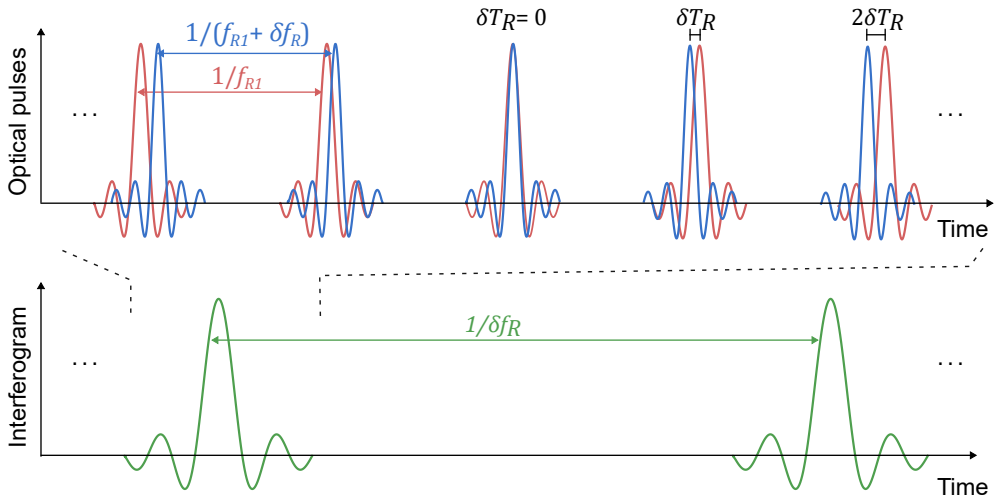

Figure 3.3: Time domain picture of the basic principle of the dual-comb technique. The two trains of pulses with periodicity of $1/f_{R1}$ and $1/(f_{R1} + \delta f_R)$ walk through each other, and their interference generates a point of the interferogram every δT_R. The maximum of the interferogram bursts, which reproduce with a periodicity of δf_R^{-1}, is obtained when the two pulses are in phase.

The interference of both combs can be easily understood as the cross-correlation of the two trains of pulses, and a point of the interferogram is obtained every δT_R. In contrast to the compression observed in the frequency domain, the interference of the two combs in the time domain results in an expansion of the time axis. The interferogram bursts reproduce with a periodicity given by δf_R^{-1}.

This elegant technique enables interactions that occur at optical frequencies to be translated and measured at RF frequencies with a compact setup freed from scanning mirrors, using cost-effective instrumentation for signal acquisition. Fast acquisition speeds in the microsecond range can be achieved, and a single acquisition contains the full information of the sample. The spectral resolution determined by the line spacing of the combs, i.e., f_{R1}.

Depending on whether it is necessary to recover the complex response of the sample or just its amplitude information, the interferometer can be configured in either an asymmetrical or a symmetrical arrangement. The characteristics of both architectures are detailed below.

Asymmetric configuration

The amplitude and phase information of a sample under test can be obtained using a setup in asymmetric or dispersive configuration. In this setup, illustrated in Fig. 3.4, one of the combs, referred to as signal or probe comb, passes through the sample. As a result, the amplitude and phase of the sample is encoded in its comb tones. A second comb, which does not interrogate the sample, serves as local oscillator.

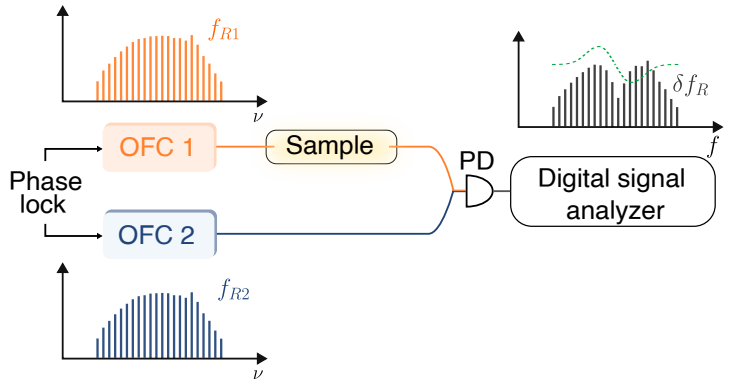

Figure 3.4: Illustration of an asymmetric or dispersive dual-comb setup in which only one of the OFCs traverses the tested sample. The amplitude and phase response (green dotted profile) of the sample can be recovered from the down-converted comb.

The complex representation of the optical field of the probe comb, $E_1(t)$, after interrogating the sample, can be expressed as

$$E_1(t) = \sum_{n=0}^{N-1} A_{1n} e^{-j(2\pi\nu_{1n}t+\phi_{1n})} t_{sn} e^{-j\phi_{sn}}, \tag{3.8}$$

where N is a positive integer denoting the number of comb teeth, A_{1n}, ν_{1n} and ϕ_{1n} are the amplitude, optical frequency and phase of the n$^{\text{th}}$ probe comb tooth, respectively, t_{sn} is the field transmission response of the sample encoded in the comb lines, and ϕ_{sn} represents the phase shift experienced by each comb line after traversing the sample. Then, both combs, probe and local oscillator, are combined.

Considering a lossless optical coupler with a 50:50 splitting ratio, the expression of the combined optical fields at the output of the coupler is $\frac{1}{\sqrt{2}}(E_1(t) - jE_2(t))$, where $E_2(t)$ is the complex representation of the optical field of the local oscillator OFC. However, this expression can be simplified to $E_1(t) + E_2(t)$ without introducing significant changes in the final result. Therefore, the optical field obtained after the combination of both OFCs can be approximated as

$$E_1(t) + E_2(t) \propto \sum_{n=0}^{N-1} A_{1n} e^{-j(2\pi\nu_{1n}t+\phi_{1n})} t_{sn} e^{-j\phi_{sn}} + \sum_{m=0}^{N-1} A_{2m} e^{-j(2\pi\nu_{2m}t+\phi_{2m})}, \tag{3.9}$$

where A_{2m}, ν_{2m} and ϕ_{2m} represent the amplitude, frequency, and optical phase of each comb tooth of the local oscillator comb.

Finally, the photocurrent obtained from the interference of both optical fields on a photodetector is given by

$$I_{PD}(t) = \mathcal{R}\langle \Big[E_1(t) + E_2(t)\Big] \Big[E_1(t) + E_2(t)\Big]^* \rangle, \tag{3.10}$$

where the $\langle\cdot\rangle$ operator represents averaging over a time interval much longer than an optical cycle, * stands for the complex conjugate, and $\mathcal{R}$ is the responsivity of the photodetector, defined as $\mathcal{R}{=}\eta q/(h\nu)$ (η being the quantum efficiency of the photodetector, q the electron charge, h the Planck constant, and ν the optical frequency). Eq. (3.10) considers that the optical field is normalized to units of W$^{1/2}$.

The photocurrent comprises the beat of all the tones of the probe comb with all the tones of the local oscillator, leading to different Nyquist zones in the resulting RF spectrum, as discussed in the subsequent section. To illustrate the expression of the photocurrent, only the beat of each probe comb tone with its counterpart of the local oscillator is considered, i.e. the beat of neighboring probe and local oscillator tones ($n = m$). At the output of the photodetector the following current is obtained

$$
\begin{aligned}
I_{PD}(t)|_{n=m} &= \mathcal{R}\sum_{n=0}^{N-1}\Big(A_{1n}e^{-j(2\pi\nu_{1n}t+\phi_{1n})}t_{sn}e^{-j\phi_{sn}} + A_{2n}e^{-j(2\pi\nu_{2n}t+\phi_{2n})}\Big) \\
&\qquad \Big(A_{1n}e^{j(2\pi\nu_{1n}t+\phi_{1n})}t_{sn}e^{j\phi_{sn}} + A_{2n}e^{j(2\pi\nu_{2n}t+\phi_{2n})}\Big) = \\
&= \mathcal{R}\sum_{n=0}^{N-1}\Big[A_{1n}^2t_{sn}^2 + A_{2n}^2 + 2A_{1n}A_{2n}t_{sn}\cos\Big(2\pi(\nu_{2n}-\nu_{1n})t + \phi_{2n} - \phi_{1n} - \phi_{sn}\Big)\Big] = \\
&= \mathcal{R}\sum_{n=0}^{N-1}\Big[A_{1n}^2t_{sn}^2 + A_{2n}^2 + 2A_{1n}A_{2n}t_{sn}\cos\Big(2\pi(\nu_{02}-\nu_{01}+n\ \delta f_R)t + \phi_{2n} - \phi_{1n} - \phi_{sn}\Big)\Big].
\end{aligned}
\tag{3.11}
$$

The first two terms within the summation in Eq. (3.11) represent direct detection components. The third term, referred to as beat term, contains the information of interest since it tracks changes in both the amplitude and the phase of the field at each down-converted frequency component ($n\ \delta f_R$). Moreover, in Eq. (3.11) it is assumed that the bandwidth of the photodetector results in averaging over a duration that is much longer than the optical frequency but shorter than any other frequency of interest.

The Fourier transform of $I_{PD}(t)$ reveals the dual-comb spectrum. It can be written as

$$
\begin{aligned}
I_{PD}(f)|_{n=m} \propto \sum_{n=0}^{N-1}\Big\{ & A_{1n}^2t_{sn}^2\delta(f) + A_{2n}^2\delta(f) + \\
& 2A_{1n}A_{2n}t_{sn}\Big[e^{j(\phi_{2n}-\phi_{1n}-\phi_{sn})}\delta\Big(2\pi(f-\delta f_0 - n\ \delta f_R)\Big) + \\
& e^{-j(\phi_{2n}-\phi_{1n}-\phi_{sn})}\delta\Big(2\pi(f+\delta f_0 + n\ \delta f_R)\Big)\Big]\Big\},
\end{aligned}
\tag{3.12}
$$

$\delta f_0 = \nu_{02} - \nu_{01}$ denoting the frequency difference of the lowest-frequency comb lines of the two combs. The combination of the two combs in frequency domain and the down-converted spectrum resulting from the interference of neighboring OFC lines is illustrated in Fig. 3.5 in panels (a) and (b), respectively.

Moreover, it is worth mentioning that the direct detection terms appearing in the photodetected current using a single photodetector can be eliminated by means of balanced photodetection, a common approach usually employed in dual-comb interferometry experiments. The main difference relies in using two photodetectors, producing two photocurrents I_{PD1} and I_{PD2} that arise from the addition and subtraction of the optical fields of both combs, as illustrated in Fig. 3.6.

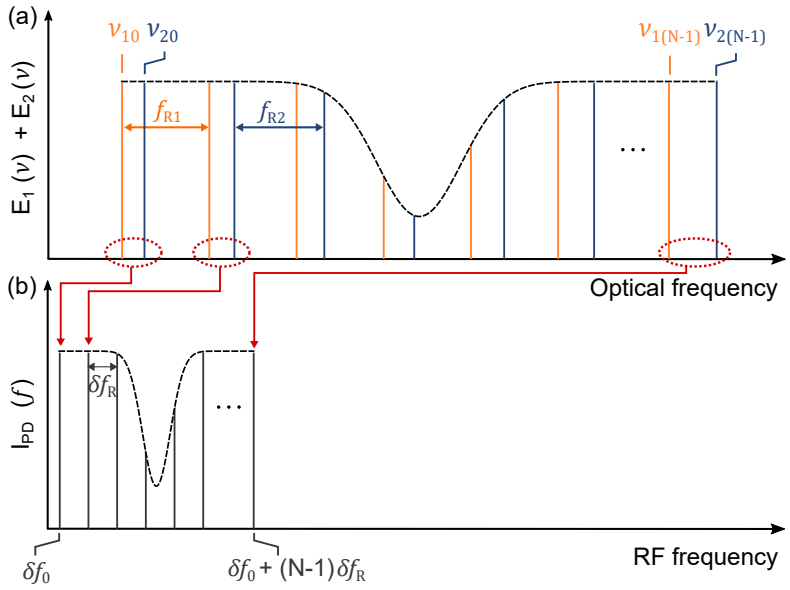

Figure 3.5: (a) Frequency-domain illustration of the optical field originating from the sum of two OFCs with repetition rates of f_{R1} (orange) and $f_{R2} = f_{R1} + \delta f_R$ (blue). (b) Down-converted RF spectrum that results from the interference on a photodetector of the two OFCs depicted in (a). Only the RF replica that arises from the beating of neighboring comb lines from the two combs is illustrated.

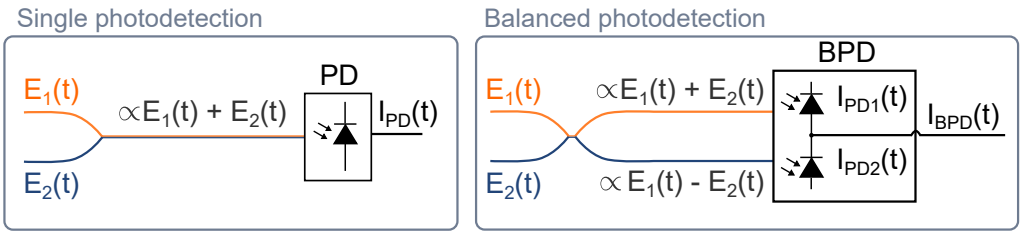

Figure 3.6: Single and balanced photodetection. The proportional operator $\propto$ responds to the simplification of the field at the output of the optical coupler, which has been considered in the formulation of the photocurrent expressions. This simplification does not account for the $1/\sqrt{2}$ factor nor for the phase shift experienced by one of the optical fields.

The expressions of $I_{PD1}(t)$ and $I_{PD2}(t)$, considering n=m, can be formulated as

$$I_{PD1}(t)|_{n=m} = \mathcal{R} \sum_{n=0}^{N-1} \left[A_{1n}^2 t_{sn}^2 + A_{2n}^2 + 2A_{1n}A_{2n}t_{sn} \cos\Big(2\pi(\delta f_0 + n\ \delta f_R)t + \phi_{2n} - \phi_{1n} - \phi_{sn}\Big) \right], \tag{3.13}$$

$$I_{PD2}(t)|_{n=m} = \mathcal{R} \sum_{n=0}^{N-1} \left[A_{1n}^2 t_{sn}^2 + A_{2n}^2 - 2A_{1n}A_{2n}t_{sn} \cos\Big(2\pi(\delta f_0 + n\ \delta f_R)t + \phi_{2n} - \phi_{1n} - \phi_{sn}\Big) \right]. \tag{3.14}$$

The current at the output of the balanced photodetector is given by the subtraction of $I_{PD1}(t)$ and $I_{PD2}(t)$. Its expression is written as

$$I_{BPD}(t)|_{n=m} = I_{PD1}(t) - I_{PD2}(t) = \\ = \mathcal{R} \sum_{n=0}^{N-1} 4A_{1n}A_{2n}t_{sn} \cos\Big(2\pi(\delta f_0 + n\ \delta f_R)t + \phi_{2n} - \phi_{1n} - \phi_{sn}\Big), \tag{3.15}$$

in which, in addition to the disappearance of the direct detection terms, the intensity of the photocurrent is increased by a factor of 2.

Symmetric configuration

A symmetric or collinear dual-comb setup can be employed when only the amplitude of the sample, and not the information related to the phase, needs to be measured. A diagram of this type of setup is shown in Fig. 3.7.

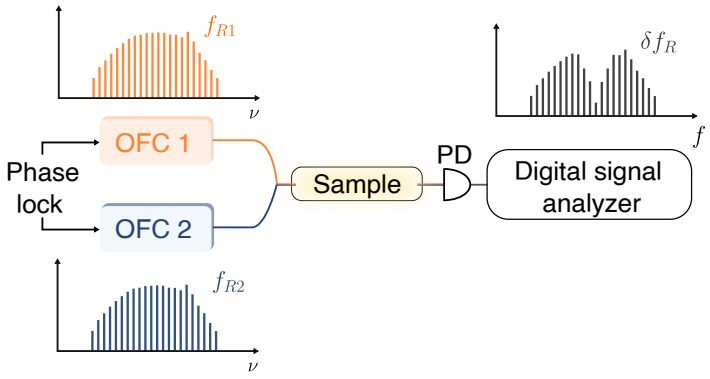

Figure 3.7: Illustration of a symmetric or collinear dual-comb setup in which both combs traverse the tested sample.

In a symmetric arrangement, both combs are combined before traversing the sample and, consequently, the information of the sample is encoded in the two OFCs. The resulting optical field after the two combs have passed through the sample can be approximated as

$$E_1(t) + E_2(t) = \sum_{n=0}^{N-1} A_{1n}e^{-j(2\pi\nu_{1n}t+\phi_{1n})}t_{sn}e^{-j\phi_{sn}} + \sum_{m=0}^{N-1} A_{2m}e^{-j(2\pi\nu_{2m}t+\phi_{2m})}t_{sm}e^{-j\phi_{sm}}. \tag{3.16}$$

Following the same procedure as that carried out in the asymmetric approach, the electrical current at the output of the photodetector can be expressed as

$$\begin{aligned} I_{PD}(t)|_{n=m} &= \mathcal{R}\sum_{n=0}^{N-1}\Big(A_{1n}e^{-j(2\pi\nu_{1n}t+\phi_{1n})}t_{sn}e^{-j\phi_{sn}} + A_{2n}e^{-j(2\pi\nu_{2n}t+\phi_{2n})}t_{sn}e^{-j\phi_{sn}}\Big) \\ &\qquad \Big(A_{1n}e^{j(2\pi\nu_{1n}t+\phi_{1n})}t_{sn}e^{j\phi_{sn}} + A_{2n}e^{j(2\pi\nu_{2n}t+\phi_{2n})}t_{sn}e^{j\phi_{sn}}\Big) = \\ &= \mathcal{R}\sum_{n=0}^{N-1}\Big[A_{1n}^2t_{sn}^2 + A_{2n}^2 + 2A_{1n}A_{2n}t_{sn}^2\cos\Big(2\pi(\nu_{2n}-\nu_{1n})t + \phi_{2n} - \phi_{1n}\Big)\Big] = \\ &= \mathcal{R}\sum_{n=0}^{N-1}\Big[A_{1n}^2t_{sn}^2 + A_{2n}^2 + 2A_{1n}A_{2n}t_{sn}^2\cos\Big(2\pi(\delta f_0 + n\ \delta f_R)t + \phi_{2n} - \phi_{1n}\Big)\Big], \end{aligned} \tag{3.17}$$

where within the beat term, only the amplitude information of the sample prevails. Although the information related to phase changes experienced by the combs when interrogating the sample is lost, the intensity interaction with the sample is greater than that obtained using the asymmetric approach. Consequently, this configuration may prove advantageous when the interaction with the sample is relatively weak, and only changes in amplitude are required for its characterization.

Finally, in both asymmetric and symmetric arrangements, an additional reference measurement is required to extract the response of the sample being interrogated. In this measurement, none of the combs pass through the sample. Then, a frequency analysis of the two RF dual-comb spectra (sample and sample-free) is typically conducted, and the amplitude and phase information is extracted for each comb line. The full response of the sample is obtained as a function of frequency after normalizing the information extracted from the measurement dual-comb spectrum with respect to the reference spectrum.

When calculating the amplitude response of the sample, different considerations need to be taken into account depending on whether the setup employed is asymmetric or symmetric. The amplitude response is obtained from the analysis of the power spectral densities of the two RF spectra: the one containing the information of the sample and the reference spectrum. The power spectral density is calculated as the squared magnitude of the Fourier transform of the photodetected current, i.e., $|I_{PD}(f)|^2$ (where $|\cdot|$ denotes the modulus operator).

If an asymmetric arrangement is used for interrogating a sample, the measured transmission response T_{asymm} follows the expression

$$T_{asymm} = \frac{\mathrm{PSD}_{sample}}{\mathrm{PSD}_{ref}} = t_{sn}^2 = T_{sn}, \tag{3.18}$$

where PSD_{sample} and PSD_{ref} represent the power spectral densities of the dual-comb spectra with and without the sample, respectively, and T_{sn} is the transmission response

of the sample in optical power units. The upper case notation in T_{asymm} and T_{sn} is used as these variables represent a power transmission response and not a field transmission response. The measured transmission, obtained from the analysis of the electrical power spectral densities, corresponds to the optical transmission in power units.

In contrast, if a symmetric arrangement is used, the measured transmission response T_{symm} is given by

$$T_{symm} = \frac{\mathrm{PSD}_{sample}}{\mathrm{PSD}_{ref}} = t_{sn}^4 = T_{sn}^2. \tag{3.19}$$

In this case, since both the probe and local oscillator combs interrogate the sample, the measured electrical transmission in power units corresponds to the square of the optical transmission in power units. Consequently, the optical intensity response of the sample must be calculated as the square root of the measured electrical transmission response. Alternatively, if logarithmic units were used, the measured electrical transmission response needs to be divided by two to obtain the optical intensity response.

3.1.1 Nyquist zones, acquisition speed, and spectral resolution

In a dual-comb interferometer, ensuring the proper operation of the system requires meeting specific conditions regarding parameters such as the compression factor and the bandwidth of the optical combs. The selection of these parameters directly influences the performance of the interferometer, affecting characteristics such as the acquisition speed or the spectral resolution. The ability to adjust these parameters varies depending on the technique used to generate the two frequency combs. GS OFCs offer wide flexibility for tuning comb operation frequencies, facilitating easy adaptation to the requirements of specific applications. Conversely, in other systems, parameters like the compression ratio must be established during the design and manufacturing process. The following discussion addresses these considerations, aiming to provide a guide for the correct design of a dual-comb system.

Nyquist zones

The arrival of the two OFCs at a photodetector generates an electrical signal that contains beat terms resulting from the interaction among all the comb lines from the two OFCs. In the preceding section, only beat terms that arise from the beating of neighboring comb lines were considered to derive the expressions for the photocurrent in both asymmetric (Eq. (3.11)) and symmetric (Eq. (3.17)) arrangements, and to illustrate the resulting down-converted dual-comb spectrum (Fig. 3.5). The beating of adjacent comb lines results in the generation of a dual-comb spectrum near DC. This spectrum is comprised within the so-called first Nyquist zone. Beat notes obtained from other combinations of tones result in several replicas of the down-converted spectrum centered around integer multiples of the repetition frequency. These replicas are known as higher order Nyquist zones. Nevertheless, all the information of the sample is contained in a

single Nyquist zone; thus, detecting the first Nyquist zone is sufficient to recover the response of the sample.

The generalized expression of the photocurrent in an asymmetric arrangement accounting for all the beating products occurring in the detector, i.e., the photocurrent obtained for $n \neq m$, can be expressed as

$$\begin{aligned} I_{PD}(t) = \mathcal{R}\Big(\sum_{n=0}^{N-1} A_{1n} e^{-j(2\pi\nu_{1n}t+\phi_{1n})} t_{sn} e^{-j\phi_{sn}} + \sum_{m=0}^{N-1} A_{2m} e^{-j(2\pi\nu_{2m}t+\phi_{2m})}\Big) \\ \Big(\sum_{n=0}^{N-1} A_{1n} e^{j(2\pi\nu_{1n}t+\phi_{1n})} t_{sn} e^{j\phi_{sn}} + \sum_{m=0}^{N-1} A_{2m} e^{j(2\pi\nu_{2m}t+\phi_{2m})}\Big) = \\ = \mathcal{R}\sum_{n=0}^{N-1}\Big[A_{1n}^2 t_{sn}^2 + A_{2n}^2 + 2A_{1n}A_{2n}t_{sn}\cos\Big(2\pi(\delta f_0 + n\ \delta f_R)t + \phi_{2n} - \phi_{1n} - \phi_{sn}\Big)\Big] + \\ \mathcal{R}\sum_{\substack{n=0 \\ \forall n\neq m}}^{N-1}\sum_{\substack{m=0 \\ \forall m\neq n}}^{N-1} 2A_{1n}A_{2m}t_{sn}\cos\Big(2\pi(\delta f_0 + (m-n)f_{R1} + m\ \delta f_R)t + \phi_{2m} - \phi_{1n} - \phi_{sn}\Big), \end{aligned} \tag{3.20}$$

where the first beat term corresponds to the beat notes falling within the first Nyquist zone and the second term represents beat notes located in higher frequency Nyquist zones. The frequency domain picture, obtained from the Fourier transform of Eq. (3.20), is described as

$$\begin{aligned} I_{PD}(f) \propto & I_{PD}(f)|_{n=m} + \\ & \sum_{\substack{n=0 \\ \forall n\neq m}}^{N-1}\sum_{\substack{m=0 \\ \forall m\neq n}}^{N-1}\Big\{e^{j(\phi_{2m}-\phi_{1n}-\phi_{sn})}\delta\Big(2\pi(f - \delta f_0 - (m-n)f_{R1} - m\ \delta f_R)\Big) + \\ & \qquad e^{-j(\phi_{2m}-\phi_{1n}-\phi_{sn})}\delta\Big(2\pi(f + \delta f_0 + (m-n)f_{R1} + m\ \delta f_R)\Big)\Big\}. \end{aligned} \tag{3.21}$$

The second Nyquist zone results from the beating of optical lines of the first comb with indices n and optical lines of the second comb with indices $m = n + 1$, and is centered around $\delta f_0 + f_{R1}$. A symmetrical spectrum (with respect to $\delta f_0 + f_{R1}$) is obtained when considering the beat notes arising from the interplay between lines of indices n and $m = n - 1$ from the first and second comb, respectively. Accordingly, the third Nyquist zone is centered around $\delta f_0 + 2f_{R1}$. It comprises beatings between comb tones with indices n and $m = n + 2$, and n and $m = n - 2$ for the folded spectrum. The three first Nyquist zones are depicted in Fig. 3.8. The figure also illustrates the mirrored spectra at each Nyquist zone: the spectra to the right of the corresponding center frequency appear shaded in green and yellow for the second and third Nyquist sets, respectively, while the folded spectra are contained within rectangles represented by dotted lines.

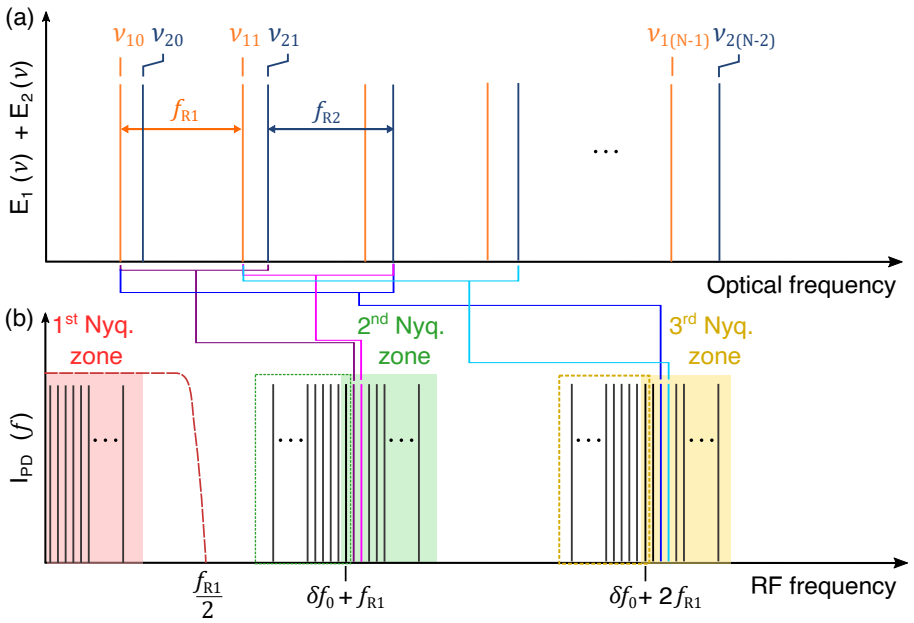

Figure 3.8: (a) Frequency domain illustration of the sum of two OFCs having repetition rates of f_{R1} (orange) and $f_{R2} = f_{R1} + \delta f_R$ (blue) and (b) resulting down-converted dual-comb RF spectrum showing the three first Nyquist zones.

In order to ensure a down-conversion process without spectral overlap or aliasing, the bandwidth of the RF comb must be contained within a spectral region limited by $f_{R1}/2$. This imposes constraints on the optical bandwidth of the OFC and the compression factor so that the following condition is satisfied

$$BW_{opt} \leq \frac{C f_{R1}}{2} = \frac{f_{R1}^2}{2\delta f_R}, \tag{3.22}$$

where BW_{opt} represents the optical bandwidth of the comb. Therefore, for a given BW_{opt}, it is necessary to increase the compression factor used as the repetition frequency decreases. That is, if the repetition frequency is decreased, the frequency offset of the two generated OFCs must be accordingly lowered.

Acquisition speed

The acquisition speed in a dual-comb experiment is defined as the minimum time needed to acquire an interferogram trace from which the information to be analyzed can be extracted. Since all the information of the measured sample is contained in a single interferogram burst, the minimum acquisition time is the inverse of the difference between the repetition frequencies of the two combs.

Although the digitization of a single interferogram enables to recover the spectral information of the sample, the acquisition of a temporal trace containing several periods of interferogram bursts enhances the SNR and allows to resolve the individual RF comb tones that arise from the Fourier transform of the interferogram trace. As the duration of

the acquired interferogram trace increases, the incremental frequency step in the Fourier domain is reduced. This incremental frequency step can be understood as the resolution bandwidth of the measurement. Considering a temporal trace with a duration of t_{acq} is acquired, the resolution bandwidth corresponds to $\Delta f_{acq} = t_{acq}^{-1}$. The acquisition time corresponding to a resolution bandwidth that results in k spectral samples between two tones of the down-converted RF comb is given by

$$t_{acq} = \frac{k}{\delta f_R}. \tag{3.23}$$

Finally, as shown in Eq. (3.22), specific conditions regarding optical bandwidth, repetition rate, and repetition rate difference must be met to prevent aliasing in the photodetection process. Therefore, ultrafast measurements on the microsecond scale, which require repetition rate differences on the order of MHz, are typically linked to comb repetition rates in the GHz range. For example, with a line spacing difference of 1 MHz and a comb repetition rate of 100 MHz, the maximum optical comb bandwidth would be restricted to 5 GHz (50 comb lines). However, increasing the repetition rate to 1 GHz allows for a maximum bandwidth of 500 GHz, corresponding to 500 comb lines evenly spaced at 1 GHz.

Spectral resolution

The spectral resolution in a dual-comb system is defined by the line spacing of the optical combs [111], since it is from these points, evenly spaced f_{R1}, where the information of the measured sample is to be extracted.

A fundamental trade-off exists between spectral resolution and acquisition speed. The spectral resolution is enhanced by reducing the repetition rate of the combs, which leads to a decrease of the repetition rate difference in order to guarantee that no overlapping occurs in the down-conversion process. As a consequence, the improvement of the spectral resolution inevitably results in an increase of the acquisition time.

Therefore, it becomes essential to choose between prioritizing resolution or acquisition speed, or finding a balance between the two, for specific applications. For applications that demand high resolution, such as spectroscopic measurements that require the characterization of absorption lines with linewidths of a few GHz or less, comb generators capable of featuring repetition rates in the MHz range are desirable. In these contexts, acquisition times typically range from milliseconds to seconds. For example, if a spectral resolution of 100 MHz is required, and a compression factor of 10^4 is considered, the resulting difference in repetition frequency is 10 kHz. Hence, the minimum acquisition time equals 0.1 ms. If a higher resolution is needed or if the compression factor must be increased, the acquisition time will also increase. Conversely, when ultra-high resolutions are not necessary but rapid variations of the sample under examination need to be captured, comb generators with frequencies in the GHz range are typically used. These systems usually have fast acquisition speeds in the microsecond range.

In addition, for the spectral resolution of a dual-comb measurement to be maintained, the linewidth of each beat note produced in the down-conversion process must be narrower than the repetition rate difference of the involved combs. In a free-running dual-comb architecture, the two combs operate independently as they are not locked to a common reference. In these arrangements, both combs experience independent fluctuations affecting the carrier-envelope offset frequency and the repetition frequency. These fluctuations depend on the characteristics of the laser sources used, such as their stability and phase noise. Therefore, if the two combs fluctuate independently, this condition is unlikely to be met, and the resulting dual-comb RF spectrum will be an incoherent spectrum with no resolved tones. Instead, when the phases of the two combs are locked together, the comb lines of the two OFCs maintain a fixed phase relationship and their beat is coherent. As a result, the obtained beat notes present linewidths below δf_R, typically in the Hz range. Additionally, these linewidths should be narrower than the inverse of the total acquisition time t_{acq}^{-1}, that is to say, the two combs should maintain their mutual coherence during the acquisition time. Although this condition is not strictly necessary, since relative frequency drifts between the two OFCs can be tracked and corrected, it is beneficial. In that case, the mutual coherence of the two combs depends on the characteristics of the common source used to phase lock the frequency combs.

3.2 Gain-switched dual frequency combs

The generation of a pair of mutually-coherent GS OFCs is analyzed in this section by means of numerical simulations based on the rate equation model described in Chapter 2.

The implementation of dual-comb interferometry using two GS combs requires a setup based on two laser diodes gain switched at two slightly different repetition frequencies, f_{R1} and f_{R2}. A third laser diode, which operates in CW and serves as master laser (ML), provides mutual coherence to the two generated combs. The typical setup used for this purpose is shown in Fig. 3.9, in which the ML injects both GS laser diodes using two optical circulators. Optical injection by a single ML is a necessary condition for the generation of mutually-coherent GS dual frequency combs, regardless of the repetition frequency used. In the previous chapter it was discussed that, under certain modulation conditions, GS combs can maintain their coherence without being externally injected and their spectra consists of resolved tones. However, if two of these individually coherent combs were employed, the resulting beat notes would exhibit fluctuations and low power.

Along with the mutual coherence requirement, the optical spectra of the two generated combs must overlap to enable injection locking with the same laser. Even though similar lasers were used, their gain spectra may be slightly different. Therefore, temperature controllers are typically employed to achieve spectral overlap. Besides stabilizing the temperature of each laser, temperature controllers also allow for the modification of the emission wavelength through the change in the refractive index of each laser induced by the temperature variation.

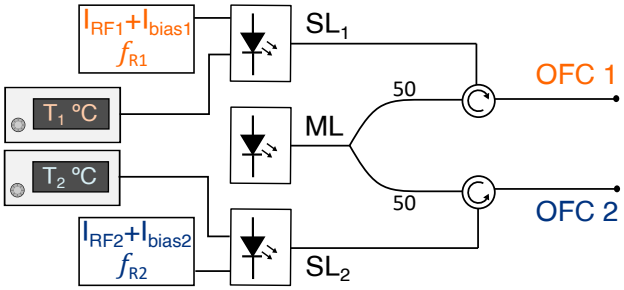

Figure 3.9: Dual-comb generator based on two GS laser diodes with optical injection from a common master laser (ML). The two GS lasers act as slave lasers (SL_1 and SL_2).

Spectral overlap in the down-conversion process

As already demonstrated when deriving the expression of the RF spectrum obtained from the multiheterodyne beating of two OFCs on a photodetector, multiple replicas of the RF comb are generated as a consequence of this process. In order to illustrate the down-converted RF spectrum resulting from the beating of two GS OFCs, simulations of this scenario have been performed. These simulations involve three lasers, and a system of equations comprising three sets of rate equations has been solved. That is, two sets of rate equations for the slave lasers to simulate the evolution of carriers, the photon density, and the phase of the optical field under optical injection, and a set of rate equations for the master laser. The parameters of the lasers are those described in Chapter 2 (Table 2.1).

In the simulation, the two GS combs are generated using trains of pulses to switch the slave lasers. The gain-switching frequencies selected for the simulations are f_{R1}= 1 GHz and f_{R2}= 1.001 GHz, configuring a moderate compression factor of 1000. Although the employed compression factor is relatively low, it is adequate to satisfy the Nyquist condition to avoid aliasing between adjacent dual-comb replicas. Moreover, a higher compression rate, in addition to prolonging simulation times, would require excessive memory resources. Injection locking is performed by a master laser driven by a CW current of 16.5 mA which, according to the power-current characteristic of this laser, corresponds to 1 mW of optical power. The ML is detuned 30 GHz with respect to the CW emission wavelength of the slaves. The electrical current that switches the lasers, shown in Fig. 3.10 (a), consists in pulses of duration τ_{pulse}=150 ps with high and low values of I_{on}= 50 mA ($\sim 4I_{th}$) and I_{off}= 5 mA, respectively. The optical pulses emitted by the two slave lasers are represented in Fig. 3.10 (b) with blue and orange line plots, reaching a maximum optical power of around 15 mW. These pulses give rise to the optical spectra presented in graphs (c) and (d), the latter being a zoom of the spectral region comprised between 2.3 GHz and 4.6 GHz.

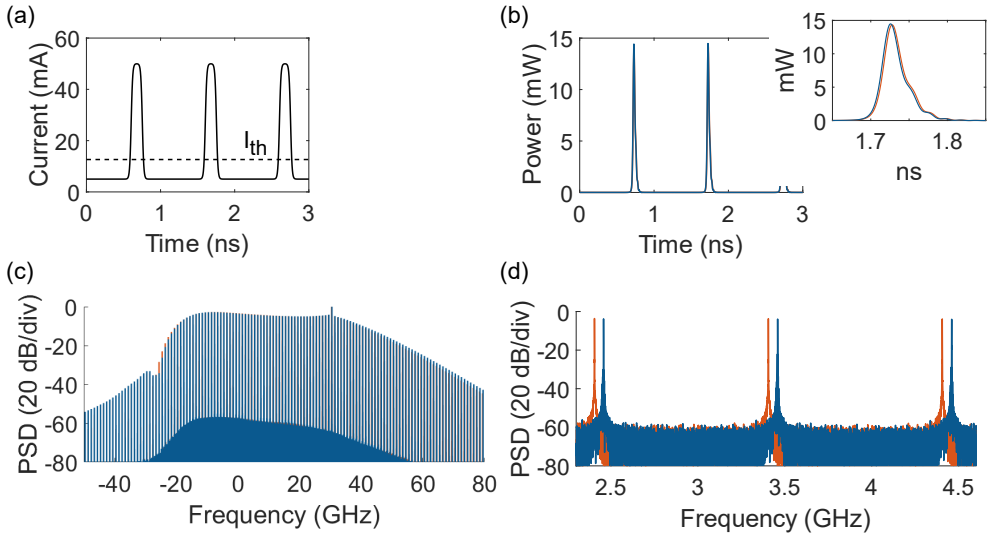

Figure 3.10: Numerical simulation of two mutually-coherent GS OFCs with repetition rates of 1 GHz and 1.001 GHz. (a) Electrical current delivered to the lasers for gain-switching operation. (b) Trains of optical pulses emitted by the two lasers. (c) Superposition of the two optical spectra from the two simulated GS combs and (d) close view where three comb lines of the two combs can be visualized.

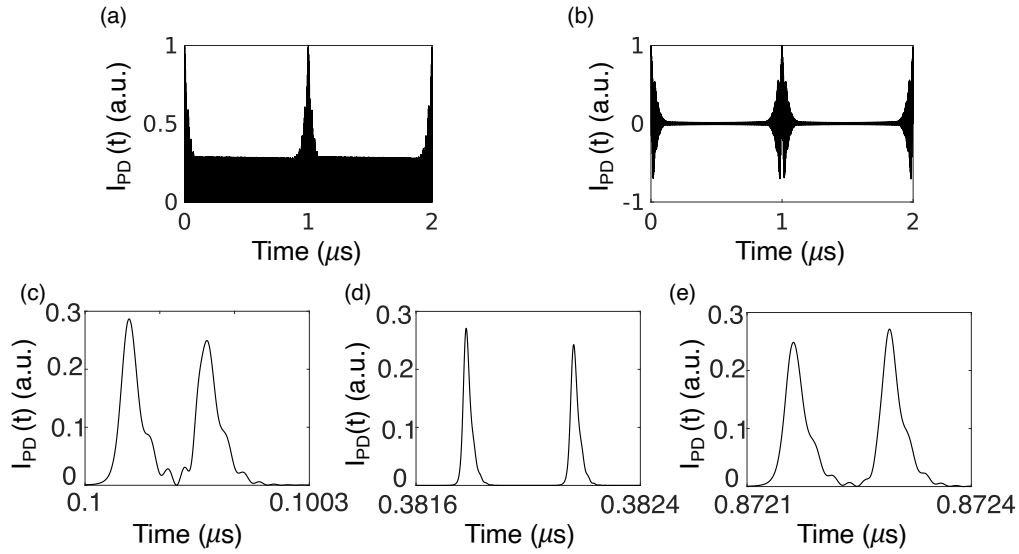

Figure 3.11: Time-domain interferograms that result from the interference of the two simulated mutually-injected GS OFCs on (a) unbalanced and (b) balanced photodetectors. Panels (c), (d), and (e) correspond to close views of the interferogram signal generated in the unbalanced photodetector. These three panels illustrate the two trains of optical pulses slipping across each other, as a result of their slightly different periodicity.

The interference between the two simulated OFCs on a photodetector is also computed. The resulting time-domain interferograms are depicted in Fig. 3.11. Panel (a) represents the interferograms generated on a single, unbalanced photodetector; while the interferogram bursts shown in panel (b) arise from the interference of the combs on a balanced photodetector. In both cases, a maximum of interference with the expected periodicity of 1 μs (δf_R^{-1}) is observed.

When unbalanced photodetection is employed, in addition to the contributions that arise when both trains of optical pulses arrive simultaneously at the photodetector, the intensities of the two pulse trains outside the interference region are also detected. Consequently, the interferogram signal reveals the slippage of one comb across the pulses of the second comb outside the interference region. This slippage is illustrated in panels (c), (d), and (e) of Fig. 3.11 for three temporal intervals comprised within an interferogram period. Conversely, with balanced photodetection, the direct detection terms do not appear in the interferogram; only the beat term remains. As a result, outside the center of the burst, the photodetected current approaches zero.

Subsequently, the down-converted frequency spectrum is obtained by performing the fast Fourier transform of the interferogram signal. The power spectral density is calculated as the squared magnitude of the photocurrent frequency spectrum. As indicated before, the two OFCs are optically injected on the blue side of their frequency spectrum, achieved by detuning the ML by 30 GHz. On the blue side of the injection peak (corresponding to optical frequencies below 30 GHz in Fig. 3.10 (c)), the obtained optical spectral width is about 50 GHz in the first 20 dB; on the red side, the 20-dB width is around 10 GHz. The RF beat note obtained from the injection tones of each OFC corresponds to a frequency of about 0 Hz. Therefore, the beat notes generated from the interference of the comb lines located at frequencies below the injection frequency would correspond to RF frequencies below 0 Hz, having a total RF bandwidth of $\sim$50 MHz below 0 Hz. Likewise, beat notes from the comb teeth located at higher frequencies than the injection frequency would correspond to RF frequencies above 0 Hz. Since negative frequencies cannot be measured, they will appear reflected on the positive side of the spectrum. As a result, the down-converted electrical spectrum that would be measured with an acquisition instrument is the one represented in Fig. 3.12 (a). The generation process of such RF spectrum is illustrated in Fig. 3.12 (b). In the first Nyquist zone, the down-converted comb that would theoretically result from the beating of the two simulated OFCs is the one comprised under the yellow envelope. The measured one lies beneath the blue envelope, and corresponds to the spectrum folded to positive frequencies. As it is shown in the figure, spectral overlap is produced as a consequence of the folding process. Within this overlap region, information cannot be unambiguously extracted; therefore, a significant portion of the spectrum is wasted.

To avoid spectral overlap several strategies can be followed. The most common approach is to include an optical element capable of introducing a frequency shift to one of the OFCs. As a result, the down-converted frequency spectrum will be shifted away from the baseband to the shifting frequency.

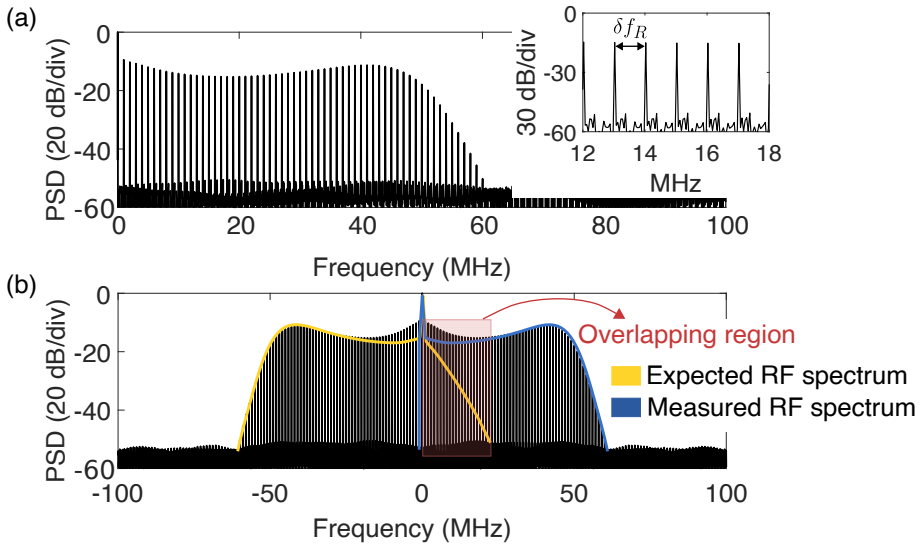

Figure 3.12: (a) Down-converted RF spectrum obtained from the interference of the two simulated GS OFCs illustrating spectral overlap of "negative" and "positive" beat notes. (b) Detail of folding process of negative beat notes to the positive side of the spectrum.

Considering the beat notes from neighboring comb lines and accounting for a frequency shift f_{shift}, the expression of the dual-comb RF spectrum derived in Eq. (3.12) can be now written as

$$I_{PD}(f)|_{n=m} \propto \sum_{n=0}^{N-1} \Big\{ A_{1n}^2 t_{sn}^2 \delta(f) + A_{2n}^2 \delta(f) + 2A_{1n}A_{2n}t_{sn} \Big[e^{j(\phi_{2n}-\phi_{1n}-\phi_{sn})} \delta\Big(2\pi(f - \delta f_0 - n\ \delta f_R - f_{shift})\Big) + e^{-j(\phi_{2n}-\phi_{1n}-\phi_{sn})} \delta\Big(2\pi(f + \delta f_0 + n\ \delta f_R + f_{shift})\Big) \Big] \Big\}. \tag{3.24}$$

This frequency shift increases the required detector bandwidth but, in return, avoids spectral overlap near 0 Hz and prevents the RF comb from being affected by low-frequency noise.

If one of the simulated OFCs is shifted by, for example, 80 MHz, the common frequency of both combs, which previously corresponded to a down-converted frequency near 0 Hz, will now shift to 80 MHz. This can be observed in Fig. 3.13 (a), showing the beat note from the injection tones of both OFCs located at 80 MHz. From the simulation results, it can be verified that as a result of shifting the down-converted signal to f_{shift}, the lowest frequency replica does not suffer from overlapping, and its entire bandwidth can be harnessed. Fig. 3.13 (b) depicts the second Nyquist zone, containing the two expected mirrored spectra. The spectrum on the right corresponds to the beating of comb lines having indices n and $m = n + 1$, with the injection beat note located at $f_{R1} + f_{shift} = 1.08$ GHz. Its corresponding image spectrum arises from the beatings of comb teeth with indices n and $m = n - 1$. In this case, the injection beat note is located at $|-f_{R1} + f_{shift}| = 0.92$ GHz.

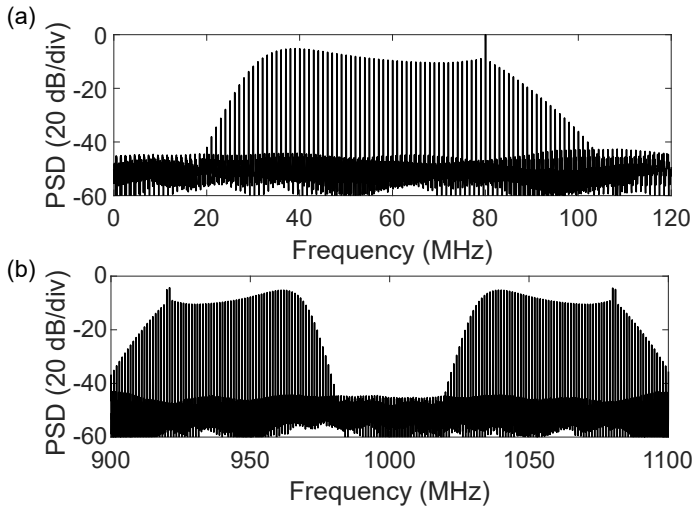

Figure 3.13: (a) Down-converted RF spectrum obtained from the interference of the two simulated GS OFCs when one of the OFCs is frequency shifted by f_{shift}= 80 MHz. Only the 1st Nyquist replica is showed. (b) Second Nyquist zone of the same simulation scenario containing the two expected mirrored replicas centered at 0.92 GHz and 1.08 GHz.

Finally, other strategies, such as the use of optical band-pass filters, can also be employed to avoid spectral overlap. This approach involves filtering out the comb lines around the common frequency of the two OFCs, which in this case corresponds to the injection peak. Fig. 3.14 (a) shows the two simulated GS combs, which have been band-pass filtered to eliminate the injection frequency and the lines around it. Since the tones near the injection frequency have been filtered out, there is no overlapping when mapping the spectrum to electrical frequencies, as shown in panel (b). This strategy can alleviate the bandwidth requirement of the detector and allows to use lower sampling rates to digitize the electrical signals. However, it reduces the optical bandwidth of the combs.

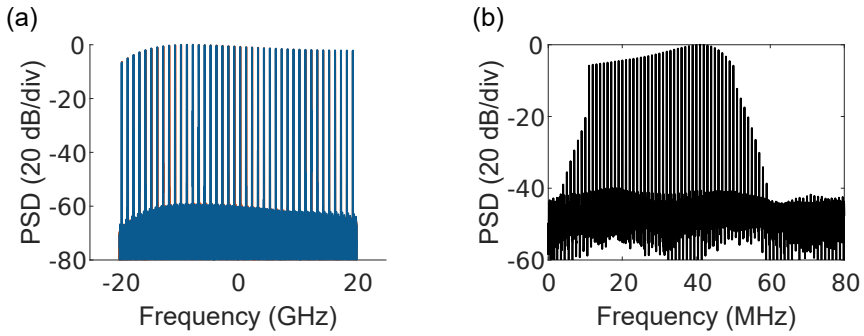

Figure 3.14: Spectral filtering process as an approach to avoid spectral overlap in the down-conversion process in dual-comb interferometry. (a) Simulated GS OFCs at 1 GHz and 1.001 GHz obtained after filtering the optical injection. (b) Obtained down-converted dual-comb spectrum from this simulation scenario demonstrating the absence of spectral overlap achieved by optical filtering.

3.3 Applications of dual-comb interferometry

Molecular spectroscopy stands as the most popular and studied application of dual-comb interferometers. This application, together with dual-comb ranging, will be discussed throughout this section, since it is in these two areas that contributions have been made in the present thesis.

3.3.1 Dual-comb spectroscopy

Dual frequency combs find their most widespread use in molecular spectroscopy. Molecular spectroscopy studies the properties of radiation emitted or absorbed by a molecule as a result of its interaction with electromagnetic radiation. Depending on the energy associated with the frequency of the incident radiation, molecules undergo different molecular transitions [112]:

- **Electronic transitions**. These transitions involve the excitation of an electron from one energy state to a higher energy state. They occur when high energy radiation, such as ultraviolet or visible radiation, interacts with a molecule.
- **Vibrational transitions**. These transitions involve the oscillations of atoms within the molecule. They occur in the infrared region, where the energy of the radiation is not sufficient to excite electrons to higher energy levels. Instead, the energy absorbed by the molecule causes its chemical bonds to vibrate.
- **Rotational transitions**. These transitions involve the rotation of the molecule around its center of mass. Pure rotational transitions typically occur in the microwave region.

The spectrum that results from the interaction between radiation and matter allows for the unique characterization of specific molecules. The infrared has traditionally been one of the most relevant and studied spectral regions, particularly the mid-infrared region (typically defined between 2.5 μm and 10 μm). This region exhibits a rich molecular fingerprint, providing valuable information about species of interest for areas such as atmospheric studies and investigations devoted to the emission of pollutants into the atmosphere.

In particular, dual-comb spectroscopy has been widely used for molecular gas spectroscopy to conduct quantitative analyses of the absorption and/or dispersion spectra of specific molecules in gaseous state in the infrared region. To perform dual-comb gas spectroscopy, either one (dispersion spectroscopy) or both (absorption spectroscopy) comb sources are transmitted through a target molecule. If the molecule resonates at one or more of the frequencies comprising the OFC, absorption will occur at those frequencies matching the vibrational frequencies of the molecule. As a result, the absorption and/or dispersion fingerprint will be imprinted in the comb spectrum. Also, for the light to traverse the sample, some of the frequencies used to probe the sample must fall within spectral regions where the sample is not strongly absorbent. Once the interference of both combs is detected, the concentration of the gas can be determined from the RF dual-comb spectrum through the analysis of the measured absorption lines. In addition

to the characterization of gases, dual-comb spectroscopy can also be used for the analysis of molecules in liquid or solid phases. For solid samples, light penetration may be more challenging than in the case of gases, depending on the sample thickness and reflectivity. In the case of liquids, molecular transitions exhibit broader profiles than those of gases, typically exceeding 100 GHz. Thus, broad OFCs covering the spectral region where the measured transition spans are required.

Vibrational transitions experienced by specific gas molecules in the infrared are usually coupled with rotational transitions. The allowed and forbidden molecular transitions of a specific molecule fundamentally depend on the structure of the molecule, and they are governed by selection rules. It is a complex subject that is beyond the scope of the thesis; nonetheless, the reader is encouraged to review the literature in case a deeper understanding of this matter is desired [112]. The purpose of dual-comb gas spectroscopy experiments developed in this thesis is to measure transitions of specific molecules, which manifest as absorption lines in the dual-comb spectrum. These absorption lines are characterized by maxima of absorbance and have specific spectral shapes and widths. The validation of the experiments is performed by comparing the measured absorbances with these data obtained from a database. One of the most commonly used databases for this purpose is HITRAN [113], which stands for high-resolution transmission molecular absorption. This database, originally developed in the 1960s, now contains absorption data of a plethora of molecules in the gas phase and it is extensively used by spectroscopists as a method of calibrating and validating their experiments.

Analysis of gas rotational-vibrational spectral lines

Spectral lines exhibit specific linewidths, which are broadened due to the motion of atoms and molecules within matter, regardless of its state –gaseous, liquid, or solid. For instance, in the case of solids, particle motion is comparatively less random and more limited than in gases, resulting in narrower spectral lines. In this section, the analysis focuses on gas spectral lines due to their relevance for the later experimental demonstrations. The discussion is based on the comprehensive treatment of this topic found in [107].

In the case of gases, the width and spectral shape of rotational-vibrational lines depend on the gas pressure. For gases at low pressures, below 1 Torr, Doppler broadening mechanism predominates. Doppler broadening is due to the random motion of particles within a gas: gas molecules within a sample have different velocities along the direction of the traversing beam, resulting in a distribution of scattered frequencies around the transition center frequency (Doppler shift). The distribution of the velocities of the molecules in the gas is described by Maxwell statistics. From the velocity distribution and considering the Doppler shift, the corresponding frequency distribution describes the spectral line.

This spectral distribution is given by

$$S_G(\nu) = \frac{c}{\nu_0}\sqrt{\frac{m}{2\pi kT}}e^{-\frac{mc^2(\nu-\nu_0)^2}{2kT\nu_0^2}}, \tag{3.25}$$

where ν_0 is the center frequency in Hz, m is the molecular mass in grams, k is the Boltzmann constant, T is the temperature in Kelvin, and c is the speed of light in vacuum in m/s. This spectral distribution expression is a Gaussian function whose standard deviation is described by

$$\sigma_G = \frac{\nu_0}{c}\sqrt{\frac{kT}{m}}. \tag{3.26}$$

The FWHM of the spectral line, $\Delta\nu_G$, is related to the standard deviation such as $\Delta\nu_G = 2\sqrt{2\ln(2)}\sigma_G$. Therefore, Eq. (3.25) can be written is terms of $\Delta\nu_G$ as

$$S_G(\nu) = \frac{2}{\Delta\nu_G}\sqrt{\frac{\ln(2)}{\pi}}e^{-\frac{4\ln(2)(\nu-\nu_0)^2}{\Delta\nu_G^2}}. \tag{3.27}$$

As the pressure increases, more collisions between molecules within the gas are produced. The exchange of energy during collisions causes a spread in the energies associated with the transitions, leading to the broadening of the spectral lines. For pressures above 1 Torr, broadening of absorption lines due to intermolecular collisions starts to become significant. The line shape of collision-broadened lines follows a Lorentzian distribution, and can be written as

$$S_L(\nu) = \frac{\gamma_L}{\pi[\gamma_L^2 + (\nu-\nu_0)^2]}, \tag{3.28}$$

where $\gamma_L = \Delta\nu_L/2$ is the half width at half maximum, $\Delta\nu_L$ being the FWHM of the Lorentzian distribution. In this case, the FWHM is proportional to the gas pressure. Additionally, gas pressure also induces a frequency shift, displacing the line center frequency to a new position at $\nu_0 + \delta P$.

Finally, for pressures ranging from 1 Torr to 100 Torr, the absorption lines exhibit both Doppler and collisional broadening contributions. These lines are fitted using a Voigt profile, defined as the convolution of Gaussian and Lorentzian distributions

$$S_V(\nu) = S_G(\nu) * S_L(\nu), \tag{3.29}$$

* being the convolution operator. Fig. 3.15 illustrates the spectral lineshapes associated with Doppler and collisional broadening, along with the Voigt profile combining both effects. These spectral distributions are calculated from Eq. (3.27), Eq. (3.28), and Eq. (3.29) for $\Delta\nu_G = \Delta\nu_L = 2$ GHz. They are normalized to their maximum values.

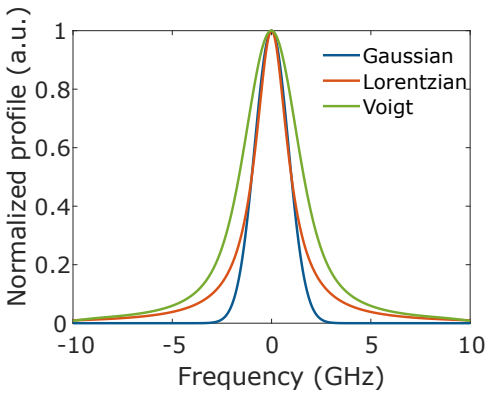

Figure 3.15: Spectral distribution of Gaussian (blue), Lorentzian (orange), and Voigt (green) lineshapes.

Regarding the concentration of absorbing species in a sample, it can be obtained from the Beer-Lambert law, which permits to determine the transmittance of a sample having a specific absorption coefficient and length. The transmittance at frequency ν, $T(\nu)$, can be written as

$$T(\nu) = \frac{I_t(\nu)}{I_i(\nu)} = e^{-\alpha(\nu)l}, \tag{3.30}$$

where $I_t(\nu)$ represents the intensity of the field transmitted through the sample, $I_i(\nu)$ is the intensity of the incident field, $\alpha(\nu)$ is the absorption coefficient at ν frequency, and l is the optical path length traversed by the field when interrogating the sample. The absorbance is calculated as the base 10 logarithm of $1/T(\nu)$ as

$$A(\nu) = -\log\Big(T(\nu)\Big) = \log(e)\alpha(\nu)l = \varepsilon(\nu)\ a\ l, \tag{3.31}$$

where $\varepsilon(\nu)$ is the absorptivity at ν frequency, and a is the concentration. The absorptivity, $\varepsilon(\nu)$, has units of concentration per length, and is typically expressed in $\mathrm{cm}^2/\mathrm{mol}$. The concentration, a, is usually expressed in $\mathrm{mol}/\mathrm{cm}^3$, and the optical path length in cm. It can be observed that the absorbance $A(\nu)$ has a linear relationship with the concentration.

Finally, if the substance is composed by various absorbing species, the total absorbance is calculated as the sum of individual absorbances of each species as

$$A(\nu) = \sum_{n=1}^{N} \varepsilon_n(\nu)\ a_n\ l, \tag{3.32}$$

where N is an integer accounting for the total number of absorbing components in the substance.

The absorptivities of different transition lines of the carbon dioxide molecule for the isotopologue exhibiting higher abundance ($^{12}C^{16}O_2$, abundance of 0.984) are shown in Fig. 3.16 across different spectral regions within the near and mid-infrared. These data have been extracted from HITRAN database [114].

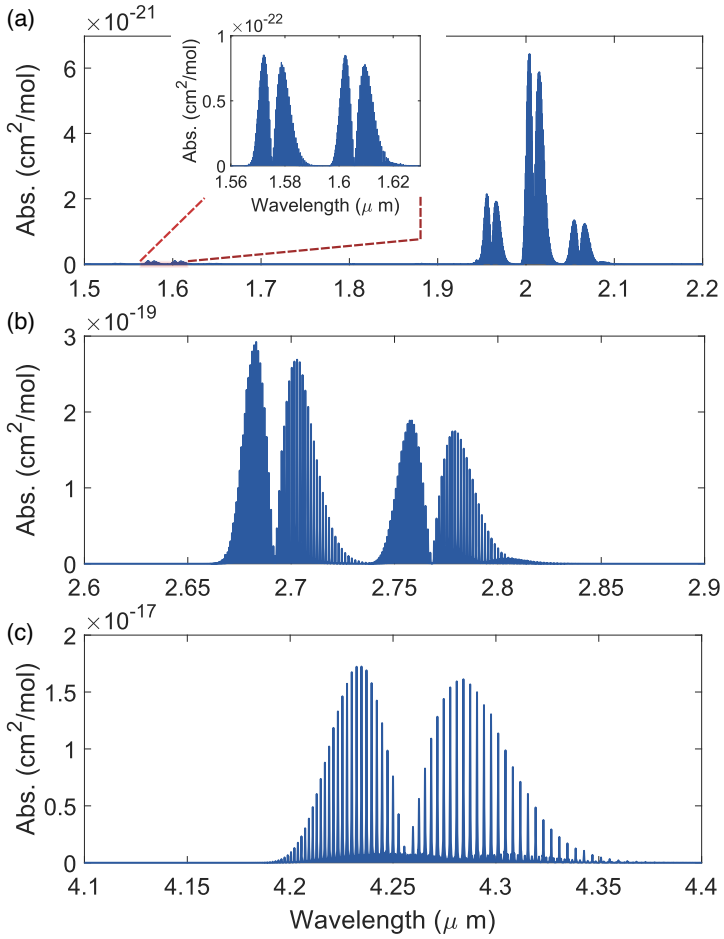

Figure 3.16: Absorptivity of CO_2 molecule ($^{12}C^{16}O_2$) in the near and mid-infrared regions. Information extracted from HITRAN database [114].

As it can be seen in Fig. 3.16, the strongest absorption occurs in the mid-infrared, and the highest absorptivity, $1.7267 \cdot 10^{-17}$ cm^2/mol, is obtained for the line centered in 4234.66 nm. Conversely, molecular absorption is weaker in the near-infrared.

Historical review of dual-comb spectroscopy

Early demonstrations on dual frequency comb generation yielded RF spectra with no discernible tones, as the two laser sources did not share a common phase reference. It was in 2008, when I. Coddington and coworkers at the National Institute for Standards and Technology (NIST) first reported the generation of a dual-comb spectrum with resolved spectral tones, obtained from two mutually-coherent OFCs [2]. The combs were generated from two stabilized mode-locked fiber lasers. After being broadened in a nonlinear fiber, the two OFCs featured a full bandwidth of 15.5 THz in the optical domain. With a spectral sampling of 100 MHz, the authors resolved the complex spectrum of the rotational-vibrational band of the hydrogen cyanide (HCN) molecule ($^{13}H^{14}CN$) comprised between 192-197 THz.

From that moment, numerous demonstrations contributing to the development, understanding, and establishment of the technique have been published. Part of the scientific community has focused its efforts on improving the technique, for instance, by increasing the coherence time of the two combs. Motivated to avoid complex and sophisticated stabilization mechanisms, some groups have proposed methods to correct frequency drifts experienced by the OFCs using real-time correction techniques [115], [116] as well as algorithms to compensate for these drifts in post-processing [117]. On the other hand, another significant part of the research has been focused on the implementation of dual-comb spectrometers across different spectral regions.

Herein, demonstrations of dual-comb spectroscopy based on gain-switched OFCs are first reviewed. Then, dual-comb spectroscopy based on other comb generators is briefly discussed.

- **Dual-comb spectroscopy based on gain-switched combs**

The first demonstration of dual-comb gas absorption spectroscopy with two GS OFCs was reported in 2016 by B. Jerez et al. [3]. The authors generated two mutually-coherent GS OFCs using a master-slave arrangement consisting of three discrete-mode lasers: one as the master laser operating in CW mode, and the other two as slave lasers under gain-switching operation. Their spectrometer featured a spectral resolution (comb spacing) of 1 GHz and a line spacing difference of 100 kHz, configuring a compression factor of 10^4. They implemented a symmetric configuration to perform gas absorption spectroscopy, and the optical combs used to interrogate the gaseous sample exhibited an optical bandwidth at 20 dB of 70 GHz. The performance of the dual-comb system was validated by measuring an absorption line of the HCN molecule. The gas was enclosed in a fiber-coupled cell with a pressure of 100 Torr and an optical path length of 5.5 cm. This pressure resulted in a FWHM of the absorption lines of approximately 8 GHz, allowing 8 spectral lines, evenly spaced at 1 GHz, to fit within the absorption line. The profile of the transition line centered at 1538.523 nm was successfully retrieved for various acquisition times, with the minimum time corresponding to the duration of a single interferogram, i.e., 10 μs. The reported dual-comb RF spectrum with a down-converted line spacing of 100 kHz and the measured absorption line for the minimum integration time are shown in Fig. 3.17 (a) and (b), respectively. In a subsequent demonstration

later that year, the same group presented a similar GS dual-comb system but using a dispersive arrangement [4]. In that work, they not only measured the absorption profile of a single HCN line but also retrieved its dispersion profile from the phase of the spectral lines of the down-converted dual-comb spectrum. Moreover, they improved the resolution of the system by a factor of two. The new resolution of 500 MHz was the best spectral resolution obtained for these systems up to the realization of the present thesis.

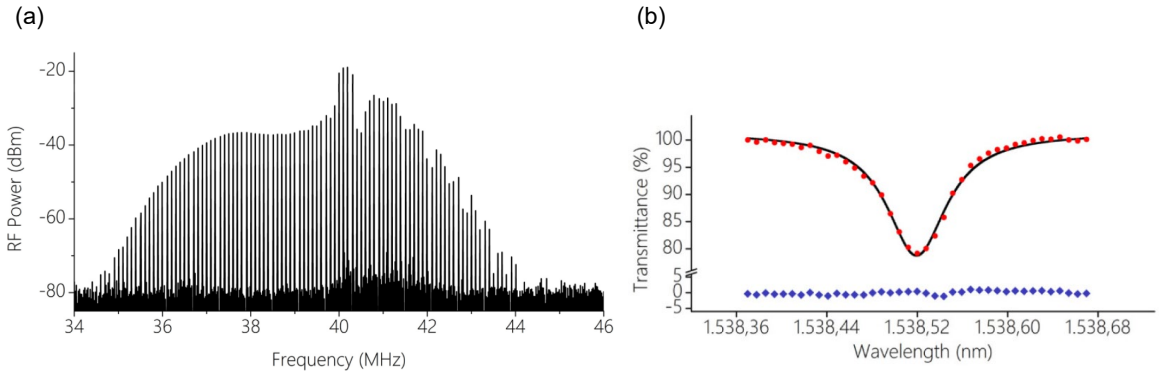

Figure 3.17: Results of the first demonstration of dual-comb spectroscopy with GS laser diodes. Figures retrieved from [3]. (a) Down-converted 1-GHz GS dual-comb spectrum used to conduct dual-comb absorption spectroscopy. (b) Measured absorption line of a hydrogen cyanide cell (gas pressure of 100 Torr and line FWHM of 8 GHz) at 1538.523 nm.

Since 2020, in addition to the contributions realized in this thesis, which will be presented in the following chapters dedicated to experimental results, two other research groups have also made significant advancements in gas spectroscopy using GS dual frequency combs. These are the group from Dublin City University led by P. Anandarajah, and a group comprising researchers from University College Cork and Tyndall National Institute in Cork. In 2020, the group from Dublin presented a contribution at the CLEO conference demonstrating the simultaneous measurement of various absorption features of hydrogen sulfide (H_2S) at different pressures, using a pair of mutually-coherent GS combs with frequencies of 1.25 GHz and 1.250125 GHz (δf_R= 125 kHz) [118]. An optical bandwidth at 10 dB of around 60 GHz was employed to measure the gas absorption. In a more recent study reported in 2023, the authors investigated the power and frequency stability of two optically-injected GS combs and also the frequency stability of their beating [119]. Regarding the optical combs, four comb teeth were analyzed. A maximum wavelength fluctuation of 2 pm (250 MHz at 1550 nm) was observed. The maximum power fluctuation was around 0.3 dB, obtained for the comb line located further away from the optical injection wavelength. Regarding the frequency stability of the down-converted beat notes of the dual-comb spectrum, a maximum frequency fluctuation below 1 kHz was obtained for a measurement time of one hour. That value, which sets the limit of accuracy and mutual coherence of the spectrometer, demonstrated the good stability of the system, achieved without the need for repetition rate control mechanisms.

The aforementioned studies were conducted at a central wavelength around 1.55 μm, motivated by the widespread availability of devices such as laser diodes and optical amplifiers working at the traditional telecommunication wavelength. However, it is worth noting that the gain-switching technique and dual-comb systems are adaptable to other wavelengths. Moreover, for spectroscopic applications, wavelengths beyond 1.55 μm are often of greater interest due to their molecular fingerprint exhibiting higher absorption intensities. Therefore, after having proved the technique at 1.55 μm, it is interesting to explore its demonstration in other spectral regions. For instance, the region comprised between 2 μm and 2.5 μm presents higher absorption intensities compared those in 1.55 μm for greenhouse gases such as CO_2 (Fig. 3.16), methane (CH_4), or ammonia (NH_3) (see Fig. 3.18). Around these wavelengths, companies such as Eblana Photonics offer discrete-mode lasers based on indium phosphide and gallium antimonide for high-speed modulation. The use of these sources can be beneficial for gas sensing applications in agricultural or industrial contexts.

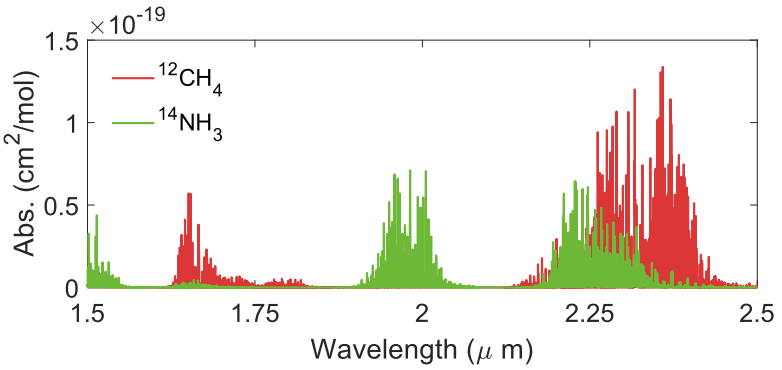

Figure 3.18: Absorptivity of methane ($^{12}CH_4$) and ammonia ($^{14}NH_3$) in a spectral region comprised between 1.5 μm and 2.5 μm. Information obtained from HITRAN database.

In this regard, the group from Cork focused its research on the development of a dual-comb system utilizing GS laser diodes operating around 2 μm. In 2022, they reported a dual-comb arrangement at this wavelength showing a high degree of mutual coherence, as evidenced by the FWHM of the beat notes (11 Hz) [17]. With such system, they conducted a proof-of-concept demonstration of CO_2 gas spectroscopy measurements [120]. They reported on the tunability of the spectral resolution of the spectrometer along a range comprised between 500 MHz and 3 GHz, achieved by changing the frequency of the sinusoidal gain-switching signals driving the slave lasers, and compared the molecular spectra obtained at different line spacings. For frequencies below the relaxation oscillations, the dual frequency combs exhibited narrow spectral widths, suppression of tones, and asymmetric envelopes, due the use of sinusoidal modulation signals for gain switching the slave lasers. Consequently, the dual OFCs generated at 2 GHz and 3 GHz were deemed the most suitable for conducting experiments, at the expense of lower resolution.

Moreover, our research group recently reported a dual-comb system based on two optically-injected GS DFB lasers to conduct gas absorption spectroscopy of CO_2 around 1572 nm [121]. The gas was enclosed in a fiber-coupled cell, and the measured absorption

line exhibited a FWHM of 5 GHz and an absorbance of 0.55 dB. The absorption line and a portion of its baseline were successfully measured with approximately 125 comb lines, which featured a repetition rate of 100 MHz. Furthermore, the approach was based on cost-effective electronics in both the transmission and receiver ends of the spectrometer.

With respect to integrated GS dual frequency combs, the first demonstration was reported in 2020 by J.K. Alexander et al. [122]. The chip was fabricated on an InP substrate. It consisted of two Fabry-Pérot slave lasers and a slotted Fabry-Pérot master laser, in which the slotted section was included to achieve single-mode operation. The optical injection from the ML to the SLs was realized by means of a multi-mode interference coupler, which showed a good degree of isolation in terms of back-coupled reflections from the slave lasers into the master. This back-coupling minimization was achieved by driving the ML well above threshold. Fig. 3.19 (a) shows the schematic of the dual-comb generator. Regarding the slave lasers, their multi-mode operation facilitated the spectral overlap of the two combs and also their injection. Finally, for the generation of the dual comb, the authors chose significantly dissimilar repetition frequencies (4.1 GHz and 5 GHz) in order to be able to measure the repetition rate difference in the optical domain with an optical spectrum analyzer (see panel (b)).

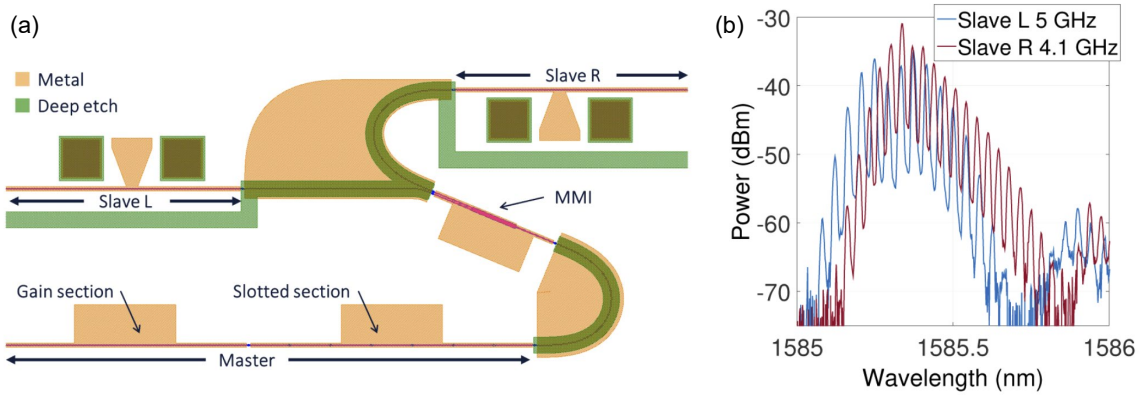

Figure 3.19: First reported fully-integrated dual-comb generator based on two GS laser diodes and an integrated master laser. Figures retrieved from [122]. (a) Scheme of the dual-comb generator consisting of two Fabry-Pérot lasers acting as slave lasers, which are optically injected by a single-mode slotted Fabry-Pérot laser by means of a multi-mode interference coupler. The device is integrated on an InP substrate. (b) Optical spectrum of the two generated GS OFCs.

To date, this has been the only demonstration of a GS dual-comb integrated system in which the optical injection of the slave lasers is achieved with a master laser on chip. A good proof-of-concept was reported in 2023 by M. Srivastava et al. [59], as discussed in previous chapter, where injection locking was performed with an external laser due to wavelength mismatch of the integrated ML and the slave laser diodes. However, the acquisition of the RF down-converted comb, its characterization, and the realization of sensing measurements with an integrated GS dual-comb system remains unreported. The current availability of InP foundries makes this goal much more feasible, and one can anticipate these achievements to be demonstrated in the very near future. These integrated systems will offer the possibility of having monolithic robust sensors featuring resolution tunability.

- **Dual-comb spectroscopy based on other comb sources**

Research on dual-comb spectroscopy was pioneered by erbium-doped fiber lasers. Due to the size of their cavities, their repetition frequencies are typically in the order of hundreds of megahertz. With optical spectra usually broadened by nonlinear techniques, these dual-comb schemes have historically allowed the simultaneous characterization of multiple absorption lines of certain gases with very good resolution and, sometimes, with unprecedented accuracy due to comb self-referencing [123]. In addition to exploring the near-infrared, spectroscopic measurements have been conducted in deeper infrared regions using nonlinear conversion techniques such as difference frequency generation [124]. These table-top systems offer good performance at the expense of their size and increased complexity due to the need for stabilization loops.

Exploring more compact and simpler solutions is thus of interest. Proposals based on the generation of both combs from a single laser simplify the system on one hand, and since both pulse trains originate from the same cavity, stabilization controls can be omitted as both combs possess good mutual coherence inherent to their generation method. In this regard, S. M. Link et al. [125] demonstrated a single-cavity semiconductor-based dual-comb system, utilizing an external-cavity mode-locked semiconductor laser as the comb source. The authors successfully retrieved the absorption profile of a water vapor line at $\sim$1 μm. In addition, on-chip dual-comb spectrometers based on microcombs have also been reported. These combs have repetition frequencies too large for gas spectroscopy, as their repetition frequencies ranging from tens of GHz do not allow resolving gas absorption lines, which typically have widths of several GHz. However, they can be good candidates for molecular spectroscopy of substances in liquid or solid state, whose absorption lines typically span a few THz [126].

Moreover, dual-comb architectures involving OFC sources featuring repetition rate tunability have demonstrated their excellent suitability for gas absorption-phase spectroscopy, as the resolution of the measurement can be easily adapted to the measured feature. In addition to gain-switched systems, electro-optic dual-comb generators are included within this category of frequency-agile dual-comb spectrometers.

Dual frequency combs based on electro-optic generation offer indeed a performance comparable to that obtained with GS dual frequency combs. Similarly to GS dual-comb spectrometers, these systems enable spectroscopic measurements with moderate bandwidths yet offering exceptional spectral resolution. Despite their limited spectral coverage, they can be tuned to the desired wavelength provided a laser source emitting in that spectral range is available. Furthermore, since only one laser is used for generating the two frequency combs, electro-optic dual-comb generators have a high degree of mutual coherence, benefiting from a simple implementation to achieve it. In Fig. 3.20, an example of an electro-optic dual-comb source is shown, where each comb is generated with a tandem formed by a phase modulator and an intensity modulator.

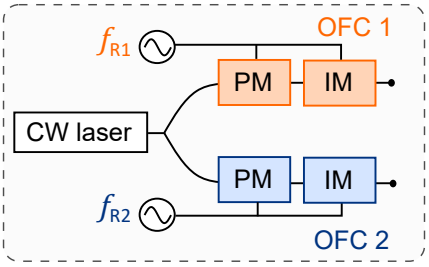

Figure 3.20: Illustration of a dual-comb generator based on two mutually-coherent electro-optic combs. Each electro-optic OFC is generated using a phase modulator (PM) followed by an intensity modulator (IM).

Electro-optic dual-comb spectrometers have showcased their validity both in the near-infrared, through the characterization of the absorption and phase profile of gases such as HCN [127], [128] and CO_2 [129], and in the mid-infrared, reached by means of difference frequency generation [130]. Additionally, in search of simpler systems, M. Soriano-Amat et al. proposed an electro-optic dual-comb spectrometer consisting of a single branch [131]. They demonstrated the generation of a dual frequency comb with a single Mach-Zehnder modulator, driven by a tailored electrical signal that basically consisted in the superposition of two pulse trains operating at slightly different repetition rates. This straightforward dual-comb generation method benefited from the linear response of the Mach–Zehnder modulator. Moreover, besides its simplicity and robustness, the authors reported a coherence time of around 1 s. In addition, since it is a common-path architecture, only the amplitude information of the sample under interrogation could be retrieved.

3.3.2 Dual-comb ranging

Dual-comb schemes are also very attractive for ranging applications, as they allow to retrieve distances by means of time-of-flight and interferometric approaches combining high precision, high accuracy, and fast measurement times [132]. Furthermore, the miniaturization of comb generators and the integration of dual-comb sources paves the way for the development of on-chip dual-comb ranging systems [133], [134] that could be deployed in real-world applications, such as drone navigators or autonomous driving systems.

The fundamentals of interferometric and time-of-flight distance measurements utilizing a dual-comb system are discussed below. Since the fundamental basis of dual-comb ranging relies on the change in the optical phase experienced by the optical signal when it travels through different optical path lengths, an asymmetric dual-comb arrangement is required. The provided description focuses on relative distance measurements rather than absolute measurements, as this is the approach employed in the experiments conducted in this thesis.

Interferometric dual-comb ranging

The interferometric approach relies on measuring the optical phase change experienced by each comb mode when traveling across a given distance. This approach enhances the precision of the measurement, since a high number of comb lines is used to determine the distance.

The measurement of relative distances is based on determining the difference between two distances, $d = |d_1 - d_2|$. A dual-comb ranging setup to conduct relative distance measurements is illustrated in Fig. 3.21 (a). First, the optical pulses from the probe comb (denoted as OFC 1 in the figure) interrogate a specific distance d_1 to a target. The optical path length traversed by the probe OFC is given by $L_{probe} = L_1 + 2d_1$, where L_1 represents the optical distance of the upper branch of the interferometer excluding the distance d_1 to the target, and the factor 2 accounts for a round-trip to the target. These pulses are then combined with the local oscillator comb. The optical distance traversed by the local oscillator comb (OFC 2) corresponds to $L_{LO} = L_2$, with L_2 being the optical length of the bottom branch of the setup. The combined fields interfere on a photodetector, generating a sequence of interferogram bursts. Subsequently, a second acquisition is performed, where the target is moved to a different position d_2. Consequently, the optical length of the probe now amounts to $L_{probe} = L_1 + 2d_2$, while the local oscillator branch remains unchanged.

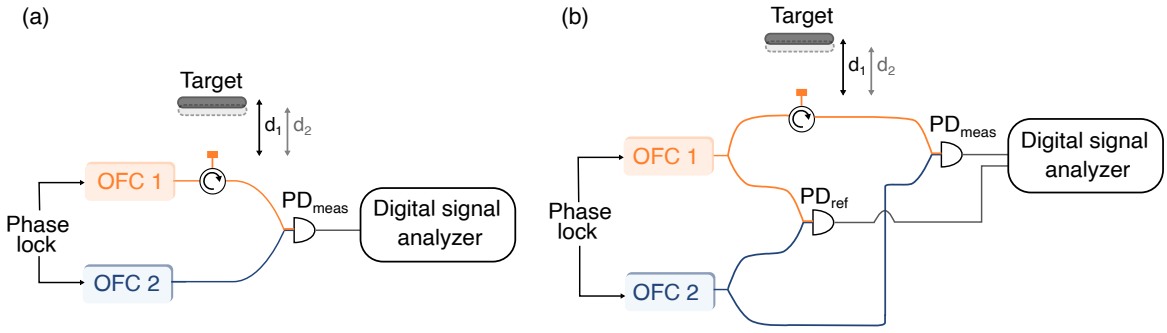

Figure 3.21: Illustration of a dual-comb ranging setup for the determination of relative distances. The measured distance corresponds to a difference of distances, $d = d_1 - d_2$. (a) Dual-comb ranging arrangement based on a single photodetector. (b) Dual-comb ranging system based on two photodetectors, one of them being used for calibration.

Measuring relative distances allows to eliminate the contributions of the optical lengths L_1 and L_2 of the two branches of the interferometer. However, it requires the acquisition of two sequential measurements, changing the distance to the target. Consequently, any drift of the system or instabilities of the optical signals between these sequential acquisitions may prevent the correct determination of the distance. This problem can be addressed by incorporating an additional photodetector into the system, as depicted in Fig. 3.21 (b). In a reference photodetector (denoted as $\mathrm{PD_{ref}}$ in the figure), a reference interferogram, which does not contain any information of the distance to the target, is generated. The reference interferograms can be used to compensate for the

instabilities between consecutive acquisitions, since they are simultaneously acquired with the measurement traces.

In order to analyze how the distance can be determined from the spectral phase of the tones of the dual-comb spectrum, an ideal scenario with a setup involving the use of a single, balanced photodetector is considered. In addition, only the first Nyquist zone is accounted for in the analysis. As derived in detail at the beginning of this chapter (see Eq. (3.15)), the photodetected current generated at the output of the balanced photodetector as a result of the beating of the probe and local oscillator combs is given by

$$I_{BPD}(t)|_{n=m} = \mathcal{R} \sum_{n=0}^{N-1} 4A_{1n}A_{2n} \cos\Big(2\pi(\delta f_0 + n\ \delta f_R)t + \phi_{2n} - \phi_{1n}\Big). \tag{3.33}$$

The information of the relative distance $d = d_1 - d_2$ can be determined from the phase of the beat term. The optical phase is expressed in terms of the propagation constant β, which is frequency dependent, and the optical path length L ($\phi = \beta L$). Moreover, in the analysis, dispersion is neglected. As a result, the optical phase of the beat term obtained for the two distances, $\phi_m(d_1)$ and $\phi_m(d_2)$, with the index m denoting the comb line index to avoid confusion with the refractive index of the medium, can be expressed as

$$\begin{aligned} \phi_m(d_1) = (\phi_{2m} - \phi_{1m})|_{d_1} &= \frac{2\pi n\nu_{2m}}{c}L_2 - \frac{2\pi n\nu_{1m}}{c}(L_1 + 2d_1) = \\ &= \frac{2\pi n(\nu_{01} + mf_R)}{c}(L_2 - L_1 - 2d_1) + \frac{2\pi n(\delta f_0 + m\delta f_R)}{c}L_2, \end{aligned} \tag{3.34}$$

$$\begin{aligned} \phi_m(d_2) = (\phi_{2m} - \phi_{1m})|_{d_2} &= \frac{2\pi n\nu_{2m}}{c}L_2 - \frac{2\pi n\nu_{1m}}{c}(L_1 + 2d_2) = \\ &= \frac{2\pi n(\nu_{01} + mf_R)}{c}(L_2 - L_1 - 2d_2) + \frac{2\pi n(\delta f_0 + m\delta f_R)}{c}L_2, \end{aligned} \tag{3.35}$$

where n is the group index of the propagation medium and c is the speed of light in vacuum.

The relative distance can be retrieved from the subtraction of the phases obtained for the two distances

$$\delta\phi_m(d) = \phi_m(d_1) - \phi_m(d_2) = \frac{2\pi n\nu_{1m}}{c}2(d_1 - d_2) = \frac{4\pi n(\nu_{01} + mf_{R1})}{c}(d_1 - d_2). \tag{3.36}$$

From Eq. (3.36) it is observed that the optical phase difference has a linear dependence with the comb line index m. The relative distance can be obtained from the slope of the straight line representing the evolution of the unwrapped phase difference with respect to m as

$$d_{interf} = \frac{b\ c}{4\pi n f_{R1}}, \tag{3.37}$$

where b denotes the slope in rad/Hz.

Finally, the maximum distance that can be measured without ambiguity –i.e. the non-ambiguity range –using an interferometric approach, can be understood from the limitation imposed by the 2π periodicity of the phase. The phase change of consecutive spectral tones must be lower than 2π to avoid ambiguity in the determination of the spectral distance

$$\phi_{1m+1} - \phi_{1m} = \frac{2\pi n f_{R1}}{c} 2d_1 < 2\pi \Rightarrow d_1 = d_{NAR} < \frac{c}{2n f_{R1}}. \tag{3.38}$$

Eq. (3.38) demonstrates that the maximum measurable distance is inversely proportional to the comb repetition rate. Therefore, to measure longer distances without ambiguity, reducing the comb line spacing is desirable.

Precision analysis of an interferometric dual-comb ranging measurement

The measured distance d is determined from the slope of the phase difference $\delta\phi_m$, which, disregarding dispersion, evolves with the comb line index as a straight line. The standard approach involves fitting $\delta\phi_m$ by a linear regression. The distance is then obtained from the slope of the fitted line. The precision of the measurement is given by the error in the distance.

The uncertainty of the interferometric distance is calculated as

$$\sigma_d = \frac{1}{4\pi}\Big(\frac{\partial d}{\partial v_g}\sigma_{v_g} + \frac{\partial d}{\partial f_{R1}}\sigma_{f_{R1}} + \frac{\partial d}{\partial b}\sigma_b\Big), \tag{3.39}$$

where v_g denotes the group velocity ($v_g = c/n$), and σ_{v_g}, $\sigma_{f_{R1}}$ and σ_b are the uncertainty of the group velocity, the repetition rate, and the slope, respectively. In the precision analysis conducted in the experimental results of this thesis, the two first terms are neglected, since the uncertainty of the group velocity and the repetition rate are much lower than the uncertainty of the slope. For GS combs, the uncertainty of f_{R1} is fixed by the precision of the RF source used to generate the gain-switching signal.

The error in the slope of the linear regression is given by

$$\sigma_b = \sqrt{\frac{\sum_{m=1}^{N}(y_m - \hat{y}_m)^2}{(N-2)\sum_{m=1}^{N}(m-\bar{m})^2}} = \frac{\sigma_{\delta\phi}}{\sqrt{\sum_{m=1}^{N}(m-\bar{m})^2}}, \tag{3.40}$$

where y_m represents the linear function formed by the evolution of the experimental phase differences at each comb line (unwrapped $\delta\phi_m$), $\hat{y}_m$ is the fitted linear function, m and $\bar{m}$ are the data points on the abscissa of the function (the harmonics of the comb spectrum) and their average value, respectively, and N is the total number of comb lines analyzed. Eq. (3.40) represents the uncertainty of the phase difference, $\sigma_{\delta\phi}$, divided by the standard deviation of the abscissa values.

Finally, the error in the distance σ_d is written as

$$\sigma_d = \sigma_b \frac{c}{4\pi n f_{R1}}. \tag{3.41}$$

Considering the number of comb lines $N \gg 1$, σ_b can be approximated [133] by

$$\sigma_b(N \gg 1) \approx \frac{\sigma_{\delta\phi}}{\sqrt{\frac{N^3}{12}}}. \tag{3.42}$$

Consequently, introducing this approximation in Eq. (3.41) results in

$$\sigma_d \approx \sigma_{\delta\phi}\sqrt{\frac{12}{N}}\frac{c}{4\pi n N f_{R1}}, \tag{3.43}$$

which indicates that the precision of the measurement improves as the factor defined by Nf_R, i.e. the bandwidth of the OFC, increases. Therefore, comb generators exhibiting wide bandwidths typically show better performance in terms of precision.

Time-of-flight dual-comb ranging

OFC generators benefiting from a pulsed nature can be used to determine distances based on time-of-flight measurements. The fundamental principle of this approach is the measurement of the delay experienced by the optical pulses when they travel through a specific distance.

In a dual-comb ranging setup, the delay experienced by the optical pulses of the probe comb when they travel across a given distance results in a corresponding delay in the interferogram. For relative distance measurements and considering a setup with a single photodetector, the determination of the delay associated with the difference of distances requires the proper synchronization of the acquisitions. Conversely, if a setup including two photodetectors for the simultaneous acquisition of reference and measurement traces is employed, the reference interferograms serve the function of synchronization signals.

This is illustrated in Fig. 3.22, which depicts the time-domain interferogram signals that would be generated at the output of each photodetector, reference and measurement, for two different distances to the target d_1 and d_2. The two sequences of interferograms on the left correspond to the target located at a distance d_1, while the sequences on the right correspond to a subsequent acquisition in which the target is moved to d_2. Since the optical lengths traveled by the signals of the reference path and the measurement paths are different, there exists a time delay between the interferograms detected by the reference photodetector and the measurement photodetector. For the distance d_1, the measurement interferograms are delayed a time Δt_1. Similarly, the delay related to the distance d_2 is Δt_2.

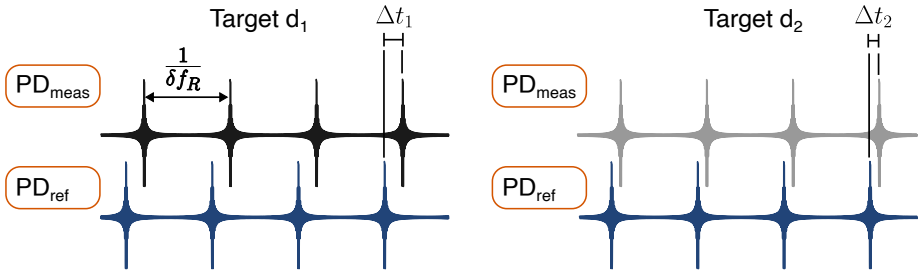

Figure 3.22: Illustration of dual-comb interferograms generated from two sequential acquisitions corresponding to two distances d_1 and d_2. Each acquisition involves capturing the interferograms at the output of the reference and measurement photodetectors.

The relative distance can be inferred from the time delay difference given by the subtraction of Δt_1 and Δt_2, $\Delta t = |\Delta t_1 - \Delta t_2|$. Both delays, Δt_1 and Δt_2, correspond to the time delay in the expanded time axis. The measured expanded delay, Δt, is related to the delay experienced by the optical pulses, $\Delta \tau$, by the dual-comb compression factor as $\Delta \tau = \Delta t / C$, where C denotes the compression factor. The expansion of the time axis enabled by the dual-comb technique permits the determination of short time delays with low-frequency electronics.

Finally, the time-of-flight distance d_{TOF} is given by

$$d_{TOF} = \frac{c}{2n}\frac{\Delta t}{C} = \frac{c}{2n}\frac{\delta f_R}{f_{R1}}\Delta t, \tag{3.44}$$

where it is considered that the optical signal travels twice (back and forth) the distances d_1 and d_2 and therefore a factor two is included in the expression.

Using this approach, the non-ambiguity range is linked to the repetition rate of the pulses used to evaluate the distance. In order to determine the measured distance without ambiguity, pulses reflected or backscattered from the target must arrive before a new pulse is transmitted through the target.

As a consequence, the non-ambiguity range is expressed as

$$d_{NAR} < \frac{c}{2nf_{R1}}, \tag{3.45}$$

where n is the refractive index of the medium and the pulses are considered to evaluate the distance twice.

It can be verified that the expression of the non-ambiguity range is the same whether derived from the round-trip time of the pulses reflected from the target (Eq. (3.45)) or from the periodicity of the optical phase (Eq. (3.38)).

Precision analysis of a time-of-flight dual-comb ranging measurement

Following the same procedure as in the interferometric scenario, the uncertainty of the time-of-flight distance can be calculated as

$$\sigma_d = \frac{1}{2}\left(\frac{\partial d}{\partial v_g}\sigma_{v_g} + \frac{\partial d}{\partial f_{R1}}\sigma_{f_{R1}} + \frac{\partial d}{\partial \delta f_R}\sigma_{\delta f_R} + \frac{\partial d}{\partial \Delta t}\sigma_{\Delta t}\right), \tag{3.46}$$

where $\sigma_{\delta f_R}$ denotes the uncertainty of the repetition rate difference of the two combs and $\sigma_{\Delta t}$ is the uncertainty of Δt. Although the time-of-flight approach is not explored in the experimental results of this thesis, the first three terms of Eq. (3.46) can usually be neglected relative to the uncertainty of Δt. Therefore, the error in the distance depends on the precision in determining the time delay between two interferograms. This precision is affected by the jitter of the optical pulses.

Historical review of dual-comb ranging

The suitability of dual-comb systems for ranging was first reported in 2009 by I. Coddington and coauthors [132]. In their work, they demonstrated the measurement of distances using two stabilized femtosecond fiber frequency combs with repetition rates around 100 MHz. They successfully measured a distance of 1 meter, close to the non-ambiguity range of the system, achieving a precision better than 5 nm within a measurement time of 60 ms. This precision was obtained by combining time-of-flight and interferometric measurements. Moreover, they proposed a technique to extend the non-ambiguity range based on the acquisition of an additional measurement swapping the roles of the probe and local oscillator OFCs. This technique, which exploited the Vernier effect, allowed the initial ambiguity range of 1.5 meters to be extended to 30 km. The authors validated this technique by measuring a fiber reel of 1139.2 meters long.

Since this initial demonstration, several works on both time-of-flight and interferometric dual-comb ranging have been reported. Although early demonstrations were based on mode-locked fiber combs, other comb generators have shown significant potential for dual-comb ranging, as discussed in this section. Additionally, techniques for extending the non-ambiguity range of dual-comb ranging systems have been proposed [132].

- **Dual-comb ranging based on gain-switched combs**

This thesis contributes to the field of dual-comb ranging with a system based on a dual frequency comb generator consisting of two optically-injected GS laser diodes. The impact of the developments presented in this document relies on the extension of the non-ambiguity range of these systems enabled by the generation of GS combs with low repetition rates.

Dual-comb ranging has been relatively unexplored with GS comb sources. However, these sources are well-suited for this application due to their ability to generate a considerable number of comb lines with relatively low line spacing using simple and robust setups. In addition, the potential for miniaturizing these semiconductor-based dual-comb systems enables their deployment in out-of-the-lab environments. The main limitation that these systems can encounter in a real-world application is the low average optical power of the comb sources. Nonetheless, this issue can be addressed by the inclusion of optical amplifiers in the transmitter side. In the case of an integrated approach, semiconductor optical amplifiers could be included in the system.

The only demonstration of dual-comb ranging using a pair of GS laser diodes with optical injection was reported by K. Hei et al. in 2021 [135]. The authors proposed a ranging system that exhibited a repetition rate tunability spanning from 1.1 GHz to 1.4 GHz. The distance was retrieved through an interferometric approach, utilizing approximately one hundred spectral lines for the estimation of the distance. The maximum non-ambiguity range of the system (obtained for the lowest repetition rate of 1.1 GHz) was approximately 136 mm. This relatively short ambiguity range was extended by measuring the same distance at different repetition rates, resulting in distances up to 2.5 m being measured. Finally, the system was validated through calibration measurements performed by means of a HeNe interferometer, demonstrating an accuracy of 12 μm based on these calibrations.

- **Dual-comb ranging based on other comb sources**

Fiber lasers offer outstanding performances in terms of precision, which is enhanced owing to the broad bandwidth of the resulting combs. Their measurement speed is in the order of hundreds of microseconds, due to their repetition rates typically being in the order of hundreds of MHz. Despite their excellent performance, these ranging systems are bulky and expensive.

The possibility of developing chip-scale dual-comb ranging systems came with the advent of microcombs, which pioneered the miniaturization of OFCs. Since microcombs feature large bandwidths, they can also offer highly precise ranging measurements. In addition, due to the high repetition rate of these combs, acquisition times drop to the order of a few microseconds. However, this high repetition rate limits the non-ambiguity range of these systems to the order of millimeters, necessitating the use of ambiguity-breaking techniques for deploying ranging measurements in real-world applications. In 2018, two different groups first reported their results on microcomb-based dual-comb ranging. Following a time-of-flight approach, M-G Suh and K. J. Vahala reported on distance measurements using two mutually-coherent microcombs generated inside a single silica

resonator pumped by a CW laser in clockwise and counterclockwise directions [134]. Being the non-ambiguity range 16 mm, they demonstrated a distance measurement of ∼4.6 mm with a precision of 200 nm, achieved through averaging up to a time of 500 ms. For a distance measurement of around 26 meters, using the Vernier effect to surpass the non-ambiguity range, the achieved precision was approximately 0.5 meters. At the same time, but following an interferometric approach, P. Trocha and coauthors demonstrated the potential of a dual-comb ranging system based on two free-running microcombs generated in two similar silicon nitride microresonators [133]. They measured distances up to 2 mm with an outstanding precision of 12 nm for an averaging time of 13 μs. Additionally, they demonstrated the ultrafast capabilities of their ranging system by retrieving the profile of an air-gun projectile moving at a speed of 150 m/s.

In addition, approaches based on semiconductor laser sources for the generation of the two OFCs have been also reported. Ranging systems based on electro-optic combs offer similar a performance as gain-switched dual-comb ranging systems, owing to the similarity of electro-optic and GS combs. In 2017, E. L. Teleanu et. al demonstrated a dual-comb ranging system based on two electro-optic frequency combs to measure rapid displacements, emulated by the vibrations of two dynamic samples with vibration frequencies from a few kHz to 50 kHz [136]. By means of a time-of-flight measurement, they measured delays between the optical pulses around 1 ps with a precision of a few femtoseconds. In distance, these values are equivalent to 100 μm and 500 nm, respectively. Moreover, using an interferometric approach they demonstrated the improvement of the precision of the measurement, obtaining a value of 0.8 nm.

Finally, a comparison of the performance of various state-of-the-art dual-comb ranging systems based on different comb sources can be found in the work of B. Martin et al. [137]. This analysis is based in the precision achieved by those systems, and includes both time-of-flight and interferometric measurements. Also, in the review reported by Z. Zhu and G. Wu [138] the reader can find a comprehensive discussion of the fundamentals of dual-comb ranging.

3.3.3 Other applications

Since the emergence of dual frequency combs, part of the research on this area has been focused on exploring novel application domains where dual-comb architectures may be advantageous over existing systems. Beyond dual-comb spectroscopy and dual-comb ranging, additional applications have been reported. Some of these are listed and briefly discussed below.

- **Fiber Bragg grating sensing**. Dual frequency combs have proven their suitability as fiber Bragg grating-based strain sensors [139]. The principle of operation of these systems relies on the detection of a change in the Bragg wavelength resulting from strain applied to the fiber Bragg grating. In this application, OFCs offer the advantage of a broader detection bandwidth for sensing the changes in the response of the fiber Bragg grating, compared to approaches based on CW lasers.

- **Distributed sensing**. This application is based on the use of the optical fiber as a sensor, leveraging its numerous sensing points to monitor parameters such as strain or temperature variations. These variations are detected from the light backscattered from the interrogated fiber, with a spatial resolution determined by the width of the optical pulses sent to the fiber. The use of dual frequency combs in this context benefits from the ability of the dual-comb technique to down-convert and compress optical information to electrical frequencies. The interrogation of 1 km of fiber with a spatial resolution in the centimeter range and the recovery of the information with a detection bandwidth in the MHz range has been demonstrated with electro-optic combs [80].

- **Spectroscopic ellipsometry**. This application related to material science permits to analyze the properties of a material such as its crystalline nature or its thickness by measuring the change of the polarization of light incident on the material. Dual frequency combs allow to perform this analysis with high spectral resolution capabilities at fast acquisition times [140]. The information is obtained from the magnitude and phase of the RF spectrum in both orthogonal polarizations of the optical field, which can be split before detection.

- **Imaging**. Among the most promising applications for dual-comb systems explored in recent years are those related to imaging. Of particular interest is hyperspectral imaging, which combines spectroscopy and imaging. In a hyperspectral imaging system, instead of capturing the intensity of incident light at three wavelengths (red, green, and blue), each pixel captures the intensity over a broad and continuous spectral range. The collected data forms a hypercube, where each pixel contains a spectrum corresponding to a specific spatial location in the scene. Dual-comb hyperspectral imaging systems have demonstrated the ability to characterize a scene across a spectral span defined by the comb bandwidth and with fine resolution [141], [142]. The dual comb illuminates a scene, and the scattered light is collected by a camera. The interferogram time is adjusted to match the frame rate of the camera, typically on the order of 1 second. During the integration time of the camera, each pixel captures an interferogram. The Fourier transform of the information retrieved by each individual pixel of the camera sensor reveals transmission or reflection information of the sample. Additionally, other imaging techniques such as frequency-domain optical coherence tomography, a standard imaging tool in fields such as ophthalmology, can benefit from OFCs as illumination sources and from dual-comb arrangements [143].

- **Indirect spectroscopic techniques**. Dual frequency combs can also enhance spectroscopic techniques where the measured signals are not direct measurements of the absorption spectrum itself but rather indirect consequences of the absorption process. Among these techniques, photoacoustic spectroscopy [144] measures an acoustic signal generated as a result of the interaction between light and the sample, employing an ultrasound transducer for this purpose. This technique, widely utilized in biomedical applications, benefits from the fact that acoustic waves experience weaker scattering when traversing biological tissues. Similarly,

other techniques such as photothermal spectroscopy [145] involve the detection of changes in the thermal properties of a sample, such as changes in the refractive index, induced by the absorption of light. Both approaches benefit from broadband interrogation and non-demanding detection systems enabled by the use of dual frequency combs.

Chapter 4

High-resolution dual-comb spectroscopy with gain-switched combs

The suitability of gain-switched optical frequency combs with low repetition rates for high-resolution dual-comb absorption spectroscopy is experimentally demonstrated in this chapter. A semiconductor-based dual-comb spectrometer with a spectral resolution of 100 MHz is developed experimentally. The two combs are generated by gain switching two laser diodes using short electrical pulse trains as gain-switching signals. The two laser diodes are externally injected by a single laser in CW operation, providing them with mutual coherence. As a result, the coherence of the system is maintained for integration times up to 80 seconds. In addition, the cost-efficiency of the spectrometer is improved by using a low-cost software-defined radio platform at the receiver end of the system. The good performance of these platforms for dual comb spectrometers is demonstrated.

The chapter is structured as follows. First, an experimental characterization of gain-switched optical frequency combs with a line spacing of 100 MHz is performed. The response of an optically injected laser under pulsed gain switching to different modulation amplitudes and different detuning conditions is analyzed in terms of the bandwidth at 10 dB and the carrier-to-noise ratio of the resulting spectra. Then, the results of performing dual-comb spectroscopy using two combs with slightly different repetition rates are presented. Finally, the replacement of a high-end digitizer by an inexpensive software-defined radio device is reported.

4.1 Introduction

The spectral resolution of dual-comb systems is determined by the line spacing of the frequency combs used. Consequently, generating OFCs with low repetition rates (<1 GHz) is desirable for spectroscopic purposes. This is especially crucial for gas spectroscopy, as gaseous samples typically exhibit absorption features with linewidths spanning a few GHz.

Prior to this thesis, dual-comb spectroscopy experiments using GS frequency combs had only been demonstrated with spectral resolutions as low as 500 MHz [4]. However, the maximum spectral resolution of the reported system was limited by the use of sinusoidal signals for the implementation of gain switching at low repetition rates. In other words, below the modulation frequency of 500 MHz and using sinusoidal currents, the poor spectral quality of GS frequency combs (in terms of spectral width and symmetry) limits their usability for spectroscopic measurements. As it has been already discussed in Chapter 2, at low repetition rates the carriers are able to follow the variations of the gain when using sinusoidal signals for gain switching the laser diodes. As a consequence of the slow modulation of the carriers, the generated OFCs present narrow bandwidths compared to those obtained at high modulation frequencies (since the broadening mechanism is different) and asymmetric spectra (due to the chirp being in phase with the optical pulses).

To fully harness the potential of GS combs for spectroscopic applications and to access narrow spectral features, it would be necessary to extend the minimum repetition rate achievable by these systems. This is precisely the motivation of the work developed throughout this document. In the first instance, this goal can be achieved by replacing sinusoidal excitation with pulsed excitation. The use of trains of short electrical pulses allows for the rapid and abrupt modulation of the laser gain. Carriers can no longer follow the gain variations, and as a result, short and chirped optical pulses are generated, yielding wide and flat optical spectra. The generation of such combs was first reported by A. Rosado and researchers from our group, with repetition rates down to 100 MHz [35]. The use of these combs for the realization of gas spectroscopy measurements in a dual-comb arrangement was demonstrated in the first publication of this thesis [146], improving the previous 500-MHz resolution of these systems by a factor of 5. The results presented in this chapter, part of which are included in the aforementioned publication, contribute to unlocking the full potential of dual-comb spectrometers based on GS OFCs and pave the way towards high-resolution dual-comb spectroscopy systems using these comb sources.

Moreover, the optimization of the system in terms of cost is presented in the second part of this chapter. The use of an affordable software-defined radio (SDR) device is demonstrated. The feasibility of using these devices in dual-comb spectrometers was first reported in the second publication of this thesis [147]. Absorption spectroscopy measurements are conducted and the accuracy of the system is validated by comparing the results obtained with such cost-efficient digitizer and those obtained using a high-priced real-time oscilloscope.

4.2 Characterization of 100-MHz gain-switched combs

In order to implement a dual-comb system using two GS OFCs with repetition frequencies of 100 MHz and pulsed excitation, an experimental characterization of the combs obtained at this repetition frequency under different laser driving conditions is first presented. This characterization is focused on the subsequent realization of spectroscopy measurements with the generated OFCs. The response of the sample under test is usually extracted by analyzing the dual-comb spectrum, for this reason, the evaluation of the generated combs is targeted on the evolution of their spectra. Such performance is analyzed via two figures of merit: the carrier-to-noise-ratio, CNR, and the bandwidth at 10 dB, Δf_{10dB}. Both figures of merit were already defined in Chapter 2 (Section 2.2.2).

4.2.1 Experimental setup

The experimental setup used for the characterization of 100-MHz GS combs is presented in Fig. 4.1.

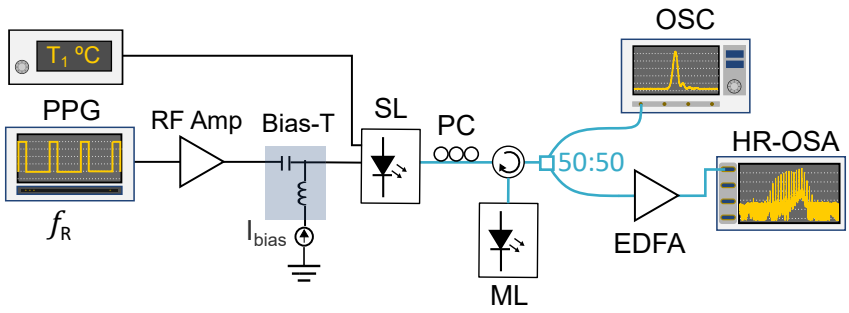

Figure 4.1: Experimental setup employed for the characterization of GS OFCs under pulsed electrical excitation. PPG: pulse pattern generator, RF Amp: RF amplifier, SL: slave laser, ML: master laser, PC: polarization controller, EDFA: Erbium-doped fiber amplifier, OSC: oscilloscope, HR: high-resolution optical spectrum analyzer.

The OFC is generated by gain switching a DFB laser (Gooch & Housego AA0701 series) acting as slave laser (SL). This laser is an InGaAsP/InP multi-quantum well laser diode and features a modulation bandwidth of ∼10 GHz. It is packaged in a 7-pin butterfly configuration and includes a thermistor and a thermo-electric cooler for the measurement and control of the laser temperature, a monitor detector, an inductance (part of the bias-tee element) in the pin that corresponds to the bias current, and an RF connector to allow for its direct modulation. The capacitor of the bias-tee element is included at the RF modulation input of the laser diode. The laser is mounted on a commercial laser mount (Arroyo Instruments 203 LaserMount) with enabled connectors for the supply of the bias current and for the temperature control of the device. The bias current is provided by a low-noise source (Arroyo Instruments 4200-DR series LaserSource), and the temperature is controlled and stabilized by means of a standard thermo-electric temperature controller (ILX Lightwave LDT-5412).

The SL is gain switched by an electrical current that consists of a DC bias current I_{bias} superimposed to a train of electrical pulses. The electrical pulses are generated by a pulse pattern generator (Anritsu MU181020A). This pulse pattern generator (PPG) can operate at a maximum bit rate of 12.5 Gb/s and is able to synthesize electrical waveforms with a maximum peak-to-peak voltage of 2.5 V. In order to switch the laser with higher amplitude electrical pulses, the output of the PPG is amplified by means of a wideband RF amplifier (Minicircuits ZVA-183W-S+). The wide bandwidth of this device (18 GHz) does not distort the rise and fall times of the electrical pulses, which need to be rapid for the switching of the laser. The amplified train of pulses is then delivered to the DFB laser through the aforementioned RF connector. A tunable external cavity laser (Pure Photonics PPCL300), which acts as master laser (ML), injects the slave laser using an optical circulator. This master laser operates over the C-band and has a measured linewidth of 60 kHz. A polarization controller ensures the alignment of the states of polarization of the SL and the ML.

The generated OFCs are measured both in time and frequency domains by means of an oscilloscope equipped with an optical sampling module and a high-resolution optical spectrum analyzer, respectively. The oscilloscope (Tektronix DSA8200) performs equivalent digital sampling and has an optical bandwidth of 20 GHz. Regarding the optical spectrum analyzer (Aragon Photonics BOSA 400 C+L), it features a resolution of 10 MHz that enables to resolve the 100-MHz comb lines. An erbium-doped fiber amplifier (EDFA, Amonics AEDFA-13-B-FA) is included at the input of the optical spectrum analyzer to increase the optical power of the signal, facilitating the measurement of the CNR of the recorded spectra. Otherwise, the noise power of the combs would be masked by the noise floor of the measurement instrument. The optical power of the BOSA measurements corresponds to the power after the amplification stage. In contrast, the optical pulses measured with the oscilloscope are not amplified. Therefore, the optical power measured and showed in this case corresponds to the power of the GS pulses. Moreover, the insertion losses of the circulator and the coupling losses of the optical coupler used (splitting ratio 50:50) are not subtracted from the measurements.

Finally, the CW characterization of the employed DFB laser is included in Fig. 4.2. Panel (a) shows the power-current characteristic of the laser diode measured at room temperature (25 ^{o}C). Its threshold current has a value of 11.35 mA. The CW emission of the laser is depicted in panel (b), measured using a 6-GHz resolution optical spectrum analyzer. Its central emission wavelength at 25 ^{o}C is 1549.73 nm.

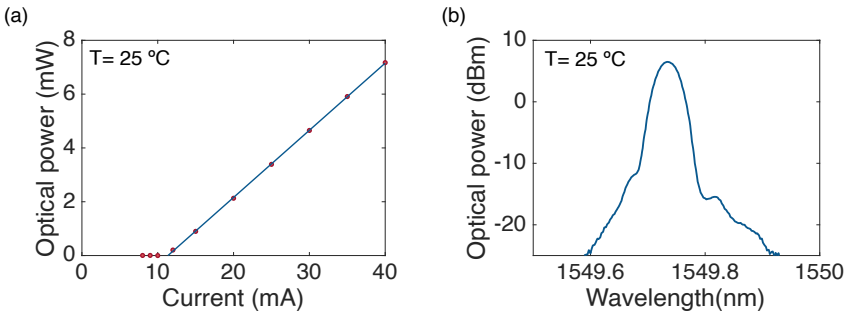

Figure 4.2: CW characterization of the DFB laser employed for the generation of GS OFCs at 100 MHz. (a) Power-current characteristic of the laser diode measured at 25 ºC. (b) Emission spectrum of the laser diode measured with an optical spectrum analyzer at 25 ºC.

4.2.2 Influence of the amplitude of the electrical pulses

The evolution of the comb properties when varying the amplitude of the electrical pulses applied to the laser is experimentally studied. The objective is to obtain OFCs with good characteristics in terms of CNR and spectral flatness for each value of the electrical pulses amplitude. For this purpose, the peak-to-peak amplitude of the AC signal generated by the PPG (V_{RF}) is systematically varied from 2 V to 10 V, in increments of 1 V. The DC component of the driving signal is adjusted in each case to maintain the good spectral quality of the combs and to ensure the proper operation of the laser in gain-switching regime. While the methodology for varying the DC current is not entirely systematic, this approach is deliberately chosen to obtain GS OFCs with good CNR values and spectral flatness across the entire amplitude range. If a fixed value of I_{bias} were set, the same I_{bias} would not allow for the simultaneous generation of good-quality OFCs in the lowest and highest amplitude scenarios due to the large amplitude variation of the AC current from 2 V to 10 V. Specifically, as the amplitude of the RF signal increases, the bias current needs to be decreased to ensure the complete extinction of the optical pulse before the onset of the second spike of the relaxation oscillations.

The experiments are performed for a fixed duration of the electrical pulses, set to a value τ_{pulse} of 200 ps. This value, together with the repetition rate of the pulses, f_R= 100 MHz, configures a duty cycle of the pulsed excitation signal of d_{cycle}= 0.02. The detuning is also fixed, ensuring injection locking in the two extremes of the RF amplitudes range. In this regard, the injection wavelength, λ_{ML}, and power, P_{ML}, are 1549.57 nm and 0.25 mW, respectively, and the temperature of the slave laser is stabilized at 25 ºC. In these conditions, the estimated detuning is ∼20 GHz.

Fig. 4.3 shows the evolution of the optical spectra (top row) and the optical pulses (bottom row) for three RF amplitudes of (a) 2 V , (b) 6 V and (c) 10 V. The comb line exhibiting the highest power corresponds to the injection peak. As the amplitude of the modulation signal increases, the dynamic chirp in the gain-switching process also increases. The greater variation of dynamic chirp over the duration of the optical pulses when the modulation amplitude is increased causes an incremental broadening of the optical spectrum, as evidenced by the depicted spectra.

Furthermore, the spectrum corresponding to the highest modulation amplitude shows a worse flatness and exhibits a ripple on the left side of the spectrum. This ripple is attributed to the excitation of the second peak of the laser relaxation oscillations, which is evidenced by observing the optical pulse corresponding to this particular case.

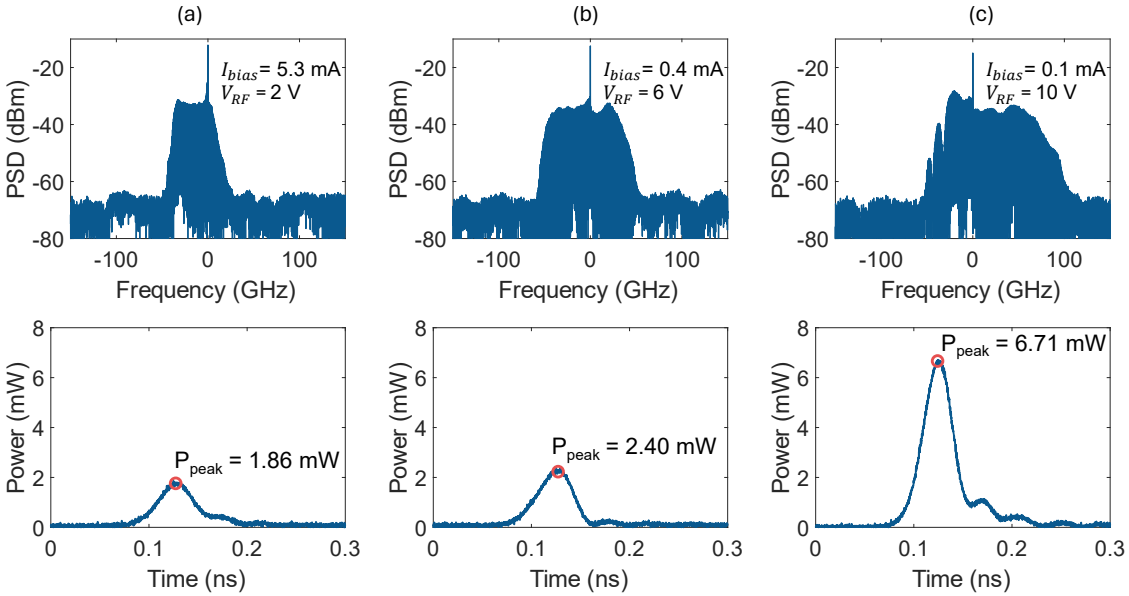

Figure 4.3: Evolution of the 100-MHz optical frequency comb spectra (top panel) and optical pulses (bottom panel) in response to increasing amplitudes of the electrical pulses (V_{RF}) that modulate the laser diode: (a) V_{RF}= 2 V, (b) V_{RF}= 6 V, (c) V_{RF}= 10 V.

The CNR and Δf_{10dB} are calculated for the spectra obtained at each V_{RF} value using a MATLAB routine. The initial step in this routine is to obtain the envelope of the comb spectrum. The injection is then band-pass filtered to exclude it from subsequent calculations. Δf_{10dB} is determined by identifying the two furthest points whose power value is 10 dB below the highest power value of the filtered envelope (see Fig. 4.4 (a)). Within Δf_{10dB}, the CNR is calculated. To do so, the 10-dB bandwidth is swept using frequency windows containing two comb lines. In each window, the CNR is calculated as the ratio of the average power of the two carriers to the average noise power of the noise floor between the two carriers. The overall CNR is calculated as the average value of the individual CNRs (in linear units) obtained at each sweeping window. This process is illustrated in Fig. 4.4 (b). The accuracy of the CNR is limited by the resolution of the measurement instrument, which is 10 MHz.

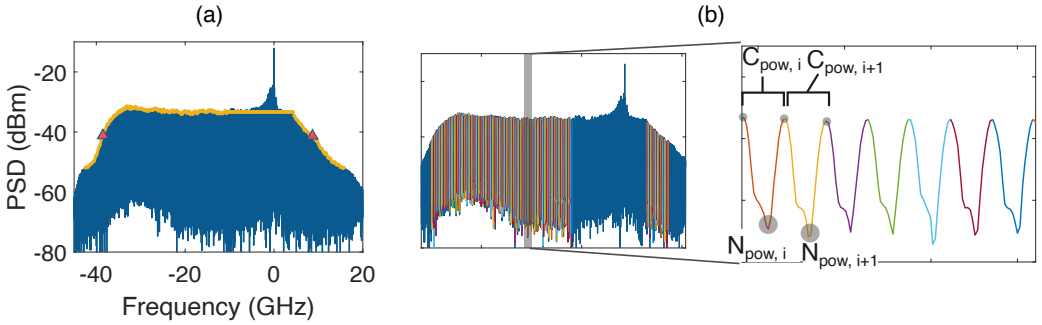

Figure 4.4: Graphical illustration of the determination of (a) the bandwidth at 10 dB of an OFC and (b) the carrier-to-noise ratio within the 10-dB spectral width.

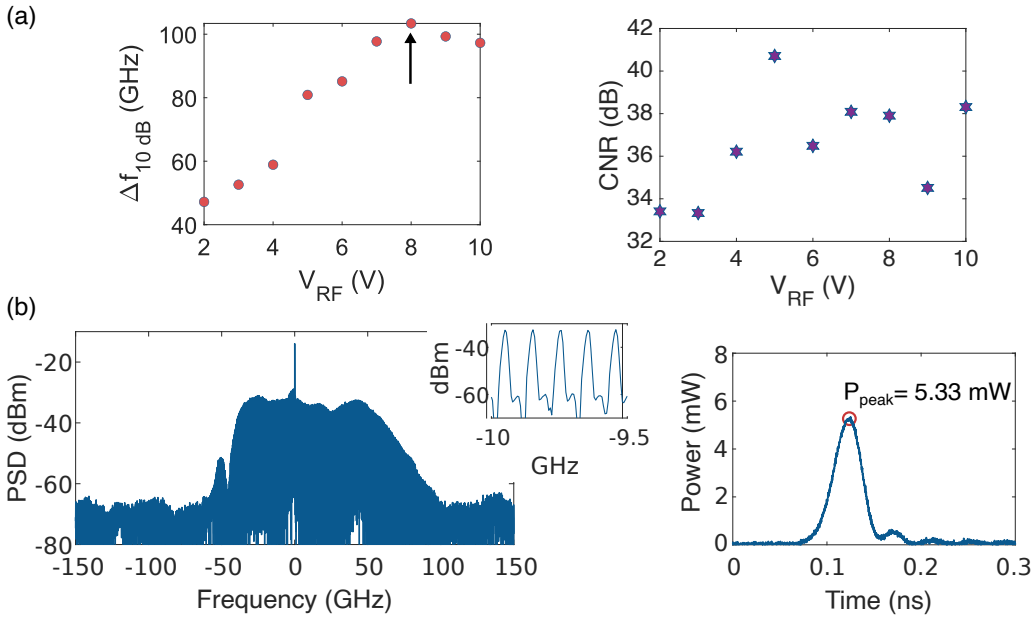

Figure 4.5: (a) (left) Evolution of the bandwidth at 10 dB (Δf_{10dB}) and (right) the carrier-to-noise ratio (CNR) with the amplitude of the pulsed signal used to gain switch the laser diode at 100 MHz. (b) (left) GS OFC spectrum and (right) optical pulse obtained for a peak-to-peak amplitude of the AC signal of V_{RF}= 8 V.

The evolution of both Δf_{10dB} and the CNR with the amplitude of the electrical pulses is depicted in Fig. 4.5. The spectral width exhibits a linear increase up to a saturation point reached for an RF amplitude value of 8 V. Beyond this point, Δf_{10dB} slightly decreases due to the appearance of ripples in the spectra, compromising the spectral flatness and therefore, the calculation of the 10-dB bandwidth. Regarding the CNR obtained after the optical pre-amplification stage, it generally ranges between 36 dB to 38 dB. These values are deemed sufficiently high for spectroscopic measurements, which typically require CNR values greater than the absorption depth of the line being measured (usually a few dB). The highest CNR obtained for $V_{RF} = 6$ V corresponds to the scenario where the comb is injected at the center of its spectrum. Compared to scenarios where injection locking occurs at the extremes of the comb spectrum, this configuration yields a higher overall CNR. OFCs optically injected at the extremes of the spectrum exhibit a high local CNR in the tones surrounding the injection, but the CNR decreases for comb teeth further away from the injection.

Finally, the graph showing the evolution of the spectral width with the amplitude of the RF gain-switching signal can be used as a design manual to configure the bandwidth of the dual frequency comb according to the bandwidth to be tested. With electrical pulses of 200 ps, spectral widths ranging from approximately 47 GHz to approximately 103 GHz can be achieved for RF amplitudes of the electrical pulses from 2 V to 10 V, respectively. If narrower widths were required, lower electrical pulses amplitudes should be configured. The GS OFC obtained for the scenario with the best Δf_{10dB} is presented in Fig. 4.5 (b), generated with $V_{RF} = 8$ V and $I_{bias} = 0.3$ mA.

4.2.3 Influence of the optical injection detuning

The variation of the optical spectrum and the optical pulses with injection detuning is also analyzed. Optical injection detuning was previously defined as the difference in emission frequencies between the slave and master lasers in CW, with the slave laser biased at its threshold current. Here, the objective is to identify how the generated combs change when they are injected into different regions of their spectrum. For this reason, a qualitative analysis has been conducted, analyzing how the OFCs evolve when they are injected in different spectral regions, without quantifying the detuning with the above definition. To achieve this, detuning variation is performed by keeping the wavelength of the master laser fixed and adjusting the temperature of the slave laser. Increasing the temperature of the slave laser causes the comb to shift towards lower frequencies.

To conduct these experiments, the previously obtained comb showing the broadest spectral width is used as a reference. Specifically, the 100-MHz OFC obtained for $V_{RF} = 8$ V, with $\tau_{pulse} = 200$ ps, and $I_{bias} = 0.3$ mA. P_{ML} is as well fixed for all these experimental realizations to 0.25 mW. The optical spectra and optical pulses obtained for three detuning conditions are shown in Fig. 4.6. Panel (a) corresponds to the comb being injected on the left side of the frequency spectrum. By increasing the temperature of the DFB laser by 3.5°C, the injection conditions presented in panel (b) are reached. Subsequently, further increasing the temperature to 31.7°C results in the OFC illustrated

in panel (c). The latter spectrum exhibits a wide spectral width and excellent flatness. However, in the spectral region opposite to the injection wavelength a poor local CNR is obtained. In terms of the optical pulses, no significant changes are observed.

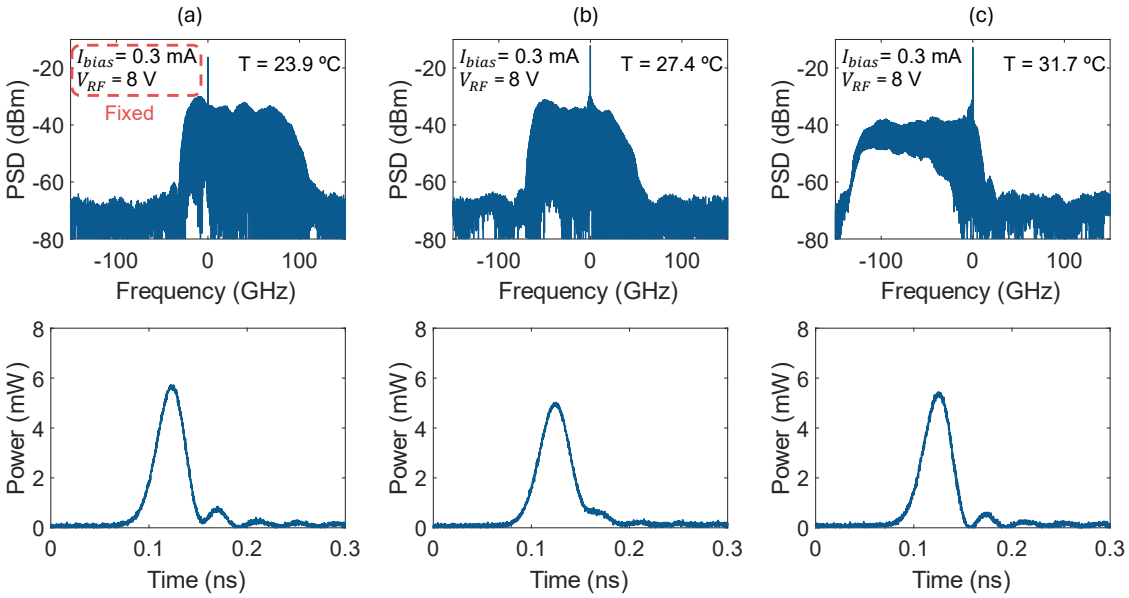

Figure 4.6: Evolution of the 100-MHz optical comb spectra (top panel) and optical pulses (bottom panel) in response to different detuning values between the emission of the slave laser and the master laser. (a) OFC injected on the left side of the frequency spectrum. (b) OFC with a reduced detuning. (c) OFC injected on the right end of its frequency spectrum.

The evolution of Δf_{10dB} and CNR is calculated as a function of the slave laser temperature, which is varied between 23.9°C and 31.7°C. This temperature range corresponds to a variation in the detuning, with the lowest temperature resulting in the injection being performed on the left side of the spectrum and the highest temperature achieving optical injection on the right side of the spectrum. Panels (a) and (b) of Fig. 4.7 show the evolution of the spectral width and the CNR with detuning, respectively. Lower values of Δf_{10dB} and a greater CNR are obtained when the OFC is injected in the center of its spectrum. This behavior can be attributed to a lower detuning between the master laser and the slave laser. Under these conditions, better locking between the ML and SL can lead to a reduction in chirp, which not only narrows the spectra but also decreases the timing jitter of the optical pulses. The reduction of the timing jitter results in lower noise in the optical pulses, leading to an improved CNR. Conversely, broader OFCs with lower CNR values are obtained when the combs are injected at the edges of the spectrum. This behavior can be attributed to an increase in the detuning between the ML and SL. In these conditions, a higher chirp in the optical pulses can lead to broader combs with a poorer total CNR, due to the degraded noise performance of the optical pulses. In the scenario depicted in panel (c) of Fig. 4.6, further detuning would push the operation outside the locking range, as the emissions of both lasers would not be sufficiently close to enable injection locking, resulting in the loss of coherence in the optical pulses.

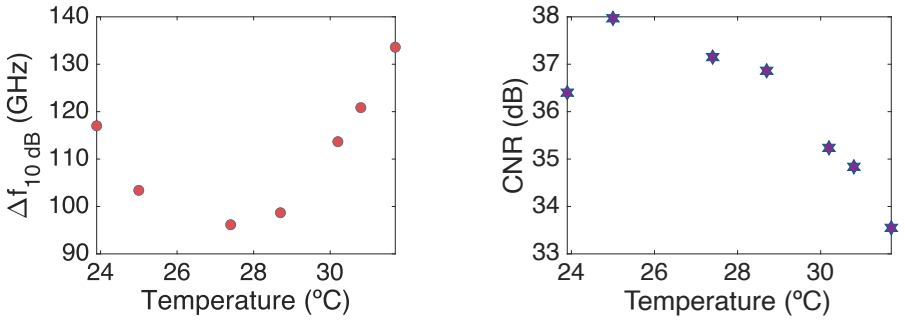

Figure 4.7: (left) Evolution of the bandwidth at 10 dB (Δf_{10dB}) and (right) the carrier-to-noise ratio (CNR) with the detuning between the master and slave emission wavelengths. The detuning is expressed in terms of the slave laser temperature, with the mid temperature values (27 ºC to 29 ºC) corresponding to decreased detunings.

4.3 Gas spectroscopy of hydrogen cyanide

The experiments conducted in this section demonstrate the practical application of GS OFCs operating at repetition rates on the order of a hundred megahertz for gas spectroscopy. Utilizing GS combs enables the retrieval of gas absorption profiles with a tunable spectral resolution, whose tunability range is now expanded to finer values thanks to the use of pulsed excitation to gain switch the laser diodes. Furthermore, as previously demonstrated, the bandwidth of the combs can be adjusted to match the width of the line being measured, facilitating effective optical power management.

In the experiments, by slightly adjusting the repetition rate of the driving trains of pulses, a dual comb with approximately 350 mutually coherent optical lines is generated and employed to successfully measure an absorption line of hydrogen cyanide. This gas is selected due to its deep absorption lines at wavelengths around 1550 nm, which is the central wavelength of the laser diodes used. Figure 4.8 illustrates the transmission of the HCN gas cell to be characterized by dual-comb spectroscopy. The gas cell (Wavelength References HCN-13-H(16.5)-25-FCAPC) contains HCN (isotopologue $^{13}H^{14}CN$) at a pressure of 25 Torr, and has an absorption length of 16.5 cm. The transmission spectrum shown in the figure is measured using the high-resolution optical spectrum analyzer and employing a tunable laser included in the instrument.

The number of lines generated by the presented system is comparable to the results achieved by electro-optic dual frequency combs employing external nonlinear broadening [148] or unconventional driving methods [149]. These results are also similar to those obtained with two acousto-optic frequency-shifting loops [150], albeit without the need of feedback stabilization systems. The performance of the GS dual-comb system is also evaluated by testing two different detection schemes and by analyzing the SNR when averaging is carried out.

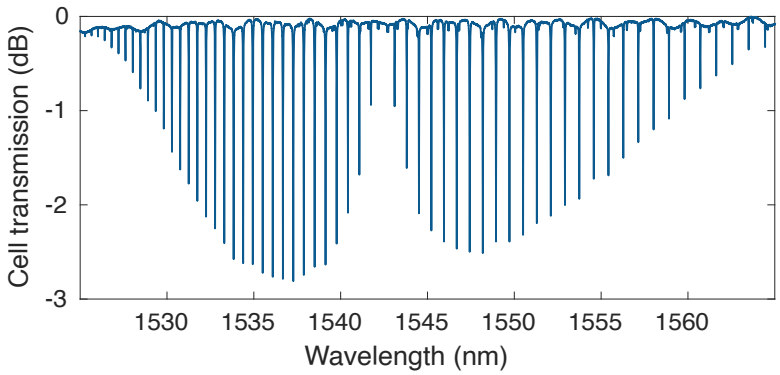

Figure 4.8: Transmission spectrum across the C-band of $^{13}H^{14}CN$ enclosed in a fiber-coupled single-pass cell at a pressure of 25 Torr and with an absorption path length of 16.5 cm, measured with a high-resolution optical spectrum analyzer via tunable laser absorption spectroscopy. The absorption line selected for the measurements is located at 1549.73 nm.

4.3.1 Experimental setup

The setup used for the realization of the experiments, which is based on a master-slave arrangement, is shown in Fig. 4.9 (a). Fig. 4.9 (b) shows a photograph of the optical part of the experimental setup, where the different components are conveniently indicated.

The two OFCs are generated by gain switching two similar DFB lasers (Gooch & Housego AA0701 series), operating as SLs. One of the lasers used has already been presented in the previous section for the characterization of GS combs (Section 4.2). The two slave lasers (denoted SL1 and SL2) are driven by the superposition of two electrical signals: a bias current (I_{bias1} for SL1, I_{bias2} for SL2) and a low-duty-cycle pulsed signal with peak-to-peak amplitude V_{RF} and pulse width τ_{pulse}. The two trains of pulses are generated by two PPGs, and feature two slightly dissimilar repetition rates of f_{R1}= 100 MHz and f_{R2}= 100.1 MHz (δf_R= 100 kHz). The operating temperature of both lasers is independently adjusted with two temperature controllers (ILX Lightwave LDT-5412) in order to control the detuning with respect to the master laser. Two optical circulators are used to inject the output power from the ML (Pure Photonics PPCL300) into the two GS DFB lasers. Polarization controllers are included in the setup to align the polarization of the optical fields, thereby maximizing the coupling between the master and slave lasers and the coupling between the optical signals circulating through the two branches of the interferometer. The OFC generated by SL2 is frequency shifted a value f_{shift}= 80 MHz using an acousto-optic modulator (AA Opto-Electronic MT80-IIR30-Fio-PM0). The implementation of the frequency shift ensures the unambiguous mapping of optical lines to RF beat notes. The optical signals coming from each laser are coupled together with a 50:50 coupling ratio and then directed either to a reference path or to a gas cell by means of two optical switches. At the output of the switches, the signal is amplified with an EDFA (Amonics AEDFA-13-B-FA) and mixed on a photodiode (New Focus 1014).

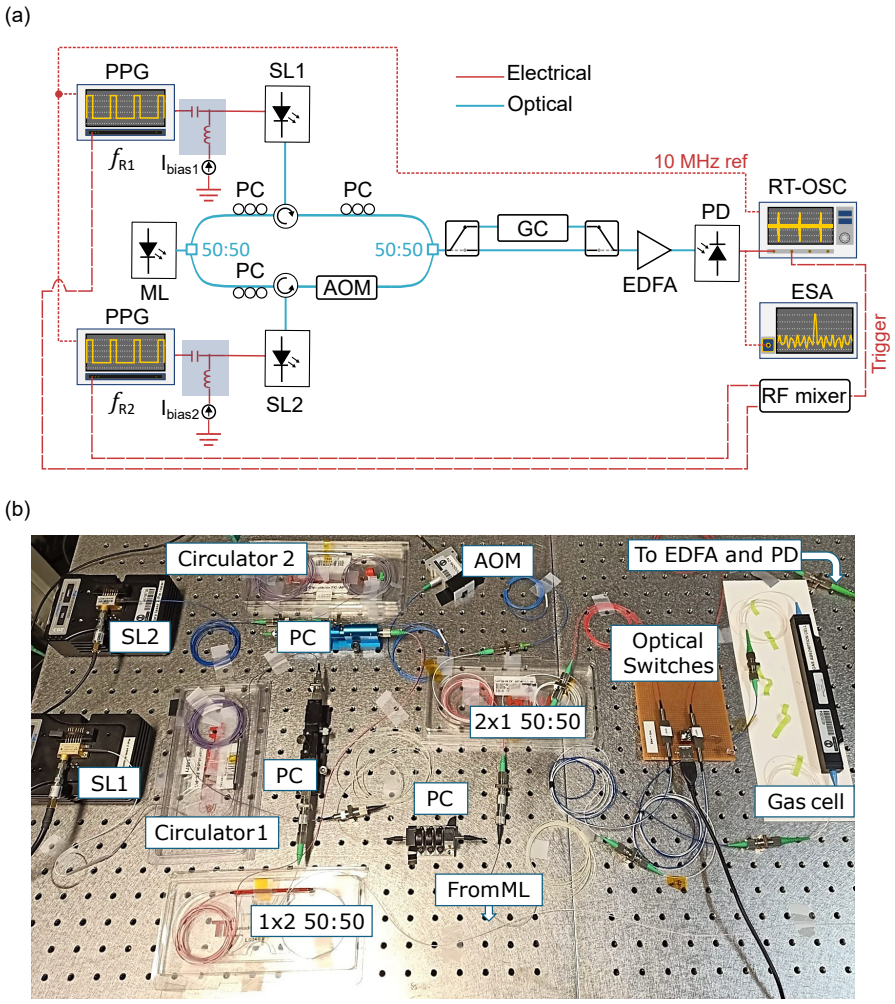

Figure 4.9: (a) Schematics and (b) photograph of the experimental setup employed for the demonstration of 100-MHz dual-comb spectroscopy using GS OFCs. PPG: pulse pattern generator, SL: slave laser, ML: master laser, PC: polarization controller, AOM: acousto-optic modulator, GC: gas cell, EDFA: Erbium-doped fiber amplifier, PD: photodetector, RT-OSC: real-time oscilloscope, ESA: electrical spectrum analyzer.

The dual-comb setup is built following a symmetric configuration, which shows stability and robustness but only allows for the retrieval of the amplitude profile of the gas line. The gas is enclosed in a sealed cell (Wavelength References HCN-13-H(16.5)-25-FCAPC) enabled with fiber connectors. The line centered around 1549.73 nm is selected for the measurements. According to the database from the National Institute of Standards and Technology (NIST) [151], the normalized transmittance of this line is 0.5592 (absorption depth of 2.52 dB). According to the manufacturer, its FWHM is around 2 GHz.

The electrical signal at the output of the photodiode is either measured with an electrical spectrum analyzer or with a real-time digital sampling oscilloscope. The electrical spectrum analyzer (Agilent E4446A) features a bandwidth of 44 GHz. This instrument

shows the power spectral density of the measured signal, with a spectral resolution determined by the bandwidth of the band-pass filter applied to the input signal. On the other hand, the real-time oscilloscope (Keysight MSOS804A) shows the time-domain electrical signal, which can be digitized with a sampling rate up to 20 GSa/s and an electrical bandwidth of 8 GHz. The trigger for the temporal measurements is obtained by mixing the signals from the two PPGs by means of an RF mixer to get the frequency difference. Synchronization of the PPGs and the oscilloscope is ensured through a shared 10-MHz reference, aligning their clocks for precise measurements.

In addition to the main setup shown in Fig. 4.9, a 6.25-GHz resolution optical spectrum analyzer (Ando AQ6315A) is used to measure the two optical spectra. In the time domain, the optical pulses corresponding to the two generated combs are measured with the oscilloscope equipped with a 20-GHz bandwidth optical module described in Section 4.2. The same oscilloscope is also used to measure the electrical excitation pulses, employing the electrical module for this purpose. This module enables to measure electrical signals with a fine resolution, since it features an electrical bandwidth of 50 GHz. Finally, the driving conditions of the DFB lasers as well as their threshold currents are summarized in Table 4.1.

Parameter	**SL1**	**SL2**
Threshold current I_{th} (mA)	11.35	11.58
Bias current I_{bias} (mA)	5.7	9.1
Peak-to-peak amplitude of electrical pulses V_{RF} (V)	2.5	1
Width of electrical pulses τ_{pulse} (ps)	200	200
Comb repetition rate f_R (MHz)	100	100.1
Master laser injection power P_{ML} (μW)	70.8	70.8

Table 4.1: Driving conditions of the lasers and modulation parameters employed for the demonstration of 100-MHz dual-comb spectroscopy with GS laser diodes.

4.3.2 Experimental results

The experimental results are organized in different subsections, which follow the steps carried out until the absorption profile is obtained. These steps include the generation of the two optical combs, the beating of the combs on the photodetector leading to the generation of the RF dual-comb, the post-processing of the data, and finally, the retrieval of the absorption profile.

Generation of two optical frequency combs

The two OFCs generated by pulsed gain switching of two optically-injected slave lasers with the parameters described in Table 4.1 yield a dual-comb system with a line spacing of 100 MHz and repetition rate offset of 100 kHz. These settings configure a compression factor C= 1000. In both cases the excitation pulses have a nominal duration of 200 ps, which corresponds to a duty cycle of the modulation signal of 2%.

The profiles of the electrical pulses measured with the 50-GHz equivalent-time oscilloscope are shown in Fig. 4.10 (a). The measured FWHM is 190 ps for both pulses, which includes the contribution of the bandwidth of the oscilloscope to the measured rise and fall times. The peak-to-peak amplitude of the pulses (2.5 V for SL1 and 1 V for SL2) corresponds to the maximum output voltage of the two PPGs used: although the two PPGs are from the same manufacturer and have the same performance in terms of the synthesizer module, one of them exhibits a higher maximum output power. For these experiments, electrical amplifiers to boost the excitation pulses have been omitted, as the bandwidth of the combs does not need to be very broad. Given that the linewidth of the absorption line is around 2 GHz, the required spectral width to capture both the absorption line and the baseline is around 30 GHz.

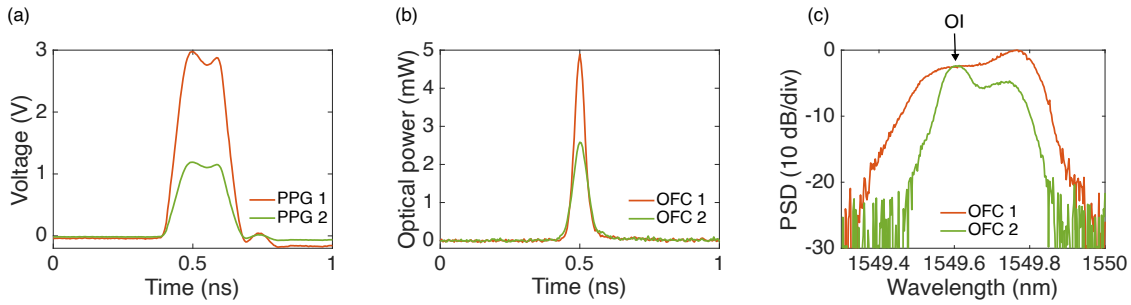

Figure 4.10: (a) Electrical pulses used to gain switch the two laser diodes: pulses from PPG1 drive SL1 and pulses from PPG2 drive SL2. (b) Optical pulses emitted by the two lasers (OFC1, OFC2) in response to gain switching. (c) Optical spectra of the two generated GS combs measured with an optical spectrum analyzer (resolution of 6 GHz). Optical injection region indicated by an arrow.

The optical pulses from each comb source are depicted in Fig. 4.10 (b). Their FWHM is 43 ps for OFC1 and 61 ps for OFC2, including the contribution introduced by the oscilloscope to these time widths. Since the slaves are switched off most of the time, optical injection plays a fundamental role in the comb generation process. Photons externally injected by the master laser serve as seeds for the generation of new GS pulses when the lasers switch on again.

In order to generate the RF dual comb, it is necessary to ensure that the two GS optical combs overlap. In addition, the overlapping area must cover the absorption region of interest. This is achieved by individually adjusting the temperature of each laser after configuring the driving signals. The visualization of this process in the optical spectrum analyzer allows for the verification of such spectral overlap, which occurs at the wavelength of interest at specific laser temperatures. Once the two combs are generated, they are optically injected. The resulting optical spectra of both combs measured with the optical spectrum analyzer are presented in Fig. 4.10 (c). As indicated in the figure, optical injection is performed at the blue side of the spectra, at λ_{ML}=1549.63 nm. Due to the resolution of the instrument the individual comb lines cannot be resolved. However, because of the use of injection locking, coherent emission is guaranteed, which leads to the generation of well-resolved optical lines in the frequency combs. This

is later evidenced from the generation of the down-converted comb. The measured envelope allows to verify the flatness of the combs as well as their optical bandwidth. In consistency with the time domain measurements, the bandwidth of OFC2 (∼35 GHz within 10 dB) is lower than that of OFC1 (∼50.5 GHz within 10 dB) because of the lower amplitude of the modulation signal of SL2. The existence region of the RF dual frequency comb corresponds to the spectral region where the two OFCs overlap. Therefore, and assuming mutual coherence between both combs, the maximum number of optical lines (spaced by 100 MHz) that can be employed in the dual-comb system is around 350 lines, which is more than enough for the spectroscopic measurements considered here.

Both OFCs are appreciably flat, especially OFC1, which features around 324 teeth within 3 dB. The generation of flat-topped OFCs is achieved by adjusting the power injected into the slave lasers and by controlling the point of the GS spectrum where optical injection is performed. Optical injection is typically performed at one end of the gain-switching spectrum due to its typical asymmetry. Specifically, it is usually performed at the edge that shows less power. This procedure can be also monitored with the optical spectrum analyzer, while the master laser frequency is finely tuned to guarantee locking and to optimize the flatness of the spectra. It is important to note that the injection wavelength should not coincide with the absorption wavelength of the gas. This is because the combs exhibit instabilities at the injection frequency, which would negatively impact the spectroscopic results.

Generation of down-converted dual-comb spectrum

The interference of the two OFCs shown above on a photodetector results in an interferogram with a periodicity of δf_R. This periodicity in this case corresponds to 10 μs (inverse of δf_R= 100 kHz). The interferogram, which is a time-domain signal, can be digitized and visualized with the real-time oscilloscope. Fig. 4.11 (a) corresponds to the interferogram trace resulting from the beating of the two GS combs, digitized with the oscilloscope at a sampling rate of 400 MSa/s. The modulus of the Fourier transform applied to this interferogram signal gives rise to a down-converted RF spectrum as the one shown in Fig. 4.11 (b). This RF comb is the result of frequency averaging two thousand spectra. Each spectra is retrieved from a temporal trace with a duration of 500 μs, i.e., containing 50 consecutive interferogram bursts. This acquisition settings yield a total measurement time of 1 s.

The temporal signals are sequentially recorded with the oscilloscope[1] and stored in a personal computer, where they are later post-processed. Furthermore, to filter out the highest Nyquist zones, the oscilloscope bandwidth is limited to 100 MHz. The prominent peak at 80 MHz corresponds to the optical injection from the master laser. Since a frequency shifter of 80 MHz is used, the injection frequency is moved away from 0 Hz to this frequency.

[1]In the case of the oscilloscope traces, their acquisition is automatized using a home-built LabVIEW program. For the acquisition of the traces using the electrical spectrum analyzer, a LabVIEW program already available in the laboratory is used.

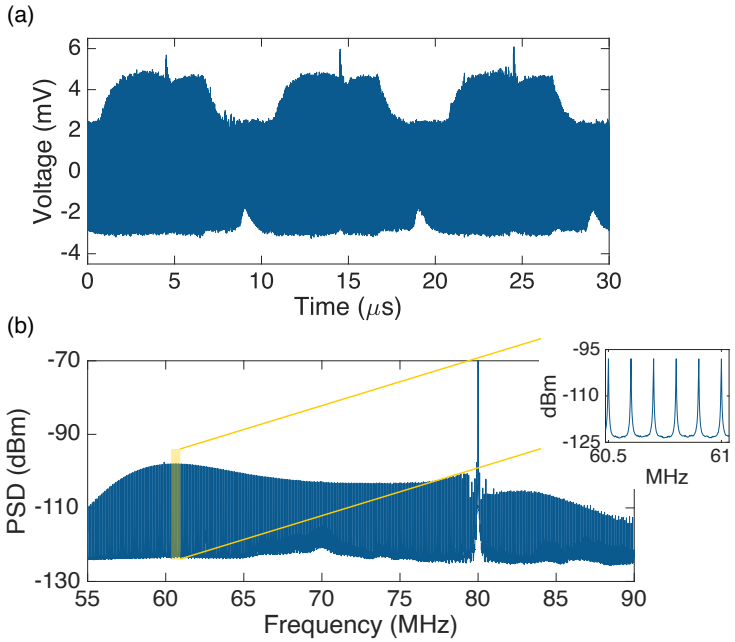

Figure 4.11: (a) Dual-comb interferograms digitized with a real-time oscilloscope at a sampling rate of 400 MSa/s. The bursts reproduce the expected periodicity of 10 μs. (b) Power spectral density of the RF dual frequency comb obtained for an integration time of 1 s.

The resulting down-converted comb exhibits a flat-top spectrum, with approximately 300 lines within 10 dB (excluding the injection peak). A close-up view of this spectrum, illustrating the line spacing of the RF comb of 100 kHz (compressed from 100 MHz by a factor of 1000), is provided in the inset of Fig. 4.11 (b).

When the digitization process is performed with the electrical spectrum analyzer, the time-domain interferograms cannot be visualized. Instead, the power spectral density is directly provided by the instrument. This instrument, based on heterodyne detection, calculates the power of the measured signal as it passes through a band-pass filter. The resolution of the measurement is configured through the resolution bandwidth parameter, which essentially represents the bandwidth of such band-pass filter. The resolution bandwidth is therefore one of the most important parameters of spectrum analyzers. For these measurements, the RF spectrum is obtained by configuring a sweeping span of 32 MHz, from 55 MHz to 87 MHz. This frequency interval contains the first Nyquist set of the RF spectrum. In order to ensure that the frequency resolution of the electrical spectrum analyzer is sufficient to resolve the RF beat notes, the number of points of each sweep is set to its maximum value (8192 points) and the resolution bandwidth is configured to 11 kHz. The number of points together with the resolution bandwidth yield a sweep time of 1 s, which sets the minimum integration time (t_{int}) for the measurements performed here with this acquisition instrument.

Fig. 4.12 shows the RF spectrum acquired with the electrical spectrum analyzer for two different acquisition times. Panel (a) corresponds to an integration or measurement time of 1 s. When comparing the RF spectrum obtained from the acquisition performed with the real-time oscilloscope to the one from the electrical spectrum analyzer for the same measurement time (Figure 4.11 (b) versus Figure 4.12 (a)), it is noticeable that the RF spectrum obtained from the spectrum analyzer exhibits higher noise. This is due to the fact that for the same acquisition time of 1 s, no averaging is performed with the electrical spectrum analyzer. Nonetheless, the noise can be reduced through averaging, which can be computed by the instrument itself. When 60 averages are performed, leading to an increase of the integration time to 1 minute, the spectrum displayed in Fig. 4.12 (b) is obtained. The inset shows a 500-kHz region of this spectrum, comprised between 60.5 MHz and 61 MHz.

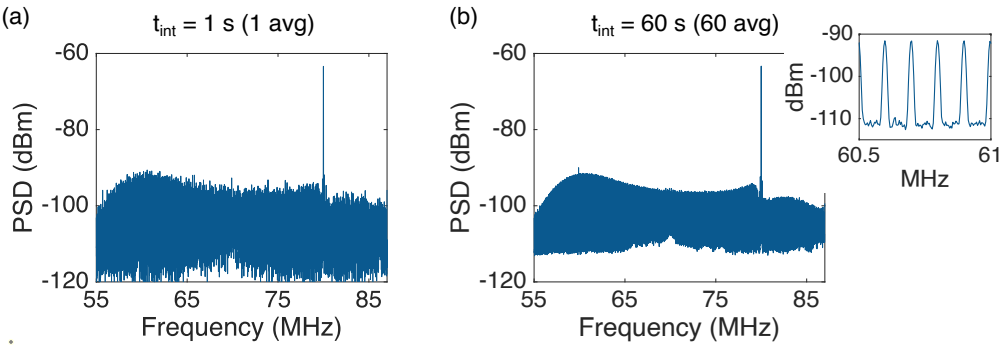

Figure 4.12: RF dual-comb spectra measured with an electrical spectrum analyzer at two integration times of (a) 1 s and (b) 60 s. The shortest integration time corresponds to one sweep of the instrument while the longest integration time corresponds to 60 averaged sweeps.

The down-converted spectra shown above are captured with the optical switches set in the reference configuration. In this scenario, the optical fields do not traverse the gas cell. To retrieve the absorption profile of the gas line, the same acquisitions have to be performed for the fields interrogating the gas. For this purpose, once the reference traces are acquired, the optical path is changed with the aid of the switches and the resulting traces are captured. This procedure is performed for both acquisition instruments, the oscilloscope and the electrical spectrum analyzer. When the light traverses the sample, the fingerprint of the gas is encoded in the two OFCs (due to the use of a symmetric setup). The RF spectra obtained from the beating of the two frequency combs containing the amplitude information of the sample for the two acquisition instruments are presented in Fig. 4.13.

The spectra obtained from the modulus of the Fourier transform of the interferogram traces retrieved from the oscilloscope are shown in Fig. 4.13 (a) for three integration times: 500 μs (obtained after processing a single interferogram trace of 500 μs), 500 ms (obtained after averaging 1000 spectra from 1000 interferogram traces of 500 μs), and 1 s (corresponding to 2000 averaged spectra). The spectra measured with the electrical spectrum analyzer for integration times of 1 s, 10 s, and 60 s are represented in Fig. 4.13 (b). They correspond to 1 frequency sweep, 10 averaged sweeps, and 60 averaged sweeps performed by the spectrum analyzer, respectively. The region where the gas absorbs can be clearly seen in the spectra. The maximum of absorption occurs at a down-converted frequency of ∼67 MHz. In addition, the evolution of the noise floor with averaging is evidenced in the figure.

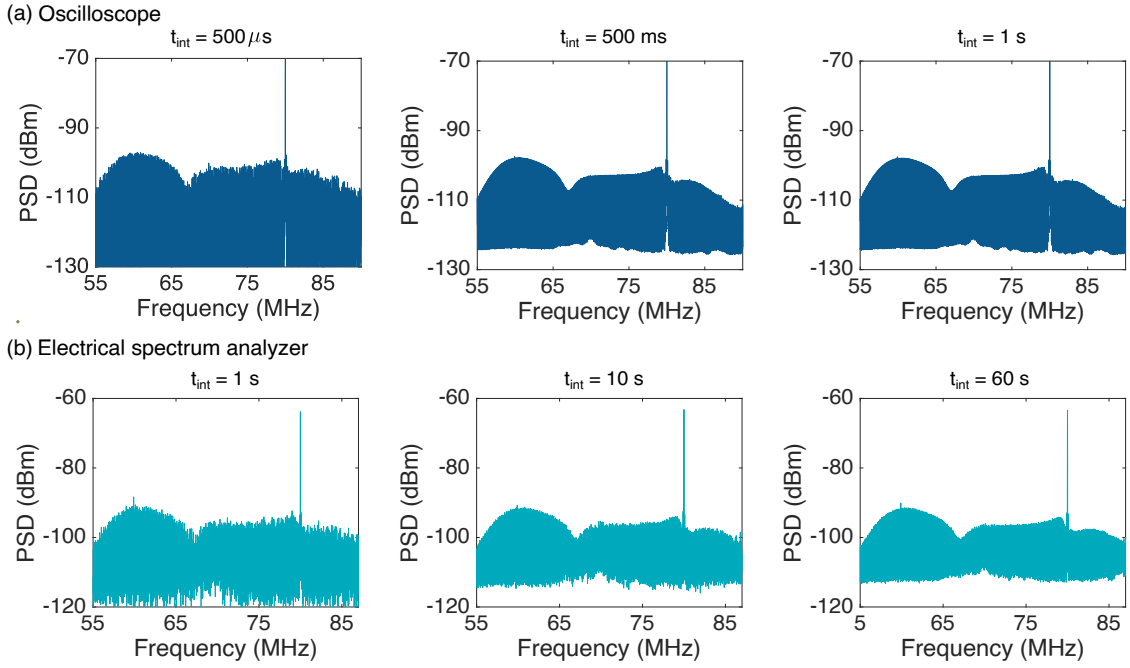

Figure 4.13: (a) Dual-comb gas spectra obtained from post-processing the oscilloscope interferogram traces. The results at three integration times are presented: 500 μs, 500 ms, and 1 s. (b) Dual-comb gas spectra measured with the electrical spectrum analyzer. Three spectra corresponding to three integration times are shown: 1 s, 10 s, and 1 minute.

Post-processing of dual-comb data

Digital processing of the retrieved data is performed offline using a home-built MATLAB code. A block diagram detailing the post-processing algorithm is shown in Fig. 4.14. When an oscilloscope is used as digitization system, the steps followed by the algorithm are:

1. The N interferogram traces captured in both positions of the optical switches are loaded in the MATLAB program: N reference (no-sample) traces and N gas traces.
2. The fast Fourier transform (FFT) of each trace is calculated. Since the information to be retrieved is on the amplitude of the comb teeth, the modulus of the FFT is computed.
3. The moduli of the FFTs corresponding to the N reference traces and to the N gas traces are averaged. The electrical power spectral density of the averaged spectra is then calculated.
4. A peak detection routine in the span corresponding to the first Nyquist zone is applied to both averaged spectra, reference and gas, to retrieve the maximum amplitude of each comb tooth. This procedure is performed using a home-built peak detection routine, based on frequency windows applied to the spectra. Each frequency window contains a single comb line. Vectors storing the locations and amplitudes of comb lines are created from this process.
5. The transmittance is obtained from the ratio of the amplitudes of the comb lines of the gas and reference spectra.
6. Differences in the envelopes of the reference and gas dual-comb spectra may appear linked to the absorption process. As a result, the baseline of the transmittance may deviate from being a flat line. To correct the baseline deviation, it is fitted to a polynomial. The fitted polynomial is then subtracted from the experimental data.
7. A Voigt profile is fitted to the final transmittance obtained after the baseline correction procedure. For this purpose, a home-built fitting routine based on optimization through a least squares algorithm is applied to the the experimental data. The output of the fitting algorithm provides a Voigt distribution fitted to the experimental transmittance and the residuals from the fitting process. The residuals correspond to differences between pairs of experimental and fitted values.

The algorithm that fits a Voigt distribution to the experimental transmittance is also detailed in Fig. 4.14. This optimization algorithm is based on the least squares method, an iterative procedure that minimizes the sum of the squares of the residuals. The algorithm stops when the change in the sum of the squares relative to its initial value is less than a user-defined tolerance value, which in this case is set to 10^{-19}. The measured transmittance and the frequency vector serve as input variables. At the output of the optimization procedure, a distribution fitted to the experimental data is returned.

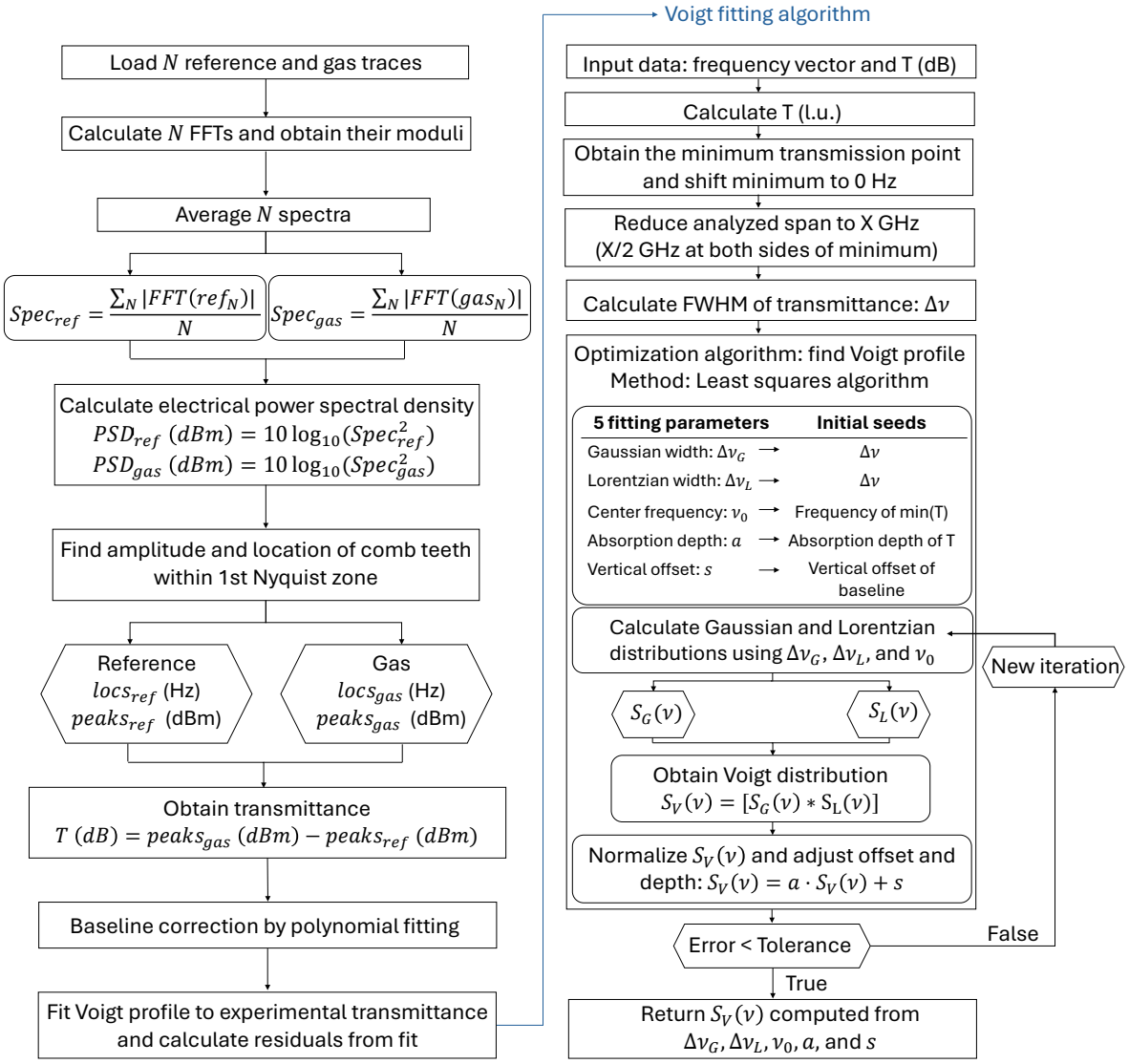

Figure 4.14: Developed MATLAB code to post-process dual-comb spectroscopy data.

The optimization algorithm follows the steps described below:

1. The Gaussian and Lorentzian spectral distributions needed to build the Voigt profile are described in linear units. The experimental transmittance is also expressed in linear units.

2. The span of the transmission profile is reduced to a narrow region containing the absorption feature and a portion of the baseline. For an absorption line exhibiting a linewidth of 2 GHz, a span of 10 GHz around the transmission minimum is usually considered (5 GHz at both sides of the minimum). In addition, the frequency vector is shifted to have the minimum centered in 0 Hz. This is performed just for convenience when presenting the results.

3. Once the data are conditioned, the optimization routine starts. The algorithm is programmed with five fitting parameters. Each fitting parameter needs an initial value (seed) to perform the first iteration of the optimization problem. For this reason, first of all, the initial seeds are calculated. Two fitting parameters correspond to the spectral widths of the Gaussian and Lorentzian distributions. As seed, the FWHM of the experimental curve is used in both cases. The center frequency of the spectral distribution is the third fitting parameter. Its seed corresponds to the minimum of transmission, which occurs at 0 Hz. The fourth fitting parameter is the absorption depth, which is used to scale the normalized fitted profile. As initial value, the depth of the experimental line is calculated as the difference between the average value of the baseline points and the transmittance minimum. Finally, the fifth fitting parameter is a vertical offset, which may be considered in case the experimental baseline of the transmission in linear units is slightly deviated from the unity.

4. The first iteration of the least squares algorithm runs with the seed values. The optimization consists in calculating the Voigt profile as the linear convolution of a Gaussian and a Lorentzian profile. The result from the convolution is then normalized, scaled, and displaced considering the offset. At each step of the algorithm, values of the fitting parameters γ that minimize the following sum are searched:

$$S = \sum_{i=1}^{n} [y_i - f(x_i, \gamma)]^2, \tag{4.1}$$

where n is the number of points of the measured transmittance, x_i and y_i correspond to the x and y values of the experimental transmittance, and f is the model function, which in our case is a Voigt distribution. The program iterates until the stopping condition described above is reached.

Finally, when utilizing the electrical spectrum analyzer for capturing the spectra, the initial steps involving the calculation of reference and molecular spectra associated with each interferogram trace are omitted. Additionally, since averaging is also conducted by the acquisition apparatus, the first step conducted is the peak detection routine. The subsequent steps follow the same previously detailed process.

Absorption spectroscopy results

The profile of the molecular transition of the interrogated cell containing $^{13}H^{14}CN$ that occurs at 1549.73 nm is retrieved for different integration times and using the two mentioned acquisition instruments. The acquisition performed with the oscilloscope enables fast measurements with good SNR, while the spectrum analyzer requires longer times to achieve the same SNR.

In Fig. 4.15 the transmission profiles of the analyzed line obtained from the electrical spectrum analyzer measurements are presented for three integration times of (a) 1 s (1 average), (b) 10 s (10 averages), and (c) 60 s (60 averages). A frequency span of 10 GHz around the absorption peak is shown. The experimental points are plotted with

blue circles, while the fitted Voigt profile is represented by a red line. The residuals of the fitting can be observed in the bottom part of each subfigure. For the longest measurement time (panel (c)), the absorption depth and the linewidth provided by the fit are T= 0.56 and FWHM= 2.3 GHz, respectively. These values are in good agreement with the transmission data provided by the NIST (T= 0.5592) [151] and the linewidth specification given by the gas cell manufacturer (∼2 GHz). For this case (t_{int}= 60 s) the standard deviation of the residuals, σ_{res}, calculated in the 10-GHz span is 0.0078.

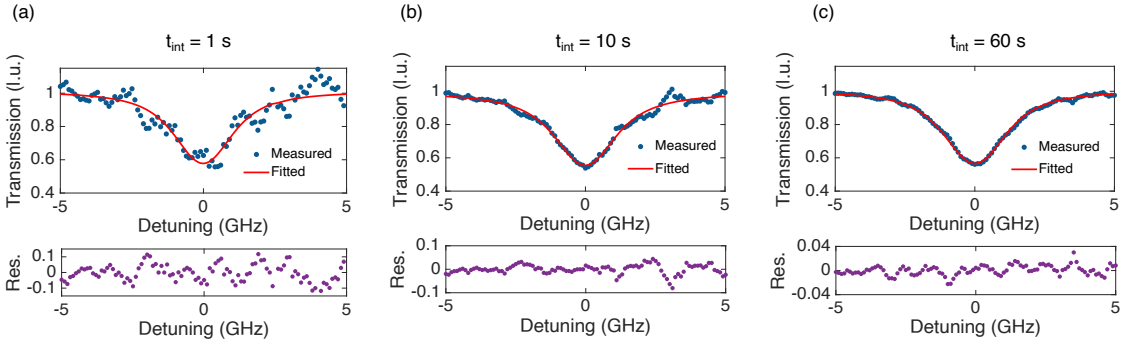

Figure 4.15: Transmission profile of a single HCN absorption line (1549.73 nm) retrieved by dual-comb spectroscopy using an electrical spectrum analyzer as digitizer. Three integration times are represented: (a) 1 s, (b) 10 s, (c) 60 s. A Voigt profile (red line) is fitted to the experimental points (blue dots).

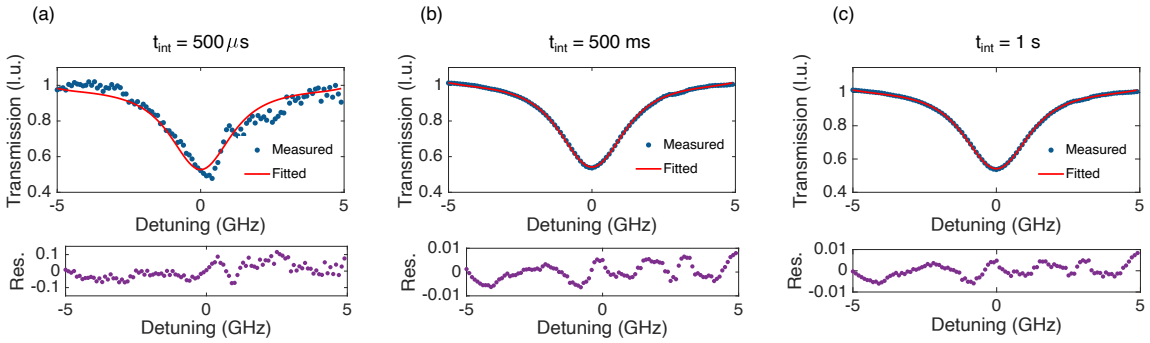

Figure 4.16: Transmission profile of the HCN line at 1549.73 nm retrieved from dual-comb spectroscopy measurements and using a real-time oscilloscope to digitize the interferograms. Three integration times are presented: (a) 500 μs, (b) 500 ms, and (c) 1 s.

On the other hand, the oscilloscope allows for faster measurements, from 500 μs up to 1 s in our case. By means of the oscilloscope, single shots of 500 μs of duration are sequentially recorded. Each shot contains 200000 samples (sampled at 400 MSa/s), which make up the 50 interferogram bursts contained in each measurement. Therefore, to achieve an integration time of 1 s, 2000 temporal traces of 500 μs are averaged in the frequency domain. The resulting transmittances obtained for three integration times are shown in Fig. 4.16: (a) 500 μs, (b) 500 ms, and (c) 1 s. The corresponding value at the minimum transmission point and the FWHM for t_{int}= 1 s are T= 0.54,

FWHM= 2.2 GHz. The residuals, shown in the bottom part of each individual plot, do not show systematic deviations. The standard deviation of the residuals for the last integration time is σ_{res}= 0.0031.

Finally, the performance of the dual-comb system in terms of signal-to-noise ratio is analyzed by means of a figure of merit defined by the product of the SNR and the number of comb lines, M. In an OFC with M comb lines, the SNR per spectral line scales with 1/M [111]. In addition, when averaging is performed, the SNR scales with the square root of the averaging factor or, equivalently, with the square root of the integration or measurement time, $\sqrt{t_{int}}$. Therefore, the basic scaling law (without performing a detailed analysis of the predominant noise sources in the system) of the SNR in an OFC when averaging is performed is SNR $\approx \sqrt{t_{int}}$/M. For this reason, the figure of merit SNR × M at an integration time of 1 s is commonly used as an indicator of the noise performance of dual-comb systems. The mutual coherence of the system is also derived from this expression, since the SNR improves with $\sqrt{t_{int}}$ provided that the mutual coherence of the two OFCs is maintained during the integration time.

In this case, the SNR is calculated as the inverse of the standard deviation of the residuals ($1/\sigma_{res}$) in a 10-GHz window centered around the transmission minimum. The calculation is performed following this reasoning since the standard deviation of the residuals provides an equivalent measurement of the noise, which decreases with averaging. If the SNR is computed by dividing the amplitude of a tooth by the average noise between two teeth, a similar value to $1/\sigma_{res}$ is obtained. Considering the number of lines in a 10-dB bandwidth, M= 350, the figure of merit for an integration time of 1 s takes values of $1.1{\cdot}10^5$ and $6.3{\cdot}10^3$ for the oscilloscope and the electrical spectrum analyzer measurements, respectively.

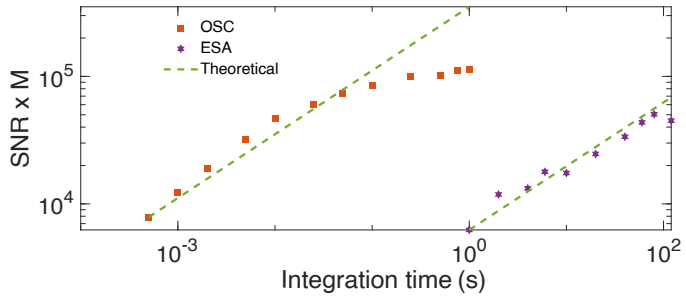

Figure 4.17: Signal-to-noise ratio in M comb lines (SNR × M) versus integration time obtained when the acquisition is performed by an oscilloscope and by an electrical spectrum analyzer.

The evolution of SNR × M with the integration time is shown in Fig. 4.17 for the two employed acquisition methods. As the expected behavior of SNR × M is to scale with $\sqrt{t_{int}}$, a logarithmic graph is chosen for the representation of these data so that a linear progression of SNR × M with t_{int} can be observed. In the case of the oscilloscope, SNR × M exhibits the expected behavior up to 100 ms. Then, the slope decreases showing a trend towards saturation at 1 s. This saturation is attributed to systematic errors in the fitting and the baseline correction process. In the case of the electrical

spectrum analyzer, the quality factor improves also according to $\sqrt{t_{int}}$ from 1 s up to 80 s. This improvement of the SNR up to 80 s indicates a very good degree of stability and coherence of the setup. Finally, the lower value of SNR $\times$ M obtained for the spectrum analyzer is related to the operation principle of this instrument, which discards a significant portion of the input power during the process by measuring the spectrum with an equivalent tunable band-pass filter.

4.4 Towards low-cost gain-switched dual-comb spectrometers

OFC generators using laser diodes offer various advantages if compared to other light sources, one of them being their cost-efficiency. In the quest for low-cost field-deployable dual-comb spectroscopy systems, the use of these sources as well as their integration seems a rather natural choice. In this regard, GS OFCs constitute good candidates.

The optimization of the cost of the optical part must be accompanied by the improvement of the cost of the electronics. On the transmission side, dual-comb spectrometers should be based on inexpensive electronics for generating the different required signals without compromising the robustness, resolution, and accuracy of the system. If the system described in the previous section for the implementation of molecular spectroscopy measurements is considered, cost reduction on the transmission end involves replacing the pulse pattern generators by a more affordable alternative. In this direction, the viability of using step-recovery diodes for the generation of the trains of pulses used to gain switch the lasers was demonstrated [152]. These devices, often known as electrical comb generators, produce electrical pulses when they are driven by a sinusoidal signal. The periodicity of the pulses is dictated by the frequency of the sinusoidal wave and their FWHM is usually in the range of hundreds of picoseconds. The sinusoidal signals required for driving these electrical comb sources can be generated with low-cost instruments such as direct digital synthesizers, as it has been recently reported by our research group [121].

To complete the picture, an improvement in terms of cost in the receiver side is also required. It is in this regard where the use of SDRs as digitization devices comes into the scene. These devices, with prices as low as $20, are good candidates for substituting sophisticated digitizers. Following the successful implementation of absorption spectroscopy with the proposed 100-MHz gain-switched dual-comb system, this section demonstrates dual-comb spectroscopy measurements in which the 20 GSa/s real-time oscilloscope is replaced by an SDR board [147].

4.4.1 The software-defined radio as digitizer

Software-defined radios are radio transceivers in which certain traditional analog components used for RF signal manipulation, such as filters, mixers, modulators, and demodulators, are replaced by digital processing in an embedded system. This helps to mitigate undesirable effects such as thermal noise or voltage drifts.

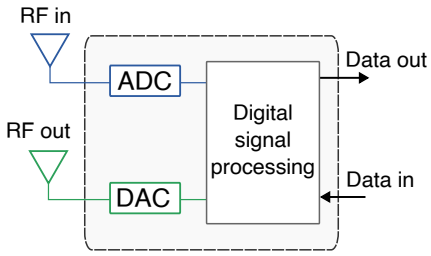

Figure 4.18: Illustration of a generic SDR transceiver.

The block diagram of a generic SDR transceiver is depicted in Fig. 4.18. In their simplest form, they consist of two antennas for receiving and transmitting RF signals, analog to digital and digital to analog converters (ADCs and DACs, respectively) and a digital signal processing unit usually based on a field programmable gate array (FPGA) or a microcontroller. The first SDRs emerged in the mid-1990s. Initially, due to limitations in the sampling capabilities of ADCs at that time, RF signals underwent down-conversion steps in the analog domain before digitization. As ADC sampling capabilities improved, ADCs have been progressively moved closer to the antennas, nowadays allowing for the direct digitization of the received RF signals. Then, down-conversion to baseband and other required steps are now performed digitally.

The maturity and versatility of SDR systems have progressively increased while costs have concurrently decreased, making them appealing tools for the transmission, acquisition, and processing of RF signals. These flexible platforms have proven to be very useful as transmitters and receivers in various applications, such as nuclear magnetic resonance spectroscopy [153], [154]. Since SDRs are often built on open-source platforms, they have also proven beneficial as key elements of optoelectronic systems, where the functionality of the system can be defined by accessing the software platform of the device. In this regard, they have been used for the development of an optical interferometer to measure photoacoustic signals induced in a dye solution [155]. Additionally, in the context of optical frequency combs, SDRs have been employed for the stabilization of the repetition rate and the offset frequency of femtosecond combs [156], serving as integral components within phase-locked loops.

In the work developed in this thesis, an SDR platform is used, for the first time as far as we are concerned, in a dual-comb system [147]. The SDR is included in the receiver end of the system, for the acquisition and digitization of dual-comb interferograms produced at the output of the photodetector. For this purpose, the SDR is tuned within the spectral region corresponding to the first Nyquist zone. The SDR selected for the dual-comb spectrometer is one of the most affordable options in the market. Specifically, an RTL-SDR is utilized [157], which possesses only receiving capabilities and integrates a USB connector for transferring output data to a personal computer. These receivers were originally developed for digital video broadcasting (DVB) signals; however, the amateur radio operators community found out that these devices were capable of receiving any signal within their tuning operation range. This was possible by operating the radio in a 'test mode', bypassing the digital television decoding stage. This enabled RTL-SDRs to be used as generic programmable radios, with a tuning range that usually spans from 25 MHz to 1.75 GHz. Within this tuning range, they can receive signals from different bands such as GPS band (global positioning system, 1.5 GHz), FM radio (199 MHz), or mobile communications bands such as 4G and 5G frequency ranges.

The name RTL-SDR derives from the fact that these receivers, originally intended to be use as DVB decoders which now function as generic SDR receivers, are built upon the Realtek RTL2832U DVB demodulator. The RTL-SDR used can receive signals within the tuning range mentioned above and generates 8-bit in-phase and quadrature (IQ) data samples at its output. The output data can be sampled at a maximum rate of 3.2 MSa/s, which limits the bandwidth of the detected signal to a maximum of 3.2 MHz (note that this is a complex signal). It is based on two devices, a digital television tuner (Rafael Micro R820T) that down-converts the received RF signal to an intermediate frequency (IF), and the Realtek demodulator that digitizes and demodulates the signal by means of an IQ demodulator. The processes that undergoes the signal received through the antenna until the output IQ data is generated are depicted in Fig. 4.19 (a).

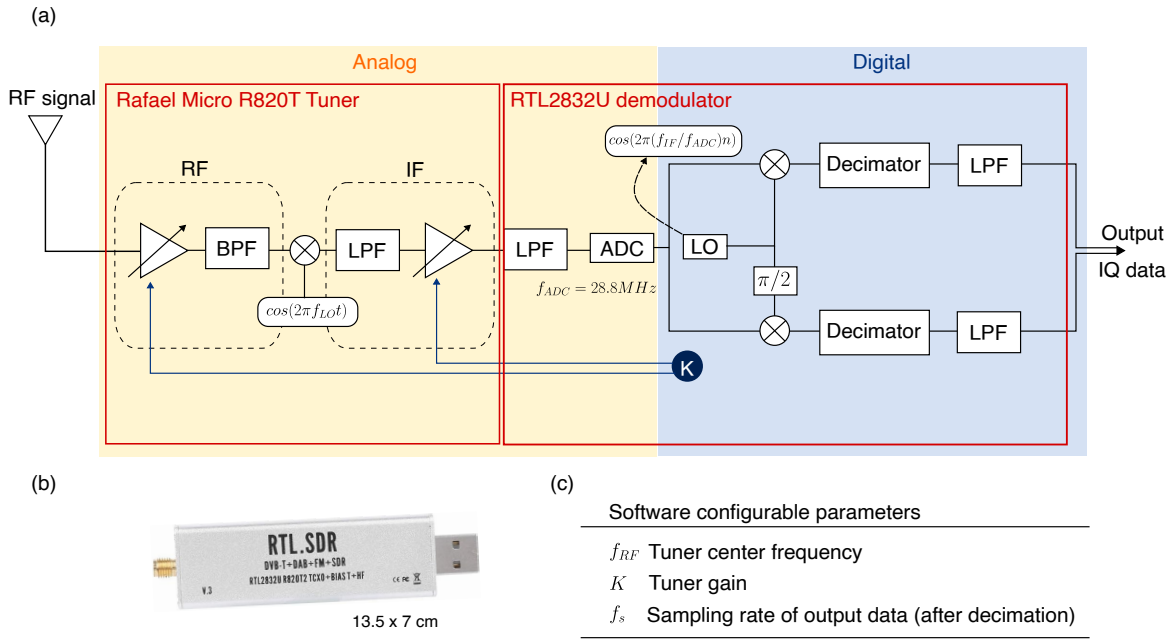

Figure 4.19: (a) Block diagram of the RTL-SDR used as low-cost digitizer in the proposed dual-comb system, adapted from [158]. BPF: band-pass filter, LPF: low-pass filter, LO: local oscillator. (b) RTL-SDR USB dongle used for the realization of the experiments. (c) SDR operation parameters that can be configured and modified via software.

First, the RF signal centered at a specific frequency within the allowed bandwidth is band-pass filtered to select a portion of the spectrum and down-converted to an IF of f_{IF}= 3.57 MHz with a voltage-controlled oscillator. The frequency of the voltage-controlled oscillator, f_{LO}, is set such that the resultant frequency after mixing the RF signal with the local oscillator is centered around f_{IF}, i.e., $f_{LO} = f_{RF} - f_{IF}$. Then, the IF signal is low-pass filtered to only allow for the replica centered around 3.57 MHz. Amplification stages are added before filtering and the gain of such amplifiers (K) can be modified through software. The IF signal is sent to the RTL2832U, where the rest of processing is performed. The IF signal is digitized by the ADC with a sampling frequency of 28.8 MSa/s. The sampled signal is sent to an IQ demodulator, which

down-converts the signal from IF to baseband and produces IQ data samples. The resulting signal is then decimated to reduce the sampling rate, and low-pass filtered. The decimation factor can be defined by the user so that the output data has a sampling rate up to 3.2 MSa/s.

An image of the RTL-SDR device is shown in Fig. 4.19 (b). The RF signal is received by an RF port enabled with an SMA connector. Communication between the SDR platform and the computer is performed using MATLAB and Simulink. A Simulink hardware support package including an interface with the RTL-SDR receiver is used. This interface enables the configuration of specific parameters, which are indicated in Fig. 4.19 (c).

4.4.2 Experimental setup

The objective of the experiments developed in this section is to replicate the dual-comb absorption spectroscopy results achieved using a real-time oscilloscope for digitization, now utilizing an RTL-SDR platform. For this purpose, the optical part of the experimental setup is identical to that presented in the previous section. Regarding the electrical part of the setup, in addition to the real-time oscilloscope, the RTL-SDR is included as acquisition system. It is controlled through a personal computer running MATLAB and Simulink. The real-time oscilloscope is synchronized to the 10-MHz common reference of the two electrical pulse generators, while the RTL-SDR is not synchronized to any instrument. In addition, since the maximum RF voltage delivered by each pulse generator is different (being 2.5 V for PPG1 and 1 V for PPG2), a wideband amplifier (Minicircuits ZVA-183W-S+) is included at the output of the second PPG in order to achieve similar driving conditions in both lasers and hence comparable OFCs. Despite being very similar to the setup already presented in Fig. 4.9, the employed setup is shown in Fig. 4.20 for the convenience of the reader.

Two commercial high-speed-modulation single-mode lasers are employed as slave lasers; a discrete-mode laser (Eblana EP1550-0-DM-H19-FM) as SL1, and a DFB laser (Gooch & Housego AA0701 series) as SL2. The central wavelength of both lasers is around 1550 nm. Despite being different lasers, both show similar CW operation. Regarding the threshold current of each laser, their values are I_{th1}= 10.1 mA and I_{th2}= 11.35 mA for SL1 and SL2, respectively. The discrete-mode laser is modulated by the superposition of a DC current I_{bias1} and a pulsed signal with a peak-to-peak amplitude of 2.5 V, which is delivered by one of the PPGs. The DFB laser acting as SL2 is modulated by the combination of I_{bias2} and the train of electrical pulses delivered by the second PPG. The maximum output voltage of this device is amplified so that the AC signal modulating SL2 shows a peak-to-peak amplitude of 3.1 V. The bias currents of the two lasers are optimized in relation to their threshold currents and the peak-to-peak voltages of the pulsed signals. The duration of the electrical pulses is configured to a value of 200 ps in both pulsed signals. The two gain-switching frequencies are f_{R1}= 100 MHz and f_{R2}= 100.01 MHz, which results in a repetition rate difference of δf_R= 10 kHz and a compression factor of C= 10^4. A higher compression factor with respect to the one used for the experiments presented in the previous section is chosen in order to compress the

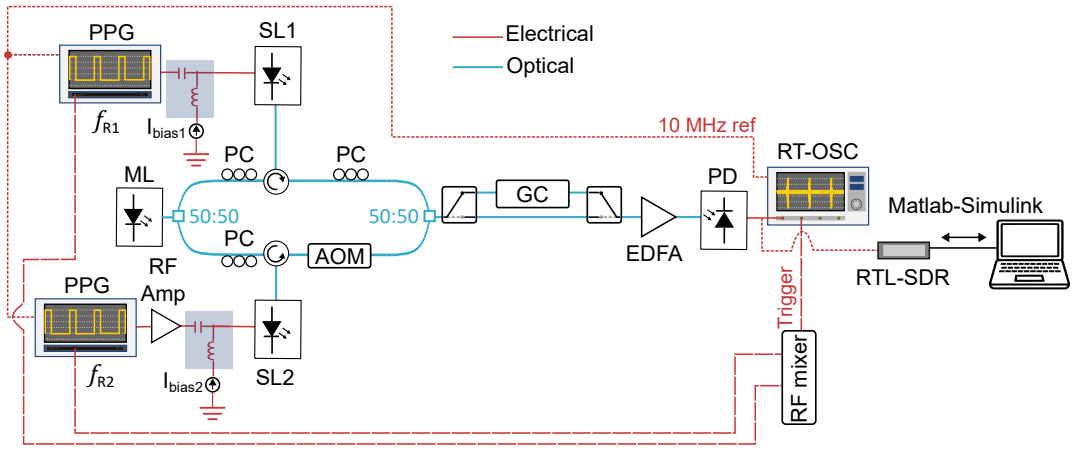

Figure 4.20: Dual-comb experimental setup utilized for the realization of gas absorption spectroscopy, employing both a high-end and an inexpensive digitizer. PPG: pulse pattern generator, SL: slave laser, ML: master laser, PC: polarization controller, AOM: acousto-optic modulator, GC: gas cell, EDFA: Erbium-doped fiber amplifier, PD: photodetector, RT-OSC: real-time oscilloscope.

optical spectrum within the bandwidth of the SDR, whose maximum value is 3.2 MHz. Finally, the emission wavelength of the master laser (Pure Photonics PPCL300) is set to 1549.57 nm, about 20 GHz away from the gas absorption line to avoid some instabilities observed close to the injection frequency. The driving conditions of the lasers and other devices included in the setup are summarized in Table 4.2.

Description	**Symbol**	**Value**
Master laser wavelength	λ_{ML}	1549.57 nm
Master laser power	P_{ML}	-11.5 dBm
SL1 DC bias current	I_{bias1}	5.1 mA
SL1 AC peak-to-peak voltage	V_{RF1}	2.5 V
SL1 AC pulse repetition rate	f_{R1}	100 MHz
SL2 DC bias current	I_{bias2}	1.4 mA
SL2 AC peak-to-peak voltage	V_{RF2}	3.1 V
SL2 AC pulse repetition rate	f_{R1}	100.01 MHz
Width of electrical pulses	τ_{pulse}	200 ps
Acousto-optic modulator frequency	f_{shift}	80 MHz

Table 4.2: Driving conditions of the lasers and other employed optical elements for the implementation of a cost-efficient dual-comb spectrometer.

4.4.3 Experimental results

The measurement of the two individual GS OFCs used to realize dual-comb spectroscopy is first presented. Then, the down-converted spectra resulting from mapping the optical spectrum into the electrical domain are shown. The offline analysis of the retrieved spectra allows to finally retrieve the transmittance of the gas line selected for the measurements.

Generation of two optical frequency combs

The selected driving and modulation parameters for the two optically injected slave lasers result in the two GS combs shown in Fig. 4.21 (a) and (b). These spectra, which are normalized to the injection power, are measured using a high-resolution optical spectrum analyzer. As f_{R1} and f_{R2} are greater than the resolution frequency of this instrument (10 MHz), the individual spectral lines composing each OFC can be resolved, as shown in Fig. 4.21 (c). This zoomed plot focuses on the region where absorption will be produced and measured. A flatness better than 2 dB is obtained along the gas absorption region.

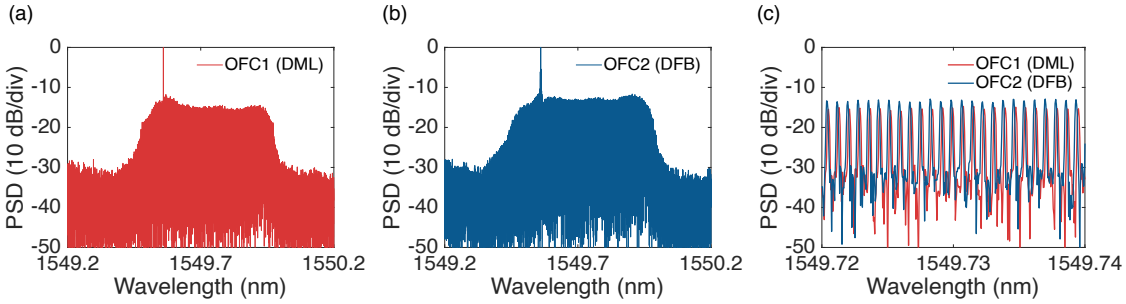

Figure 4.21: Optical spectra of the two slightly detuned GS OFCs generated by (a) a discrete-mode laser and (b) a DFB laser, measured with a 10-MHz optical spectrum analyzer (BOSA). (c) Zoomed view of the two superimposed optical spectra.

The comb generated by gain switching the discrete-mode laser shows a 10-dB bandwidth of ∼65 GHz and a CNR of ∼23 dB, calculated within Δf_{10dB}. The comb generated by the DFB laser features a slightly higher Δf_{10dB} of 70 GHz and a CNR of ∼24 dB. The optical 10-dB bandwidth resulting from the overlap of the two spectra is then limited to the lower bandwidth, i.e., 65 GHz. Within this bandwidth, there are 650 optical lines evenly spaced by 100 MHz in the case of OFC1 and 100.01 MHz in the case of OFC2. For the two individual comb spectra to overlap, the central frequency of both lasers is finely tuned using temperature controllers. After finding stable temperature conditions of both slave lasers ensuring their spectral overlap, the master laser wavelength is selected to guarantee locking and to obtain a flat comb region at the gas absorption frequencies.

Generation of down-converted dual-comb spectrum

The interferograms generated after the interference of both OFCs recorded with the real-time oscilloscope and the radio device are depicted in Fig. 4.22 (a) and (b), respectively. Regarding the acquisition with the oscilloscope, it is performed at a sampling rate of 200 MSa/s, and the analog bandwidth of the oscilloscope is limited to 100 MHz to filter the frequencies that are outside the bandwidth of interest. Five hundred single shots of 2 ms are recorded sequentially, each of them containing 20 interferograms having a periodicity of 100 μs (inverse of δf_R). The low amplitude of the interferogram signal is caused by a bad response of the photodetector used, whose degraded performance was detected after the realization of the experiments. Nonetheless, the experiments could be carried out with such a weak signal without a clear degradation of the results.

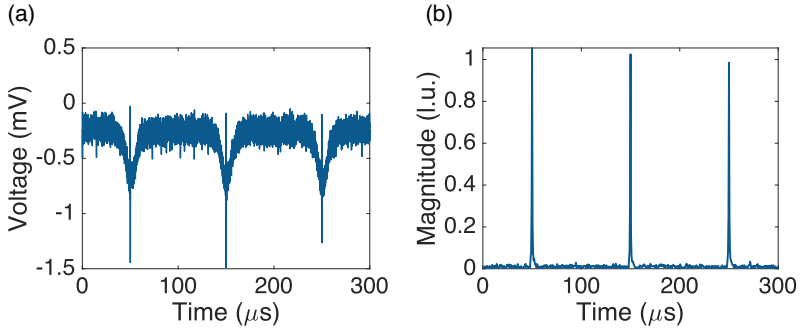

Figure 4.22: (a) Time domain interferogram trace digitized with the oscilloscope. (b) Magnitude of the IQ data samples acquired with the SDR representing the modulus of the complex interferogram traces.

On the other hand, the digitization with the SDR is configured to be performed at a much lower sampling rate of 2 MSa/s. The working principle of SDR platforms is very appropriate for these measurements, as they shift the center frequency of the signal with a tunable local oscillator before digitizing, allowing the use of lower sampling rates than those that would be required for directly sampling the signal. These sampling rates are further reduced after the decimation operation. The local oscillator frequency is configured through the software interface to a value of 82 MHz, which is where the maximum absorption occurs. Then, the spectrum centered around the absorption peak is digitized with a bandwidth of 2 MHz (limited by the employed sampling rate). Considering the compression factor, the electrical bandwidth of 2 MHz corresponds to an optical bandwidth of 20 GHz. With the linewidth of the measured line being around 2 GHz, the optical bandwidth of 20 GHz is wide enough to retrieve both the line profile and a portion of the baseline. The configuration of the SDR yields temporal traces of 10 ms, each of them comprising 100 interferograms. Since the SDR demodulates the input signal into IQ data, a complex signal is obtained from the digitization process. The normalized magnitude of the IQ data, with the bursts showing the expected periodicity, can be seen in Fig. 4.22 (b). The visible differences between the interferograms displayed in Fig. 4.22 are a consequence of the signal processing performed by the SDR, which results in a complex interferogram signal. Despite operating with this complex signal to obtain the dual-comb spectrum, only the magnitude of the signal is illustrated.

The RF spectra are obtained from the Fourier transform of the entire interferogram traces. This means that neither the traces acquired with the oscilloscope nor those acquired with the SDR are truncated before calculating the Fourier transform. Consequently, the minimum integration time of the system corresponds to the duration of the recorded traces, which is 2 ms for the oscilloscope and 10 ms for the SDR. Fig. 4.23 shows the obtained RF spectra at different integration times: 100 ms, 500 ms, and 1 s. For each integration time, the reference spectrum is plotted together with its corresponding measurement spectrum. The depicted spectra are the result of frequency averaging individual spectra, each individual spectra corresponding to integration times of 2 ms (when considering the oscilloscope signals) or 10 ms (for the SDR traces). The top graphs (Fig. 4.23 (a), (b) and (c)), showing the reference spectra in yellow and the gas spectra in blue, correspond to the dual-comb spectra obtained from the oscilloscope traces. The RF spectra depicted in the bottom part of the figure, with the gas-free spectra in red and the measurement spectra in green, are obtained from the SDR data. For the integration time of 1 s, five hundred oscilloscope spectra and one hundred SDR spectra are averaged in the frequency domain.

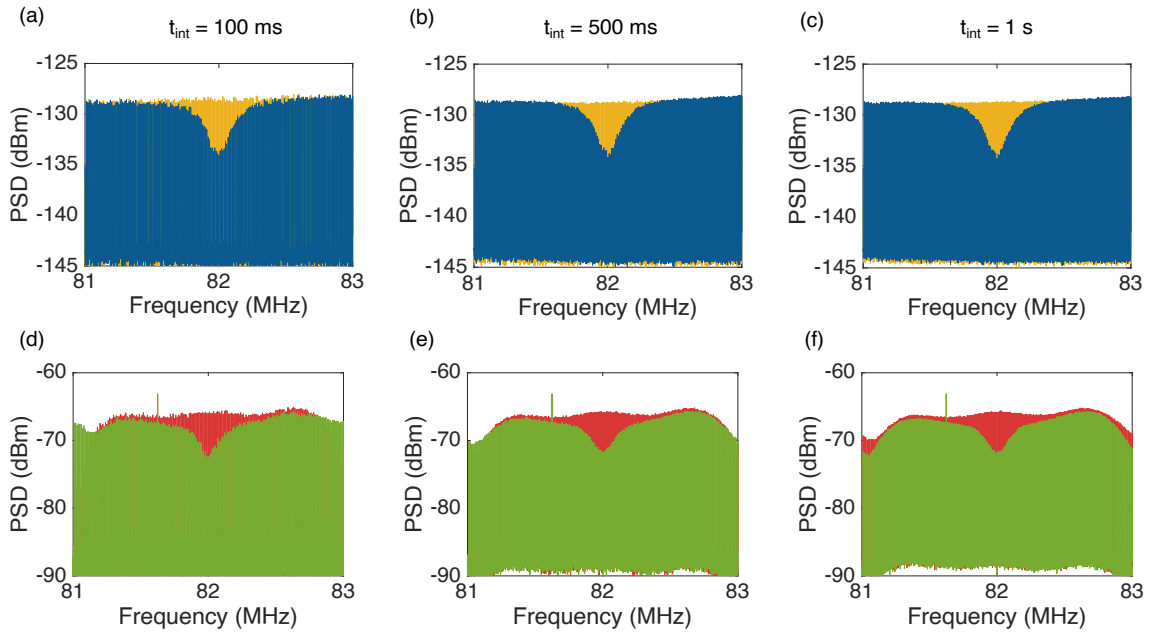

Figure 4.23: Down-converted dual-comb spectra obtained after calculating the fast Fourier transform of the interferogram traces acquired with the oscilloscope (top) and the SDR (bottom). Frequency averaging is performed, resulting in averaging times of 100 ms, 500 ms, and 1 s.

The spectra recorded with the SDR present a spurious tone, which in addition exhibits a higher power than the comb tones. A closer look to the recorded spectra, provided in Fig. 4.24, allows to identify the frequency of such undesired tone: 81.625 MHz.

The spurious tone does not overlap with any comb teeth. Therefore, it will be filtered in the post-processing peak detection routine and its presence will not affect the results. In terms of the SNR of the acquired signals, by observing Fig. 4.24 it is evident that the SDR signal exhibits higher power and a slightly better SNR. This difference is attributed to the two amplification stages in the radio platform. Consequently, the signal power received by the radio can be increased depending on the gain of these amplifiers, which can be adjusted using the Simulink user interface. In this case, the gain of both amplifiers is set to a value of 20 dB, ensuring good conditioning of the detected signal. Saturation is observed when the gain is increased to 40 dB.

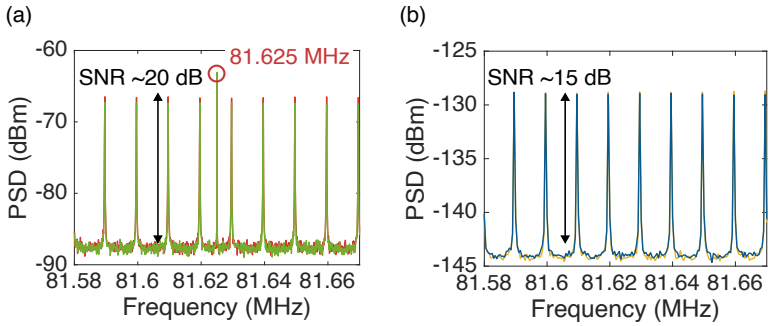

Figure 4.24: Dual-comb spectra obtained with (a) the SDR platform and (b) the oscilloscope showing a reduced span of 90 kHz.

Finally, regarding the frequency resolution of the measurements, the acquisition of 2-ms-length traces at 200 MSa/s performed with the oscilloscope corresponds to a frequency step in the transformed domain of 500 Hz, resulting in 20 spectral points between two down-converted dual-comb teeth. For the SDR acquisition, a frequency step as low as 100 Hz is obtained. In both cases, the frequency step, which can be interpreted as the resolution bandwidth of the retrieved spectra, fully guarantees the proper characterization of the individual dual-comb spectral lines.

Absorption spectroscopy results: performance comparative of low-cost and high-end digitizers

The absorption line of the HCN gas cell centered around 1549.73 nm is chosen again for these experiments. The same fiber-coupled gas cell containing $^{13}H^{14}CN$ with a pressure of 25 Torr and an absorption path length of 16.5 cm, already presented in the previous section, is used. The line profile is extracted following the post-processing procedure detailed in Section 4.3.2. The transmission profiles retrieved for integration times of 100 ms, 500 ms and 1 s are presented in Fig. 4.25. They are the result of normalizing the previously shown frequency-averaged measurement spectra with their corresponding reference counterparts. The profiles shown in the top half of the figure are obtained after post-processing the oscilloscope interferograms. The profiles included in the bottom part of the figure are obtained from post-processing the SDR IQ traces. Each panel includes the experimental profile (represented with dots), a Voigt profile fitted to the measured profile (represented with solid lines), and the residuals from the fitting process

(indicated by black dots). The analyzed and fitted span corresponds to a bandwidth of 15 GHz around the minimum of transmission, which is centered in 0 Hz for convenience. A clear reduction of the noise and the uncertainty in the measurement is produced as a consequence of the averaging process. This noise reduction is translated in the progressively decreasing standard deviation of the residuals, σ_{res}.

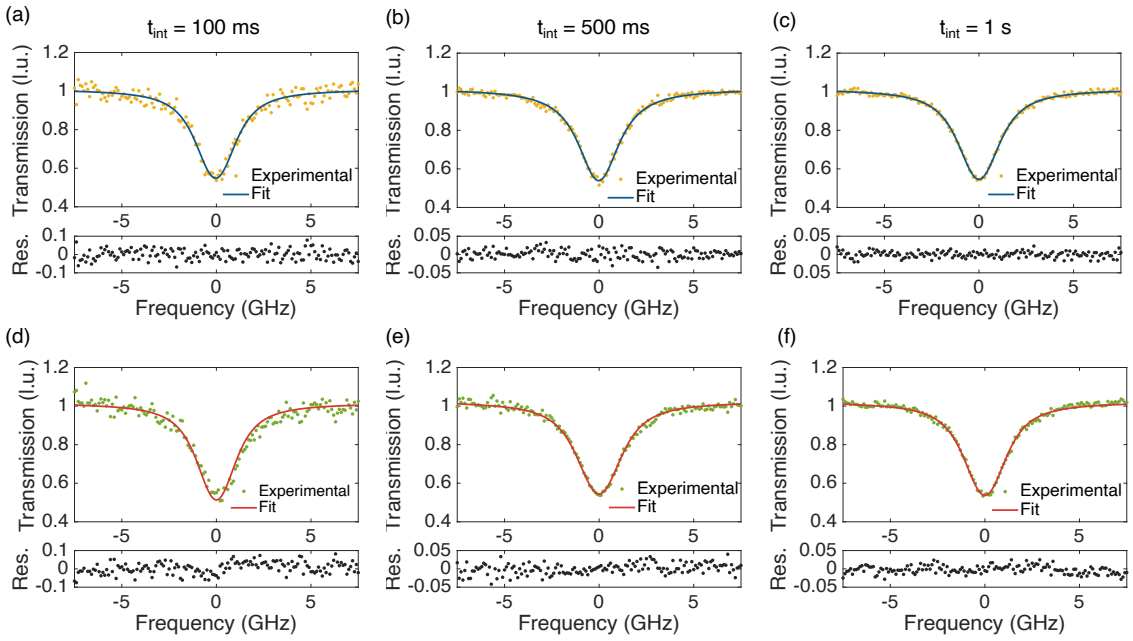

Figure 4.25: Transmission profile of the HCN absorption line centered at 1549.73 nm retrieved from post-processing the data samples digitized with a real-time oscilloscope (top panel) and a RTL-SDR device (bottom panel) at three integration times.

The minimum transmission value and the width of the absorption line, both extracted from the fitted data, along with the standard deviation of the residuals obtained with the two employed digitizers for t_{int}= 100 ms, t_{int}= 500 ms, and t_{int}= 1 s are indicated in Table 4.3.

	$\mathbf{t_{int}}$**= 100 ms**	$\mathbf{t_{int}}$**= 500 ms**	$\mathbf{t_{int}}$**= 1 s**
T_{osc}	0.548	0.538	0.545
T_{SDR}	0.513	0.544	0.536
$FWHM_{osc}$	2.1 GHz	2.2 GHz	2.1 GHz
$FWHM_{SDR}$	2.2 GHz	2.2 GHz	2.2 GHz
$\sigma_{res\ osc}$	0.027	0.012	0.011
$\sigma_{res\ SDR}$	0.034	0.015	0.016

Table 4.3: Parameters extracted from the characterization of the 1549.73 nm absorption line of HCN obtained for three different integration times and using both a real-time oscilloscope and an SDR platform as digitization instruments.

For the longest integration time of 1 second, the transmission obtained with the oscilloscope is 0.545 (absorption depth of 2.62 dB), with a standard deviation of the residuals of 0.011. This value, considering the mentioned σ_{res}, is in good agreement with the value reported by the NIST for this line (T= 0.5592). On the other hand, the transmission obtained with the SDR for this integration time is 0.536, having a greater deviation of 0.016 %, but also very close to the expected value.

Finally, the attainable signal-to-noise ratio of the described dual-comb spectrometer is analyzed. For this purpose, the evolution of the figure of merit defined by the product of the SNR and the number of comb lines with the integration time is studied. As it was performed in the previous section, the SNR is calculated as the inverse of σ_{res}. The number of lines considered for the calculations is M= 200. Although the down-converted dual-comb spectrum exhibits a higher number of lines, only the tones within the detection bandwidth of the software defined radio are considered.

Considering the basic scaling law of the SNR with integration time or the number of averages, an increase of the figure of merit with the square root of the integration time is expected (SNR $\times$ M $\approx \sqrt{t_{int}}$). The evolution of this figure of merit with averaging is illustrated in Fig. 4.26. The dashed lines represent the theoretical trend in each case. For the oscilloscope, a linear increase of the SNR is observed up to a measurement time of 500 ms. After this point, the function shows a saturation trend. Similarly, the measurements performed with the radio show a linear behavior up to 500 ms. However, a slightly lower performance in terms of SNR is achieved in this case.

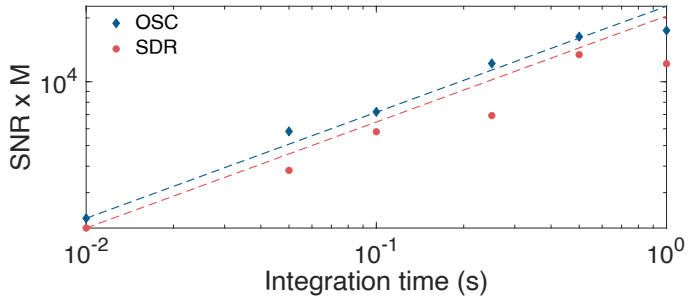

Figure 4.26: Evolution of the signal-to-noise ratio of the system with integration time, evaluated for the two digitization systems: oscilloscope (blue traces) and SDR (red traces).

At an integration time of 1 s, and considering 200 comb lines, the values of the figure of merit for the oscilloscope and the SDR are $1.7{\cdot}10^4$ and $1.2{\cdot}10^4$, respectively. Considering the 10-dB bandwidth of the down-converted comb, which is around 6.35 MHz, the number of lines increases to 635. In this case, the new values of SNR $\times$ M are $5.4{\cdot}10^4$ and $3.8{\cdot}10^4$. The achieved SNR per comb line at 1 s is 85 for the oscilloscope and 60 for the SDR. Both indicators demonstrate a good degree of mutual coherence at 1 s.

4.4.4 Analysis of symmetric and asymmetric configurations

In addition to the implementation of a symmetric dual-comb arrangement, the accuracy of the results obtained when employing an asymmetric dual-comb architecture is explored. For this purpose, different asymmetric configurations are analyzed:

1. An asymmetric configuration with the gas cell measured in transmission.
2. An asymmetric setup with the gas cell configured in reflection. In this case, different attenuation factors are introduced in order to emulate an open-air approach.

The experimental setup built for this purpose is presented in Fig. 4.27. The driving conditions of the lasers are those indicated in Table 4.2. Since an asymmetric configuration is used, one of the combs (designated OFC1) interrogates the gas cell. This comb is sampled by a local oscillator comb (denoted OFC2). When a transmission configuration is used, the device under test is the fiber-coupled gas cell. On the other hand, for the gas cell to be measured in reflection configuration, an optical circulator is used. The sample is connected to port 2 of the circulator. The optical field at this port, which can be attenuated by a variable attenuation factor, passes through the sample and is reflected back to the circulator by a fiber retroreflector. When a reflection configuration is used, the optical field scans the sample twice. Therefore, this factor of two must be taken into account when obtaining the transmission profile. Finally, the electrical interferogram traces are digitized only with the real-time oscilloscope.

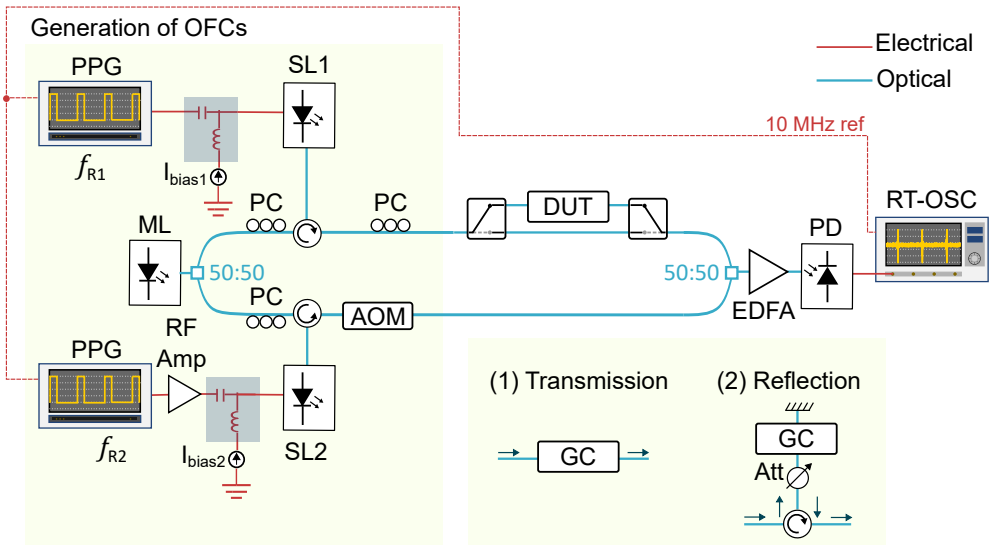

Figure 4.27: Dual-comb spectroscopy setup implemented in asymmetric configuration, in which only OFC1 interrogates the device under test (DUT). The DUT, which is a gas cell, is measured either (1) in transmission or (2) in reflection configuration. The acronyms have been defined in Fig. 4.20.

The transmission profiles obtained from each scenario, for an integration time of 1 second, are shown in Fig. 4.28. The minimum transmittance values obtained from the fitted profile when the gas cell is measured in (a) transmission and (b) reflection configurations

are T= 0.53 and T= 0.55, respectively. These values are in good agreement with the NIST value. The transmission profiles obtained when the gas cell is measured in reflection configuration with attenuation factors of (c) 6 dB and (d) 10 dB show minimum transmittances of T= 0.52 and T= 0.51, respectively. These values exhibit a larger deviation from the NIST value for this absorption line (T= 0.5592) of approximately 6% and 9%, respectively. Nevertheless, the fit shows systematic errors in the region around the absorption maximum in both cases. If the transmission minimum provided by the experimental data is considered instead of that given by the fitted profile, the minimum transmission values, which are T= 0.55 and T= 0.54, respectively, show a better agreement with the value reported by NIST.

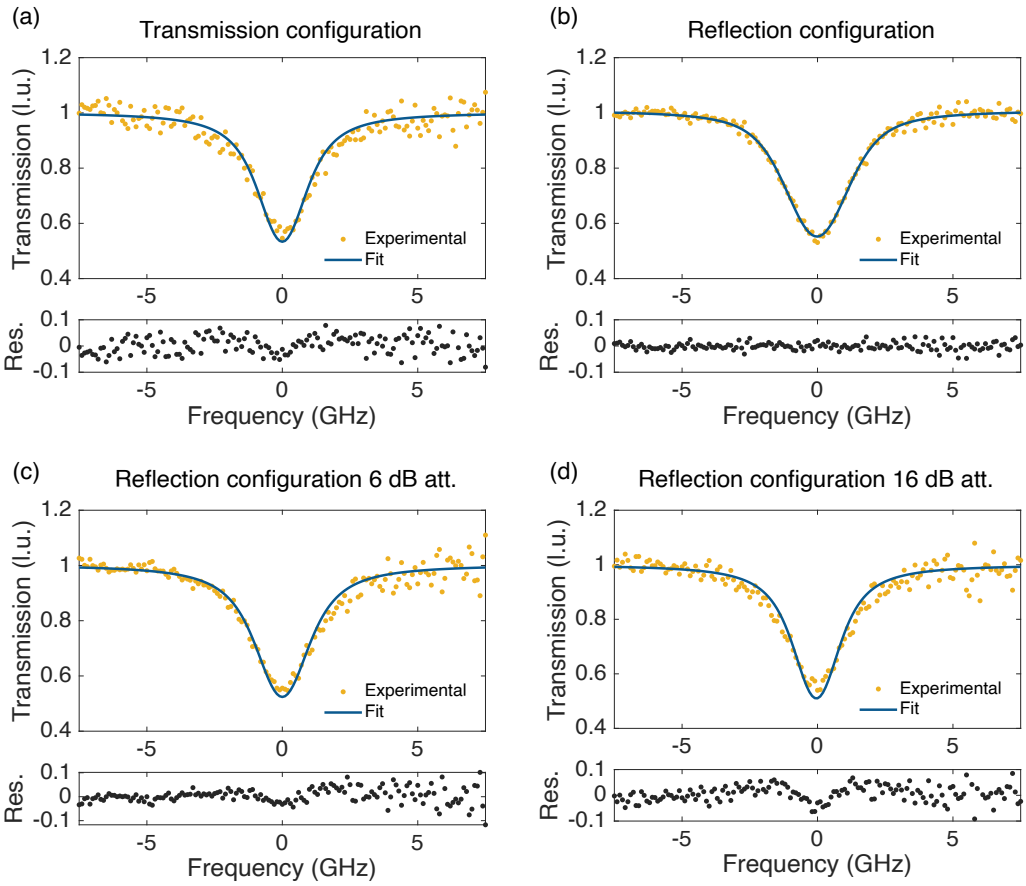

Figure 4.28: Absorption line of HCN cell measured using a dual-comb setup in asymmetric configuration with the gas cell configured in (a) transmission, (b) reflection, (c) reflection with a 6 dB of attenuation, and (d) reflection configuration with an attenuation factor of 16 dB.

Finally, the SNR analysis in terms of the standard deviation of the residuals is performed. The SNR values obtained for different integration times are compared to those obtained with the dual-comb setup in symmetric configuration. The results of this analysis, considering M= 200 comb lines to maintain consistency with the values obtained in the previous section, are shown in Fig. 4.29. It can be observed that the system performance improves for longer integration times up to saturation at 500 ms.

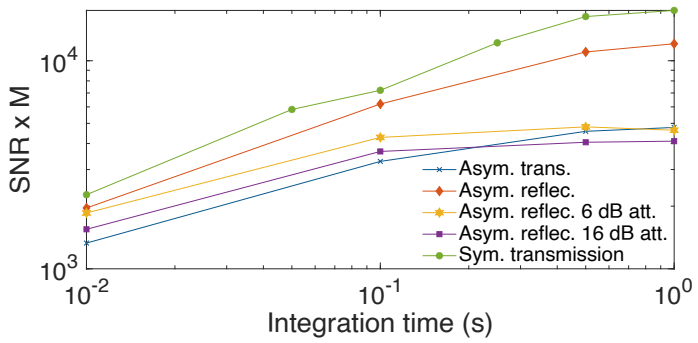

Figure 4.29: SNR performance achieved for different averaging values and different dual-comb architectures evaluated in terms of the product SNR × M versus integration time. The number of comb lines considered for the study is M= 200.

The symmetric configuration provides the highest signal-to-noise ratio, achieving a SNR × M at 1 s of $1.7{\cdot}10^4$. A similar performance is obtained from the asymmetric-reflection configuration, which reaches a value of SNR × M at 1 s of $1.2{\cdot}10^4$. In the symmetric configuration both OFCs interrogate the sample, and in the asymmetric reflective arrangement a single comb interrogates the sample twice. In both cases a deeper absorption feature is encoded in the combs if compared to a single interrogation of the gas cell, which leads to the determination of the gas profile with a better noise performance. The asymmetric-transmission and asymmetric-reflection configurations with the probe OFC being attenuated result in lower SNR values. Nonetheless, the transmission profile has been successfully retrieved under all the shown conditions, and higher attenuation factors could be accommodated by the system.

4.5 Conclusions

In this chapter, the realization of absorption spectroscopy measurements using a dual-comb architecture based on two GS OFCs featuring a fine spectral resolution of 100 MHz has been demonstrated. This spectral resolution has been achieved through the use of pulsed gain-switching signals. In addition, the cost-efficiency of these systems has been improved by means of the use of affordable digitization devices in the receiver side of the spectrometer.

The significance of these results lies in the improved resolution of dual-comb spectroscopy measurements compared to existing demonstrations using GS laser diodes modulated with sinusoidal signals. The use of sinusoidal signals to modulate the lasers limits the generation of low-repetition-rate OFCs with good spectral characteristics for the realization of spectroscopy. By sinusoidally modulating the lasers, the achievable combs are limited to the frequency range of the relaxation oscillations of the employed lasers, which is in the order of a few GHz. These repetition frequencies, however, are usually high for the resolution requirements of most spectroscopic measurements. The dual-comb system presented here, in which the sinusoidal modulation signals are replaced by trains of short electrical pulses, constitutes a solution to this limitation since it opens the

possibility of implementing dual-comb spectroscopy with GS laser diodes at repetition rates below 1 GHz. The system is capable of generating a flat-topped RF dual-comb, with a tunable bandwidth up to 100 GHz. The dual-comb system introduced in this chapter enables the acquisition of spectroscopy measurements requiring fine resolutions and permits the measurement of narrow absorption lines with widths of a few GHz keeping advantages such compactness, robustness, easy and simple implementation, low cost, and suitability for photonic integration.

- Characterization of 100-MHz gain-switched combs

In the first section of this chapter, an experimental characterization of GS combs with pulsed modulation and a comb repetition rate of 100 MHz has been performed. The increase in the width of the generated combs when increasing the amplitude of the pulsed signal has been demonstrated under fixed detuning and pulse width conditions, and with an optimized DC current for each AC voltage value. This behavior is identical to that reported for high-frequency modulation using sinusoidal signals. The increase of the spectral width with the modulation amplitude is attributed to the increasing dynamic chirp as a result of the abrupt modulation of the laser. In the analyzed driving conditions, a good performance in terms of carrier-to-noise ratio has been demonstrated. The evolution of the spectral width with the variation of the detuning between the emission frequency of the master laser and the slave laser has been experimentally studied, showing the increase of the 10-dB bandwidth with the detuning. In conditions of low detuning, the better locking conditions allowed for the reduction of the noise and the chirp, which resulted in OFCs exhibiting higher values of carrier-to-noise ratio and lower spectral widths. This experimental demonstration serves as a useful guide for selecting the driving conditions best suited to achieve the desired comb characteristics for the selected application.

- Gas spectroscopy of hydrogen cyanide

In this section, a dual-comb system that combines pulsed gain switching and optical injection to perform spectroscopy measurements with a spectral resolution of 100 MHz has been experimentally demonstrated. The system is capable of producing two mutually-coherent combs with 350 spectral lines within 10 dB, covering an optical bandwidth of 35 GHz. The compression factor of the system has been set to 10^3, so RF bandwidths of only tens of megahertz are involved. The efficient frequency down-conversion into the RF domain permitted to measure the optical bandwidth with a slow-speed digitizer, as is inherent in dual-comb systems.

The system has been tested through the realization of absorption spectroscopy measurements of a single spectral line of hydrogen cyanide. The consistency of the measurements has been verified by using two different acquisition instruments: an oscilloscope, which allowed to retrieve the time-domain interferogram signals, and an electrical spectrum analyzer, which allowed for slower measurements and permitted to directly obtain the power spectral density of the temporal interference signals. The retrieved transmission lines, at different integration times and using the two digitizers, showed good agreement with the values reported in the literature. The narrow linewidth of the measured line,

which is around 2 GHz, verified the capability of performing fine resolution measurements with our system. In addition, the SNR performance of the system has been analyzed. For an integration time of 1 second and using the oscilloscope, the figure of merit defined by the product SNR×M, where M is the number of lines used to detect the absorption feature, reached a value of $1.1{\cdot}10^5$. This value is comparable to SNR values reported for other dual-comb systems ($2{\cdot}10^4$ in [148] using two mutually-coherent electro-optic OFCs, $2{\cdot}10^5$ in [159] using two acousto-optic OFCs). The measured SNR showed the expected evolution with the averaging time up to hundreds of milliseconds for the oscilloscope and up to tens of seconds in the case of the electrical spectrum analyzer, with a trend towards saturation for longer measurement times. This saturation trend is attributed to systematic errors in post-processing. The good degree of mutual coherence of the system has been achieved without employing stabilization controls nor post-correction algorithms. The mutual coherence time could be extended by improving the stabilization of the system or by using a master laser exhibiting a lower linewidth.

- Towards low-cost gain-switched dual-comb spectrometers

In the final section of this chapter, a solution to reduce the cost of dual-comb spectrometers has been proposed. This solution involves using a software-defined radio receiver for the digitization of the interferogram traces. The use of these radio platforms is demonstrated for the first time in this thesis for dual-comb spectroscopy measurements. A dual-comb setup involving gain-switched combs with a spectral resolution of 100 MHz has been employed to measure a hydrogen cyanide absorption line. The transmission results obtained using both a real-time oscilloscope and the SDR receiver as digitizers demonstrate the feasibility of using radio platforms for these types of measurements.

One of the most basic radio receivers in the market (whose cost is around $20) with a maximum bandwidth of 3.2 MHz has been used. Despite the low bandwidth of the receiver, dual-comb down-conversion process together with the use of a high compression factor of 10^4 allowed for the compression of the absorption information comprised in an optical bandwidth of 20 GHz into an electrical span of 2 MHz. The reported results represent a significant advancement in the search for cost-efficient dual-comb systems. The combination of inexpensive comb sources such as laser diodes, and the utilization of affordable electronics at both the transmitting (through the use of step recovery diodes and digital synthesizers) and receiving ends (by means of software defined radios) contribute to the development of dual-comb gas sensing systems based on affordable technology, without compromising the reliability and validity of the measurements.

Chapter 5

Improving the resolution of gain-switched dual-comb spectrometers

This chapter is devoted to the experimental generation of gain-switched optical frequency combs with ultra-low line spacings of a few megahertz or less. Reducing the repetition rate of the comb sources in a dual-comb absorption spectroscopy system affects its spectral resolution, resulting in a sensing system capable of measuring narrower features. In other dual-comb systems, such as those dedicated to measuring distances, a reduced repetition rate increases the maximum measurable distance without ambiguity. Therefore, the generation of low-repetition-rate gain-switched combs expands the application range of gain-switched dual-comb architectures.

Firstly, a technique for decreasing the repetition rate based on pulsed gain switching is proposed. By means of using trains of pulses with low repetition rates, gain-switched combs with line spacings down to 2.5 MHz are experimentally demonstrated. However, this approach compromises the average optical power of the resulting combs. A balance between low repetition rate and average optical power is achieved with the densification of the two gain-switched combs using two external phase modulators. Following this approach, a dual-comb spectrometer capable of retrieving a spectral feature of about 360 MHz is demonstrated.

5.1 Introduction

The generation of high-quality GS OFCs with repetition rates on the order of a hundred MHz was enabled by the use of pulsed electrical signals to switch the lasers. This brought the possibility of using GS laser diodes as comb sources for dual-comb spectroscopy applications where spectral lines with linewidths of a few GHz needed to be resolved. These combs, which exhibit flat and sufficiently broad spectra to measure a single spectral feature, were proved highly beneficial for dual-comb spectroscopy in the previous chapter.

One of the main advantages of gain-switched dual-comb systems, besides their semiconductor nature, is their ability to easily change the repetition rate of the two involved combs and hence the spectral resolution of the spectrometer. Gain-switched dual-comb spectrometers represent versatile systems that permit the resolution of the spectroscopic system to be adapted to the spectral resolution requirements of the interrogated sample. This tunability can be achieved within the tuning range of the repetition rate of GS combs, which typically spans from tens of GHz to a hundred MHz. Achieving lower repetition rates, in the order of a few megahertz or below, would enable gain-switched dual-comb systems to access high-resolution applications.

In this chapter, several strategies for decreasing the repetition rate of GS combs, or in other words, for increasing the spectral resolution of dual-comb arrangements, are explored and discussed. The first explored technique represents the most straightforward approach for generating low-repetition-rate GS OFCs. It relies on decreasing the frequency of the train of pulses used to modulate the laser diode acting as the slave laser. This method, based on the intensity modulation of the laser, results in frequency combs with low average optical power due to the reduction of the duty cycle of the optical signal as the repetition rate decreases. To address this, strategies involving gain switching the laser diodes with pulsed excitation signals comprising more than one pulse per period –i.e., multi-pulse approaches –have also been explored in the course of this thesis. While these approaches can alleviate the low average power issue, they result in combs with poor spectral flatness and require further investigation. These multi-pulsed strategies are included in an appendix to this chapter (please, refer to Appendix A).

A balance between average optical power and good spectral characteristics can be achieved through densification techniques. The densification of an OFC allows to reduce the comb line spacing, as additional spectral lines to those already existing in the comb are generated. The use of electro-optic phase modulators (EOPMs) for this purpose enables the creation of new spectral lines without power loss. Since the phase of the optical pulses is modulated rather than their intensity, the optical power of the non-densified OFC is redistributed among the new generated components. This strategy was first introduced for electro-optic combs [160]. In their work, N. B. Hébert et al. densified an electro-optic frequency comb using an EOPM driven by a PRBS. The original electro-optic comb repetition rate of 100 MHz was reduced down to 787 kHz. They beat the densified comb with a non-densified electro-optic OFC to perform dual-comb spectroscopy measurements in quasi-integer ratio mode, a technique that enhances the acquisition speed at the expense of a greater post-processing complexity.

The densification of a gain-switched OFC was first demonstrated by P. Lakshmijayasimha and coauthors [51]. The authors reported the densification of a GS comb featuring a repetition rate of 6.25 GHz by means of external phase modulation. The EOPM was driven by a sinusoidal signal with a frequency corresponding to a sub-harmonic of the comb repetition rate. This strategy resulted in the densification of the GS comb by a factor of 16, i.e., the repetition rate of the non-densified comb was lowered down to 390 MHz. However, the use of sinusoidal signals to drive the EOPM limited the densification factor, as well as the spectral flatness of the densified comb. These limitations arise from the evolution of the amplitudes of the comb lines created by phase modulation with an EOPM, which follow the Bessel functions of the first kind. On the other hand, the use of a pseudorandom binary sequence instead of a sinusoidal signal to modulate the EOPM allows to obtain a highly densified gain-switched combs while preserving their spectral flatness, as was recently demonstrated by A. Rosado et al. [161]. In their work they densified a single GS OFC, which originally featured a line spacing of 1 GHz, down to a comb spacing of 488 kHz. With a densification factor as high as 2044, they experimentally obtained a comb exhibiting 180000 spectral lines within an optical bandwidth at 10 dB of 90 GHz. In addition, the authors carried out a numerical analysis to study the dependence of the spectral flatness of the densified comb with the amplitude of the binary sequence used to drive the phase modulator, and showed that the optimum value (the value in which the flatness reaches the highest value) is obtained when this amplitude is very close to the half-wave voltage of the modulator.

The second section of this chapter is devoted to the implementation of a dual-comb spectrometer based on two densified GS OFCs. The validity of the system is demonstrated by the successful retrieval of the reflection profile of a Fabry-Pérot filter, which features a nominal transition profile of 363.2 MHz. In addition to the experimental realizations, a description of the fundamentals of the phase modulation of optical pulses by a pseudorandom binary sequence is included, providing intuitive insights into the spectral characteristics of the densified combs. These results, included in the third publication of this thesis [162], open up the possibility of using GS dual-comb systems for high-resolution applications with a simple, cost-effective, and integrable perspective.

5.2 Gain-switched combs with repetition rates below 100 MHz

This section discusses the extension of the repetition rate of GS combs down to a few MHz, which is achieved by decreasing the frequency of the pulsed electrical excitation signal. The generation of OFCs with a line spacing as low as 2.5 MHz is demonstrated. However, gain switching the laser diode using trains of pulses with low duty cycles results in combs with low average optical power and significant power differences between the optical injection tone and the surrounding comb tones. As a complementary approach, the search for more power-efficient methods based on the use of multi-pulsed electrical sequences to generate GS combs is explored in Appendix A.

Two comb spectral characterization techniques are carried out in this section: a technique based on the direct measurement of the comb spectrum using an optical spectrum analyzer, and a self-heterodyne approach, which enables for the indirect measurement of the optical spectrum through the electrical spectrum.

5.2.1 Experimental setup

The experimental setup used for the generation and characterization of low-repetition-rate combs obtained by pulsed gain switching of laser diodes is illustrated in Fig. 5.1. The comb generation side is identical to that presented in the previous chapter. It is based on the classical master-slave configuration, with the slave laser being gain-switched by a train of short electrical pulses at a chosen repetition rate. Different pulsed gain-switching signals are explored, all of them provided by a 12.5 Gb/s pulse pattern generator (PPG).

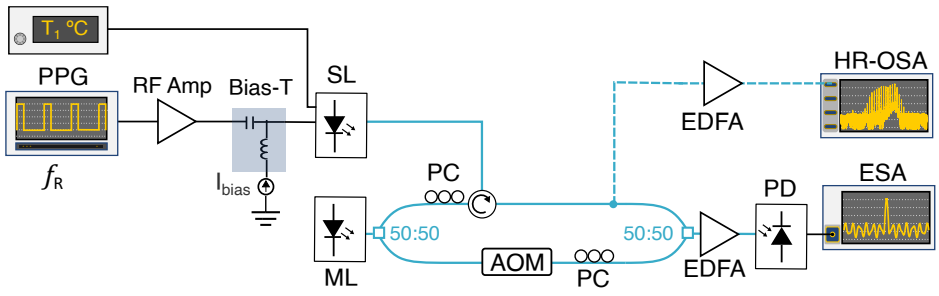

Figure 5.1: Experimental setup used for the generation and measurement of low-repetition-rate GS OFCs under pulsed electrical excitation based on heterodyne detection. PPG: pulse pattern generator, RF Amp: RF amplifier, SL: slave laser, ML: master laser, PC: polarization controller, EDFA: erbium-doped fiber amplifier, ESA: electrical spectrum analyzer, HR-OSA: high-resolution optical spectrum analyzer.

The optical spectra of the generated combs are measured using a high-resolution optical spectrum analyzer (Aragon Photonics BOSA 400 C+L). However, for combs with a repetition rate below the resolution of this analyzer (10 MHz), an alternative measurement technique is required. To measure OFCs with repetition rates equal to or less than 10 MHz, a heterodyne setup is employed. This heterodyne setup relies on detecting the beating of the optically-injected comb with a frequency-shifted version of the injected field. At the output of the photodetector, the electrical spectrum corresponding to the down-converted optical spectrum is obtained. The power spectral density of the electrical spectrum is measured using an electrical spectrum analyzer. The frequency shifter, which provides a shift of f_{shift}= 80 MHz, ensures the measurement of the RF spectrum without overlapped beat notes. In contrast, if a frequency shift were not employed, the common frequency of the two signals traversing the two interferometer branches, namely the frequency of the optical injection, would be located in the RF spectrum at 0 Hz. Consequently, the tones with an optical frequency below the injection frequency would correspond to down-converted "negative" frequencies, which in the spectrum analyzer measurement would be reflected to "positive" frequencies. This folding process would result in the overlapping of spectral lines. The use of a frequency shifter, together with a convenient choice of repetition rate, avoids these issues.

The slave laser is a discrete-mode laser (Eblana EP1550-0-DM-H19-FM) with a central wavelength around 1550 nm, specifically enabled for high-speed modulation. The master laser is a tunable laser with a tunability range across the C-band (Pure Photonics PPCL300). To measure the combs, two EDFAs are used, each one placed at the input of a measurement instrument (high-resolution optical spectrum analyzer and electrical spectrum analyzer). These amplifiers compensate for the average power reduction experienced by the combs when their line spacing is decreased. For the detector, a wide-bandwidth photodetector (New Focus 1014) with a bandwidth of 44 GHz is selected for the measurements.

A 100-MHz GS OFC measured through the two described characterization techniques, using a high-resolution optical spectrum analyzer and self-heterodyne detection, is shown in Fig. 5.2. The figure demonstrates that the heterodyne measurement is capable of reproducing the BOSA measurement up to a detected bandwidth of approximately 20 GHz. Although the bandwidth of the detector is 44 GHz, it exhibits linearity issues above 20 GHz attributed to a lack of calibration of the detector. Consequently, the heterodyne measurements presented in this section will be retrieved from a reduced span of 10 GHz. This span is sufficiently broad to analyze the presence of resolved tones in the generated combs.

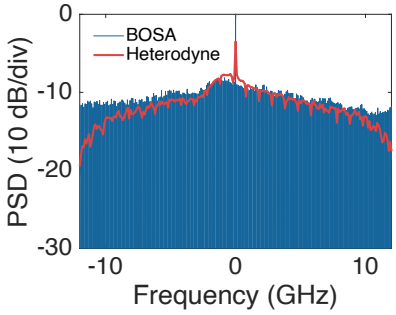

Figure 5.2: GS OFC retrieved from BOSA (blue) and self-heterodyne (red) measurements.

5.2.2 Experimental results

For the generation of GS combs with different repetition rates, two conditions are fixed: the ML wavelength, which is set to 1549.73 nm, and the width of the electrical pulses, set to 200 ps. The temperature of the slave laser is optimized in each case to inject the comb in the blue side of its frequency spectrum and ensure locking.

An OFC with a line spacing of 100 MHz serves as the initial configuration. The optical spectrum, measured using a high-resolution optical spectrum analyzer, is displayed in Fig. 5.3 (a). The frequency corresponding to the injection is shifted to 0 Hz for representation and analysis purposes. This comb is generated by driving the laser diode with a current formed by the superposition of a bias current of I_{bias}= 1 mA and a train of pulses showing a peak-to-peak amplitude of V_{RF}= 8 V. The ML power is P_{inj}= 0.1 mW (-10 dBm). The employed gain-switching parameters enable the generation of a broad frequency comb with a 10-dB bandwidth of Δf_{10dB}= 120.6 GHz (1206 optical lines). The comb exhibits a good CNR of 24.5 dB. The zoomed view of the figure reveals a relatively weak locking regime. Under these conditions, injection locking could be improved by either decreasing the detuning between the master and slave lasers or by increasing the injection power. Fig. 5.3 (b) and (c) show the optical spectra obtained when the gain-switching frequency is reduced to 50 MHz and 25 MHz, respectively.

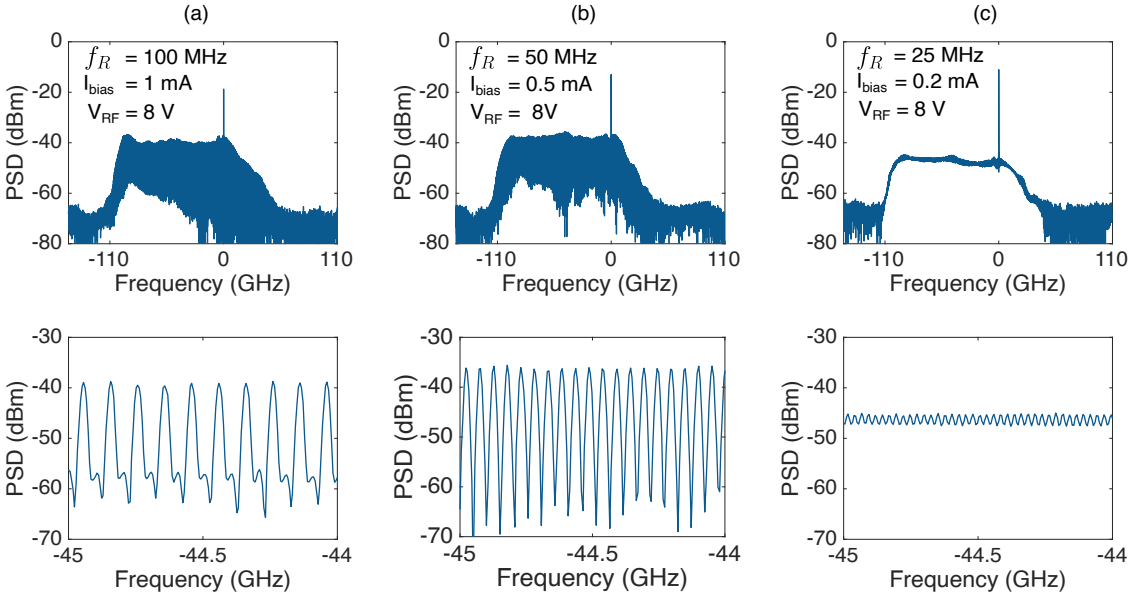

Figure 5.3: OFC spectra obtained by pulsed gain switching of an optically injected laser diode at different repetition rates of (a) 100 MHz, (b) 50 MHz and (c) 25 MHz. The optical spectra are measured with a 10-MHz-resolution optical spectrum analyzer (BOSA). The panels on the lower row provide a closer view of a spectral region spanning 1 GHz.

The amplitude of the electrical pulses is not changed, in order to obtain combs with broad spectral widths. Since V_{RF} is fixed, and so is the duration of the electrical pulses, the bias current needs to be optimized for each repetition rate. A lower repetition rate of the pulse train corresponds to a longer period of the gain-switching signal. During this period, the laser is powered by the superposition of two currents (DC and AC) throughout the pulse duration, and only by the bias current for the remainder of the period. Consequently, as the signal period increases, more current accumulates along the period. To achieve laser driving conditions that enable the emission of an optical pulse without exciting the second peak of the laser relaxation oscillations, and considering a fixed amplitude and duration of the electrical pulses, the bias current needs to be progressively decreased with the repetition frequency. The GS combs with f_R= 50 MHz and f_R= 25 MHz are obtained by configuring the bias current to I_{bias}= 0.5 mA and I_{bias}= 0.2 mA, respectively. For a repetition rate of 25 MHz, the comb tones cannot be resolved with the high-resolution optical spectrum analyzer, since only two sampling points are used to measure each comb line.

Below 25 MHz, the presence of resolved tones cannot be determined by measuring the optical spectrum with the BOSA. Therefore, the characterization of such combs is carried out based on the results obtained from the self-heterodyne approach. A GS OFC showing a repetition rate of 10 MHz measured using the optical spectrum analyzer is included in Fig. 5.4 (a). The driving conditions to obtain this comb are I_{bias}= 0 mA, V_{RF}= 8 V, and τ_{pulse}= 200 ps. The ML power is increased to P_{inj}= 0.5 mW (-3 dBm). The results obtained from the self-heterodyne detection scheme are shown in Fig. 5.4 (b). This graph depicts a span of 500 MHz of the electrical spectrum, measured with the electrical spectrum analyzer. In order to avoid overlapping of the harmonics, the repetition rate of the comb is slightly modified to 11 MHz, ensuring that there is not a significant change in the spectrum compared to that obtained for f_R= 10 MHz.

A total bandwidth of 5 GHz is measured with the electrical spectrum analyzer in sequential steps of 50 MHz. Each portion of the spectrum of 50 MHz is measured using the maximum number of points enabled by the instrument (8192 samples) and using a resolution bandwidth of 5 kHz. These settings allow to retrieve the comb lines with sufficient resolution. The measured electrical spectrum contains both direct detection and beating terms, since balanced photodetection is not used. A detail of a portion of the electrical spectrum, from 60 MHz to 100 MHz, is shown in panel (c). The comb tone corresponding to the injection wavelength appears at f_{shift}= 80 MHz. The direct detection lines are located at multiples of the repetition rate, which in the figure correspond to frequencies of 66 MHz, 77 MHz, 88 MHz, and 99 MHz. The beat notes are located at frequencies $f_{beat} = |f_{shift} \pm nf_R|$, where the absolute value accounts for the folding of negative frequency components to positive ones. The beat notes that arise from optical frequencies above the injection frequency correspond to the tones indicated as "positive" beats, centered in 69 MHz, 80 MHz, and 91 MHz. The tones with frequencies of 63 MHz, 74 MHz, 85 MHz, and 96 MHz correspond to folded beat notes ($f_{shift} - nf_R$, with n being 13, 14, 15, and 16, respectively). The electrical spectrum demonstrates the generation of coherent comb lines with good CNR.

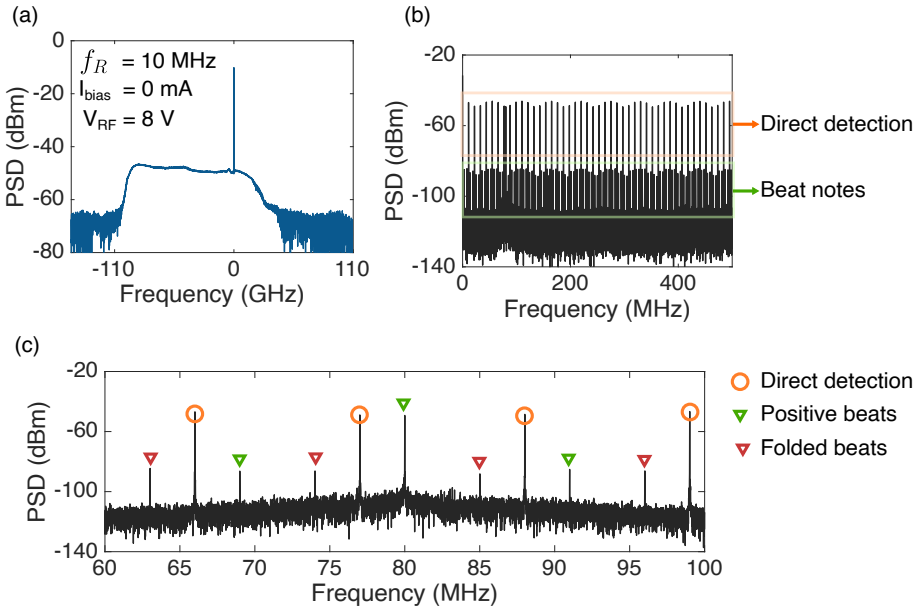

Figure 5.4: (a) Optical spectrum of a GS comb obtained with f_R= 10 MHz measured with the BOSA. (b) Electrical spectrum of the same OFC (f_R modified to 11 MHz), retrieved from self-heterodyne measurements. Unbalanced photodetection is used; therefore, the electrical spectrum includes the contributions from both direct detection and beat terms. (c) Detail of a 40-MHz region around f_{shift} specifying the origin of the detected tones.

The reconstruction of the electrical spectrum based on the reorganization of the detected beat notes is shown in Fig. 5.5. This reconstruction is performed using a home-built MATLAB code, which sweeps the retrieved electrical spectrum and locates and stores the power and frequency values of the beat notes located at both sides of the injection frequency. Panel (a) illustrates the measured 5-GHz span which, after the reconstruction process, consists in a total bandwidth of 10 GHz around the injection frequency. The injection frequency is translated to 0 Hz for convenience. A detailed view of a 400-MHz span is also shown, revealing an additional modulation with a frequency of 55 MHz. This modulation is attributed to the selected acquisition parameters. The reconstructed bandwidth is superimposed to the optical spectrum measured with the BOSA (see panel (b)), showing good agreement between both measurements. The two power spectral densities are normalized for comparison purposes.

Finally, the optical spectra acquired from the BOSA measurements and the reconstructed spectra corresponding to GS combs generated at repetition rates of f_R= 5 MHz and f_R= 2.5 MHz are shown in Fig. 5.6 (a) and (b), respectively. For both frequencies, the bias current is set to the minimum one, i.e. 0 mA, and the ML power is set to 0.5 mW. The comb at 2.5 MHz constitutes the GS OFC with the lowest reported repetition rate. It features a bandwidth at 10 dB of 102 GHz, corresponding to 41000 comb lines evenly spaced f_R. The duty cycle of the emitted optical signal is very low (around 0.01%, considering optical pulses with a FWHM of 40 ps). As a consequence, the average optical power is also low and so is the power per comb line, which is obtained by dividing the average power among the 41000 comb lines.

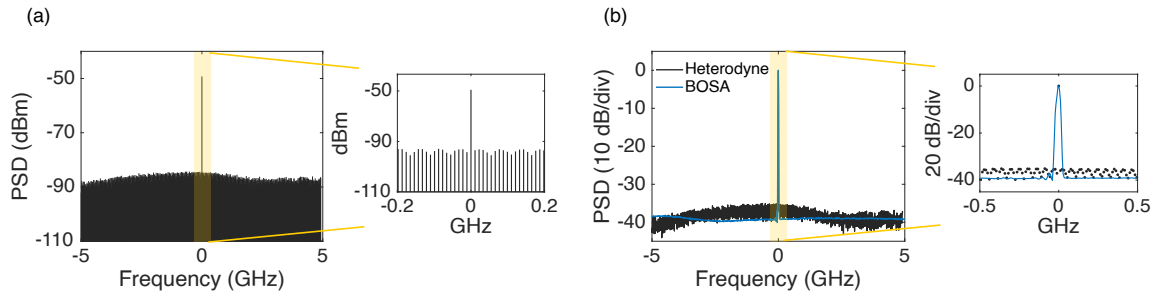

Figure 5.5: (a) Optical spectrum reconstructed from the self-heterodyne measurements and (b) comparison of the BOSA measurement and the reconstructed spectrum. The results corresponds to a gain-switching frequency of 11 MHz.

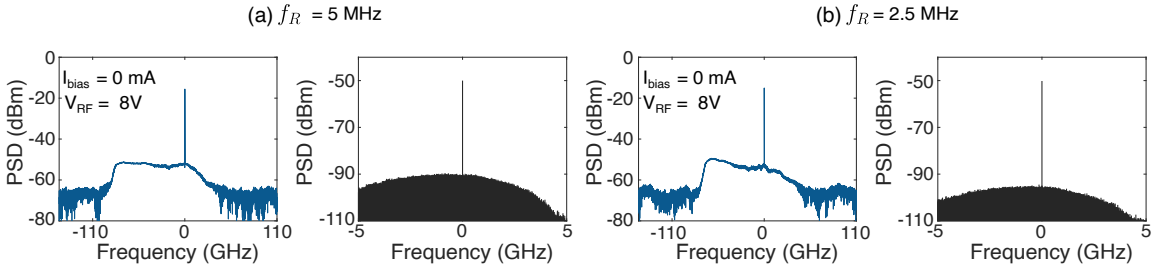

Figure 5.6: Optical spectra measured with the BOSA (blue plots) and reconstructed spectra from the electrical measurements (black) obtained for two repetition rates of (a) 5 MHz and (b) 2.5 MHz.

The obtained combs, especially those operating at frequencies below 50 MHz, reveal the power compromise inherent in using pulsed excitation signals with low duty cycles. Along with the low average power of the combs, a large power difference between the injection line and the rest of the spectral tones is observed.

The combs presented include an amplification stage, and the current of the EDFA is conveniently configured in each scenario to obtain an average optical power of 1 mW at its output. This ensures the generation of comb spectra with comb line powers above the noise level of the measurement instrument, making them useful for dual-comb interferometry applications. However, as a consequence of amplification, the peak power can saturate the detectors used, imposing certain limitations when deploying such dual-comb systems. If optical amplification were used but the optical injection were filtered out, the limit would be set by the peak power of the amplified optical pulses. Considering this, the power limitations of these combs lead to the search for alternative methods capable of producing GS frequency combs with low line spacings and adequate average power levels.

5.3 Densification of gain-switched combs

In the quest for GS combs with a line spacing in the few MHz or sub-MHz range that exhibit neither degradation of average optical power nor of the spectral flatness, the technique of comb densification comes into play. This technique, recently demonstrated for the generation of GS OFCs with repetition rates as low as 488 kHz [161], is validated here to perform high-resolution dual-comb spectroscopy using two densified gain-switched combs.

High densification of GS OFCs is achieved by means of the external phase modulation of the combs, using maximum length sequences (MLSs) as the driving signals for the phase modulators. In addition, the use of these sequences allows for the optimization of the spectral flatness of the resulting combs, as discussed in the subsequent section.

5.3.1 Fundamentals of comb densification

The external phase modulation of an OFC results in the generation of new spectral components in the comb spectrum. This technique is referred to as densification, since a denser OFC featuring a higher number of spectral lines is obtained after this process. Moreover, it is a lossless method (except for the insertion losses introduced by each phase modulator), and the optical power of the non-densified comb is redistributed among the total number of lines obtained after densification. In this section, an analytical and numerical description of the densification of a comb is presented. The densification is performed by means of the phase modulation of an OFC using an MLS to drive the EOPM. These sequences, are a type of PRBS and have unique properties in terms of their autocorrelation and their spectral flatness. The power spectral density of the resulting spectrum reveals why the use of this type of sequence allows to obtain highly densified and flat combs.

The optical field of an OFC that is externally modulated by means of an EOPM driven by an MLS of order M and length L (L=2^M-1) can be written as

$$\begin{aligned} E_{dens}(t) &= \sum_{n=0}^{N-1} A_n e^{j(2\pi\nu_n t+\phi_n)} e^{j\phi_{PRBS}(t)} = \\ &= \sum_{n=0}^{N-1} A_n e^{j(2\pi\nu_n t+\phi_n)} \sum_{m=0}^{L-1} e^{jb_m\beta u(t-mT_b)}, \quad b_m = [0,1][m(modulo L)], \end{aligned} \tag{5.1}$$

where A_n, ν_n, and ϕ_n represent the amplitude, frequency, and phase of a comb line with index n, respectively, N is a positive integer representing the number of comb lines, and $\phi_{PRBS}(t)$ is the pseudorandom phase imparted in each optical pulse. The pseudorandom signal is described as a sequence of L bits with bit time T_b. Each bit is defined by a rectangular function $u(t)$ with duration T_b shifted to the corresponding positions. The periodic character of the MLS is defined by the modulo operator. In addition, the amplitude of each bit of the sequence is configured by the coefficients b_m

and by β, which determines the phase shift provided to the optical pulses. This phase shift is controlled through the voltage applied to the phase modulator, V_{EOPM}, as

$$\beta = \pi \frac{V_{EOPM}}{V_\pi}, \tag{5.2}$$

where V_π is the half-wave voltage of the modulator. If the bit rate of the MLS matches the repetition rate of the non-densified OFC ($1/T_b = f_R$), some comb pulses (dictated by the binary sequence) will experience a phase shift of β rad (when $b_m = 1$), while the phase of some other comb pulses will remain unchanged (when $b_m = 0$). As a result, L new spectral lines are generated between each original comb teeth, i.e., a densified comb with repetition rate $f_{dens} = f_R/L$ is obtained. In the experiments, $\beta \sim \pi$ rad, which optimizes the flatness of the densified comb [161].

The phase modulation of the comb pulses with discrete values 0 and π radians can be expressed as an amplitude modulation with values 1 and -1, respectively. Then, Eq. (5.1) can be written as

$$E_{dens}(t) = \sum_{n=0}^{N-1} A_n e^{j(2\pi\nu_n t+\phi_n)} \sum_{m=0}^{L-1} a_m u(t - mT_b), \qquad a_m = [1,-1][m(moduloL)], \tag{5.3}$$

a_m being amplitude coefficients.

The power spectral density of $E_{dens}(t)$ can be calculated as the Fourier transform of its autocorrelation function, as stated by the Wiener–Khinchin theorem. Considering a single comb line at ν_0 frequency, the continuous autocorrelation of the densified comb described in Eq. (5.3) is

$$\begin{aligned}
&\mathcal{R}_{DD}(\tau)|_{N=1} = \int_T E_{dens}(t+\tau) E^*_{dens}(t) dt = \\
&= \int_T A_0 e^{j(2\pi\nu_0(t+\tau)+\phi_0)} \sum_{m=0}^{L-1} a_m u(t+\tau-mT_b) A_{0'} e^{-j(2\pi\nu_{0'}t+\phi_{0'})} \sum_{m'=0}^{L-1} a^*_{m'} u(t-m'T_b) dt = \\
&= A_0^2 e^{j2\pi\nu_0\tau} \int_T \sum_{m=0}^{L-1} a_m u(t+\tau-mT_b) \sum_{m'=0}^{L-1} a^*_{m'} u(t-m'T_b) dt = \\
&= A_0^2 e^{j2\pi\nu_0\tau} \wedge (\tau/T_b), \qquad a_m = a_{m'} = [1,-1][m(moduloL)],
\end{aligned} \tag{5.4}$$

where * denotes the complex conjugate, and $T = LT_b$ is the period of the signal.

The result of the autocorrelation integral of the two MLSs [163], $\wedge(\tau/T_b)$, is the triangular function defined as

$$\wedge(\tau/T_b) = \begin{cases} 1 - |\tau|/T_b & |\tau| < T_b \\ -1/L & else \end{cases}, \tag{5.5}$$

which is also periodic with period $T = LT_b$. This autocorrelation function is illustrated in Fig. 5.7, which shows an MLS of length L, time of bit T_b and period T, with amplitudes between -1 and 1, and its autocorrelation in panels (a) and (b), respectively.

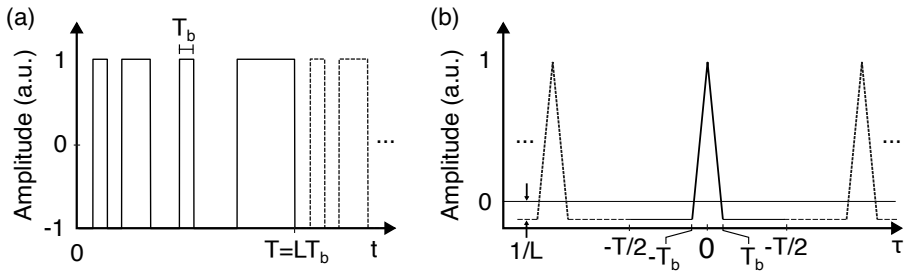

Figure 5.7: (a) Illustration of an MLS of order of length L, bit time T_b, and period $T = LT_b$, and (b) its autocorrelation function.

The power spectral density of the densified comb is calculated as the Fourier transform of $R_{DD}(\tau)$. Using the Fourier transform properties, the expression obtained for the power spectral density is

$$S_{dens}(f)|_{N=1} = \overbrace{A_0^2\delta(f-\nu_0)}^{\text{A}} * \left[T_b \left(\underbrace{\frac{\sin(2\pi f T_b) - \sin(\pi f L T_b)}{\pi f L T_b}}_{\text{B}} + \underbrace{\text{sinc}^2(\pi f T_b)}_{\text{C}} \right) \underbrace{\frac{1}{LT_b} \sum_{k=-\infty}^{\infty} \delta\left(f - \frac{k}{LT_b}\right)}_{\text{D}} \right], \tag{5.6}$$

$*$ being the convolution operator and $\delta(f)$ the Dirac delta function. The power spectral density corresponds to a squared sinc centered at the comb line frequency, sampled at $1/(LT_b)$, and with the nulls occurring at multiples of f_R. In Eq. (5.6) four components have been indicated by capital letters. The first component (A) accounts for the shift of the sinc shaped spectrum to the comb frequencies (ν_0 in this case). The second term (B) emerges from the phase modulation of the optical pulses with values 0 and π, and determines the suppression of the optical carrier, which is enhanced for longer sequence lengths. The third term (C) corresponds to an intensity modulation. The fourth term (D) accounts for the sampling, and comes from the periodic character of the autocorrelation signal.

Fig. 5.8 (a) illustrates the result of the analytical power spectral density of Eq. (5.6) obtained for N=1 comb line, L= 127 bits, ν_0= 0, and $T_b = 1/f_R$= 2 ns. The result is a spectrum with a line spacing of f_{dens}=f_R/L= 3.937 MHz.

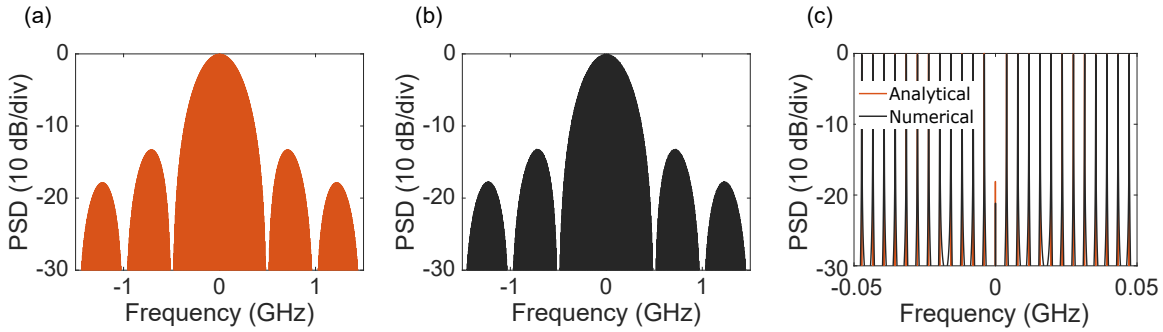

Figure 5.8: (a) Analytical and (b) numerical power spectral density corresponding to the phase modulation of an optical carrier centered at 0 Hz. The optical pulses are modulated by an MLS of length 127 bits. (c) Zoomed view with analytical (orange) and numerical (black) results superimposed.

The analytical power spectral density is compared to the power spectral density obtained from a numerical simulation, shown in Fig. 5.8 (b). In the numerical simulation, the optical field of a single comb line is phase modulated by an MLS of the described characteristics. Then, the autocorrelation of the densified comb field is computed, and the power spectral density of the autocorrelation is finally calculated. A comparison of the two spectral densities is provided in panel (c), showing good agreement of the two results.

The extension for N lines of the autocorrelation of the densified field can be written as

$$\begin{aligned}\mathcal{R}_{DD}(\tau) = &\int_T \sum_{l=0}^{N-1}\sum_{p=0}^{N-1} A_l A_p e^{j(2\pi(\nu_l-\nu_p)t+2\pi\nu_l\tau+\phi_l-\phi_p)} \\ &\sum_{m=0}^{L-1} a_m u(t+\tau-mT_b)\sum_{m'=0}^{L-1} a^*_{m'}u(t-m'T_b)dt = \\ &= \sum_{l=0}^{N-1} A_l^2 e^{j2\pi\nu_l\tau} \wedge (\tau/T_b) + \int_T \sum_{\substack{l=0\\ \forall l\neq p}}^{N-1}\sum_{\substack{p=0\\ \forall p\neq l}}^{N-1} A_l A_p e^{j(2\pi(\nu_l-\nu_p)t+2\pi\nu_l\tau+\phi_l-\phi_p)} \\ &\sum_{m=0}^{L-1} a_m u(t+\tau-mT_b)\sum_{m'=0}^{L-1} a^*_{m'}u(t-m'T_b)dt,\ a_m = a_{m'} = [1,-1][m(modulo L)],\end{aligned} \tag{5.7}$$

where * denotes the complex conjugate. The first addend $(\sum_{l=0}^{N-1} A_l^2 e^{j2\pi\nu_l\tau} \wedge (\tau/T_b))$ corresponds to trivial terms representing the product of the amplitude of each comb line and the autocorrelation function of the PRBS. In frequency domain, this conforms

a superposition of sampled sinc^2 spectra, each spectrum being centered at a comb line. The second addend includes not trivial cross-terms that must be considered to solve the autocorrelation integral, as these terms depend on t. Due to the presence of these cross-terms, the extension for N lines is performed numerically. The numerical simulation is based on the field expression of a densified comb, where the amplitude of each comb line is the unity and the phase of each comb tooth is considered to be constant. As before, a comb with a repetition rate of $f_R = 500$ MHz is densified by a factor of 127 using an MLS of order 7. In this simulation, a total of $N = 5$ comb teeth are configured.

The superposition of five individual power spectral densities corresponding to five optical carriers phase-modulated by the aforementioned binary sequence is illustrated in Fig. 5.9 (a). The spectra correspond to carrier frequencies of $\nu = [0, 0.5, 1, 1.5, 2]$ GHz. These individual power spectral densities are obtained from the numerical approach, although they could have been calculated analytically. By observing the superposition of the squared sinc functions centered on the optical carriers, one can easily understand why the phase modulation of a comb using an MLS results in a flat spectrum: the maximum of each sinc^2 spectrum coincides with the nulls of the other spectra, thereby creating a flat spectrum. Furthermore, the flatness is enhanced as the number of comb lines increases.

Next, the superposition of five spectral densities is compared to the power spectral density that arises from a densified comb with $N = 5$ comb lines, depicted in Fig. 5.9 (b). This figure illustrates that the power spectrum does not correspond to the sum of the individual spectra shown in panel (a). The cross-terms resulting from the beating of each comb line with all the other lines contribute to the amplitudes of the spectral tones.

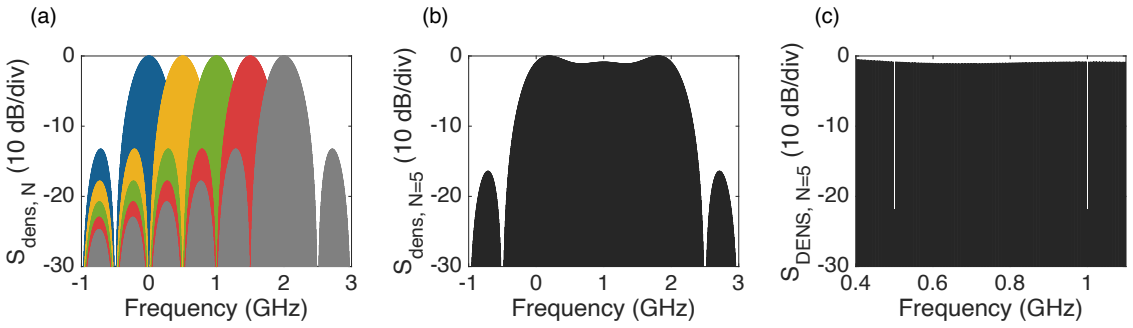

Figure 5.9: (a) Superposition of 5 spectra corresponding to the phase modulation of 5 optical carriers by means of the PRBS described in the text. (b) Power spectral density of a phase-modulated OFC with 5 comb lines, obtained numerically. (c) Closer view of (b).

Fig. 5.9 (c) constitutes a closer view of panel (b), showing the expected carrier suppression at the locations of the non-densified comb teeth (i.e, at multiples of f_R= 500 MHz). The carrier is not totally suppressed due to the fact that the length of the MLS is an odd number, and therefore the number of 0s and 1s differs in one bit.

Finally, it is also noteworthy that the use of an MLS for the pseudorandom phase modulation of the optical pulses is essential for optimizing the spectral flatness of the generated OFC. The enhanced spectral flatness of these types of pseudorandom binary sequences is a consequence of their distribution of 0s and 1s, which ensures a uniform energy distribution across the frequencies that comprise the spectrum. Fig. 5.10 illustrates the densified comb spectrum obtained when the densification is performed using both an MLS and a randomly generated PRBS that does not meet the properties of MLSs.

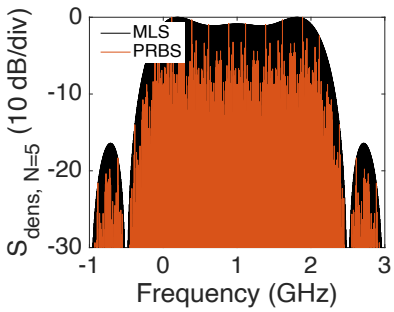

Figure 5.10: OFC spectrum obtained by densification using an MLS (black) and a randomly PRBS (orange).

5.3.2 Experimental setup

The experimental setup developed for the realization of dual-comb spectroscopy measurements using two densified GS OFCs is shown in Fig. 5.11. The part of the setup dedicated to the generation of the two densified GS combs is identified with a gray rectangle. The part where dual-comb spectroscopy is conducted is marked with a yellow, dashed block.

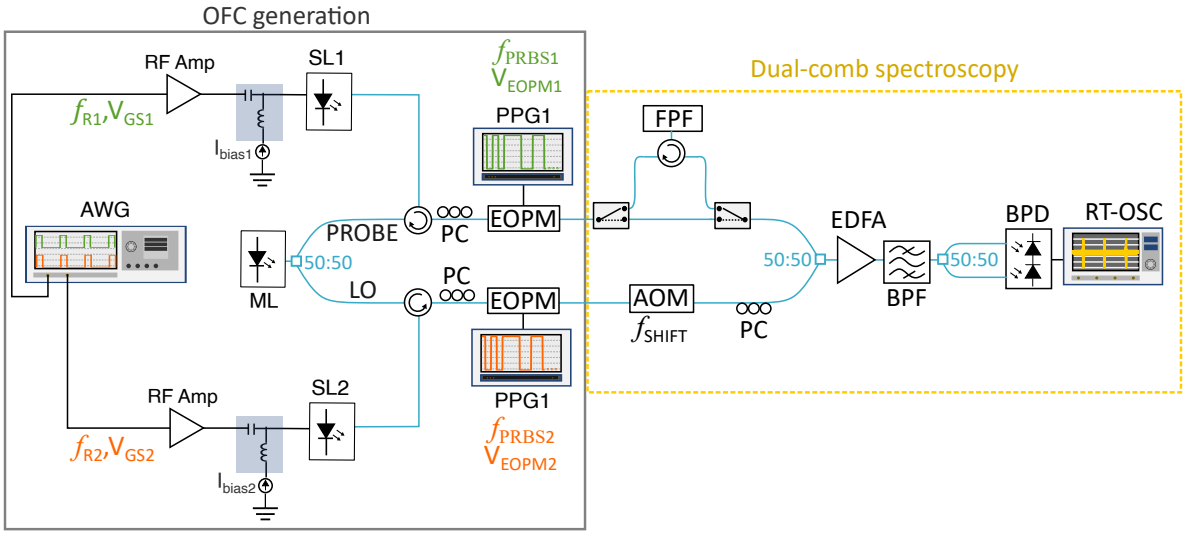

Figure 5.11: Setup dedicated to perform dual-comb spectroscopy with ultra-high resolution capabilities, based on two densified GS OFCs. The device used to test the capabilities of the system is a Fabry-Pérot filter (FPF). AWG: arbitrary waveform generator, PPG: pulse pattern generator, SL: slave laser, ML: master laser, PC: polarization controller, EOPM: electro-optic phase modulator, AOM: acousto-optic modulator, EDFA: erbium-doped fiber amplifier, BPF: band-pass filter, BPD: balanced photodetector, RT-OSC: real-time oscilloscope.

Regarding the generation of the two detuned OFCs, the same procedure used in the dual-comb experiments discussed so far is followed. This procedure relies on gain switching two commercial laser diodes (Eblana EP1550-0-DM-H19-FM), which are externally seeded by the same master laser. The optical fibers of the devices and components within the master-slave section are polarization-maintaining fibers and, as a consequence, the two polarization controllers often used to align the states of polarization of the ML and the SLs are dismissed in this experiment.

The two SLs are switched at frequencies of f_{R1} = 499.995 MHz and f_{R2}= 500 MHz, respectively, conforming a repetition rate difference of 5 kHz and a high compression factor of C= 10^5. The AC signals used to gain switch the two lasers consist in two trains of electrical pulses featuring the two mentioned frequencies, which are generated by means of a 16 GSa/s arbitrary waveform generator (Tektronix AWG70000B). Each AC signal is superimposed to a DC bias current provided by a low-noise current source (Arroyo Instruments 4200-DR series LaserSource). In addition, although not depicted in the setup, two temperature controllers allow for the slight modification of the operating temperature of the slave lasers and for the stabilization of the diodes at the two selected temperatures. Due to the great similarity of the two SLs, they are driven by the same parameters: both bias currents are configured to I_{bias1}= I_{bias2}= 3 mA, the peak-to-peak amplitude of the pulsed signals is set to V_{GS1}= V_{GS2}= 5.5 V (after amplification), and the electrical pulses have a duration of τ_{pulse1}= τ_{pulse2}= 200 ps. The superposition of the DC and AC signals results in the switching of the lasers between I_{off} ∼0 mA and I_{on} ∼102 mA, from below to above their threshold currents. The ML, a tunable semiconductor laser (Pure Photonics PPCL300) injects its light on both SLs, so that every new optical pulse builds up with the same phase. It also transfers its linewidth (∼60 kHz) to the SLs. The power and wavelength of the ML are configured to P_{inj}= 0.25 mW and λ_{inj}= 1549.6 nm, respectively, ensuring injection locking.

Once the two mutually-coherent GS OFCs are generated, they are externally densified using two EOPMs (Thorlabs LN65S-FC, Covega 053). The two modulators exhibit an electro-optic bandwidth of 10 GHz. Also, a polarization controller is placed at the input of each phase modulator to ensure the efficient densification of the combs. Each phase modulator is driven by an MLS with bit rate matching the repetition rate of the comb to be densified. The two required MLSs are generated by two pulse pattern generators (Anritsu MU181020A). For this purpose, the frequency of the synthesizer module of each pattern generator driving each EOPM is conveniently set to f_{R1} and f_{R2}. By doing so, the bit time of the PRBS matches the repetition rate of the train of optical pulses and it is ensured that each bit modulates a single optical pulse (see Fig. 5.12).

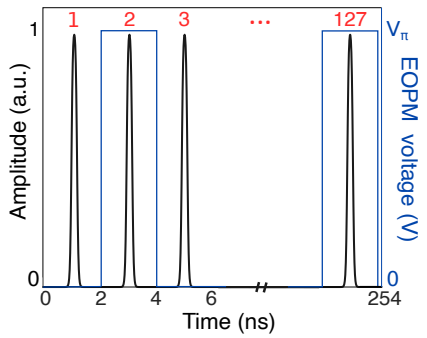

Figure 5.12: Illustration of 127-bit PRBS superimposed to train of optical pulses with f_R= 500 MHz. Time of bit T_b= $1/f_R$.

The length of both MLSs is 127 bits. The amplitude of the two binary sequences needs to be adjusted to the V_π voltage of each modulator in order to modulate the phase of the optical pulses with values of 0 and π rad. For this purpose, the half-wave voltage of the two modulators was measured for a modulation bandwidth of 500 MHz using a high-resolution optical spectrum analyzer before the realization of the dual-comb experiments. The half-wave voltage was retrieved from the characterization of the optical spectrum that results from the phase modulation of a CW laser when varying the amplitude of the RF signal that drives the modulator. The evolution of the power of the carrier and the sidebands allowed to determine V_π, whose value is around 4.5 V for both modulators. Then, the bits of the PRBSs have a low value of 0 V and a high value of 4.5 V. All these settings result in the generation of two densified combs with repetition rates f_{dens1}=f_{R1}/127= 3.9369685 MHz and f_{dens2}=f_{R2}/127= 3.9370079 MHz. The frequency offset, which determines the interleaving of the down-converted tones, is δf_{dens}= 39.37 Hz.

Each densified comb travels along one branch of the interferometric setup. One of them, acting as probe comb, interrogates the device under test. The second OFC acts as the local oscillator. The device used to test the resolution capability of the system is a narrow Fabry-Pérot tunable filter (FPF, Micron Optics TF2FMJ) with a nominal FSR of 272.38 GHz, a finesse of 750, and a FWHM of 363.2 MHz. It is measured in reflection configuration using an optical circulator. After probing the filter, the probe comb is combined with the local oscillator comb in an optical coupler. Then, they are amplified by means of an EDFA, resulting in an average optical power of ∼1 mW at the input of the photodetector. An optical filter (EXFO XTM-50-SCL-U) filters the amplified spontaneous emission noise. Finally, the two signals beat in a 100-MHz balanced photodetector (Koheron PD100BAC) and are digitized using a real-time oscilloscope (Keysight MSOS804A).

To obtain the reflection response of the Fabry-Pérot etalon, two sequential acquisitions are performed: a first acquisition in which the probe passes through the Fabry-Pérot filter, followed by a reference measurement in which the probe does not interrogate the filter. The optical path traversed by the probe OFC is configured by means of two optical switches. Also, it is worth mentioning that the two PRBS generators, the arbitrary waveform generator, and the oscilloscope share a common 10-MHz reference signal. This ensures the proper synchronization of the optical pulses and the modulation signals and triggers the interferogram signal in the oscilloscope.

5.3.3 Design of the densified gain-switched dual-comb spectrometer

The design of the proposed dual-comb spectrometer is flexible with respect to two key parameters: the densification level and the gain-switching repetition rate. The trade-off between the two determines the spectral resolution and the acquisition speed, which can be tailored to meet specific performance requirements.

The densification factor can only be an integer (2^M-1). By simply increasing the length of the MLS, higher densification and hence lower repetition rates can be achieved. However, it is important to consider the required SNR, as higher densification factors result in lower power per comb line. As for the repetition rate of the non-densified GS combs, it can be tuned from tens of GHz to hundreds of MHz. For low repetition rates the duty cycle of the pulsed optical signal is relatively low, resulting in low average powers. Since power is a significant challenge for GS OFCs at these frequencies, the use of higher OFC frequencies in the GHz range together with longer densification sequences can help address this issue. By adjusting these two parameters, it becomes relatively simple to customize the spectrometer to suit the specific measurement requirements. In our experiment, an OFC with a line spacing of 500 MHz is densified by a factor of 127. This densification factor is chosen in order to measure the spectral feature with good resolution. As a result of the selected parameters, the FWHM of the filter of 363.2 MHz is interrogated with approximately 92 comb lines.

In addition, a careful design of the repetition rate difference of the combs needs to be carried out in order to prevent aliasing in the down-conversion process. As it was discussed in Chapter 3, in the down-conversion process dual-comb replicas appear at multiples of the comb line spacing. Therefore, the lower the repetition rate of the OFC, the closer the replicas appear, and a higher compression factor is required. A higher compression factor implies a lower repetition rate difference, resulting in an increase in the acquisition time. The system here proposed includes an acousto-optic modulator that shifts one of the OFCs by f_{shift}= 80 MHz. This ensures that the down-conversion process is carried out without ambiguity. With this frequency shift, the replicas of the RF spectrum appear at $|f_{shift} \pm nf_{dens}|$, n being an integer and the absolute value accounting for the folding of beat notes to the positive side of the frequency spectrum. In the system here described, and considering the frequencies involved, the first Nyquist zone is centered at the acousto-optic modulator frequency, and the two closest neighboring replicas are centered around 77.48 MHz ($|f_{shift} - 40f_{dens}|$) and 81.42 MHz ($|f_{shift} - 41f_{dens}|$). Both replicas are mirrored replicas. Fig. 5.13 illustrates a region of the down-converted frequency spectrum that would be obtained in the described scenario, showing the dual-comb spectrum at 80 MHz and its two nearest replicas. In the illustration, the two interfering combs are considered to be optically injected in the blue side of their frequency spectrum. In addition, a total optical bandwidth of 60 GHz, distributed asymmetrically around the injection, is considered[1]. As depicted in the figure, the selected compression factor of 10^5 prevents spectral aliasing in down-conversion. The compression factor limit in this scenario is approximately $3{\cdot}10^4$. Moreover, with regard to the acquisition with the oscilloscope, it is necessary to ensure that the sampling rate meets the Nyquist sampling theorem. Considering the scenario illustrated in Fig. 5.13, the minimum sample rate that can be employed is around 170 MSa/s. In the experiments, the selected sampling rate for digitizing the interferometric signals is 250 MSa/s.

[1]These assumptions are made based on the experimental results, which will be detailed in a later section. Therefore, the illustration reproduces the experimental down-converted frequency spectrum.

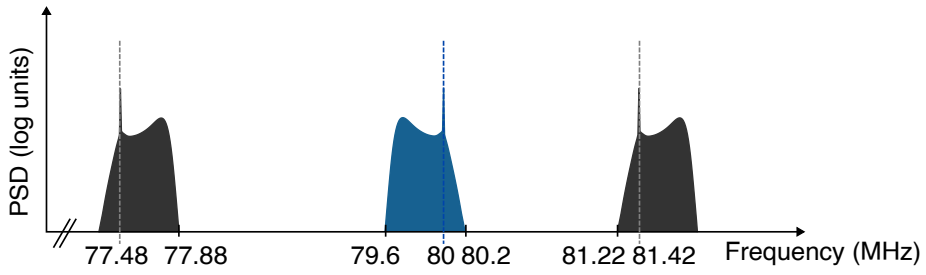

Figure 5.13: Sketch of the down-converted frequency spectrum that would be obtained in the described dual-comb experiment with two densified GS OFCs. A region around the acousto-optic modulator frequency (f_{shift}= 80 MHz) is illustrated. A repetition rate after densification of ∼3.937 MHz is considered, and the compression factor is 10^5.

Finally, the necessity for high compression, coupled with the low repetition rate of the combs, results in relatively prolonged acquisition times. With the aforementioned experimental parameters, the minimum acquisition time is approximately 25 ms, which corresponds to the acquisition of a single interferogram burst. In order to visualize the discrete tones in the RF spectrum, derived from the acquisition of several periods of the interferogram signal, single-shot acquisitions of 250 ms are captured in the experiment. However, the acquisition of such long interferogram traces results in demanding memory requirements, given that heavy files must be stored and subsequently processed.

5.3.4 The device under test: the Fabry-Pérot filter

The device selected for testing the high-resolution dual-comb absorption spectroscopy system is a Fabry-Pérot filter, defined by its FSR, finesse ($\mathcal{F}$), and FWHM ($\Delta\nu_{FP}$). The values of these characteristics were already detailed in the description of the experimental setup. In this subsection, prior to the presentation of the experimental results, a theoretical analysis of the transmittance and reflectance of a Fabry-Pérot etalon is provided. In the description, ideal conditions of no absorption within the cavity and identical reflectivities of the two mirrors of the cavity are assumed.

As it was introduced in Chapter 2, the FSR of a resonant cavity is a parameter that defines the frequency separation of the cavity resonances. The FSR of the cavity and the spectral width of the resonances are related by the finesse, which indicates how narrow the resonances are with respect to their frequency distance. Considering this, the finesse can be written as

$$\mathcal{F} \equiv \frac{\mathrm{FSR}}{\Delta\nu_{FP}} \approx \frac{\pi}{2\mathrm{arcsin}(1/\sqrt{F})}, \tag{5.8}$$

F being the coefficient of finesse, which is related to the reflectivity of the two mirrors forming the cavity.

Considering that both reflective surfaces have a reflectivity R, the coefficient of finesse becomes

$$F = \frac{4R}{(1-R)^2}. \tag{5.9}$$

Assuming these considerations, the transmittance function of the Fabry-Pérot etalon is expressed as

$$T_{FP} = \frac{1}{1 + F\sin^2(\delta_\varphi/2)}, \tag{5.10}$$

where δ_φ is the phase shift experienced by a resonator wave when traversing a round-trip of the cavity.

Considering normal incidence for the field entering the cavity, the phase shift is expressed as

$$\delta_\varphi = 2kl = \frac{4\pi nl}{c}\nu, \tag{5.11}$$

k being the wavenumber, and ν being the frequency.

Finally, in absence of absorption, the reflectance of the Fabry-Pérot filter, calculated as $R_{FP} = 1 - T_{FP}$, is given by

$$R_{FP} = \frac{F\sin^2(\delta_\varphi/2)}{1 + F\sin^2(\delta_\varphi/2)}. \tag{5.12}$$

5.3.5 Experimental results

Following the procedure described in the preceding chapter for dual-comb experiments, the results first demonstrate the generation of two similar densified GS OFCs. Subsequently, the generation of an RF dual frequency comb featuring a down-converted line spacing of 39.37 Hz (optical line spacing of approximately 3.937 MHz after upconversion) is demonstrated. Finally, the retrieval of the reflection profile of one of the cavity resonances of the measured Fabry-Pérot etalon with a dual-comb system is presented.

Generation of two optical frequency combs

First, the two GS OFCs before and after densification are measured in time and frequency domains. The comb spectra are measured using an optical spectrum analyzer with a spectral resolution of 10 MHz (Aragon Photonics BOSA 400 C+L). The optical pulses are measured employing an equivalent-time sampling oscilloscope equipped with an optical module, which allows to measure an optical bandwidth of 20 GHz. In these characterizations, an EDFA is also used to amplify the optical signal to an average

optical power of 1 mW. Fig. 5.14 (a) shows the optical pulses generated by one of the optically-injected GS laser diodes. The intensity of the optical pulses after densification shows no difference to the pulses depicted in the figure, since only the phase of the pulses is changed. The optical pulses have a measured FWHM of 50 ps. Fig. 5.14 (b) includes the optical spectrum of one of the non-densified 500-MHz GS OFC (blue) and the optical spectrum obtained after densification (green). The spectral resolution of the BOSA does not allow to individually resolve the spectral lines of the densified comb (see panel (c)), which features a line spacing of approximately 4 MHz. The spectral width at 10 dB of both combs, excluding the injection peak from this calculation, is around 48 GHz. The maximum attainable spectral width for these combs is around a hundred GHz, but they were designed to fit the device under test, avoiding the loss of power per comb line that would entail an excess of bandwidth. The power per comb line of the densified OFC shows a decrease corresponding to the increase in the number of lines by a factor of 127, although it cannot be properly measured using the BOSA.

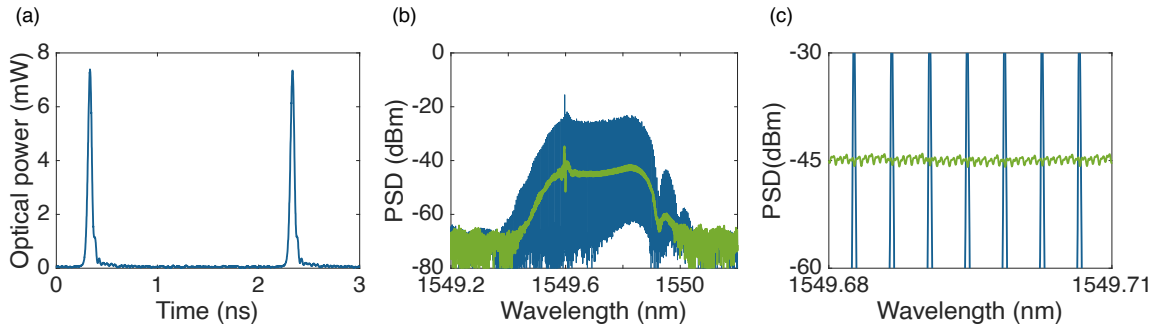

Figure 5.14: (a) Optical pulses of the GS OFC featuring a periodicity of 2 ns (f_R= 500 MHz). (b) Non-densified (blue) and densified (green) gain-switched OFCs measured with the BOSA. (c) Close view of (b).

Generation of down-converted dual-comb spectrum

The retrieved interferogram trace comprises bursts every δf_R^{-1}, which in the scenario here considered corresponds to a periodicity of 0.2 ms. This interferogram signal results from the cross-correlation of the two trains of optical pulses from each OFC, featuring periodicities of f_{R1}^{-1} and f_{R2}^{-1}, respectively. The optical pulses have a phase distribution defined by the distribution of zeros and ones in the PRBS of length 127 bits and therefore, every 127 optical pulses the phase sequence repeats. Consequently, the interferogram is constituted by sub-sequences of 127 bursts that introduce an additional periodicity of δf_{dens}^{-1}=25.4 ms.

A portion of the raw interferogram trace digitized with the oscilloscope at 250 MSa/s is shown in Fig. 5.15. The interferograms show the expected periodicity, as depicted in the closer view included in the figure.

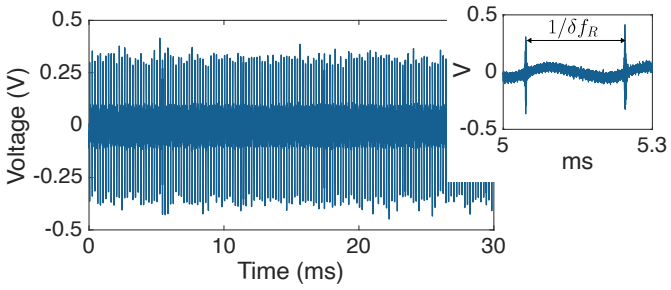

Figure 5.15: Portion of the raw interferogram trace digitized with the oscilloscope (optical switches in reference position). The inset shows the periodicity of individual interferograms.

The interferogram traces acquired with the oscilloscope at 250 MSa/s have a duration of 250 ms. Five sequential acquisitions are performed, comprising five acquisitions in the reference configuration and five acquisitions interrogating the filter. Each acquisition contains 1250 interferograms with the periodicity of δf_R^{-1}, and around 10 sub-sequences with periodicity of δf_{dens}^{-1}, arising from the densification. A total of 62.5 million samples are acquired per interferogram trace. The temporal interval between sampling points is 4 ns. In this configuration, there are ten samples between two consecutive tones of the down-converted dual-comb spectrum, which enables the visualization of resolved tones.

Once the acquisition is performed, the retrieved data is subjected to offline digital signal processing. First, a band-pass filter (between 79.5 MHz and 80.3 MHz) is applied to the interferogram traces, and the dual-comb spectrum located around the acousto-optic modulator frequency shift is analyzed. The obtained filtered interferogram is plotted in Fig. 5.16 (a). After the filtering process, the frequency components of the densified comb prevail, resulting in the filtered interferogram showing a periodicity that corresponds to the densified line spacing.

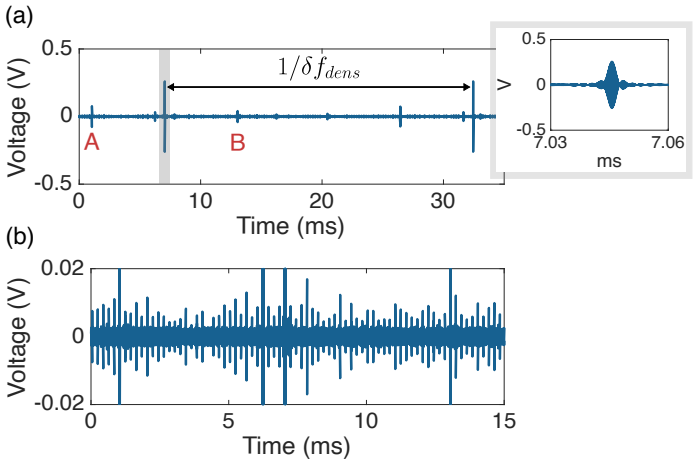

Figure 5.16: (a) Interferogram trace obtained after applying a band-pass filter to the raw interferogram showing a periodicity. The main bursts show a periodicity of 25.4 ms and a peak-to-peak amplitude of ∼500 mV. A zoomed view of a filtered burst can be observed in the inset. (b) Residual contribution of the interferograms with periodicity δf_R in the filtered trace.

In addition to the main bursts of greater amplitude, replicas of smaller amplitude appear to the left and right of it. Two of these replicas are indicated in the figure with capital letters A and B. The origin of these replicas is not clear, it could be attributed to the presence of additional peaks in the cross-correlation of the optical pulses due to the correlation of sub-sequences of 0 s and 1 s within the 127-bit MLS. Moreover, there is a residual contribution of non-densified frequency components (∼100 times smaller than the densified interferogram bursts after filtering), depicted in Fig. 5.16 (b). All the information present in the filtered interferogram traces (main bursts and attenuated 0.2-ms bursts) is utilized to obtain the filter response.

Subsequently, the fast Fourier transform of each interferogram trace is calculated, and the magnitudes of the frequency-domain data are averaged. The power spectral densities obtained for a single interferogram trace and after averaging five spectra are shown in Fig. 5.17 for both the (a) reference and (b) sample configurations. The notch of the Fabry-Pérot etalon can be clearly distinguished in the center of the sample spectrum (see inset of panel (b)). The averaged RF spectra are analyzed in terms of three figures of merit: the CNR, the Δf_{10dB}, and the spectral flatness. The latter is calculated for three thousand comb lines in a region comprised between 79.7 MHz and 79.81 MHz. The reference spectrum features a CNR= 16 dB, a Δf_{10dB}= 4.8 kHz, and a spectral flatness of 0.93. The down-converted spectral width corresponds to an optical bandwidth before down-conversion of 48 GHz, which is in agreement with the bandwidth at 10 dB of the measured optical spectra. Similar values are obtained for the spectrum that includes the response of the filter (CNR = 17.6 dB, Δf_{10dB}= 4.8 kHz, spectral flatness of 0.92).

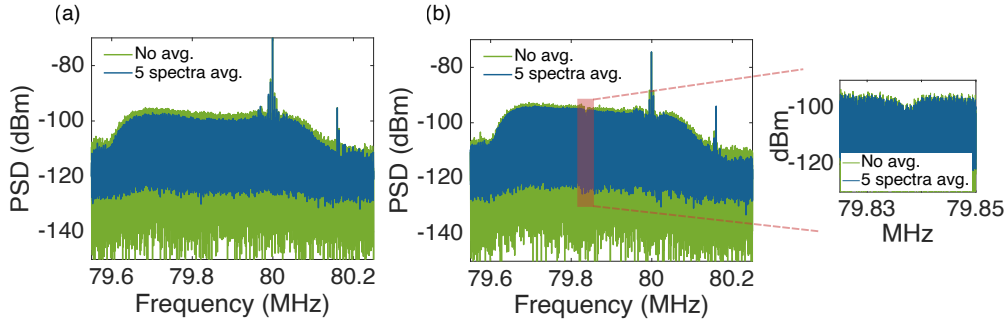

Figure 5.17: Densified dual-comb spectra obtained from a single interferogram trace (green) and after frequency averaging five spectra (blue). (a) Reference spectra. (b) Measurement spectra containing the reflection profile of the Fabry-Pérot filter.

Both down-converted combs exhibit a sufficiently broad bandwidth to measure a single Fabry-Pérot resonance and to record the baseline: a total of 12000 comb lines are comprised within the 10-dB bandwidth, and around 90 teeth lie within the nominal FWHM of the Fabry-Pérot resonance. In fact, the bandwidth could be further reduced by decreasing the amplitude of the electrical pulses used to switch the lasers, resulting in a higher power per comb line. Additionally, both combs demonstrate excellent performance in terms of CNR and flatness, which are essential characteristics for performing spectroscopic measurements. This technique demonstrates the feasibility of reducing the line spacing of the combs without compromising the spectral flatness.

Characterization of Fabry-Pérot filter reflection profile

The Fabry-Pérot filter is first characterized with the high-resolution optical spectrum analyzer. The tunable laser of this instrument interrogates and measures the insertion losses of the device. The filter is measured in transmission and reflection configurations. The transmission profile is depicted in Fig. 5.18 (a), showing a transmission contrast factor (defined as the ratio between the maximum and minimum of transmission) of approximately 36 dB. The reflection profile is included in Fig. 5.18 (b). This profile shows a lower contrast of 2.4 dB. The measured reflection profile does not show the expected behavior, as the reflectance does not correspond to the complement of the transmittance, i.e. $R_{FP} \neq 1 - T_{FP}$ (in linear units).

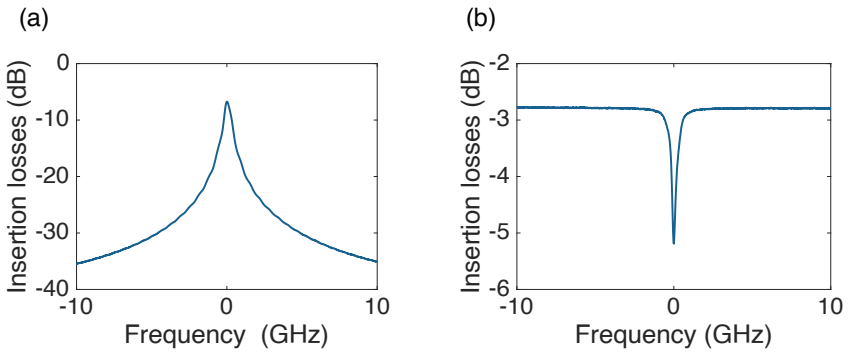

Figure 5.18: (a) Transmission and (b) reflection profiles of the Fabry-Pérot filter used for the demonstration of the high resolution capability of the proposed densified dual-comb spectrometer measured through tunable laser absorption spectroscopy using the BOSA.

The discrepancies between the two responses can be attributed to additional losses when the filter is operated in reflection. Despite the lower reflection contrast, since the objective of the dual-comb experiment is to test the validity of the system for measuring samples with absorption profiles with narrow bandwidths, the reflection response of the filter is still valid for this purpose.

The measured FWHM of the filter is verified to be consistent with the nominal FWHM specified by the manufacturer. For this purpose, the measured transmittance and reflectance are normalized to show a contrast between 0 and 1, enabling to compare them with the nominal response. It is verified that the normalization process does not modify the linewidth of the profiles. The results from this comparison are presented in Fig. 5.19. In both graphs, a resonance of the Fabry-Pérot filter computed using the nominal specifications is depicted with a dotted red line. The obtained FWHM for the measured transmission profile is 497.8 MHz, which represents a deviation of 37% from the nominal specification. For the reflection profile, the FWHM is 383.5 MHz, indicating a deviation of 5.6% from the nominal specification.

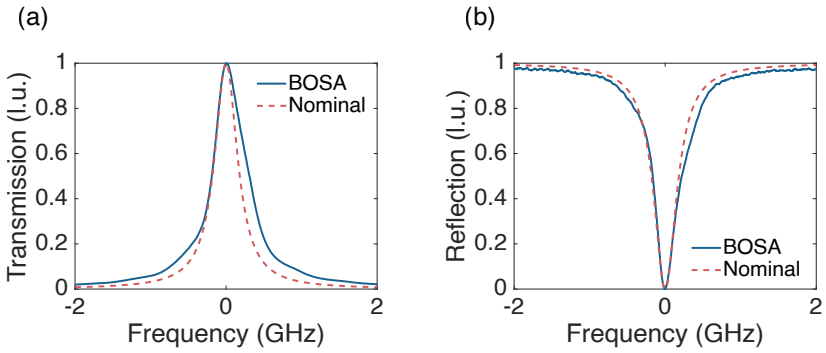

Figure 5.19: Comparison of nominal and measured (a) transmission and (b) reflection profiles of the Fabry-Pérot filter used in dual-comb spectroscopy experiments.

The stability of the filter is also evaluated, taking four consecutive measurements with the optical spectrum analyzer. The four realizations are collected within a total time of one minute and thirty seconds. The result of this test, presented in Fig. 5.20, illustrates the significant instability of the filter over the measurement time (maximum deviation of ∼1.4 GHz). This instability, attributed to thermal fluctuations, can result in the broadening of the measured profile.

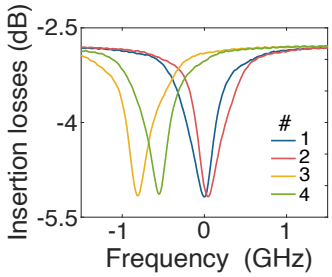

Figure 5.20: Evaluation of the stability of the Fabry-Pérot filter.

Following the initial characterization conducted via tunable laser absorption spectroscopy, the reflection profile of the Fabry-Pérot etalon is obtained through dual-comb spectroscopy. The result is obtained from the spectral averaging of five interferogram traces, each of them with a temporal length of 250 ms. This constitutes a total integration time of 1.25 s. The data are processed using a home-built MATLAB script, following the same procedure to that indicated in the code diagram described in the previous chapter. Firstly, the intensity of each comb tooth of the two RF spectra (reference and measurement) is extracted by means of a peak detection routine. Then, the reflection profile is calculated as the ratio of the line intensities containing the filter information to the corresponding reference intensities, all expressed in linear units.

The profile retrieved from this process shows fluctuations on the baseline. Consequently, in addition to applying a baseline correction algorithm, which consists in a fourth order polynomial fitting of the baseline, the reflection response is low-pass filtered. The purpose of the applied low-pass filter is to smooth the baseline of the data without altering the reflection profile. Finally, due to the low reflection contrast of the measured Fabry-Pérot resonance, the experimental reflection profile expressed in linear units is normalized. This normalization allows to use the expression of the reflectance described by Eq. (5.12) to fit the experimental reflection profile.

The Fabry-Pérot reflection profile obtained after post-processing the measured data is illustrated in Fig. 5.21 (a), represented by a blue dotted line. The ideal reflectance of a Fabry-Pérot etalon is fitted to the experimental data by means of a least squares optimization algorithm using two fitting parameters: the FSR and the finesse. The fitted profile is represented in the graph by a red solid line. In addition, the residuals from the fitting (green dotted line) are included in the bottom part of the figure, having a standard deviation of σ_{res}= 0.105. A comparison of the profile retrieved from dual-comb spectroscopy (blue trace), the profile fitted to it (red line), and the response obtained from the tunable laser absorption spectroscopy measurements (green line) using the optical spectrum analyzer (after normalization) is included in Fig. 5.21 (b). This comparison demonstrates the good agreement between the profile fitted to the experimental dual-comb spectroscopy data and the Fabry-Pérot reflection profile measured with the BOSA.

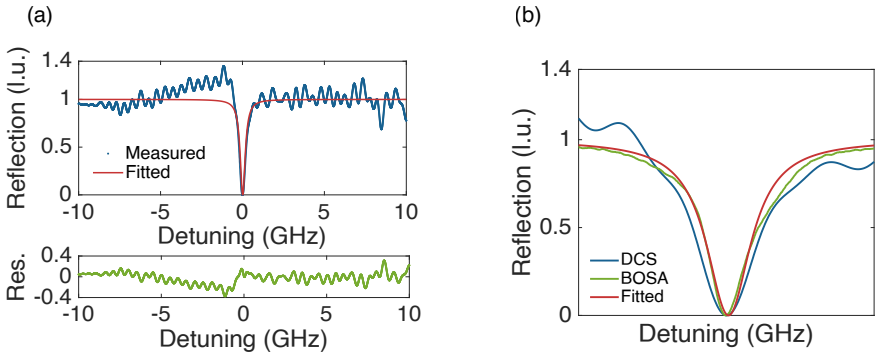

Figure 5.21: (a) Normalized Fabry-Pérot reflection profile obtained from dual-comb spectroscopy measurements, presented in linear units. The measured profile is plotted with blue circles and the fitted profile with a red solid line. The residuals are displayed in the bottom part of the figure. (b) Reflection profile measured via dual-comb spectroscopy and nominal profile fitted to it (blue and red, respectively), and normalized reflectance measured through tunable laser absorption spectroscopy (green).

Although the band-pass filter applied to the experimental response resulted in a reduction of the ripple of the baseline, this ripple can still be discernible, as illustrated in the figure above. The ripple occurs at a frequency of 500 MHz, which corresponds to the frequency of the non-densified comb. This phenomenon is attributed to the instability of the two EOPMs during the course of the experiments, manifested as fluctuations in the V_π values of the two employed modulators over the measurement time. These fluctuations lead to a variation in the amplitudes of the comb lines across different acquisitions. In order to minimize fluctuations in the intensity of the comb teeth of sequentially-retrieved dual frequency combs, the amplitude of the two PRBSs driving the EOPMs was finely adjusted during the experimental realizations. This fine adjustment, which aimed to align the amplitudes of the PRBSs with the fluctuating V_π value of the modulators, was conducted by visually examining the spectrum corresponding to the interferogram signal retrieved in real-time on the oscilloscope. Nevertheless, despite the careful tuning of the two binary sequences, the experimental procedures remained challenging, and the

ripple observed in the retrieved reflection profile is indicative of the intensity variation of different dual-comb spectra. This phenomenon results in an increase in the standard deviation of the residuals. Nevertheless, despite the relatively high standard deviation of the residuals, the percentage variation of the experimental FSR, finesse, and FWHM, compared to the nominal characteristics of the filter, is less than 1%. This variation is lower than that obtained when measuring with the BOSA, since the measurement time is reduced from seconds (BOSA) to milliseconds (dual-comb spectroscopy). Table 5.1 provides the nominal FSR and finesse of the tested device, along with the experimental values extracted from the fit, as well as the FWHM resulting from these two parameters.

	Nominal	**Experimental**	**Variation**
FSR	272.38 GHz	272.5 GHz	0.04%
Finesse	750	749.3	0.09%
FWHM	363.2 MHz	363.7 MHz	0.14%

Table 5.1: Nominal specifications of the Fabry-Pérot filter used for the experimental demonstrations and experimental characteristics obtained via high-resolution dual-comb spectroscopy.

5.4 Conclusions

In conclusion, various approaches for generating gain-switched optical frequency combs with repetition rates in the few MHz range (having the potential to be further reduced to the sub-MHz range) have been demonstrated. A good balance between optical power and spectral flatness is achieved by means of the phase modulation of gain-switched combs, an approach that effectively reduces the comb line spacing by the generation of additional spectral tones between pairs of comb lines. A dual-comb spectrometer based on two phase-modulated gain-switched combs is demonstrated. This spectrometer, validated through the measurement of a narrow Fabry-Pérot resonance with a fine resolution of around 4 MHz, improves the state-of-the-art resolution of gain-switched dual-comb spectrometers by a factor of 25.

These demonstrations focus on the suitability of dual-comb architectures involving gain-switched comb generators for applications requiring high resolution. The significance of these results lies in the expanded range of achievable resolutions for dual-comb architectures based on GS combs, now enabling resolutions ranging from tens of GHz (without external phase modulation) down to values below 1 MHz (with external phase modulation). The achieved repetition rates allow the measurement of absorption features with linewidths as low as tens of MHz using a robust arrangement that gathers the benefits of gain-switched comb sources.

- Gain-switched combs with repetition rates below 100 MHz

In the first section of this chapter, the generation of low-repetition-rate gain-switched combs employing pulsed electrical signals has been discussed. The comb source benefited from simplicity, as it only comprised two commercial semiconductor lasers. The approach involved a trivial procedure based on decreasing the frequency of the train of pulses used to gain switch the laser diode. With this approach, frequency combs featuring repetition rates as low as 2.5 MHz have been demonstrated.

The presence of well-resolved spectral tones has been validated from the characterization of the optical spectrum via a self-heterodyne approach. To achieve a repetition frequency of 2.5 MHz, the repetition rate has been progressively reduced, while maintaining fixed injection conditions and a fixed duration and amplitude of the electrical pulses. Under these fixed conditions, combs with progressively lower repetition frequencies have been obtained by reducing the continuous bias current supplied to the lasers. This ensured that the lasers were switched on and off without exciting the second peak of the relaxation oscillations of the laser, maintaining the same RF amplitude in all scenarios. The OFC at the lowest demonstrated repetition rate (i.e. 2.5 MHz) showed a flat envelope and a 10-dB bandwidth of 102 GHz, comprising 410000 spectral lines within this bandwidth. However, the generated combs exhibited low average optical power and high peak power, as reducing the repetition rate resulted in a low duty cycle of the optical signal. In addition, the efficiency of the injection power with respect to the rest of the lines forming the comb was very low. It was evidenced in the measured optical spectra, in which the tone corresponding to the injection had a power value of approximately 40 dB higher (a factor of 10^4 in linear units) than the rest of comb lines.

- Densification of gain-switched combs

In order to achieve a compromise between average optical power and spectral line spacing, the densification of GS combs has been explored. This technique is based on the external phase modulation of GS combs using an MLS as the driving signal of the phase modulator. This approach, already reported for the densification of a single electro-optic comb and a single GS comb, has been utilized in this thesis for the simultaneous densification of the two frequency combs comprising a dual-comb interferometer. Although the technique results in a higher complexity of the comb source, which now includes electro-optic phase modulators in the two branches of the dual-comb interferometer, it permits to decrease the line spacing of the comb lines without power loss and to maintain a good spectral flatness.

Firstly, an analytical study of the phase modulation of a train of optical pulses by means of an MLS has been carried out. This study, together with numerical simulations, demonstrated why the use of an MLS as the signal driving the phase modulator enables the generation of highly densified and flat combs. Then, a sensing system based on two-densified GS OFCs with optical injection has been demonstrated. The resolution of the proposed system was 3.937 MHz, and the dual-comb obtained featured 12000 sampling points in a 10-dB optical bandwidth of 48 GHz. The system has been validated by retrieving the reflection response of a Fabry-Pérot filter with a nominal linewidth of

363.2 MHz. The percentage variation of the experimental results with respect to the nominal data of the filter was demonstrated to be lower than 1%.

The implemented system remarkably surpasses the previously established minimum line spacing limit by a factor of 25. It is worth mentioning that the employed resolution, as well as the spectral width, has been specifically designed for measuring the linewidth of the tested device. Nonetheless, the approach shows flexibility in the achievable spectral resolution and sub-MHz resolutions can be achieved by simply using longer bit sequences, with the only limitation being the SNR. Additionally, the proposed system could be highly beneficial for other comb generation techniques, particularly those in which line spacing depends on cavity length as in such cases achieving repetition rates in the range of a few MHz would require cavity lengths of hundreds of meters. Furthermore, although in terms of spectral resolution the performance of densified GS OFCs is comparable to that of electro-optic combs, where sub-MHz resolutions have been reported [80], the comb bandwidth is less constrained in this approach. Finally, although densification allows to reduce the line spacing of OFCs with no power loss, the effective management of average power of GS combs still remains a noteworthy challenge, particularly in specific application contexts.

Chapter 6

Dual-comb ranging with gain-switched combs

This chapter presents the experimental implementation of a dual-comb interferometer based on two gain-switched combs for distance measurements. The distance is determined by analyzing the spectral phase of the comb lines. This interferometric approach allows for enhanced precision compared to time-of-flight methods, as the information from multiple comb lines is used to calculate the distance. Furthermore, the ability to modify and reduce the repetition frequency of the combs to the MHz range or below through densification techniques effectively extends the non-ambiguity range of the system. As a result, a versatile and precise ranging system based on semiconductor lasers is obtained.

First, the system is validated using two gain-switched combs with repetition rates of 100 MHz and 100.01 MHz. Open-path measurements are conducted to determine a distance of 4 millimeters. The non-ambiguity range of the system of 1.5 meters is subsequently extended to tens of meters by the electro-optic phase modulation of the two gain-switched optical frequency combs.

6.1 Introduction

Light detection and ranging systems, widely known by the acronym LIDAR, are a well-established technology for measuring distances using laser sources. From their inception, various LIDAR technologies have been developed, and different books and scientific articles cover this subject [164], [165]. These systems find a widespread application range both in scientific and industrial contexts, and depending on the architecture of the LIDAR, they not only allow to measure distances but also other magnitudes such as velocity and atmospheric variables (aerosols, gases, etc.).

In general terms, laser ranging is based on the determination of the distance to a target from the analysis of the light backscattered from the target. This technique typically relies on measuring the time delay, phase shift, or frequency change of the reflected light relative to the transmitted laser beam. Time-of-flight LIDARs involve the use of pulsed laser light. In such systems, the distance is determined from the delay experienced by the optical pulses after traveling a complete round-trip to a target. They offer simplicity and allow to attain large ambiguity ranges, which are set by the periodicity of the optical pulses. However, they impose high demands on the system components, requiring transmitters and detectors with high bandwidths capable of handling high peak powers. Alternatively, the implementation of modulation techniques in a CW laser source permits to relax the bandwidth requirement of ranging systems and to improve their sensitivity, enabling the use of lasers with low power capabilities such as laser diodes. Under this category, frequency-modulated continuous-wave (FMCW) LIDARs have proven to effectively provide distance and velocity measurements with sub-micrometer precision and non-ambiguity ranges typically on the order of tens of meters [166]. These systems are based on the frequency modulation of the transmitter using a periodic RF chirped signal. The light backscattered from the target is beaten with a local oscillator, whose frequency is also modulated by the same chirped signal. The beat note generated in a photodetector, located at the frequency difference between the local oscillator and the backscattered beam, provides the information of the distance.

A novel type of LIDAR systems emerged with the advent of OFCs. These ranging systems allow to improve the performance of single-wavelength approaches, since many coherent optical carriers generated by a single laser source simultaneously interrogate the target [167]. Among these comb-based LIDAR technologies, dual-comb LIDARs stand out as particularly powerful systems, offering the potential to improve the precision of conventional interferometric ranging techniques down to the nanometer level while also enabling the use of low-bandwidth components and electronics [132]. As discussed in Chapter 3, there is an inherent trade-off between non-ambiguity range and acquisition speed, and the precision of the measurement improves for broader comb spectra. Many of the existing ranging demonstrations using dual frequency combs rely on the use of frequency comb generators with line spacings in the GHz range. While these approaches allow to measure distances with fast update rates in the microsecond range, the maximum measurable distance without ambiguity is limited to a few millimeters. Therefore, the practical use of such solutions requires the use of distance disambiguation techniques.

Commonly, a technique based on the realization of two measurements swapping the frequencies of the probe and the local oscillator is carried out. This yields two distances that differ by an integer multiple of the difference of the ambiguity range obtained in each scenario, i.e. $m\ \Delta d_{\mathrm{NAR}} = m(d_{\mathrm{NAR\,2}} - d_{\mathrm{NAR\,1}})$, where m is a positive integer and d_{NAR} denotes the non-ambiguity range. The value of the integer factor m can be determined from the two measurements, and the non-ambiguity range is now inversely proportional to the repetition rate difference of the two combs. In practice, a non-ambiguity range of a few millimeters can be extended to kilometers.

With the motivation of assessing distances in the kilometer range without the use of disambiguation techniques, a dual-comb ranging system based on low-repetition-rate GS frequency combs is proposed and experimentally demonstrated in this chapter. First, the gain-switched dual-comb ranging system is validated using two mutually-coherent GS OFCs with a repetition rate of 100 MHz. Subsequently, the further extension of the non-ambiguity range through the densification of the two GS combs is proposed and demonstrated in the second section of this chapter. The selected repetition rate of the ranging system results in a non-ambiguity range of 38 meters (in-air setup). An open-path relative distance of 2 mm is first measured, followed by a proof-of-concept measurement of a 10-meter-long fiber cord. The proposed densified ranging system shows promise for measuring maximum non-ambiguity ranges of hundreds of meters to a few kilometers, with the SNR of the system being the main limitation. Therefore, it represents a viable intermediate approach between long-range and short-range systems, allowing the measurement of distances up to a few kilometers with a single acquisition and with a simple and stable system comprising three semiconductor lasers and two electro-optic phase modulators.

6.2 Dual-comb ranging with 100-MHz gain-switched combs

This section is devoted to the experimental validation of a dual-comb ranging system based on low-repetition-rate GS combs. The proposed dual-comb generator is based on two optically-injected discrete-mode lasers operating in gain-switching regime. The gain-switching signal, which consists in a train of short electrical pulses featuring a repetition rate of 100 MHz, enables the generation of two stable and spectrally flat combs.

The system is tested by measuring an open-path relative distance of 4 millimeters. The influence of the number of interferogram bursts in the analyzed interferometric sequences on the measured distance is studied. Also, the variability of the retrieved distance based on analyses of various independent realizations acquired by the system is evaluated Finally, the impact of averaging on the precision of the system is analyzed, and the Allan deviation is calculated for interferogram sequences comprised of different interferogram bursts per sequence.

6.2.1 Experimental setup

The experimental setup is depicted in Fig. 6.1. The comb generation side comprises three semiconductor lasers arranged in a master-slave configuration: two slave lasers (SL1 and SL2) and a master laser for optical injection. The two slightly-detuned OFCs are generated by gain switching the two slave lasers, which are commercial discrete-mode lasers (Eblana EP1550-0-DM-H19-FM). Both slave lasers share a common phase reference provided by the ML (Pure Photonics PPCL300). The gain-switching signal of each laser is provided by a low-noise current source (Arroyo Instruments 4200-DR series LaserSource), which delivers the DC current, and a pulse pattern generator (Anritsu MU181020A), delivering an RF pulsed signal. Moreover, although not depicted in the setup, two temperature controllers are used to stabilize the temperature of the two slave lasers. In addition, wideband amplifiers (Minicircuits ZVA-183W-S+) boost the signal at the output of each pulse generator in order to generate broad GS combs. The driving conditions of the slave lasers and the master laser are detailed in Table 6.1. The selected frequencies of the trains of pulses result in the generation of two OFCs featuring repetition rates of f_{R1}= 100 MHz and f_{R2}= 100.01 MHz.

The part of the setup dedicated to the implementation of ranging measurements is configured according to an asymmetric arrangement in which only the probe comb is directed towards the target. In the detection side, two pairs of balanced photodetectors (Koheron PD100BAC) are employed in order to simultaneously capture a calibration measurement (recorded by the reference balanced photodetector) and a measurement containing the information of the distance (recorded by the measurement photodetector). Once the combs are generated, first, the local oscillator is frequency-shifted by f_{shift} = 80 MHz using an acousto-optic modulator. Subsequently, the two comb branches are split with a 50:50 ratio. One pair of combs is directed to the reference photodetector, and the remaining halves of the combs are used for distance measurement.

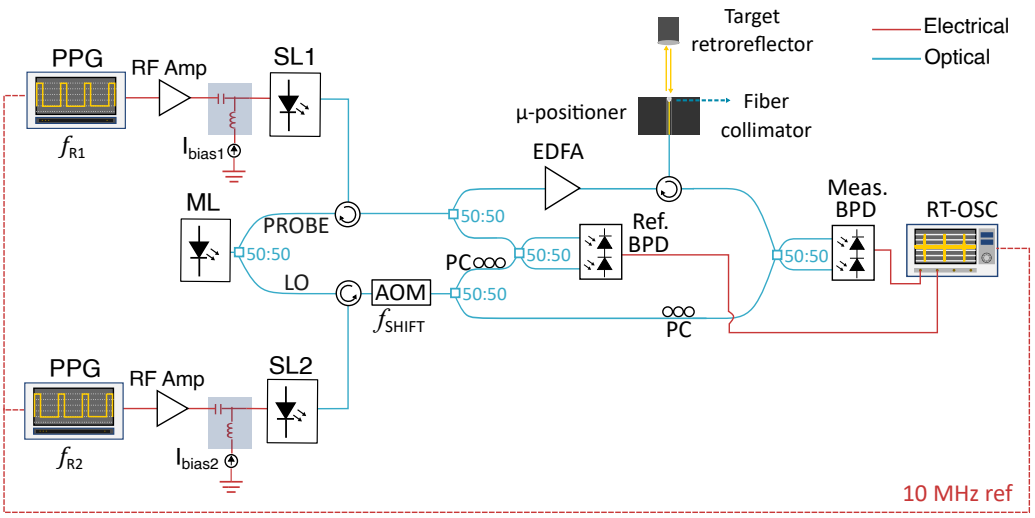

Figure 6.1: Experimental setup for the implementation of dual-comb ranging using gain-switched combs. Open-path relative distances are determined using the proposed setup. PPG: pulse pattern generator, SL: slave laser, ML: master laser, RF Amp: RF amplifier, PC: polarization controller, AOM: acousto-optic modulator, EDFA: erbium-doped fiber amplifier, BPD: balanced photodetector, RT-OSC: real-time oscilloscope.

Description	Symbol	Value
Master laser wavelength	λ_{ML}	1549.28 nm
Master laser power	P_{ML}	-3 dBm
SL1 DC bias current	I_{bias1}	0.8 mA
SL1 AC peak-to-peak voltage	V_{RF1}	8 V
SL1 AC pulse repetition rate	f_{R1}	100 MHz
SL2 DC bias current	I_{bias2}	0.7 mA
SL2 AC peak-to-peak voltage	V_{RF2}	7.1 V
SL2 AC pulse repetition rate	f_{R1}	100.01 MHz
Width of electrical pulses	τ_{pulse}	200 ps

Table 6.1: Driving conditions of the lasers for the implementation of dual-comb ranging at a repetition rate of 100 MHz.

The probe comb used to interrogate the distance is amplified using an EDFA (Thorlabs EDFA100S) and then sent to the target via an optical circulator. The distance measurement setup is connected to port 2 of the circulator. The optical fiber at port 2 is mounted on a manual micro-positioner stage (Thorlabs NanoMax 3-axis flexure stage), which allows to vary the distance to the target. The distance is varied by means of precision differential micrometers (Thorlabs DRV3), which provide a maximum variation of 8 mm in steps of 500 μm with a resolution of 0.5 μm. The optical field at this port is first collimated, and the collimated light is then directed towards a specular retroreflector prism (Thorlabs PS976M-M01B), which serves as target. The retroreflector is carefully

aligned to ensure that the reflected light is collected again by the optical fiber at port 2 of the circulator. The reflected probe comb is received at port 3 of the circulator and combined with the local oscillator. The combined combs are finally detected on the measurement photodetector. The two interferogram sequences at the output of each photodetector are digitized with a real-time oscilloscope (Keysight MSOS804A). Synchronization of the electrical signals is achieved by locking the two pulse pattern generators and the oscilloscope to a common reference.

To perform relative distance measurements, two measurements are conducted by varying the in-air distance traveled by the probe comb. This is achieved by manually adjusting the position of the optical fiber that launches the probe comb to the target (and subsequently collects the reflected light) between two positions of the micrometer stage where the fiber is mounted on. In the first acquisition, the distance information d_0 is retrieved. Subsequently, the fiber position is changed, resulting in an open-path distance of d_1. In both acquisitions, the signal from the reference photodetector is stored. The simultaneous acquisition of reference and measurement signals allows for the compensation of system drifts. Finally, polarization controllers are included in the setup to align the state of polarization of the probe and local oscillator before coupling the two fields.

6.2.2 Experimental results

The experimental results are organized as follows. First, the generation of the two mutually-coherent combs is presented, including an analysis of figures of merit related to their spectral quality. Subsequently, the detected interferograms and the corresponding down-converted spectra are analyzed. The post-processing steps employed to extract the distance information are then detailed. Finally, the results of the distance measurements and the analysis of the precision of these measurements are provided.

Generation of two optical frequency combs

The first step is the generation of the two mutually-coherent combs. The two laser diodes employed for the generation of the two OFCs are of the same model and manufacturer, and possess very similar characteristics. This similarity is evidenced by the generation of two nearly identical OFCs, achieved under comparable laser driving conditions.

For the generation of the combs, they are initially monitored in absence of optical injection using an optical spectrum analyzer. Under these conditions, two incoherent spectra, without resolved spectral tones, are observed. The temperature of each laser is then slightly adjusted until the two incoherent spectra overlap. Once this is achieved, the optical injection wavelength is chosen to maximize the spectral flatness of both combs, and the injection power is adjusted to ensure operation in the locking regime. This process, with the specified gain-switching parameters, results in the two GS combs shown in Fig. 6.2, which are measured with a high-resolution optical spectrum analyzer. Both combs exhibit similar characteristics in terms of spectral width, flatness, and carrier-to-noise-ratio. In addition, their coherence is proved by the presence of defined

comb lines (see closer view provided in panel (b)). The OFC generated by SL1 features a 10-dB bandwidth of Δf_{10dB}= 116.3 GHz and a carrier-to-noise ratio within this bandwidth of CNR = 20.74 dB. Analogously, these figures of merit calculated for the comb generated by SL2 are Δf_{10dB}= 114.8 GHz and CNR = 21.14.

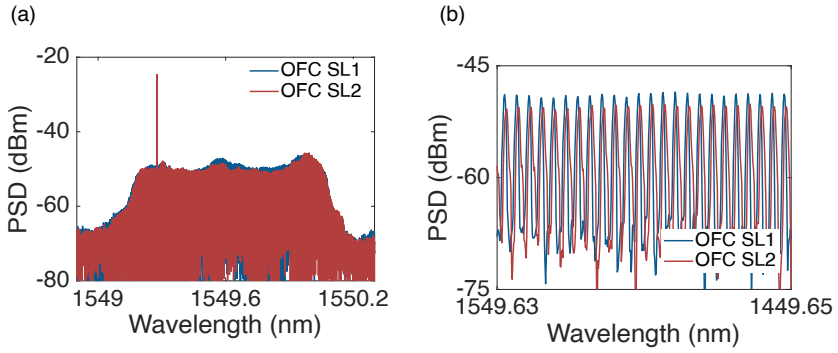

Figure 6.2: (a) Optical spectra of the two GS 100-MHz OFCs employed for dual-comb ranging. The spectra are measured with a high-resolution (10 MHz) optical spectrum analyzer (BOSA). (b) Zoom of a 0.02 nm region.

When spectroscopic measurements were performed, the spectral width of the combs was adjusted to match the width of the line being measured. This adjustment ensured that the bandwidth of the combs was sufficiently broad to accommodate the measurement of both the absorption feature and the baseline, while avoiding excessive broadening that would result in the inefficient use of power on unnecessary lines. In contrast, for dual-comb ranging experiments using an interferometric approach for the determination of the distance, the bandwidth of the combs needs to be maximized. This maximization allows to retrieve the distance from a greater number of spectral lines, thereby increasing the precision of the measurement. It is for this reason that both pulsed electrical excitation signals have been amplified, as a greater spectral width is achieved through a greater excursion of the carriers (resulting in a greater dynamic chirp). Therefore, with the obtained spectral widths and with the line spacing of the combs being 100 MHz, around 1150 spectral tones in a 10-dB bandwidth can simultaneously measure the configured distance. In addition, taking into account that the measurements are conducted in air and that the probe comb travels to and from the target, the non-ambiguity range of the system is 1.5 meters.

Generation of down-converted dual-comb spectrum

The mixing product occurring in the two photodetectors of the system, reference and measurement photodetectors, gives rise to two interferogram sequences. The reference or calibration interferogram sequence serves to compensate for drifts experienced by the system during the realization of the experiments, ensuring the correct determination of the interrogated distance. This interferogram sequence contains the information of the optical distance corresponding to the paths traversed by the probe and local oscillator combs until they reach the reference photodetector, $L_{ref,probe}$ and $L_{ref,LO}$, respectively.

On the other hand, the interferogram sequence captured in the measurement photodetector, in addition to the setup internal distance, includes the information of the distance to be measured. In a first acquisition, this distance will have a value of d_0 and consequently, the total optical distance traversed by the probe comb amounts to $L_{meas,probe} + 2d_0$. In a subsequent acquisition, this distance will be $L_{meas,probe} + 2d_1$. In both acquisitions, the distance traveled by the local oscillator OFC to the measurement photodetector is given by $L_{meas,LO}$. As the proposed ranging system is based on the retrieval of relative distances, the contribution of the optical distances $L_{ref,probe}, L_{meas,probe}, L_{ref,LO}, L_{meas,LO}$ is eliminated, and only the relative distance $2d = 2(d_1 - d_0)$ remains.

Fig. 6.3 (a) shows a single interferogram burst recorded by the real-time oscilloscope. The acquisition of the oscilloscope is configured to 200 MSa/s. Therefore, the temporal duration of a single interferogram of $\delta f_R^{-1} = 100$ μs corresponds to 20000 samples. This duration determines the fastest acquisition speed of the proposed system. The resulting dual-comb spectrum, obtained by the fast Fourier transform of the temporal signal, is depicted in Fig. 6.3 (b). The displayed spectrum corresponds to that located in the first Nyquist zone, with the optical injection tone centered at the acousto-optic modulator frequency, i.e., 80 MHz. Since only a single period of the interferogram signal is considered, the dual-comb spectrum does not show the individual down-converted lines but still contains the distance information, as later demonstrated.

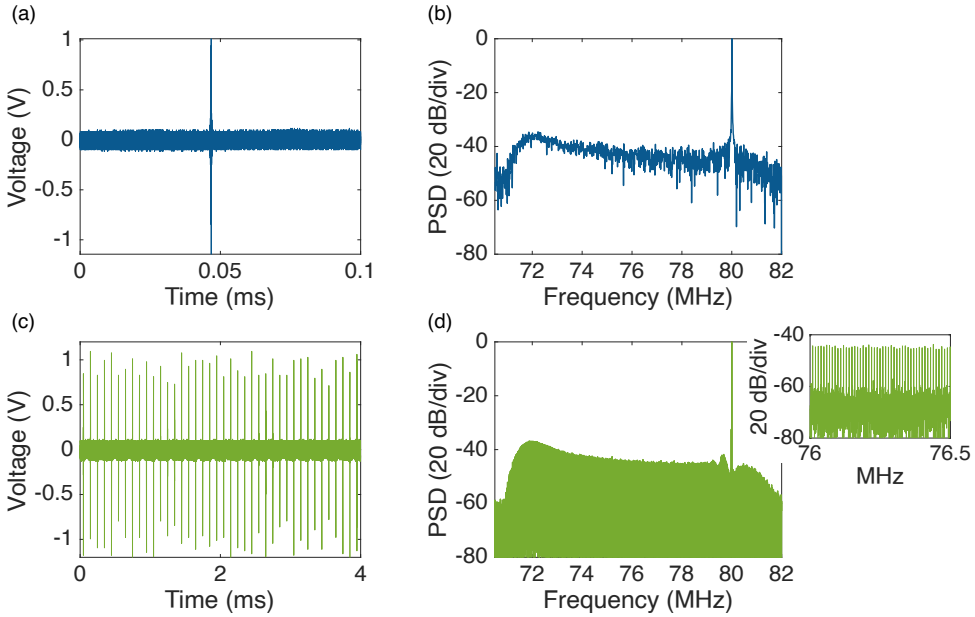

Figure 6.3: (a) Single interferogram burst digitized with the oscilloscope and (b) corresponding dual-comb spectrum. (c) Digitized time-domain interferogram sequence comprising 40 interferogram bursts and (d) spectrum obtained after Fourier transforming said sequence. The inset shows the down-converted beat notes, which are evenly spaced by δf_R=10 kHz.

An interferogram sequence containing a total of 40 interferogram bursts and its corresponding spectrum are shown in Fig. 6.3 (c) and (d), respectively. This acquisition, performed in a total measurement time of 4 ms, results in a down-converted spectrum that exhibits resolved individual lines due to the periodicity of the Fourier-transformed temporal signal (see inset of panel (d)). In both scenarios, single burst and 40 bursts, the same up-converted spectral resolution of 100 MHz is maintained. The second scenario provides better signal-to-noise performance, at the expense of a slower acquisition speed.

Post-processing of dual-comb ranging data

Digital signal processing of the interferometric data is performed offline, using a home-built MATLAB code. The determination of the relative distance is achieved through the analysis of four time-domain interferogram sequences. Two simultaneously acquired sequences (one at each photodetector) linked to the distance d_0, and two simultaneously acquired traces corresponding to the distance d_1.

The digitized interferogram sequences are first conditioned to ensure that all four sequences contain the same number of interferogram bursts, N_{interf}. Additionally, N_{interf} must be an integer; otherwise, errors may be induced.

After this, the dual-comb spectra of the four interferogram signals are obtained. A peak detection routine is then performed to extract the position of each down-converted comb line, as it is at these positions that the phase information is to be analyzed. Once the positions of the comb lines of the four spectra are identified, the spectral phase of each comb line is extracted. Following this process, the spectral phase at each comb line m for the reference and measurement interferogram sequences containing the information of the distances d_0 and d_1 are obtained, denoted $\phi_{r0,m}$, $\phi_{m0,m}$, $\phi_{r1,m}$ and $\phi_{m1,m}$, respectively. The expression of these spectral phases, according to the analysis described in Chapter 3 (Eq. (3.34), Eq. (3.35)), is given by

$$\phi_{r0,m} = \phi_{r1,m} = \frac{2\pi n(\nu_{01} + mf_R)}{c}(L_{ref,LO} - L_{ref,probe}) + \frac{2\pi n(\delta f_0 + m\delta f_R)}{c} L_{ref,LO}, \tag{6.1}$$

$$\phi_{m0,m} = \frac{2\pi n(\nu_{01} + mf_R)}{c}(L_{meas,LO} - L_{meas,probe} - 2d_0) + \frac{2\pi n(\delta f_0 + m\delta f_R)}{c} L_{meas,LO}, \tag{6.2}$$

$$\phi_{m1,m} = \frac{2\pi n(\nu_{01} + mf_R)}{c}(L_{meas,LO} - L_{meas,probe} - 2d_1) + \frac{2\pi n(\delta f_0 + m\delta f_R)}{c} L_{meas,LO}, \tag{6.3}$$

where n is the refractive index of the medium, while the remaining symbols have been previously defined. In the case of in-air measurements, n=1 is considered.

Once the phase information at the comb lines of the four digitized sequences is extracted, the distance can be determined. First, for each distance, the phase values of the reference comb lines is subtracted to that of the measurement comb lines. This operation gives rise to two differences of phases at each beat note m, $\Delta\phi_{d0,m}$ and $\Delta\phi_{d1,m}$,

$$\begin{aligned}\Delta\phi_{d0,m} &= \phi_{m0,m} - \phi_{r0,m} = \\ &= \frac{2\pi n(\nu_{01} + mf_R)}{c}(L_{meas,LO} - L_{meas,probe} - 2d_0 - L_{ref,LO} + L_{ref,probe}) + \\ &\quad \frac{2\pi n(\delta f_0 + m\delta f_R)}{c}(L_{meas,LO} - L_{ref,LO}),\end{aligned} \tag{6.4}$$

$$\begin{aligned}\Delta\phi_{d1,m} &= \phi_{m1,m} - \phi_{r1,m} = \\ &= \frac{2\pi n(\nu_{01} + mf_R)}{c}(L_{meas,LO} - L_{meas,probe} - 2d_1 - L_{ref,LO} + L_{ref,probe}) + \\ &\quad \frac{2\pi n(\delta f_0 + m\delta f_R)}{c}(L_{meas,LO} - L_{ref,LO}).\end{aligned} \tag{6.5}$$

Finally, from the subtraction of the two differences of phases the information of the relative distance d can be obtained. The expression of this phase difference, $\Delta\Phi$, is given by

$$\Delta\Phi = \Delta\phi_{d1,m} - \Delta\phi_{d0,m} = \frac{2\pi n(\nu_{01} + mf_R)}{c} 2(d_1 - d_0). \tag{6.6}$$

It can be verified that Eq. (6.6) does not depend on other optical distances rather than the ones to be determined, i.e, d_1 and d_0.

Finally, the phase information at each comb line given by $\Delta\Phi$ is unwrapped, and a straight line is fitted to the unwrapped $\Delta\Phi$ using the method of least squares. Then, the distance is obtained from the slope of the fit. The error on the distance, derived from the error on the slope σ_{slope}, is provided as a precision indicator. The results are analyzed based on varying numbers of interferogram bursts included in each sequence. Furthermore, the impact of averaging is also studied. When averaging is applied, it is performed in the final step of the process; specifically, the unwrapped $\Delta\Phi$ are averaged.

Free-space 4-mm relative distance measurement

A relative distance of 4 mm is measured following the described procedure. First, sequences containing a single interferogram ($N_{interf} = 1$) are analyzed. The four spectra associated to the four interferogram bursts lack defined peaks. Consequently, a peak detection routine is not conducted in this instance; instead, all the information in the spectrum is collected. This approach is feasible because the down-converted spectrum

that corresponds to the analysis of a single interferogram is composed of data points with a frequency spacing of $\delta f_R = 10$ kHz. The down-converted spectral region between 71.8 MHz and 79.2 MHz is selected for the extraction of the information. In this region, the dual-comb spectrum is flat, and the injection peak, which introduces instabilities in the measurement, is avoided. As a result, 740 frequency data points are employed to determine the relative distance.

The top panels of Fig. 6.4 –panels (a), (b), (c), and (d) –show the four unwrapped spectral phases obtained from the four analyzed interferogram bursts. The graphs demonstrate that the spectral phases corresponding to the calibration measurement (ϕ_{r0} and ϕ_{r1}) exhibit a linear trend. On the other hand, the unwrapped phases corresponding to the interferograms obtained when the probe comb is transmitted through the open-path distance (ϕ_{m0} and ϕ_{m1}), deviate from linearity. The evolution of the spectral phase between successive comb lines is expected to be linear, and the loss of linearity is attributed to the unwrapping procedure. However, even though ϕ_{m0} and ϕ_{m1} deviate from being linear when unwrapped, the unwrapped phase differences associated with the two distances d_0 and d_1 are indeed linear, as demonstrated in Fig. 6.4 (e) and (f). In addition, it should be noted that although all the spectral phases in the figure have been unwrapped to allow for the visualization of their line-by-line evolution, the unwrapped values are not used when operating with the phases. Only the final phase difference, $\Delta\Phi$, is unwrapped. The unwrapped $\Delta\Phi$, from which the distance information is obtained, is depicted in panel (g).

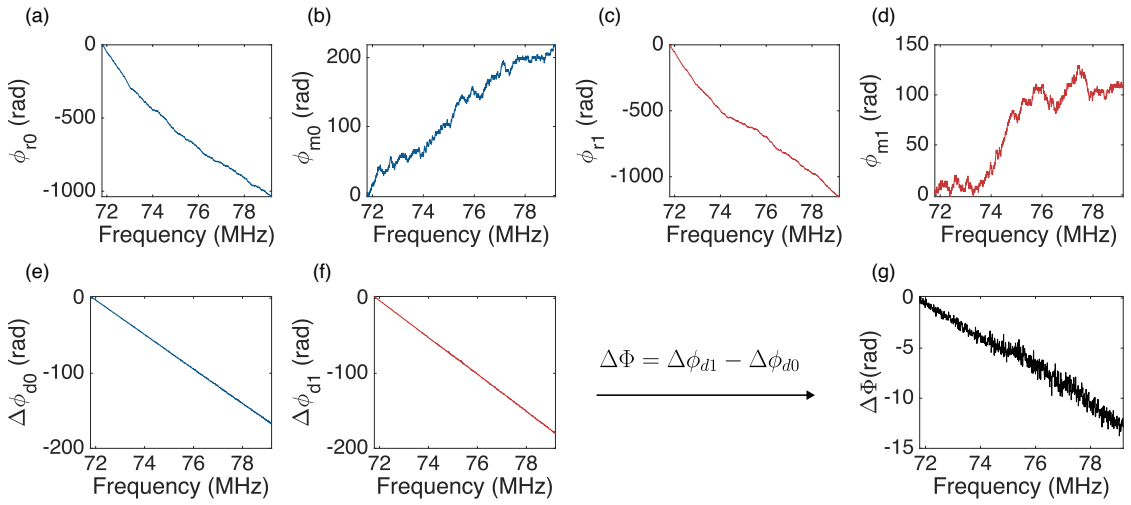

Figure 6.4: Spectral phases obtained from the analysis of a single interferogram in free-space 4-mm dual-comb ranging measurements. (a) Unwrapped calibration phases and (b) unwrapped measurement phases obtained for an interrogated free-space distance d_0. (c) Unwrapped calibration and (d) measurement phases retrieved from the acquisition corresponding to the distance d_1. (e) Unwrapped phase difference calculated by subtracting the calibration phases from the measurement phases for the distance d_0, and (f) for d_1. (g) Unwrapped difference of phase differences from which the relative distance d is extracted.

The relative distance obtained from processing a single set (without averaging) of interferometric sequences containing a single interferogram is shown in Fig. 6.5 (a). The distance, derived from the slope of the fitted straight line depicted as a solid red line, is $d = 3.9528$ mm, with an error of 22.5 μm. This error reflects the accuracy of the fit, and it is expected to decrease with averaging due to the reduction in the deviation of the experimental phase difference.

The evolution of the phase difference function with averaging is shown in Fig. 6.5 (b) and (c). Panel (b) depicts the result obtained after averaging fifteen unwrapped $\Delta\Phi$, yielding a distance of $d = 3.9947$ mm with an error of 6.6 μm. The phase difference shown in panel (c) corresponds to an averaging factor of 25, resulting in a measured distance of 3.9833 mm and a reduced error of 5.4 μm.

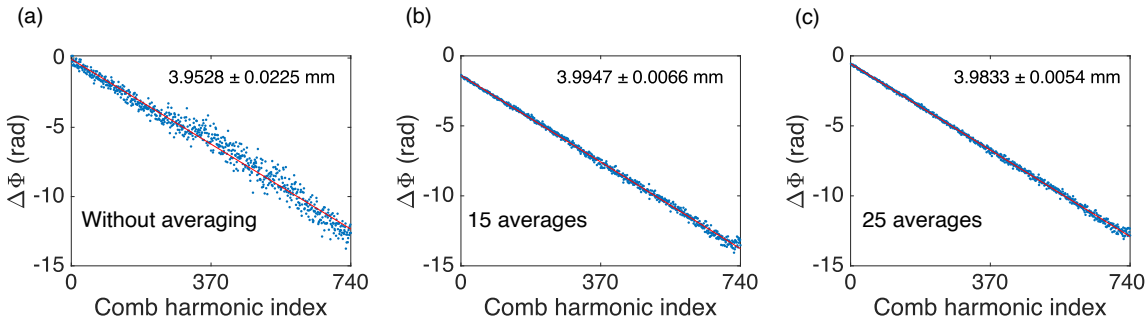

Figure 6.5: Unwrapped phase values obtained for 740 data points after post-processing single-interferogram sequences (blue plots) and least-squares fit performed to the experimental data (red line). Results obtained (a) without averaging, (b) by averaging 15 phase lines, and (c) by averaging 25 phase lines. The distance, indicated in each panel, is obtained from the slope of the fit. The error on the distance is obtained from the error on the slope.

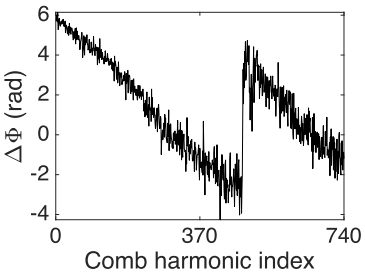

Figure 6.6: $\Delta\Phi$ obtained after an erroneous unwrapping process

The different interferogram bursts are extracted from the same temporal trace, i.e., a long interferometric sequence is acquired with the oscilloscope and then divided into single interferogram bursts. When analyzing single interferogram sequences, the unwrapped $\Delta\Phi$ curves do not always follow a linear trend due to errors in the unwrapping process (see Fig. 6.6). When this occurs, the distance obtained from the spectral phase difference does not show a reliable value. To avoid these errors, a threshold that requires the obtained distance to be between 3.8 mm and 4.2 mm is defined.

Then, the number of interferogram bursts included in a sequence is increased to $N_{interf} = 40$, and the decrease in the dispersion of the experimental data with averaging is also studied in this scenario. Fig. 6.7 shows the spectral phases obtained from fifteen interferogram sequences, each sequence containing 40 interferograms. Panels (a), (b), (c), and (d) depict the evolution of the unwrapped phases obtained in the

two photodetectors for the two distances d_0 and d_1 when processing the fifteen interferometric sequences. As before, the calibration phases maintain a linear trend, while the measurement phases deviate from linearity. The subtraction of the calibration and measurement phases at each distance provides the phase differences plotted in panels (e) and (f). Finally, the unwrapped phase that arises from the subtraction of the two phase differences $\Delta\phi_{d0}$ and $\Delta\phi_{d1}$ is shown in Fig. 6.7 (g). Fifteen $\Delta\Phi$ lines are obtained, which will be subsequently averaged to determine the distance. The offset difference, noticeable when comparing the fifteen $\Delta\Phi$ lines, is attributed to phase instabilities of the master laser between sequential acquisitions.

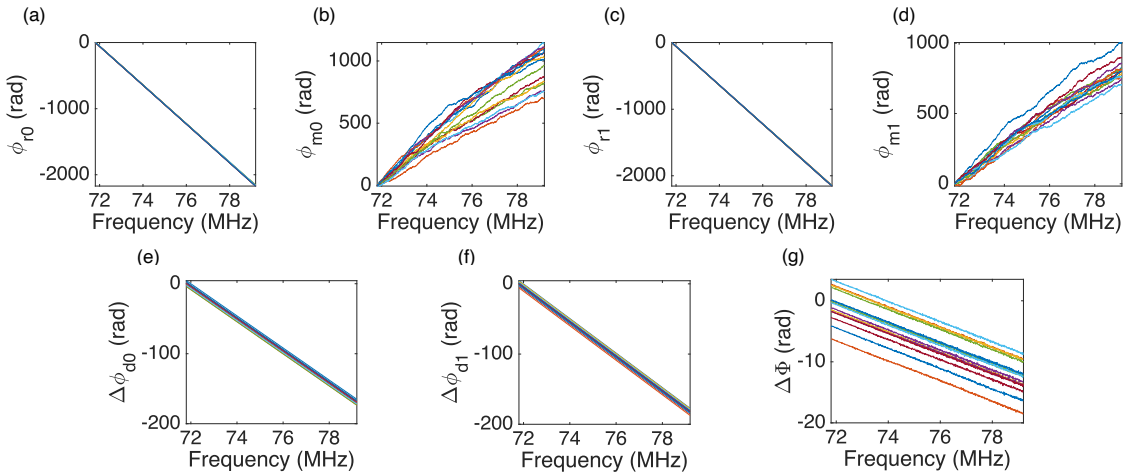

Figure 6.7: Unwrapped spectral phases obtained from the analysis of fifteen sequences comprised by N_{interf}=40 interferogram bursts in free-space 4-mm dual-comb ranging measurements. (a), (b) Calibration and measurement phases obtained for d_0. (c), (d) Calibration and measurement phases obtained for d_1. (e), (f) Unwrapped phase differences $\Delta\phi_{d1}$ and $\Delta\phi_{d0}$. (g) Phase difference $\Delta\phi_{d1} - \Delta\phi_{d0}$

The distance calculated from the slope of $\Delta\Phi$ obtained from the analysis of sequences including N_{interf}= 40 interferograms is shown in Fig. 6.8. In this case, in contrast to the previous scenario where sequences with a single interferogram were analyzed, all the obtained phase lines $\Delta\Phi$ provide a reliable distance value within the established margins. The absence of erroneous $\Delta\Phi$ experimental curves can be attributed to the better CNR of the down-converted spectra. Furthermore, this scenario results in a reduction in the variability of the obtained distance, as evidenced in Fig. 6.8 (b) and (c), which represent the results obtained for 15 and 25 averages, respectively. Both figures yield the same distance value of d= 3.9306 mm. For 15 averaged phase lines, the residuals from the fitting process are very low, as reflected by the low error value of 0.9 μm. This error is reduced to 0.7 μm when the number of averages increases to 25. In these graphs, the number of averages represents the number of $\Delta\Phi$ functions averaged. In terms of the total number of averaged interferogram bursts, these quantities correspond to 600 and 1000 interferograms, respectively. In addition, in terms of averaging times, these numbers are equivalent to 60 ms and 100 ms.

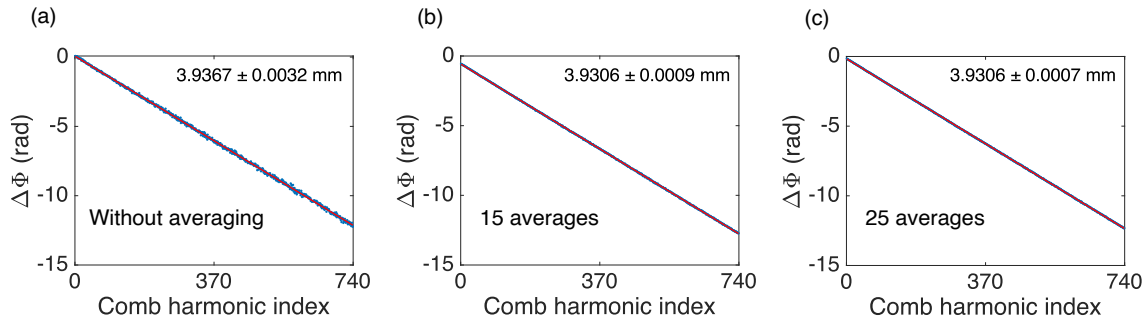

Figure 6.8: Spectral phases $\Delta\Phi$ obtained for 740 comb lines from the analysis of interferogram sequences of N_{interf}=40 bursts and extracted distance. Results obtained (a) without averaging, (b) by averaging 15 phase lines, and (c) by averaging 25 phase lines.

Precision analysis of the system

The variability of the distance values retrieved from different acquisitions is first analyzed. This analysis indicates the reproducibility of the measurements. Fig. 6.9 (a) shows the distances obtained from sixty-three sets of interferogram sequences with N_{interf}=1 burst per sequence. To obtain this result, 100 sets of interferogram sequences were analyzed, i.e. 100 independent realizations sequentially captured with the real-time oscilloscope. The reliability condition (3.8 mm$<d<$ 4.2 mm) was then applied to the obtained distances resulting in sixty-three distance values falling within the boundaries. Consequently, 37% of the analyzed sequences led to unreliable results. An average distance of 3.9663 mm is obtained, with a standard deviation of 9.64%.

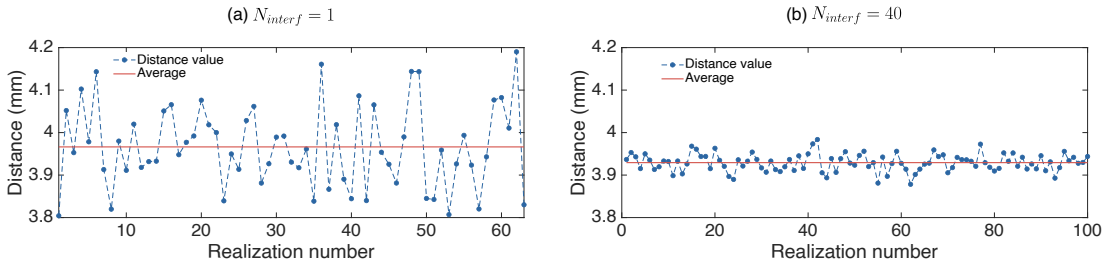

Figure 6.9: Variability of the distance obtained from the analysis of different sequentially-acquired interferometric realizations. The blue dots joined by a dashed line represent the experimental distance values and the red solid line represents their average value. (a) Results obtained from the analysis of traces comprised by one single interferogram and (b) by 40 interferogram bursts.

The variability of the measured distance is reduced by including a higher number of bursts in the analyzed interferogram sequences, as evidenced in Fig. 6.9 (b), which corresponds to the analysis of 100 independent realizations, each realization containing N_{interf}= 40 bursts. In this case, all the analyzed sequences yielded distance values that met the reliability condition. The standard deviation decreases to 2.04%, with the average distance being 3.9293 mm.

The impact of averaging on the achievable precision is also studied. This analysis is performed with sequences comprised of N_{interf}= 40 interferogram bursts. As before, the interferometric sequences used for the analysis correspond to independent and sequential acquisitions of the oscilloscope in order to avoid biased results. Fig. 6.10 (a) shows the evolution of the measured distance (blue curve) with averaging. The error bars indicate the error on the distance. The error on the distance reflects accurate values when increasing the number of averages, as depicted in the inset of the figure. The estimated distance obtained for the maximum measurement time of 400 ms, achieved by averaging one hundred $\Delta\Phi$ phase lines, is 3.9293 mm. This value is the same as the one obtained from the average distance derived from one hundred realizations, indicating the validity of the results. The red line on the graph depicts the evolution of the coefficient of determination (R-squared coefficient) obtained from the fitting.

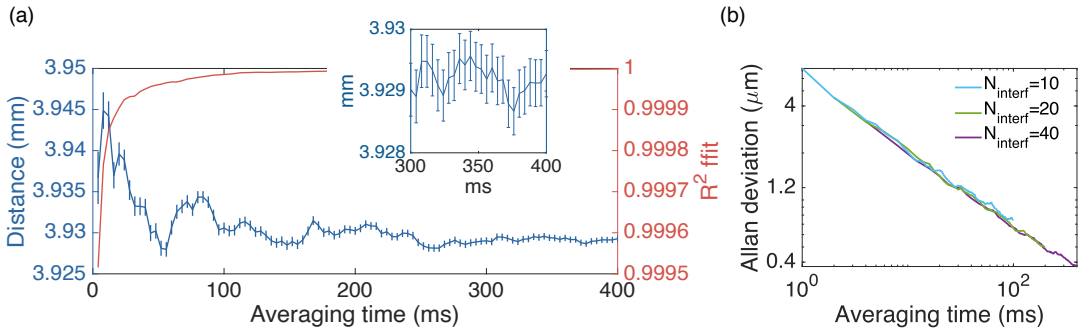

Figure 6.10: (a) (blue) Evolution of the measured distance with averaging. The information is retrieved from the analysis of interferogram sequences containing 40 interferogram bursts per sequence. The error bars indicate the error on the distance. (red) Evolution of the R-squared coefficient of the linear regression with averaging. (b) Allan deviation obtained from the analysis of interferogram sequences including 20 (green) and 40 (purple) bursts.

Finally, the Allan deviation as a function of the averaging time is computed. It is calculated as the evolution of the error on the distance (σ_d) with the averaging time for three scenarios: N_{interf}= 10, N_{interf}= 20 and N_{interf}= 40. The results are shown in Fig. 6.10 (b), demonstrating similar outcomes for the three analyzed scenarios. This graph shows that the achievable precision improves with averaging. The best precision, obtained for the maximum analyzed averaging time of 400 ms, is 0.5 μm.

6.3 Extension of the non-ambiguity range using densified gain-switched combs

This section is devoted to the demonstration of the extension of the non-ambiguity range of a dual-comb ranging system based on two GS laser diodes. It is achieved through the densification of the two GS combs by means of two EOPMs driven by maximum length sequences.

The system is first validated by the measurement of an open-path distance of 2 millimeters. In addition, the improvement of the precision of the measurement with averaging is analyzed up to an averaging time of 1.24 seconds. Finally, initial demonstrations on the measurement of a longer distance of 10 meters are presented.

6.3.1 Experimental setup

The setup employed for the realization of the experiments is shown in Fig. 6.11. The OFC generation side, delineated by a gray block, comprises two densified GS comb generators. The same configuration and driving parameters as those detailed in the previous chapter for dual-comb spectroscopy with densified GS OFCs (Section 5.3.2) are employed. As a result, two phase-locked densified GS combs with frequencies of f_{dens1}= 3.9369685 MHz and f_{dens2}= 3.9370079 MHz (δf_{dens}= 39.37 Hz) are generated at the output of each EOPM. The reduction of the repetition rate to a few MHz allows to increase the non-ambiguity range of the system. In the case of an open-path approach, where the optical signal travels to the target and back, the non-ambiguity range corresponding to the densified repetition rate is approximately 38 meters. When considering an in-fiber distance in a transmission configuration, the non-ambiguity range is approximately 52 meters.

To assess the validity of the ranging system, first, an open-air distance of 2 mm is measured. The same setup and strategy as those indicated for dual-comb ranging with non-densified GS combs is followed, although in this experiment the target is an optical mirror. In a subsequent experiment, aiming to test the extended non-ambiguity range of the system, a single-mode fiber cord with a length of 10 meters is interrogated. An optical switch allows for the selection between a reference path, in which the two ports of the switch are interconnected, and a measurement path, in which the probe comb traverses the fiber cord.

Finally, in the two experiments, the two beating signals produced by the two balanced photodetectors are digitized using a real-time oscilloscope. Again, the clock of the oscilloscope is synchronized to the 10-MHz reference signal of the RF generators, which include the arbitrary waveform generator and pulse pattern generators.

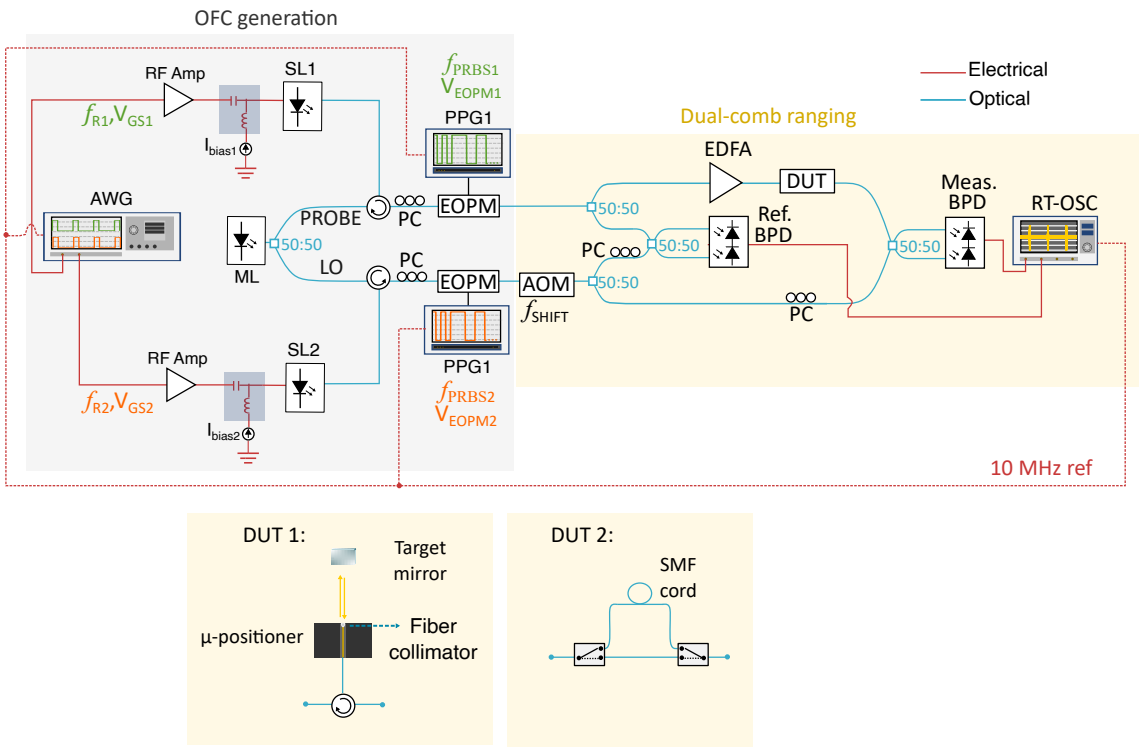

Figure 6.11: Block diagram of the experimental setup implemented to perform dual-comb ranging with an increased non-ambiguity range. Two distances are evaluated to validate the results: an open-path distance of 2 mm, device under test (DUT) 1, and an in-fiber distance of 10 m, DUT 2. AWG: arbitrary waveform generator, PPG: pulse pattern generator, SL: slave laser, ML: master laser, PC: polarization controller, EOPM: electro-optic phase modulator, AOM: acousto-optic modulator, EDFA: erbium-doped fiber amplifier, BPD: balanced photodetector, RT-OSC: real-time oscilloscope, SMF: single-mode fiber.

6.3.2 Experimental results

The experimental results begin with the illustration and characterization of the retrieved interferogram sequences and the resulting down-converted densified spectra. The optical spectra are not included here, as the same densified combs showed in ultra-high resolution spectroscopic experiments are utilized (refer to Section 5.3.5). Following this, the determination of the open-path 2-mm distance is presented, and the precision of the measurement is analyzed. The experimental results conclude with a proof-of-concept demonstration of an in-fiber distance measurement of 10 meters.

Generation of down-converted spectrum

The interferograms generated at the output of the two balanced photodetectors included in the setup, when considering the free-space configuration with an open-path relative distance of 2 mm, are represented in Fig. 6.12. The oscilloscope is configured with a digitization rate of 250 MSa/s, and long traces comprised by $62.5{\cdot}10^6$ samples are acquired.

Fig. 6.12 (a) displays a segment of the interferogram sequences produced by each photodetector (calibration and measurement) for an interrogated distance d_0. The left panel presents the raw sequences digitized by the oscilloscope, consisting of interferogram bursts with a periodicity δf_R^{-1} of 0.2 ms. The right panel corresponds to the interferogram sequences obtained after applying a band-pass filter to the raw data. This filter retains the information from the first Nyquist zone, and the configured band-pass bandwidth encompasses the range from 79.6 MHz to 80.6 MHz. The resulting interferogram reproduces with the periodicity of the densified repetition rate difference, i.e. δf_{dens}^{-1}= 25.4 ms, as discussed in the previous chapter. Consequently, given the acquisition settings, the total measurement time per interferogram sequence is 250 ms, which includes 1250 non-filtered bursts with a periodicity of 0.2 ms or, equivalently, approximately 10 filtered bursts at 25.4 ms. Portions of the raw interferogram sequences obtained by adjusting the position of the launching fiber to d_1 are provided in Fig. 6.12 (b).

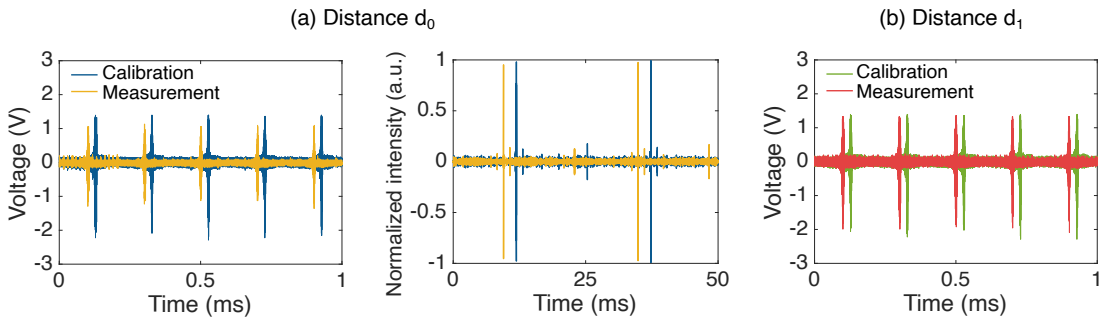

Figure 6.12: (a) (left) Dual-comb raw interferograms and (right) band-pass filtered interferograms provided by the calibration (blue) and measurement (yellow) balanced photodetectors for an open-air distance d_0. (b) Raw interferograms (green: calibration photodetector, red: measurement photodetector) acquired for an open-path distance d_1.

The dual-comb spectra obtained from the Fourier transform of the band-pass filtered calibration and measurement interferogram traces corresponding to the distance d_0 are shown in Fig. 6.13. The close-up view in the right panel verifies the presence of well-defined beat notes. The information of the distance is determined from the analysis of the beat notes located between 80.05 MHz and 80.25 MHz. The number of down-converted tones in that 200-kHz span amounts to 5080 tones. The down-converted tones exhibit a frequency spacing of 39.37 Hz. The selected spectral region is characterized by high spectral flatness. The spectral flatness calculated within this region is approximately 0.9 for the four RF spectra (reference d_0 spectrum 0.9, reference d_1 spectrum 0.92, measurement d_0 spectrum 0.92, measurement d_1 spectrum 0.94).

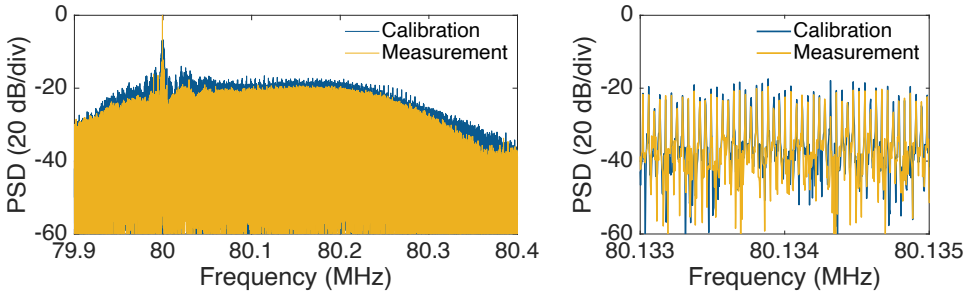

Figure 6.13: (left) Modulus of the fast Fourier transform applied to the filtered calibration (blue) and measurement (yellow) interferogram sequences. (right) Zoom of a 200-kHz span of the two RF spectra.

Free-space 2-mm relative distance measurement

The interferogram sequences are post-processed offline following the procedure described for the non-densified experiments. The acquired traces are truncated to ensure they contain an integer number of interferogram bursts and they are subsequently band-pass filtered. The conditioned interferogram sequences contain 1240 non-densified bursts and 10 densified bursts.

The four unwrapped spectral phases, obtained from the phase of the Fourier transform of the four filtered interferogram sequences at the locations of the beat notes, are shown in Fig. 6.14. As it was observed in the non-densified ranging measurements, the spectral phase of each comb line exhibits a slight deviation from linearity in its evolution.

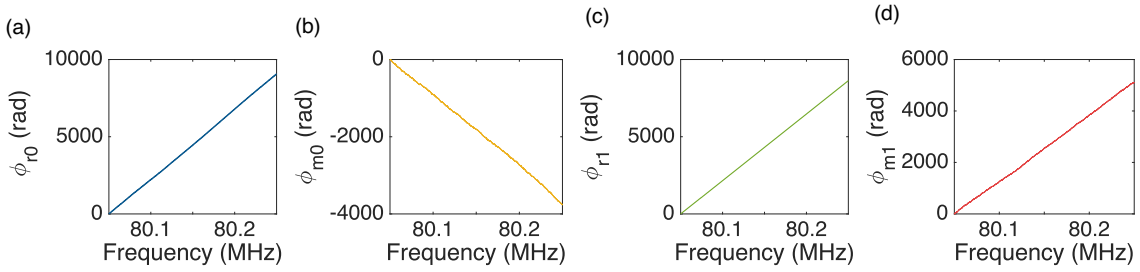

Figure 6.14: Unwrapped spectral phases calculated from the phase of the fast Fourier transform applied to the four interferogram sequences: (a) calibration d_0, (b) measurement d_0, (c) calibration d_1, and (d) measurement d_1. Only the phase values at the locations corresponding to the down-converted comb lines are considered.

The unwrapped spectral phase difference obtained for each configured distance, $\Delta\phi_{d0}$ and $\Delta\phi_{d1}$, are shown in Fig. 6.15 (b) and (c), respectively. The function obtained when unwrapping the subtraction of the two spectral phase differences, which contains the information of the relative distance on its slope, is depicted in panel (c). This graph reflects the result obtained without averaging $\Delta\Phi$ functions.

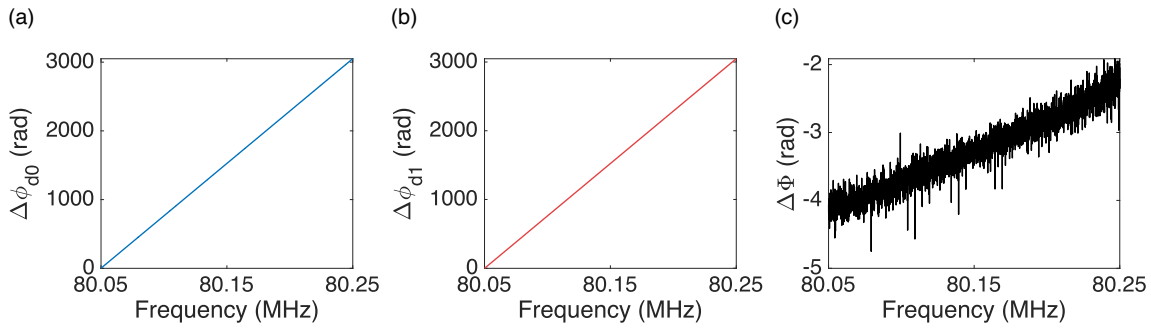

Figure 6.15: (a) Unwrapped phase difference obtained by subtracting the calibration spectral phase d_0 from the measurement spectral phase d_0. (b) Unwrapped phase difference obtained by subtracting the calibration spectral phase d_1 from the measurement spectral phase d_1. (c) Unwrapped phase difference obtained by subtracting $\Delta\phi_{d0}$ from $\Delta\phi_{d1}$.

A reduction in the dispersion of the data points is observed when averaging different $\Delta\Phi$ lines, resulting in an improvement in the precision when determining the distance. The evolution of $\Delta\Phi$ with averaging is illustrated in Fig. 6.16. Panel (a) corresponds to the result obtained without averaging. Panel (b) is obtained after averaging five unwrapped $\Delta\Phi$ curves. The distance is obtained from the slope of the fitted straight line, depicted in red in both graphs. The error on the distance decreases from 7.5 μm, obtained without averaging, to 4.6 μm, obtained with averaging. Therefore, as expected, averaging results in a better accuracy of the least-squares fit and in an enhanced precision of the measurement.

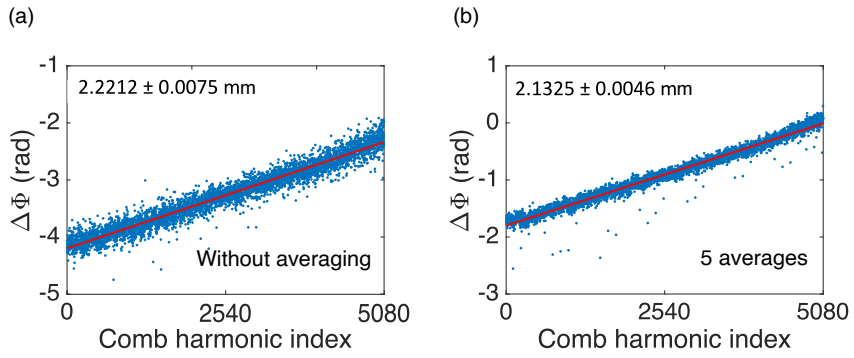

Figure 6.16: Unwrapped spectral phase difference $\Delta\Phi$ versus beat note index analyzed for 5080 RF tones (a) without averaging and (b) averaging five $\Delta\Phi$ functions. The blue dots represent the experimental points, and the red line corresponds to the linear fit applied to these points.

Precision analysis of the system

The precision of the system, as demonstrated in the non-densified experiments, improves when averaging several spectral phase difference functions. However, in the densification scenario, the acquisition of very long traces or the acquisition of several traces implies the use of digitizing and post-processing systems exhibiting demanding memory requirements. This is due to the fact that, in the densified dual-comb interferometry experiments, the acquisition speed is slower than in the non-densified case, since the minimum acquisition time corresponds to the duration of a densified interferogram. This time, compared to the non-densified case, is relatively high, as the decrease of the repetition frequency of the OFCs (and the subsequent reduction of the spectral separation between the replicas in the down-converted Fourier domain) forces to increase the compression factor or, equivalently, to decrease the repetition rate difference of the two combs.

In the context of this experiment, the minimum acquisition speed is 25.4 ms. Acquiring an interferometric trace consisting of ten 25.4 ms bursts at the specified digitization rate entails the acquisition of 62.5 million samples. Acquiring traces with a higher number of bursts, or a greater number of traces, to average a relatively high number of spectral phases depends on the capacity of the oscilloscope and the system used to post-process the data. For these measurements, the oscilloscope capacity was not set to its maximum (205 million samples). Nonetheless, the memory requirements were demanding, as each acquisition stored 62.5 million samples from the calibration signal and 62.5 million samples from the measurement signal for the two distances d_0 and d_1. Additionally, five sequential acquisitions were performed and later post-processed. Although additional sets could have been acquired to enhance the statistical reliability of the results, the validation of the system can be evaluated based on the attained result.

The distances obtained from the slope of five unwrapped $\Delta\Phi$ functions, extracted from the analysis of independent realizations, are provided in Fig. 6.17 (a). An average distance of 2.1325 mm is estimated, with a standard deviation of 6.24%. Finally, the precision of the free-space densified ranging system considering an interrogated relative distance of 2 mm, obtained from the Allan deviation, is shown in Fig. 6.17 (b).

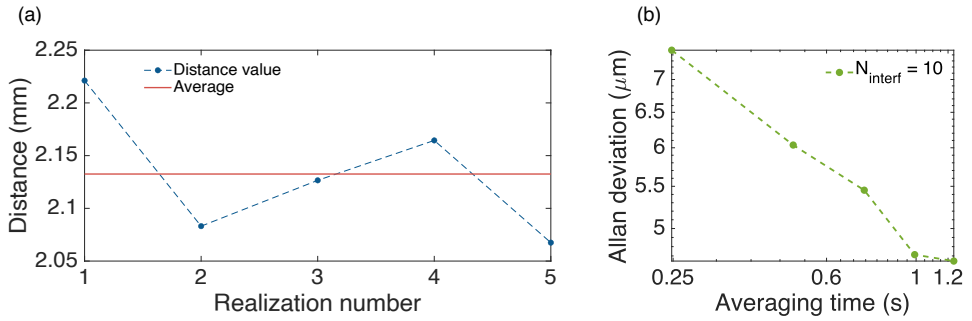

Figure 6.17: (a) Variability of the distance retrieved from post-processing five independent realizations (blue dots joined by dashed line) and average distance value (red solid line). (b) Evolution of the Allan deviation when averaging up to five unwrapped $\Delta\Phi$ functions derived from the analysis of interferogram sequences with 10 densified bursts per sequence.

The Allan deviation is calculated for traces of 10 densified interferograms per sequence. In this scenario, the achieved precision is lower than that obtained in the non-densified experiments when analyzing sequences with the same number of bursts per sequence. Therefore, this approach allows for an extension of the non-ambiguity range at the expense of lower performance in terms of precision. The best precision, obtained for an averaging time of 1.24 seconds, is 4.65 μm.

In-fiber 10-meter ranging measurement

Finally, a proof-of-concept demonstration to test the extended measurement range that can be determined with the densified dual-comb ranging system is carried out. The device under test used for this purpose is a standard single-mode fiber with a length of ∼10 meters, which is measured in transmission configuration.

The driving conditions of the densified dual-comb generator remain the same for these experiments. A single realization (with and without interrogating the fiber cord) of 125 million points is acquired with the real-time oscilloscope. With a sampling rate of 250 MSa/s, the measurement time per interferogram sequence amounts to 500 ms. The number of non-densified and densified bursts in that measurement time corresponds to 2500 and approximately 20, respectively. The interferogram sequences are conveniently processed to include 18 densified bursts (2400 non-densified interferograms).

In accordance with the aforementioned procedure, the distance information is extracted from the slope of the spectral phase difference $\Delta\Phi$, defined by 5080 comb lines. Fig. 6.18 shows the obtained result. The experimental data points are depicted by blue dots in the figure. The distance is extracted from the straight line fitted to the measured $\Delta\Phi$ points, which is represented by a solid red line in the graph. A distance of 9.9616 meters is estimated, with a precision of 900 μm. This precision, which is obtained without averaging, is expected to improve if several $\Delta\Phi$ functions were averaged. The accuracy of the system could be evaluated by comparing the measured distance with the measurement of an optical frequency domain reflectometer.

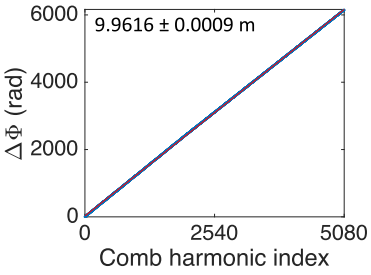

Figure 6.18: Unwrapped difference of spectral phases versus comb line index for an in-fiber distance measurement of ∼10 meters.

6.4 Conclusions

In this chapter, a ranging system based on two optically-injected GS OFCs has been demonstrated. The use of low-repetition-rate GS frequency combs has been proposed as a solution to increase the non-ambiguity range of these systems. Without implementing techniques to break the non-ambiguity range, the ranging system based on two densified GS OFCs with the repetition frequencies demonstrated in this chapter would enable the measurement of free-space distances of up to 38 meters (considering a round trip of

the optical signal to the target). This measurement range makes the system useful for realistic applications. The proposed system could find applicability in medium-distance ranging fields, including unmanned autonomous vehicles (enabling obstacle detection at medium distances), environmental monitoring and agriculture (for measuring the height of different species and vegetative density), and mapping, among others.

Dual-comb ranging systems based on GS combs offer a balance between precision and non-ambiguity range when compared to systems based on other comb sources. They provide measurement ranges comparable to those obtained with mode-locked combs based on fiber cavities, but with the possibility of being integrated on a chip. Although the attainable bandwidths are considerably lower than those typically observed in mode-locked fiber lasers, good precision values can be achieved through averaging. The stability of GS dual-comb architectures and the excellent mutual coherence of the combs, due to both comb generators being seeded by a common master laser, permits averaging times above 1 second, as demonstrated in this chapter in the densified GS dual-comb ranging system. Furthermore, in addition to the balance between precision and measurement range, GS dual-comb ranging systems exhibit other key features, such as the frequency agility of the comb generators. This frequency agility allows the easy modification of the comb repetition rate, thereby enabling the convenient adjustment of the non-ambiguity range.

Finally, the main limitation of the system is the low average power of the generated combs, which represents a substantial challenge, particularly for long open-path distances. For the proposed distance range (up to a few kilometers), losses could be mitigated through amplification. Nonetheless, further studies and expanded results for such free-space distances are necessary to fully validate this statement.

- Dual-comb ranging with 100-MHz gain-switched combs

In the first section of this chapter, open-path ranging measurements have been demonstrated with a GS dual-comb interferometer exhibiting a non-ambiguity range of 1.5 meters. Two GS OFCs featuring a repetition rate of 100 MHz have been generated for this purpose, comprising 1150 spectral tones in a 10-dB bandwidth of 115 GHz to simultaneously measure the desired distance. The two combs showed well-resolved tones with a carrier-to-noise ratio of around 21 dB.

The system has been validated by measuring a relative distance of 4 millimeters in an open-path configuration, in which only the probe comb was used to interrogate said distance. Ranging measurements have been performed using an interferometric approach based on the analysis of the spectral phase of the generated combs. Distance measurements with a measurement time as fast as 100 μs have been demonstrated. Additionally, the influence of the length of the analyzed interferogram sequences and the impact of spectral averaging on the precision of the measurements has been evaluated. It has been demonstrated that the precision of the system improves from 22.5 μm to 3.2 μm as the number of analyzed interferogram bursts increases from one to 40 bursts. Then, the precision has been further improved by averaging the spectral phase difference lines obtained from the analysis of multiple sets of interferogram sequences,

each containing 40 bursts per sequence. The Allan deviation of the measurement for this scenario demonstrated a precision of 0.5 μm for a maximum analyzed averaging time of 400 ms. A lower precision is expected to be obtained for higher averaging times, since the Allan deviation at the maximum analyzed averaging time does not show a trend towards saturation. In addition, the variability of the measured distance has been studied. Calculated from the analysis of independent realizations, this variability decreased as the number of bursts included in the interferogram sequence increased, which is equivalent to performing temporal averaging and thereby enhances the precision of the measurement. Finally, the reproducibility of the measured distance has been demonstrated. The distance obtained by averaging 100 distance values from the analysis of 100 independent realizations (without spectral phase averaging) has been found to be the same as the distance obtained from the analysis of 100 averaged sequences. This indicates the consistency and reliability of the results.

- Extension of non-ambiguity range enabled by densified gain-switched combs

In the second section of the chapter, the non-ambiguity range of the system has been extended by densifying the two GS combs using two EOPMs that externally modulate the optical phase of such combs. The repetition rates used resulted in a non-ambiguity range of 38 meters, considering a free-space arrangement. The approach successfully demonstrated the possibility of extending the maximum measurable distance in a simple manner, without the need of performing additional measurements for disambiguation. The spectral phase analysis has been conducted within a down-converted spectral range of 200 kHz, including 5080 beat notes evenly spaced by 39.37 Hz. The interferometric analysis has been conducted with sequences including various bursts per sequence, since this approach yields a better precision.

First, an open-path distance of 2 millimeters has been successfully measured. Sets of interferometric sequences comprising 10 densified bursts have been analyzed, resulting in a minimum acquisition time of 254 ms, which is larger than that of the non-densified scenario due to the reduced repetition rate of this approach. The 2-mm distance has been measured with a precision of 4.6 μm for an averaging time of 1.24 s. Despite the relatively long measurement time, the ability to perform measurements over periods exceeding 1 second highlights the good stability of the proposed system. Finally, a proof-of-concept measurement of a longer distance has been conducted to test the capability of the system for retrieving distances near its non-ambiguity range. A 10-meter fiber cord has been measured, resulting in the determination of the distance with a precision of 900 μm.

Chapter 7

Exploring other dual-comb interferometers

This chapter constitutes the final experimental chapter of this dissertation. In it, the results obtained during an international research stay at Chalmers Ultrafast Photonics group are presented. The experiments, conducted in collaboration with Israel Rebolledo-Salgado, represent the first demonstration of dual-comb interferometry with two mutually-coherent microcombs operating in the normal dispersion regime. This achievement was made possible during the three-month stay, thanks to the expertise of the group in the generation, control, and stabilization of the microcombs. The results, included in the fourth publication of this thesis, demonstrate the successful measurement of the phase response of a device under test showing excellent agreement between the measured and programmed phase profiles. These experiments validate the potential of systems based on normal-dispersion dual microcombs in terms of stability and coherence.

First, the generation of the two microcombs acting as probe and local oscillator is detailed. Then, the line spacing of one of the microcombs is measured via electro-optic down-conversion. Finally, the down-conversion of the two microcombs, which results in the generation of a dual-comb spectrum, is detailed, and the retrieval of the programmed phase profile is demonstrated.

7.1 Introduction

Dissipative Kerr solitons in microresonators enable the generation of on-chip coherent OFCs. These mode-locked states arise in high-quality-factor cavities fabricated from materials exhibiting third-order nonlinearity, when the cavity is appropriately pumped by a CW laser. The formation of these localized structures is easily achieved when the microresonator exhibits anomalous group velocity dispersion. For this reason, microcombs generated in anomalous-dispersion cavities were first reported and their dynamics have been thoroughly studied over the past years [88]. However, many nonlinear materials exhibit normal dispersion from the visible to the mid-infrared range [96]. As a consequence, it is necessary to engineer the dispersion of the devices in order to generate microcombs in the anomalous dispersion regime. Dispersion engineering involves specific dimensions of the waveguides that may be challenging to fabricate.

At present, silicon nitride stands out as the most extensively studied and mature platform for microcomb generation. This material exhibits low optical losses, is compatible with CMOS fabrication processes, and has a wide transparency window (from the visible to the near-infrared), which expands the application range of such combs to various areas, including biophotonics, sensing, and optical communications. Yet, at these wavelengths, silicon nitride exhibits normal dispersion. Although the formation of microcombs in normal-dispersion cavities is challenging due to the lack of modulation instability, different strategies such as the use of coupled cavities have proven to enable microcomb generation [99]. As a result, the possibility of generating microcombs in devices featuring normal dispersion alleviates the requirements for dispersion engineering and allows standard and mature processes to be used for the fabrication of the waveguides. Furthermore, normal-dispersion microcombs offer higher conversion efficiency compared to those generated in the anomalous dispersion regime [98].

In the work developed in this chapter, two microcombs generated in microresonators exhibiting normal dispersion are used to perform dual-comb interferometry. Each microcomb is generated in a coupled-cavity system consisting of two linearly-coupled cavities, in which the interaction between mode families of the two cavities at specific wavelengths enables to achieve local anomalous dispersion and hence trigger the formation of an OFC. The two cavities feature different sizes, inspired by the system reported by Ó. Helgason et al. [100]. This arrangement results in the longitudinal modes of the two cavities showing a large Vernier frequency, promoting mode interactions at targeted wavelengths while minimizing disruptions across other wavelengths. Furthermore, the integration of microheaters on top of the cavities enables precise control over the wavelengths where mode interactions occur. This configuration facilitates the generation of the two microcombs using a single laser to simultaneously pump both systems, thereby ensuring mutual coherence between the generated combs.

The use of the proposed system for dual-comb interferometry is validated by phase-sensitive measurements, and the quadratic phase profile of a programmed optical filter is successfully retrieved. The two combs operate at a repetition rate of 49.98 GHz with a repetition rate difference of 830 kHz, allowing to map the information of an optical

spectrum spanning 5.8 THz in a single acquisition at measurement times as fast as a few microseconds. These results are part of the fourth publication included in this thesis [168]. This publication represents, to the best knowledge of the authors, the first demonstration of dual-comb interferometry with two microcombs operating in the normal dispersion regime.

7.2 Dual-comb interferometry with normal dispersion microcombs

Two normal-dispersion microcombs are generated to perform dual-comb interferometry. Each microcomb is generated in a Si_3N_4 chip fabricated at Myfab Chalmers. Each chip contains a coupled-cavity system based on two linearly-coupled cavities, main and auxiliary, with dissimilar radii. This coupled-cavity system is referred to in the literature as a photonic molecule [169]. A microscope image of the photonic molecule used is shown in Fig. 7.1 (a). The main cavity has a radius of 455.6 μm, resulting in an FSR of the longitudinal modes of 49.97 GHz. The auxiliary cavity has a smaller radius of 47.4 μm, resulting in an FSR of 480.4 GHz. As illustrated in the sketch of Fig. 7.1 (b), there is a resonance of the auxiliary cavity every 10 resonances of the main cavity.

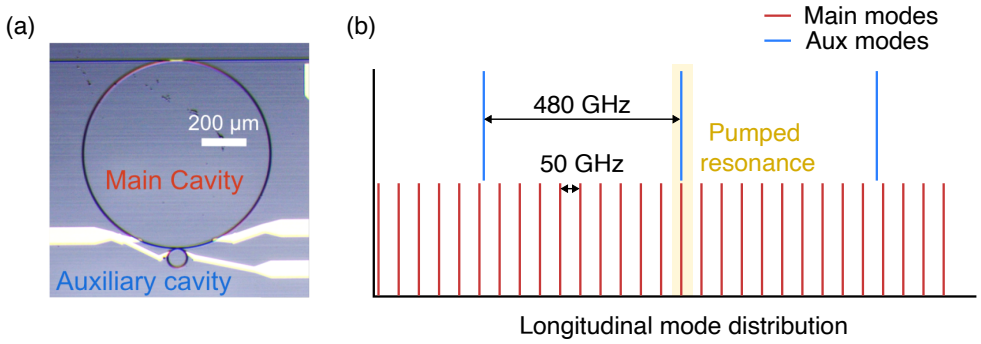

Figure 7.1: (a) Microscope image of the photonic molecule used for the realization of dual-comb interferometry with microcombs exhibiting normal group velocity dispersion. (b) Diagram illustrating an approximate distribution of the longitudinal modes of the main and auxiliary cavities. (a) and (b) taken from [168].

The waveguides forming the cavities, consisting of a Si_3N_4 core and a silica cladding, have dimensions of 1.6 μm width $\times$ 600 nm height. The quality factor of the cavity is Q=12.8·10^6. The fundamental transverse mode of the main cavity operates in the normal dispersion regime ($\beta_2 > 0$). Due to the coupled-cavity architecture, there exists coupling between transverse modes of both cavities. This interaction between modes induces a local change in the dispersion, allowing to assess anomalous dispersion at the wavelengths where these mode crossings occur. Provided that the photonic molecule is conveniently pumped with a CW laser emitting at a wavelength close to the wavelength of a mode crossing, modulation instability can be easily triggered, leading to the initialization of the microcomb.

The design includes two microheaters, each one positioned on top of a microcavity –one on the main cavity and the other on the auxiliary cavity. The inclusion of these two microheaters is crucial for generating two mutually coherent microcombs using a single pump laser. This is necessary because, although the two chips where the combs are generated are nominally identical, non-idealities in the fabrication process lead to practical differences between them. These differences can cause the two photonic molecules to have different FSRs, resulting in mode crossings occurring at slightly different wavelengths in each chip, which complicates the initialization of both combs with the same pump wavelength. In contrast, the two microheaters allow independent shifting of the resonances in each cavity via thermo-optic effect, providing control over the wavelengths at which the mode crossings occur. Therefore, the ability to modify the position of the resonances by applying voltage to the microheaters makes the formation of the two mutually-coherent combs controllable and deterministic.

The two chips are mounted on two probe stations, and the global temperature of each chip is controlled and stabilized by means of a Peltier cell and a temperature controller. Light is fed into and extracted from the chip through two lensed fibers, whose position is controlled using motorized micro-positioning stages. In addition, three DC probes (two for signal, one for ground) deliver the electrical signal to the microheaters. A photograph of the probing station is provided in Fig. 7.2.

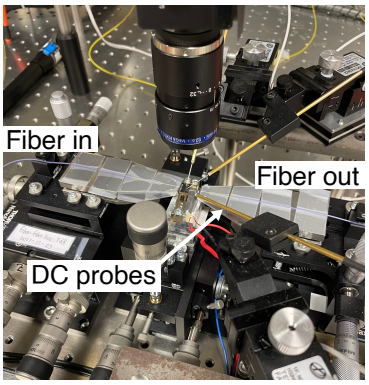

Figure 7.2: Photograph of the probe station utilized for the generation of one of the microcombs.

7.2.1 Experimental setup

The experimental setup built to realize dual-comb interferometry with two normal-dispersion microcombs is depicted in Fig. 7.3. A tunable CW laser (Toptica CTL) is used to pump both chips. The pump wavelength is set to 1555.63 nm, which corresponds to the location of a mode crossing in both systems at the experimental conditions. The pump is optically amplified using an EDFA (Amonics AEDFA-33-B-FA), and band-pass filtered (Koshin Kogaku filter) to eliminate the amplified spontaneous emission noise outside the comb band. Then, the optical signal is divided in two paths for the generation of the two OFCs.

The optical signal in one of the two branches, corresponding to the local oscillator comb, is frequency-shifted using an acousto-optic modulator (Brimrose AMF-25-4-1550-2FP), which introduces an f_{shift} of 24.3 MHz. Before injecting the light into the two photonic molecules, two polarization controllers ensure the alignment of the polarization state of the injected light with that of the fundamental mode propagating within the chip.

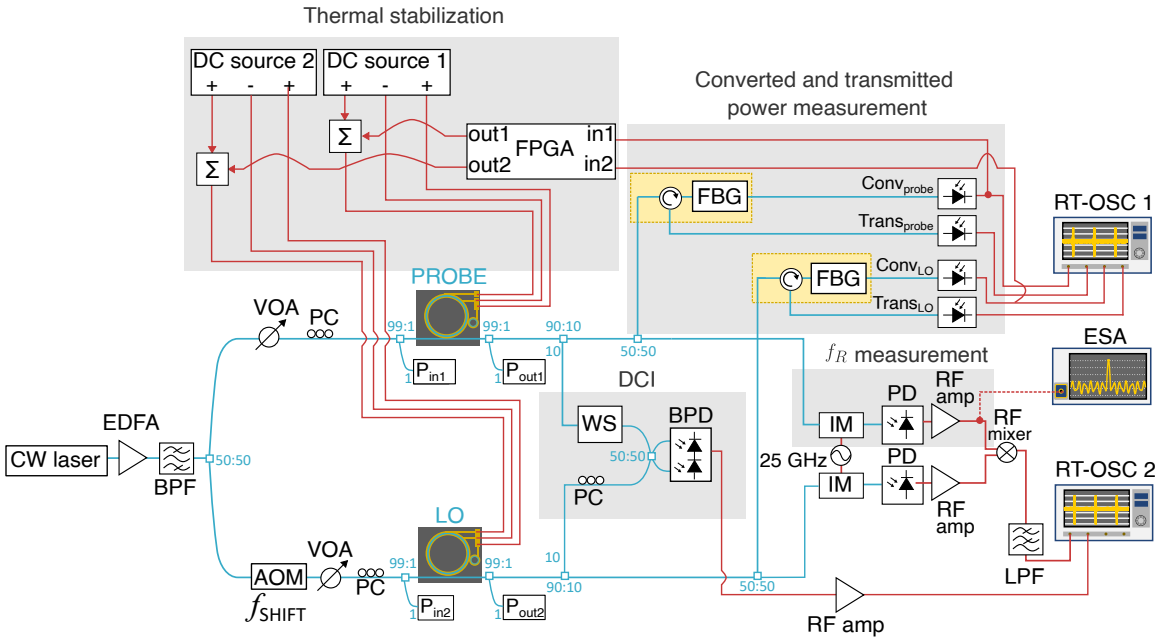

Figure 7.3: Experimental setup for performing phase-sensitive dual-comb interferometry with normal-dispersion microcombs. Four subsections, each serving a specific purpose detailed in the main text, are highlighted with gray blocks: thermal stabilization of the microcombs, measurement of converted and transmitted power, dual-comb interferometry, and measurement of the repetition rate of the microcombs. EDFA: erbium-doped fiber amplifier, BPF: band-pass filter, AOM: acousto-optic modulator, VOA: variable optical attenuator, PC: polarization controller, WS: wave-shaper, BPD: balanced photodetector, RF amp: RF amplifier, IM: intensity modulator, PD: photodetector, FBG: fiber Bragg grating, LPF: low-pass filter, ESA: electrical spectrum analyzer, RT-OSC: real-time oscilloscope.

Additionally, variable optical attenuators are used to ensure that the same power is injected into both chips. As a result, an optical power of 15.5 dBm is measured at the input of each chip (∼35.5 mW) by means of two power meters (P_{in1}, P_{in2})[1]. The optical power measured at the output of each chip measured by the power meters P_{out1} and P_{out2} is 12 dBm (∼15.85 mW), and the coupling losses per chip facet are estimated to be around 1.75 dB.

The setup is divided into sections, each marked by gray rectangles, with each section serving a specific purpose that will be later explained in detail. The thermal stabilization section prevents the chips from experiencing thermal drifts over time, which can cause the cavity resonances to shift and can lead to the extinction of the combs. The section dedicated to monitoring the transmitted and converted powers is involved in the generation process of the two microcombs, as discussed later. Additionally, a portion of the OFCs will be used to measure the repetition rate of the combs, and another portion will be dedicated to perform dual-comb interferometry.

7.2.2 Experimental results

The experimental results first detail the generation of the two mutually-coherent microcombs with slightly different repetition rates. Then, a down-conversion technique to measure the line spacing of the combs is discussed. Subsequently, the efficient down-conversion to the electrical domain achieved by dual-comb interferometry is presented, and the dual-comb interferograms and the obtained RF spectra are shown. Finally, the extraction of the quadratic phase profile of the device under test is demonstrated.

Generation of two 50-GHz normal-dispersion microcombs

The comb generation process in the normal-dispersion photonic molecule starts with the search for resonances corresponding to the main and auxiliary cavities. For this purpose, a frequency scan is performed with the pump laser. The visualization of the transmitted power on an oscilloscope after opto-electronic conversion allows to identify the main and auxiliary resonances as the frequency scan is performed. The transmitted power corresponds to the power of the pump wavelength, therefore, a power drop is measured when the pump is tuned into a resonance. The simultaneous measurement of the converted power, which corresponds to the power of the comb lines without the contribution of the pump, allows to determine whether comb lines have been created.

To measure the transmitted and converted power, the two combs are band-pass filtered in order to separate the contribution of the pump (transmitted) from the rest of the comb lines (converted). Band-pass filters based on Bragg gratings (Advanced Optics Solutions tunable FBG) are used for this purpose. The reflected wavelength (Bragg wavelength)

[1]To measure the optical power delivered to the chips, the optical signal is divided into two paths using an optical coupler with a 99:1 splitting ratio. The two power meters are placed at the coupler output corresponding to 1% of the input power, and the power delivered to the chip of 15.5 dBm is calculated for ideal conditions without considering excess losses. The same reasoning is followed for the optical power at the output of the chips.

corresponds to the wavelength of the pump, while the transmitted band corresponds to a portion of the comb lines. Then, the optical power in the two branches of the interferometer, corresponding to this process applied to the probe and local oscillator OFCs ($\text{Conv}_{\text{probe}}$, $\text{Trans}_{\text{probe}}$, Conv_{LO}, Trans_{LO}), are detected in four photodetectors (Thorlabs DET08CFC) and measured in a real-time oscilloscope (R&S RTA4004, denoted in the setup as RT-OSC 1).

After this analysis, an operating point where an auxiliary resonance is close to a resonance of the main cavity is chosen. In addition, a finer tuning assessed by the microheater corresponding to the auxiliary cavity allows bringing the auxiliary resonance closer to the main resonance. As a result of the proximity of the two resonances, a mode crossing is induced causing the main resonance to red-shift. This process allows for the generation of a dissipative Kerr soliton in the photonic molecule [99].

The most challenging aspect of generating the two microcombs is the identification of a suitable operating point that corresponds to a common pump wavelength. Once this point is found, and following the described procedure for the two photonic molecules, the two microcombs shown in Fig. 7.4 are obtained. The resulting spectra correspond to the formation of a dark-soliton in the coupled-cavity system, with the spectral tones evenly spaced by an FSR of the main cavity.

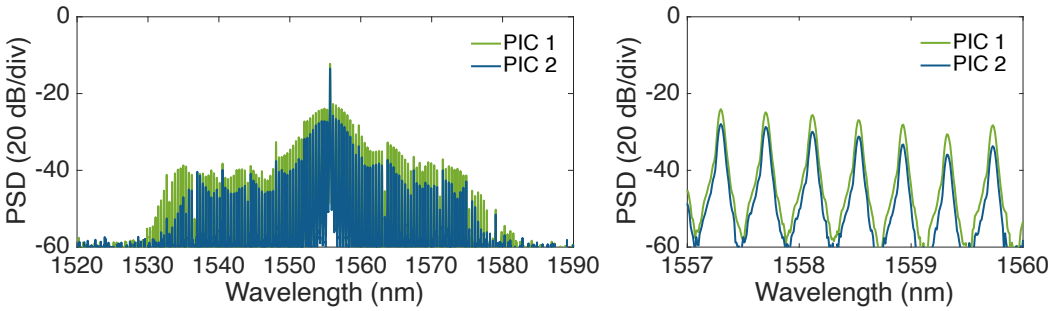

Figure 7.4: Optical spectra of the two normal-dispersion microcombs generated to perform dual-comb interferometry, measured with an optical spectrum analyzer.

The two combs exhibit a total spectral width of ∼5.8 THz. In addition, a high conversion efficiency of 51% is achieved, calculated as the ratio of the comb power (without considering the pump) and the pump power. Moreover, the combs remain stable over time owing to an implemented thermal control loop. Without temperature-control mechanisms, temperature drifts cause the resonances of the photonic molecule to shift. These shifts alter the comb state and, in the worst-case scenario, can cause the combs to extinguish when the resonances deviate far from the established operating point. Due to the alteration of the comb state, changes in the repetition rate of the combs are observed [168]. Conversely, implementing a temperature control loop maintains a fixed comb state with reduced fluctuations in the repetition rate of the generated combs. As a result of these reduced fluctuations, the beat notes of the resulting dual-comb spectrum exhibit reduced linewidths.

The thermal stabilization control is based on a feedback loop programmed in an FPGA (Red Pitaya STEMlab 125-14)[2]. The objective is to maintain a fixed comb state, characterized by a specific repetition frequency and power. To achieve this, the power of the comb lines (excluding the contribution of the pump), i.e., the converted power, is monitored and kept constant. The converted power is fed into the FPGA and configured as a reference point. When variations in the converted power are detected, indicating a change in the comb state caused by a deviation in the cavity resonances, a correction signal is generated. This signal acts on the voltage applied to the microheater of the main cavity. The correction signal, which is an electrical signal of a specific voltage, is added to the voltage provided by the DC source powering the microheater, allowing to correct the drifts experienced by the resonances of the main cavity.

Comb repetition rate measurement

Considering the dimensions of the main cavity, the estimated repetition rate of the microcombs is 49.97 GHz. To accurately measure this repetition rate, each comb can be detected using a photodetector. The spectrum of the resulting signal will correspond to frequency notes evenly spaced by the comb repetition rate. However, this approach requires photodetectors and an oscilloscope or an electrical spectrum analyzer with a bandwidth of at least 50 GHz.

To measure the repetition rate using more readily available components and instruments, a down-conversion approach based on the electro-optic modulation of the microcombs is employed. For this purpose, the microcombs are externally modulated using an electro-optic intensity modulator driven by a highly stable oscillator operating at f_{mod}= 25.1 GHz. Using this procedure every comb line is modulated, resulting in the generation of additional sidebands spaced by f_{mod} on both sides of the original comb lines. The repetition rate of the comb can then be inferred from the beat note generated by two neighboring sidebands corresponding to two consecutive comb lines, as illustrated in Fig. 7.5 (a). In this particular scenario, only two sidebands, each resulting from the modulation of contiguous comb lines, fall within two original comb lines. The beat note of the two newly generated tones corresponds to f_{beat} = 219.838 MHz, which can be easily measured using regular equipment. Fig. 7.5 (b) shows the down-converted repetition rate of one of the two microcombs. The comb repetition rate can be calculated as $f_R = 2f_{mod} \pm f_{beat}$. Given the previous knowledge of the FSR of the main cavity, the repetition rate is determined to be f_R= 49.98 GHz.

[2]The thermal stabilization system was already developed in Chalmers group, and its development is not a contribution from this dissertation.

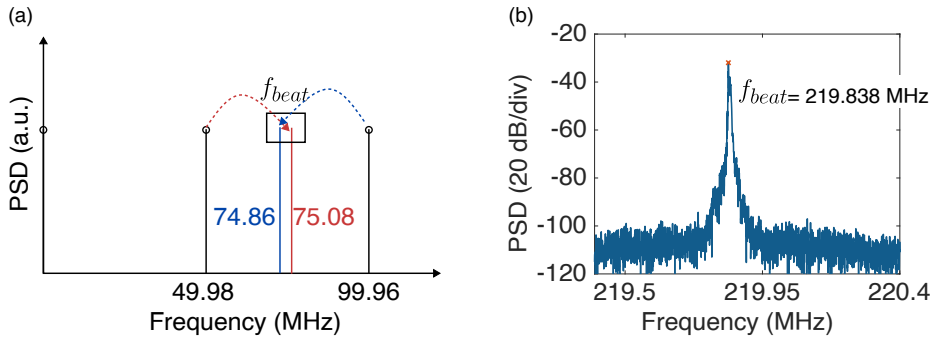

Figure 7.5: (a) Down-conversion of the comb repetition rate via the electro-optic modulation of the microcomb. For a comb repetition rate of 49.98 GHz and an electro-optic modulation frequency of 25.1 GHz, two sidebands arising from the intensity modulation of the microcomb fall within two original comb lines. The repetition rate of the microcomb can be obtained from f_{beat}. (b) Down-converted beat note obtained from the intensity-modulation of one of the two microcombs, measured with an electrical spectrum analyzer.

Generation of down-converted dual-comb spectrum

The capabilities in terms of coherence and frequency stability of the two generated microcombs are demonstrated by conducting dual-comb interferometry. The changes induced in the comb state depending on the position of the resonances of both cavities, which affect its repetition rate [168], are beneficial for dual-comb interferometry. Since the two combs need to exhibit slightly different repetition frequencies, having some control over the repetition rate difference constitutes a major advantage of the proposed system. By controlling the voltage applied to the microheater positioned over the main cavity in one of the two photonic molecules, the difference in repetition frequencies is finely tuned to ensure the effective compression of the comb.

The repetition rate difference is measured by mixing the beat notes obtained from the down-conversion process of the repetition rate of both combs. After detecting the two intensity-modulated combs, the DC component of the electrical signals is eliminated and the filtered signals are amplified (Minicircuits ZFL-500HLN+, Wenteq Microwave ABL0015-0012317) and mixed in an RF mixer (Mini-circuits ZFM-4). The beat note obtained from the mixer, with a frequency of δf_R, is monitored during the measurements using a real-time oscilloscope (Tektronix DSA71604, denoted RT-OSC 2 in the setup). The acquisition of this signal, together with the interferograms, allows capturing the possible drifts that the repetition rate may experience during the experiments. Considering a repetition rate difference of around 830 kHz estimated from the δf_R signal visualized during the experiments, the compression factor from the optical to the electrical domain of approximately $6{\cdot}10^4$ allows to compress the comb optical bandwidth of 5.8 THz to an electrical bandwidth of around 100 MHz. In this experiment, where the repetition frequency is very high, the spectral replicas in the down-converted frequency spectrum are centered at multiples of 49.98 GHz. Therefore, the requirement for the compression factor to avoid spectral overlap is relaxed to factors on the order of 100. The compression factor achieved here exceeds the minimum necessary by more

than a factor of 100, enabling ultrafast measurements where interferometric information can be acquired at microsecond speeds using photodetectors and sampling modules with low bandwidths.

The information to be retrieved by dual-comb interferometry consists in a phase profile encoded in one of the two microcombs. For this purpose, an optical filter featuring a quadratic phase profile is programmed in a waveshaper (Finisar waveshaper). When the probe comb passes through the waveshaper, its amplitude is not changed, but a quadratic phase is encoded in some of its comb lines. The width of the filter is programmed to be 25 nm (3.12 THz), which corresponds to approximately 62 comb lines. The local oscillator comb and the probe comb are combined in a 50:50 optical coupler and then interfere in a balanced photodetector (Thorlabs PDB425C). The resulting interferogram signal is amplified before being digitized (JDS H301-1210). Then, this signal and the sinusoidal signal containing the information of δf_R are digitized using two channels of the real-time oscilloscope operating at a sampling rate of 312 MSa/s.

Three interferogram signals are sequentially acquired with the oscilloscope: a reference signal in which the programmed filter does not introduce any phase or amplitude changes in the probe comb, and two signals in which the filter induces a quadratic phase in the probe comb with positive and negative signs, respectively. A portion of the interferogram signals obtained in the three scenarios, together with the corresponding signal for monitoring the repetition rate difference, are included in the top panels of Fig. 7.6: (a) reference acquisition, (b) positive-sign quadratic phase profile convolved with the probe comb, and (c) negative-sign quadratic phase profile imprinted on the probe comb.

The digitized temporal traces have a duration of 2.1 ms. This duration, considering a repetition rate difference of around 830 kHz, corresponds to 1750 interferogram bursts per sequence. The three interferogram sequences are first divided into sub-sequences comprised by 25 interferograms each. The extraction of the sub-sequences is performed using the zero-crossing points of the corresponding sinusoidal signal acquired to monitor the repetition rate difference. The duration of each sub-sequence leads to a resolution bandwidth in the frequency domain of 33.2 kHz, which allows to spectrally resolve the down-converted beat notes. A total of seventy sub-sequences of 25 bursts are extracted from each acquired interferogram signal. Each sub-sequence is Fourier transformed and the seventy Fourier spectra are then frequency averaged to reduce the variance of the noise power. The lower panels of Fig. 7.6 show the averaged spectra obtained for the three described scenarios. The repetition rate difference of the three down-converted dual combs show deviations between acquisitions, especially when comparing the reference dual-comb spectrum with the two measurement spectra. Despite the variations in the frequency spacing of the RF combs, a good SNR is obtained in all three cases, and it can be observed that the three spectra maintain the same spectral shape. Since the programmed phase information is obtained by comparing each tone of the measurement comb with each tone of the reference comb, and there is a complete correspondence between the tones despite the deviations in the repetition rate difference, the phase extraction can be correctly performed.

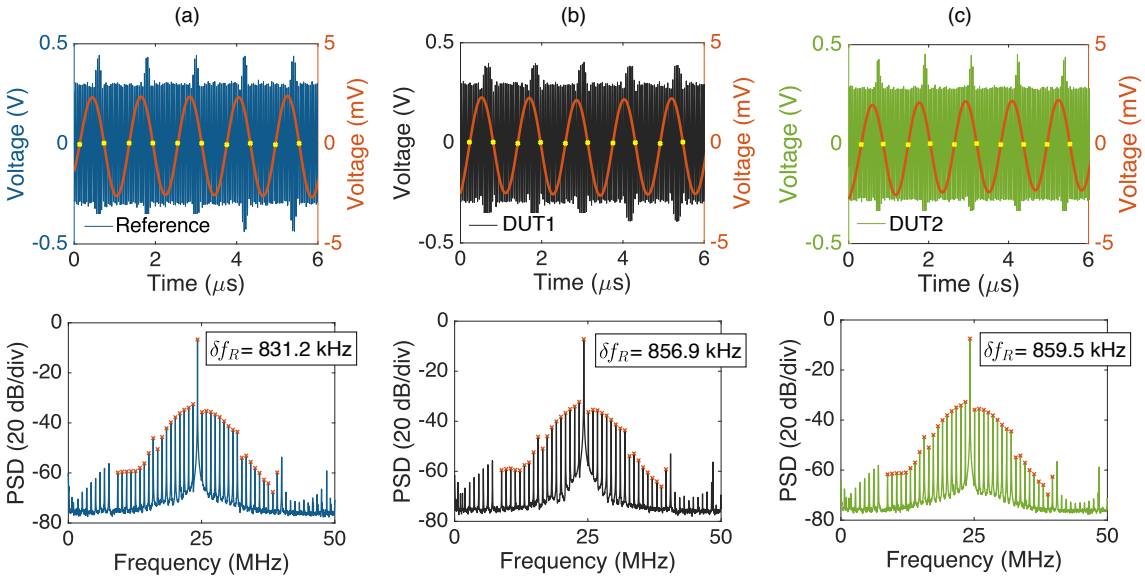

Figure 7.6: (Top) Portion of the digitized dual-comb time-domain interferograms. Each interferogram sequence is plotted together with a synchronization signal (depicted in orange), whose frequency corresponds to δf_R. The three panels correspond to three sequential acquisitions: (a) reference trace, where the device under test (DUT) information is not imprinted on the probe comb; (b) measurement trace, with a quadratic phase profile of positive sign imprinted on the probe comb; and (c) second measurement trace, with a quadratic phase profile of negative sign configured as the DUT. (Bottom) Down-converted RF spectra obtained from the fast Fourier transform of the interferogram traces acquired in the three mentioned scenarios. Seventy spectra are averaged in frequency. The down-converted repetition rate is specified in each case, and the beat notes where the DUT information is extracted are marked in orange.

Measurement of the phase profile of the device under test

The objective is to extract the spectral phase of the comb lines of the reference and measurement down-converted combs, $\phi_{r,m}$ and $\phi_{m,m}$, respectively, with m denoting the indices of the comb lines. Then, the programmed phase profile can be obtained by subtracting both spectral phases. Fig. 7.7 (a) depicts one of the programmed phase profiles overlapped to the optical spectrum of one of the two generated microcombs.

First, the positions of the down-converted beat notes, from which the phase information is to be extracted, are identified using a peak detection routine applied to the averaged Fourier spectra. Thirty-six spectral lines around the pump are considered in this analysis. Then, for each of the seventy sub-sequences of interferograms, the phase of the fast Fourier transform is computed. The spectral phase values corresponding to the locations of the down-converted comb lines are obtained. This procedure, applied to both the reference and one of the measurement signals, results in the seventy spectral phases shown in Fig. 7.7 (b). The upper panel depicts the unwrapped spectral phases obtained from post-processing the reference signal, while the lower panel corresponds to one of the two measurement signals (the one corresponding to a negative quadratic profile).

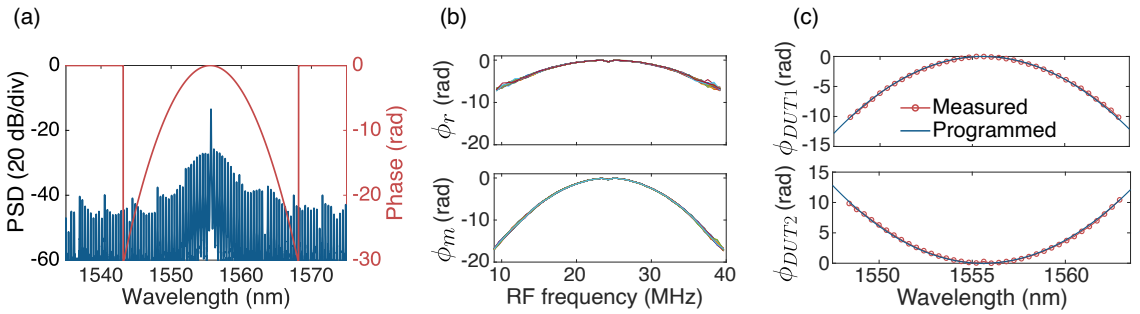

Figure 7.7: (a) Optical spectrum of one of the generated microcombs (blue trace) together with the phase profile of one of the programmed optical filters operating as DUT (red trace). (b) Evolution of the spectral phase of 37 comb lines obtained from the analysis of seventy interferogram sequences of the reference signal (top) and one of the measurement signals (bottom). (c) Measured phase profiles through dual-comb interferometry (red) versus programmed phase profiles (blue).

For each of the seventy spectral phases obtained, the spectral phase value of each comb line of the reference RF spectrum is subtracted from that of the measurement RF spectrum. Therefore, seventy spectral phase difference functions, $\Delta\phi_m = \phi_{m,m} - \phi_{r,m}$, are obtained. Finally, the phase profile of the device under test, ϕ_{DUT}, is obtained by averaging the $\Delta\phi_m$ functions. Fig. 7.7 (c) shows the two phase profiles retrieved. The experimental values, depicted with a solid red line and dot markers indicating the data points, show excellent agreement with the programmed phase profile. Thus, the precise alignment between the programmed phase and the recovered phase, with no visible deviations, demonstrates the measurement accuracy of the dual-comb interferometer.

7.3 Conclusions

In this chapter, a dual-comb interferometry system based on OFCs with significantly different spectral characteristics in terms of bandwidth and repetition rate from those previously shown in this thesis has been explored. The significance of the results here presented lies in the demonstration of dual-comb interferometry using microcombs operating in the normal dispersion regime, which had not been previously reported in the literature. As most materials used for the fabrication of nonlinear microresonators exhibit normal dispersion in spectral regions such as the visible and near-infrared, the ability to generate normal-dispersion microcombs with good characteristics in terms of stability, carrier-to-noise ratio, or coherence, enhances the potential for implementing microcomb-based systems in applications beyond the laboratory environment. The absence of a necessity for careful dispersion engineering of the waveguides constituting the cavities, together with the capacity of using standard CMOS-compatible fabrication processes, permits the large-scale fabrication of these devices using mature processes.

Two microcombs exhibiting a high repetition rate of 49.98 GHz and a repetition rate difference of 830 kHz have been generated. Each microcomb has been generated using a system formed by two linearly-coupled cavities with different radii, fabricated in silicon nitride. The combs exhibited a line spacing corresponding to the FSR of the main cavity (49.98 GHz). The smaller auxiliary cavity (FSR of approximately 480 GHz) provided a distinct family of resonances, inducing mode coupling between modes of the two cavities. This mode coupling, which locally influenced the dispersion of the system, enabled access to anomalous dispersion at the points where coupling occurred. A dark soliton has been generated when the pump was appropriately tuned into one of these points, as evidenced by the generation of normal-dispersion microcombs with line spacing corresponding to the FSR of the main cavity. Furthermore, the integration of microheaters into the coupled-cavity system enabled the shifting of resonance positions, thereby providing control over the wavelengths at which mode coupling occurred. This approach facilitated the generation of two microcombs using a single pump laser under controlled conditions. Additionally, the thermal stabilization mechanism included in the system allowed to prevent thermal drifts affecting the position of the resonances, maintaining a fixed comb state.

Moreover, the repetition rate of the generated combs has been measured using equipment with non-demanding bandwidth. The technique used, based on the intensity modulation of the microcombs after their generation, enabled the down-conversion of the comb repetition rate. By mixing the down-converted repetition rates of each comb, a signal corresponding to the difference in their repetition rates has been obtained. This signal, which enabled monitoring of the repetition rate difference between the two combs, proved to be very useful in the post-processing of the interferogram traces.

Finally, phase-sensitive dual-comb interferometry using the two generated microcombs has been proven. The measurement of two quadratic phase profiles using the spectral phase information of 36 beat notes around the pump has been demonstrated. The measured phase profiles closely matched the programmed profiles. The interferometric information has been obtained from the analysis of 70 interferogram traces, each comprised by 25 interferogram bursts. This resulted in a total acquisition time of 2.1 ms. The Fourier spectrum of each 25-interferogram sequence has been measured with a resolution bandwidth of 33.2 kHz, which allowed to resolve the RF beat notes and to unequivocally detect the locations of the beat notes where the phase information was extracted from. Moreover, faster measurement rates could be obtained from the analysis of a single sequence of 25 interferograms, resulting in a decrease of the acquisition time from 2.1 ms to 30 μs.

In conclusion, the controlled and deterministic generation of two normal-dispersion microcombs locked to the same pump laser has been demonstrated. The stability of the combs during the measurement time and their mutual coherence have been evidenced by the successful recovery of the phase profile of a device under test via dual-comb interferometry. These results represent a significant contribution to the applicability and potential of on-chip normal-dispersion combs and paves the way towards the implementation of systems based on these microcombs in environments out of the lab.

Chapter 8

Conclusions and outlook

This chapter presents the conclusions drawn from the work carried out in this dissertation. Future research lines to be pursued as a continuation of this doctoral thesis are also proposed. Although detailed conclusions have been provided in each experimental chapter, here the most relevant achievements are highlighted.

8.1 Conclusions

This thesis focuses on the development of gas sensing and ranging systems utilizing dual-comb architectures based on OFCs generated by gain switching of semiconductor lasers.

- In the field of **gas sensing**, the novelty of this thesis lies in the **enhancement of the spectral resolution** of GS dual-comb systems. Although GS dual-comb spectrometers cannot compete in spectral coverage with systems based on other comb generators, they can outperform in spectral resolution. Moreover, this spectral resolution is tunable due to the frequency agility of GS comb sources. Prior to this work, the spectral resolution of GS dual-comb spectrometers was limited to approximately 500 MHz, which constrained the potential of such systems since the minimum spectral width that could be measured was on the order of a few GHz. Through the advancements presented in this thesis, this resolution limit has been significantly extended, enabling the measurement of spectral features with linewidths as fine as 360 MHz with a **spectral resolution of approximately 4 MHz**. This improvement greatly enhances the utility and application of GS dual-comb systems in high-resolution sensing. The improvement in spectral resolution has been achieved through the **generation of OFCs with low repetition frequencies**. First, using **trains of electrical pulses as gain-switching signals**, along with external optical injection, the generation of GS combs with line spacings from 100 MHz to 2.5 MHz was demonstrated. Then, through the **electro-optic densification of the GS combs**, which potentially allows to decrease the repetition rate below the megahertz range.

In the pursuit of implementing a high-spectral-resolution gain-switched dual-comb spectrometer, a **design guide for obtaining low-repetition-rate GS combs** using pulsed electrical excitation and external optical injection with specific spectral characteristics **tailored for dual-comb spectroscopy applications** has been provided. This guide is based on an analysis of the influence of the amplitude of the gain-switching signal and the optical injection detuning on the spectral properties of the resulting combs. By controlling the pulse amplitude, it has been shown that the spectral width of the combs can be accommodated to the width of the measured sample, up to **maximum comb bandwidths of around 100 GHz**. By adjusting the optical injection detuning, the spectral flatness of the GS OFC can be optimized. Specifically, injecting the GS combs at the bandwidth end showing less optical power compensates for their asymmetry and improves their flatness.

The **measurement of an HCN absorption line** exhibiting a **spectral width of 2 GHz** has been demonstrated using two optically-injected GS combs with repetition frequencies of 100 MHz generated by pulsed excitation. The improvement of the SNR through spectral averaging has been proven. Additionally, it has been shown that the **mutual coherence** of the two frequency combs can be maintained for **integration times of up to 80 seconds without** the need for **phase or frequency stabilization methods or post-correction techniques**. The exceptional stability and coherence of the system are inherent to the comb generation technique, as both OFCs are injected by the same master laser.

The OFCs obtained by means of pulsed gain switching at repetition rates of a few megahertz featured good characteristics in terms of flatness and spectral width; however, their average optical power has been shown to be compromised due to the low duty cycle of the gain-switching signals, and optical amplification is usually required for the combs to exhibit an acceptable CNR. To overcome this limitation, the **densification of the two GS combs** comprising the spectrometer has been proposed to **achieve GS combs with repetition rates in the megahertz range without compromising the average optical power of the system**. The external densification of the two combs using two EOPMs driven by maximum length sequences has been proven to be an effective method for **further increasing the spectral resolution** while maintaining the flatness and CNR of the combs. Then, the experimental implementation of a **densified GS dual-comb spectrometer** has been demonstrated. Two externally-injected GS combs with repetition rates of 500 MHz have been densified by a factor of 127, resulting in a new comb spacing of around 4 MHz. This approach, based on the phase modulation of the GS optical pulses, involved no power loss. The densified spectrometer has been validated by the **measurement of a Fabry-Pérot resonance featuring a linewidth of around 360 MHz**, interrogated with 90 comb lines within said linewidth. An optical bandwidth of 48 GHz was compressed to an electrical bandwidth of 4.8 kHz, and the optical information was extracted using a balanced photodetector with a bandwidth of only 100 MHz. The down-converted dual frequency comb that contained the information of the Fabry-Pérot resonance exhibited a CNR of 17.6 dB and an excellent spectral flatness of 0.92, which was achieved by configuring the amplitude of the signals driving the EOPMs to the half-wave voltage of the devices. The great performance in terms of

flatness of the RF dual-comb spectrum allowed to perfectly identify the footprint of the filter on the spectrum. Moreover, the spectral resolution of 4 MHz, which was specifically designed for measuring the Fabry-Pérot resonance with good resolution, could be further reduced to the sub-MHz range by increasing the length of the maximum length sequences that drive the EOPMs.

Additionally, motivated by the **development of compact and inexpensive dual-comb spectrometers**, and building on the demonstrated viability of dual-comb spectrometers based on low-repetition-rate GS combs, **an affordable digitizer to be included in such systems has been proposed**. The effective compression of the optical information to a bandwidth in the megahertz range allowed the use of a low-cost **software-defined radio platform to digitize the gas absorption information**. This approach not only significantly reduces the cost of the dual-comb spectrometer but also minimizes the footprint of the spectroscopy system while maintaining the measurement accuracy. Remarkably, even without locking the software-defined radio to a system reference signal, mutual coherence has been demonstrated up to an integration time of 1 second.

In summary, the demonstrations reported in this thesis represent a significant advancement for **GS dual-comb spectroscopy systems**, since now it is possible to attain **spectral resolutions ranging from a few GHz down to values below 1 MHz**, achievable with densification. This broader spectral resolution range expands the versatility of dual-comb spectrometers based on GS OFCs.

- In the field of **ranging**, the capability to generate low-repetition-rate gain-switched combs has been leveraged for dual-comb ranging measurements. By decreasing the repetition rate of the combs, it is possible to **achieve longer non-ambiguity ranges**, as the non-ambiguity range is inversely proportional to the repetition rate of the combs. In this context, an asymmetric dual-comb architecture, where only the probe comb is used to interrogate the distance to be measured, has been employed to measure distances using an **interferometric procedure**. This interferometric approach offers greater precision compared to time-of-flight-based techniques, with the precision improving for broader comb bandwidths. However, a challenge arises in balancing precision and non-ambiguity range, as frequency combs with broader bandwidths typically feature higher repetition frequencies. To address this, low-repetition-rate GS combs present a promising solution by offering a **balance between precision and measurement range while maintaining system simplicity and integrability**. GS OFCs with bandwidths around 100 GHz and repetition rates below the megahertz range can be achieved using a system composed of three semiconductor lasers in a master-slave configuration and two electro-optic phase modulators. In contrast, similar bandwidths in electro-optic frequency comb systems often require multiple cascaded modulators, adding complexity to the setup.

A **dual-comb ranging system based on two optically-injected GS laser diodes** has been proposed and validated by measuring relative distances, i.e., the displacement of a target between two positions. Although the setup enables the measurement of absolute distances, this would require the precise determination of the optical lengths traveled by the two combs until they reach the photodetector. First, dual-comb ranging measurements utilizing two GS OFCs generated by pulsed gain switching two optically-

injected discrete-mode lasers have been demonstrated. The selected repetition rate of 100 MHz enabled to **resolve free-space distances** of up to **1.5 meters** without ambiguity, with a minimum **measurement time of 100 μs**. The system has been validated by measuring an open-path relative distance of 4 mm. The precision of the measurements has been evaluated using the Allan deviation, which quantifies the evolution of the error on the distance in relation to the measurement time. By post-processing sequences containing 40 interferogram bursts per sequence, the **precision** improved from 3.2 μm, measured over a 4-ms period without averaging, to **0.5** μm, after **averaging one hundred phase difference functions over 400 ms**. The analysis of sequences comprising ten interferograms per sequence yielded comparable precision while facilitating acquisition speeds fourfold faster. Furthermore, greater precision is anticipated for longer measurement times, as the Allan deviation did not reach saturation within the maximum analyzed time frame.

Following the successful demonstration of the feasibility of the system using pulsed excitation, a **ranging system based on two densified GS combs** has been presented. The phase of the optical pulses from two GS combs, generated through pulsed gain switching, have been modulated using a pseudo-random phase pattern. This resulted in two densified combs with a comb repetition rate of 4 MHz and a repetition rate difference of approximately 40 Hz. Although this setup introduces additional complexity due to the need for two EOPMs, it enabled the **extension of the non-ambiguity range** without compromising the average optical power. With this system, a maximum range of **38 meters** can be measured without ambiguity and in a single acquisition. However, increasing the non-ambiguity range comes at the cost of reduced acquisition speed. Under the experimental conditions demonstrated in this thesis, the **minimum acquisition time** was **25.4 ms**, corresponding to the duration of a single interferogram burst. Then, a relative distance measurement of 2 mm to a target has been demonstrated using the densified setup, with propagation in air and the probe comb traveling a round-trip to the target.

In non-densified dual-comb ranging experiments, analyzing sequences with multiple interferogram periods improved the precision, attributed to temporal averaging. Therefore, in the densified dual-comb ranging experiment, the post-processing analysis has been conducted using sequences comprising 10 bursts of densified interferograms. In this scenario, the minimum acquisition time was 254 ms. A maximum acquisition time of 1.24 s was analyzed, corresponding to the averaging of five unwrapped spectral phase differences. Under these conditions, the 2-mm distance was measured with a **precision of 4.6 μm**. This precision is lower than that obtained in the non-densified experiment, since fewer averages have been implemented in the densified scenario (five averages in the densified experiment versus one hundred averages in the non-densified experiment). To compare both results, the acquisition time would need to be increased to 25.4 seconds. Under the digitization conditions used in the experiment, this would correspond to acquiring 100 temporal traces of 62.5 million points, requiring significant processing capabilities. Finally, an initial demonstration showing the viability of the system for measuring ranges of tens of meters has been presented through a **proof-of-concept experiment using a 10-meter fiber cord**.

In summary, low-repetition-rate GS combs have been also proved beneficial for the extension of the non-ambiguity range in dual-comb ranging measurements. By means of the external densification of the two GS combs, the maximum range to be measured without ambiguity can be significantly enhanced from around 1 meter (without densification) up to a few kilometers (attainable with comb repetition rates of hundreds of kilohertz). Then, the proposed system represents a promising **medium-range solution**.

- Finally, the realization of **dual-comb interferometry with microcombs** has been also explored during the international research stay developed within the Ultrafast Photonics Group in Chalmers University. **Phase-sensitive ultrafast dual-comb interferometry** has been demonstrated using **two microcombs exhibiting global normal GVD**.

The devices used to generate each microcomb consisted of two cavities made of silicon nitride waveguides, which were linearly coupled and featured significantly different radii (being the radius of the main cavity 455.6 μm and the radius of the auxiliary cavity 47.4 μm). The **coupled-cavity configuration** enabled to **achieve local anomalous GVD** at specific wavelengths where coupling between transverse modes of the two cavities occurred. This resulted in the effective generation of a dissipative Kerr soliton propagating in the main cavity, which gave rise to an OFC with a line spacing corresponding to the round-trip time of the main cavity. In contrast to the experiments developed in the rest of the doctoral thesis, focused on the generation and application of combs with low repetition rates, the employed microcombs exhibited **high repetition frequencies of 49.98 GHz**, and a **broad spectral bandwidth of 5.8 THz**. The compression of the optical spectrum by means of the configuration of a repetition frequency difference of around 830 kHz enabled to recover the spectral information in microsecond timescales. Moreover, the inclusion of thermal microheaters in the cavities provided control in the generation of the two microcombs and facilitated the use of a single laser to pump both microcombs, essential to provide them with mutual coherence. Finally, the generated combs showed a long-term stability thanks to a thermal stabilization control developed by the Chalmers group.

In summary, the potential of normal-dispersion microcombs for dual-comb interferometry applications has been demonstrated. This represents a significant advancement in the field, as prior to the publication of the work that included the results from the experiment developed during the international research stay, dual-comb interferometry had only been demonstrated using microcombs operating in the anomalous dispersion regime. The ability to use **combs with normal dispersion alleviates the need for dispersion engineering** required to achieve anomalous dispersion in third-order nonlinear materials such as silicon nitride. Consequently, these results enhance the practicability and applicability of microcomb-based dual-comb interferometry systems for real-world applications.

8.2 Outlook

The work conducted during this doctoral thesis can be further extended to address unresolved issues and opens up different lines of research with scientific interest to be explored. Below, some of these potential research directions are summarized.

In the field of spectroscopy:

- **Implementation of a remote gas sensing system.** In-fiber absorption spectroscopy measurements have been conducted during this thesis. However, the evaluation of a gain-switched dual-comb spectrometer for the detection of absorbing species in an open-path environment remains undone. Therefore, the study of the sensitivity and the performance in terms of SNR of the system should be realized, focusing on its deployment outside the laboratory environment under non-ideal conditions. Optical amplification stages would need to be included in the setup and the affection of amplified spontaneous emission noise on the results would need to be examined. Similarly, the inclusion of electrical amplification stages to amplify the obtained interferograms could be studied. Moreover, the implementation of an asymmetric configuration to extract the absorption information from the analysis of the phase (related to the dispersion profile of the gas) could be also beneficial for low SNR scenarios.

- **Development of a compact and portable gain-switched dual-comb spectrometer.** A natural step following the evaluation of the spectrometer in a real and harsh environment would be the development of a compact, portable prototype capable of performing real-time absorption measurements. Based on the system proposed in this dissertation, the primary focus should be on the development of the electronics of the system. To implement a cost-effective instrument, the electronics should leverage devices such as step-recovery diodes, software-defined radio platforms, and FPGAs for signal generation and real-time digital processing.

- **Integration of the dual-comb system in a photonic chip.** The compactness and overall footprint of the dual-comb spectrometer can be further improved by integrating the three lasers (master and slave lasers) involved in the setup in an indium phosphide photonic circuit. Moreover, although the generation of two GS OFCs on indium phosphide chips has been demonstrated, key steps such as beating the two on-chip generated combs on a photodetector and generating time-domain interferograms and a down-converted dual-comb spectrum have yet to be demonstrated. Additionally, the application of on-chip GS dual-comb interferometers remains unexplored.

- **Use of a coherent IQ receiver.** The evaluation of the performance of the dual-comb spectrometer using a coherent receiver could be also explored. The detection of IQ information of the interferogram signals could eliminate the need for a frequency shifter or optical injection filtering to unambiguously resolve the down-converted spectrum.

- **Extension of the GS dual-comb spectrometer to mid-infrared wavelengths.** The mid-infrared range exhibits stronger molecular signatures than the near-infrared, making it of greater interest for spectroscopic applications. Techniques such as difference frequency generation or the use of optical parametric oscillators have demonstrated the translation of frequency combs from the near-infrared to the mid-infrared. While dual-comb spectroscopy has already been demonstrated in the mid-infrared range for several comb generators, such as electro-optic combs and microcombs, it has only been reported for GS combs around 2 μm. Translating GS combs to the mid-infrared would allow for the measurement of gas absorption for substances like methane, carbon dioxide, and hydrogen sulfide. Specifically, the translation of densified GS combs would enable the measurement of absorption features of gases with Doppler-limited bandwidths, leveraging the ultra-high resolution capabilities of the densified approach.

In the field of ranging:

- **Further evaluation of the densified GS dual-comb ranging system.** The completion of the results on dual-comb ranging using a pair of densified GS OFCs represents a natural evolution of the work presented in this thesis. The results presented herein demonstrated the viability of the system for measuring open-path distances well below the non-ambiguity range. Furthermore, a proof-of-concept in-fiber measurement was conducted to evaluate a distance on the order of the non-ambiguity range. To further this research, additional in-fiber measurements would be necessary to comprehensively analyze the precision of the system. Additionally, it would be valuable to conduct open-path measurements to test the measurement range near the maximum range of the system. However, this measurement could not be performed during the thesis as the measured relative distance was controlled by a micro-positioner with a maximum displacement capability of only a few millimeters.

- **Evaluation of the accuracy of the dual-comb ranging system.** The precision of the system was evaluated by analyzing the error on the slope of the linear regression fitted to the experimental phase values. However, the accuracy of the measurement still needs to be assessed. This could be done by integrating an additional interferometer in the system to evaluate the same distance as the probe comb.

- **Exploration of related applications.** In the dual-comb ranging system presented, the influence of the different path lengths of the interferometer branches led to the necessity of measuring relative distances instead of absolute distances, in order to eliminate the contribution of the unequal lengths of the two arms in the setup. This system can be particularly beneficial for measuring the thickness of a sample, as in optical coherence tomography, where the measurement inherently involves extracting the relative distance between two surfaces. Dual-comb-based optical coherence tomography has already been demonstrated at 1.55 μm [170] and 1.3 μm [143]. However, examining biological tissues requires shorter wavelengths that can penetrate these tissues effectively. The ability to perform gain switching at different wavelengths, provided suitable laser diodes are available, would enable the development of a dual-comb optical coherence tomography system for biomedical applications.

- **Exploration of dual-comb ranging with normal-dispersion microcombs**. With regard to the last chapter of this dissertation, the use of two normal-dispersion microcombs for ranging would enable to perform ultrafast measurements. Additionally, the combination of normal-dispersion microcombs with gain-switched lasers to enhance the properties of any of these two comb generators can be a potential research direction.

Appendix A

Gain-switched combs based on multi-pulsed electrical excitation

The generation of GS combs using pulsed gain-switching signals consisting of more than one pulse per period is discussed in this Appendix. This approach aims to increase the average optical power of the combs, which has been proved highly compromised when utilizing low-frequency gain-switching signals with a single pulse per period (Chapter 5).

The basic idea involves adding additional pulses to a classical train of pulses that originally consists of only one pulse per period. This technique was first tested experimentally, using various approaches to generate multi-pulsed gain-switching signals. All of these multi-pulsed signals were designed so that the newly added electrical pulses are positioned in a way that avoids introducing a new periodicity into the signal or altering the repetition frequency of the comb. Moreover, a condition to ensure that all optical pulses were equal was imposed. For this condition to be met, the carriers and photons in the laser cavity must reach steady state before the subsequent electrical pulse starts. Therefore, in order to know the time needed for the carriers and photons to reach steady state, optical simulations of a GS OFC using single-pulsed excitation are conducted. The simulations are based on the rate equation model described in Chapter 2. A discrete-mode laser, characterized by the parameters detailed in said chapter, is used as slave and master laser. In the simulation scenario, the frequency of the excitation signal is f_R= 100 MHz and the electrical pulses have low and high current values of I_{off}= 4.3 mA and I_{on}= 44.3 mA, respectively, and a temporal duration of τ_{pulse}= 200 ps. Optical injection power is P_{inj}= 0.5 mW and the detuning between the ML and the SL emission is ∼33 GHz. The results from the optical simulation are shown in Fig. A.1. Panels (a), (b), and (c) show the profile of the injected current and the calculated evolution of the carrier density, the optical power emitted by the slave laser together with the frequency chirp, and the resulting optical spectrum, respectively. These results depict the typical behavior of a laser diode operating in gain-switching regime. In the simulation conditions, the carrier density reaches steady state after approximately 300 ps. Considering the time required for the carrier density to reach steady state, there exists a limitation on the maximum number of pulses in the multi-pulsed signal and hence the maximum duty cycle.

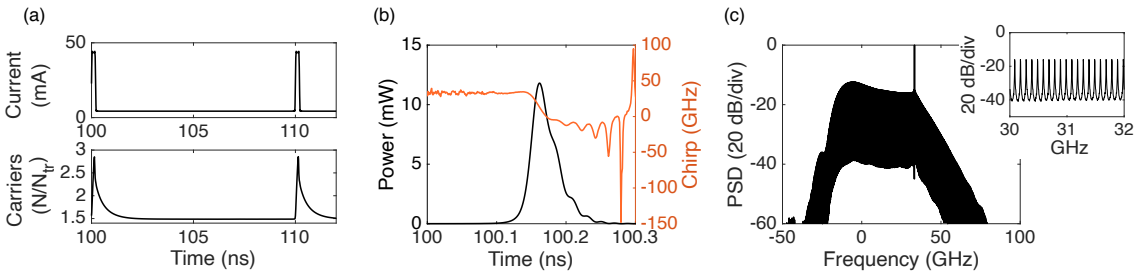

Figure A.1: Numerical simulations of single-pulsed GS OFCs featuring a repetition rate of f_R= 100 MHz. (a) Single-pulsed excitation current and evolution of the carrier density normalized to the transparency carrier density. (b) Resulting optical pulses and frequency chirp. (c) Normalized optical spectrum.

Subsequently, a numerical simulation with the previously described conditions but using a multi-pulsed gain-switching signal with two pulses per period is conducted. The two electrical pulses are separated by a delay of 800 ps, as depicted in Fig. A.2 (a).

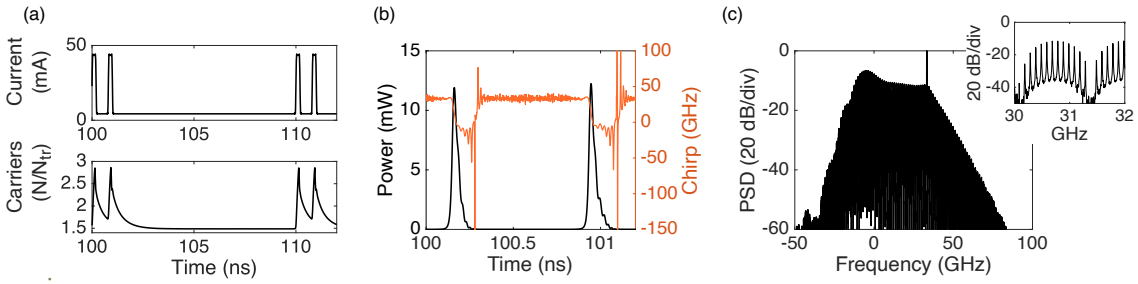

Figure A.2: Numerical simulations of 100-MHz multi-pulsed GS OFCs, with 2 pulses per period. (a) Multi-pulsed gain-switching signal and carrier density. (b) Optical pulses and frequency chirp of the multi-pulsed scenario. (c) Normalized optical spectrum.

It can be seen that the carrier density reaches its steady-state value before the onset of the next build-up of the carriers. Consequently, the shape and chirp of the two optical pulses within the period are quite similar, as depicted in panel (b). The optical spectrum from this simulation is included in Fig. A.2 (c). Since two pulses are emitted per period, the duty cycle is increased from 2% to 4%. However, as it is evidenced in the zoomed view of panel (c), a ripple in the optical spectra appears. This ripple, which in this particular case has a frequency of 1.3 GHz, appeared with all the multi-pulsed signals experimentally tested, compromising the flatness of the resulting combs.

To understand the origin of the amplitude modulation observed in the optical spectrum of the multi-pulsed GS combs, the multi-pulsed approach is analyzed analytically. Fig. A.3 illustrates a generic multi-pulsed excitation current $I_{multi}(t)$, which consists of a series of N pulses having the same temporal width τ_{pulse}. The sequence of N pulses is periodic with period T_R=$1/f_R$. The starting time of a pulse i within the period is defined as t_{i-1}. The excitation current switches between I_{off} and I_{on}. When these values are

properly selected for gain switching the laser diode, a sequence of optical pulses with approximately the same intervals as the excitation electrical pulses will be generated.

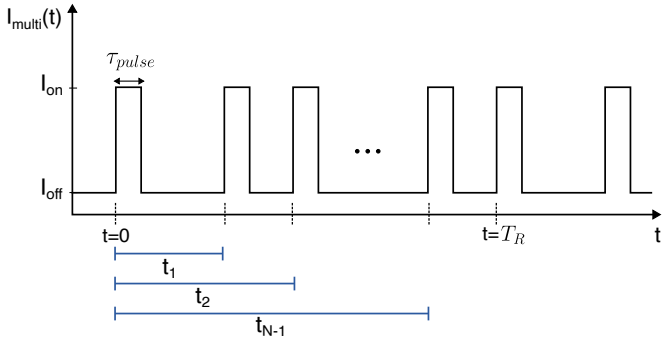

Figure A.3: Illustration of the multi-pulsed excitation current $I_{multi}(t)$ proposed for gain switching a laser diode. The number of pulses introduced in the sequence is defined by the integer N.

The electric field of a periodic train of pulses with period T_R and a single pulse per period can be described as a Fourier series

$$E_1(t) = \sum_{k=-\infty}^{\infty} A_k e^{\frac{jk2\pi t}{T_R}}, \tag{A.1}$$

where A_k are the spectral or Fourier coefficients of $E_1(t)$ and k is an integer denoting the harmonic index. They indicate the portion of $E_1(t)$ in each harmonic. The spectral coefficients can be written as

$$A_k = \frac{1}{T_R} \int_0^{T_R} E_1(t) e^{-\frac{jk2\pi t}{T_R}} dt. \tag{A.2}$$

The addition of several pulses per period provides a complex function, whose phase depends on the delay between pulses. The multi-pulsed signal can be formulated as the sum of the described periodic signal $E_1(t)$ plus delayed versions of this signal, considering the delays t_i described before. For N= 2 pulses, the resulting multi-pulsed signal can be expressed as

$$E_{multi}(t)|_{N=2} = E_1(t) + E_1(t - t_1) = \sum_{k=-\infty}^{\infty} C_k e^{\frac{jk2\pi t}{T_R}}, \tag{A.3}$$

where C_k are the spectral coefficients of the multi-pulsed signal containing N=2 pulses. The spectral coefficients follow the expression below

$$C_k|_{N=2} = A_k(1 + e^{-\frac{jk2\pi t_1}{T_R}}). \tag{A.4}$$

The power spectral density of the harmonics can be obtained from the squared magnitude of the spectral coefficients of the multi-pulsed signal. For N=2 pulses it can be written as

$$|C_k|_{N=2}|^2 = 2|A_k|^2\Big[1+\cos\Big(\frac{2\pi k t_1}{T_R}\Big)\Big], \tag{A.5}$$

following a cosine dependence with the corresponding maxima and minima. Eq. (A.5) can be understood as the frequency-domain equivalent of classical interference patterns, with a maximum at zero frequency and other maxima at frequencies given by $f_{max} = \pm m/t_1$, and m being an integer. In addition, it should be noted that the maxima and minima of Eq. (A.5) may or may not correspond to the frequency of the harmonics, depending on the ratio defined by T_R/t_1.

The extension for N pulses of the expression of the spectral coefficients (Eq. (A.4)) is given by

$$C_k|_N = A_k\Big[1+\sum_{i=1}^{N-1} e^{-\frac{jk2\pi t_i}{T_R}}\Big], \tag{A.6}$$

and the power spectral density of the spectral coefficients in this case can be expressed as

$$|C_k|_N|^2 = 2|A_k|^2\Big[1+\sum_{i=1}^{N-1} \cos\Big(\frac{2\pi k t_i}{T_R}\Big)\Big]. \tag{A.7}$$

This analysis, which is performed for the electrical excitation current, can be translated into the optical domain provided that all optical pulses are equal. Fig. A.4 (a) shows the power spectral density of the previously described multi-pulsed electrical sequence with N= 2 pulses per period with a first pulse starting in t=0 and the second pulse starting in t_1= 800 ps. Panel (b) depicts the optical spectrum obtained in a numerical simulation when an optically-injected laser diode is gain switched with such multi-pulsed sequence. It is verified that both spectra convey the same information in terms of spectral shape. The simulation confirms that when all optical pulses are identical, the expression for the spectral coefficients derived for the multi-pulsed electrical signal (Eq. (A.4)) is valid for analyzing the amplitude of the spectral coefficients corresponding to the optical pulse train. In the simulations, both spectra consist of harmonics showing a line spacing of f_R= 100 MHz. The ripple observed in the comb lines with a frequency of 1.3 GHz corresponds to $1/t_1$.

Given the equivalence in shape between the spectrum of the gain-switching electrical signal and the spectrum of the resulting optical comb, the search for frequency combs with flat spectra can be performed using the electrical spectra, enabling faster computation.

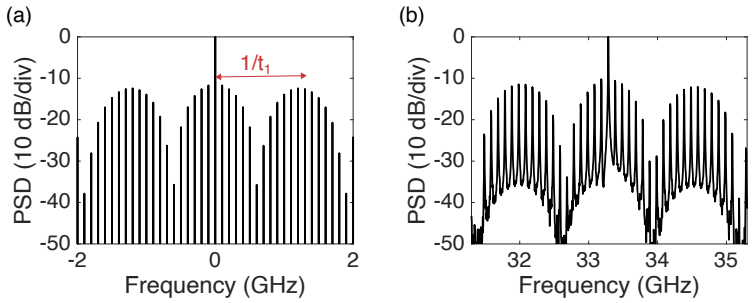

Figure A.4: (a) Electrical power spectrum of a multi-pulsed excitation signal with N= 2 pulses having a temporal separation of t_1= 800 ps. (b) Optical power spectrum obtained when an optically-injected laser diode is modulated by the described multi-pulsed signal.

Spectral optimization of multi-pulsed gain-switched combs

The introduction of additional pulses in the pulsed gain-switching signal leads to optical spectra with significant power variation in their comb lines. The objective is to generate OFCs with maximum flatness using multi-pulsed signals, allowing for an increase in the average optical power of low-repetition-rate GS combs without significantly degrading their spectral properties. An optimization algorithm can then be developed to design multi-pulsed sequences that maximize the flatness of the comb harmonics.

The figure of merit used to evaluate the flatness of the resulting comb spectra is the spectral flatness, previously described in Eq. (2.16) of Chapter 2. The optimization is conducted using a home-built iterative algorithm running on MATLAB. The program generates a user-defined number of multi-pulsed sequences, each with N pulses per period. All the generated electrical sequences satisfy the condition that imposes a minimum temporal distance of 300 ps between consecutive pulses, corresponding to the time needed for the carriers to reach steady state. For each electrical sequence, the power of each harmonic is extracted. Finally, the standard deviation of the spectral coefficients is computed, and the multi-pulsed signal that results in a comb spectrum with the lowest standard deviation is selected as the optimum sequence. The number of harmonics analyzed corresponds to an electrical bandwidth of 10 GHz.

Electrical simulations are performed for two repetition rates of f_R= 50 MHz and f_R= 1 MHz, with 500 iterations of the algorithm. For a line spacing of 50 MHz, the spectral flatness values obtained for different numbers of pulses included in the gain-switching signal, ranging from 1 to 20, are analyzed. For a repetition rate of 1 MHz, the maximum number of pulses included is 100. The results of the spectra showing the optimum and worst spectral flatness values for the two specified repetition rates are included in Fig. A.5. For the multi-pulsed excitation signal with f_R= 50 MHz and N= 20 pulses, the best and worst spectral flatness values obtained are 0.621 and 0.075, respectively. For f_R= 1 MHz and N= 100 pulses, the best and worst spectral flatness values are 0.576 and 0.535, respectively.

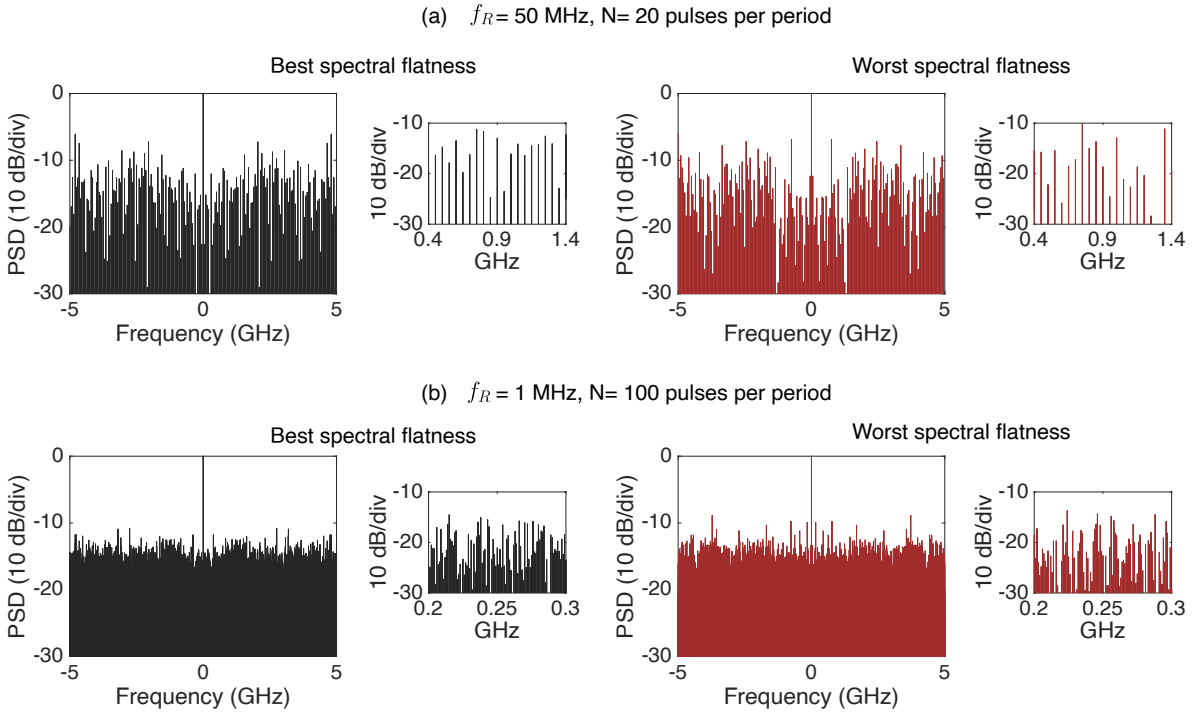

Figure A.5: (a) Electrical spectra of 50-MHz multi-pulsed sequences with 20 pulses per period showing the best (black) and worst (red) spectral flatness characteristics. (b) Analogous results obtained for multi-pulsed sequences featuring a repetition rate of 1 MHz and 100 pulses per period.

The evolution of the optimum spectral flatness when varying the number of pulses per period is shown in Fig. A.6, for the two repetition rates of (a) 50 MHz and (b) 1 MHz. The spectral flatness experiences an exponential decay as the number of pulses increases, showing a saturation trend around N= 10 pulses for the two repetition rates. In both cases the spectral flatness saturates at a value around 0.55.

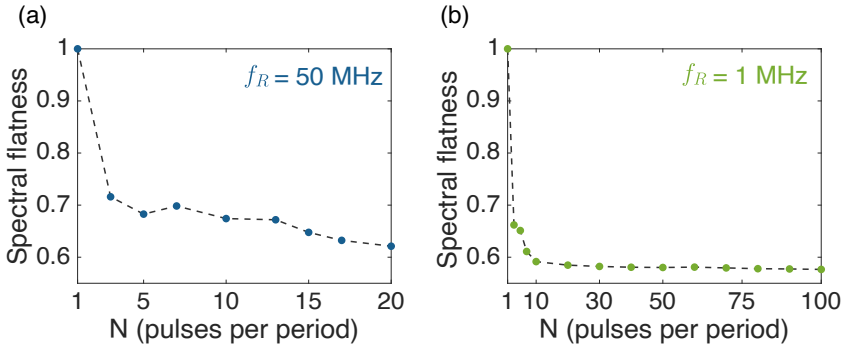

Figure A.6: Optimum spectral flatness values obtained for multi-pulsed sequences having different number of pulses per period. The results are obtained for two repetition rates of (a) 50 MHz and (b) 1 MHz.

Finally, as a proof-of-concept demonstration, a GS OFC obtained with a multi-pulsed gain-switching signal of 50 MHz containing N= 5 pulses per period is experimentally generated. The obtained spectrum is compared to the optical spectrum of a GS comb generated by gain switching the optically-injected discrete-mode laser using a train of electrical pulses with a single pulse per period. The experimental setup used is the one described in Fig. 5.1 of Chapter 5. The gain-switching signal has a DC value of I_{bias}= 0.2 mA, and a peak-to-peak amplitude of V_{RF}= 8 V. Both trains of pulses, single and multi-pulsed, are generated by a pulse pattern generator, and the pulse width of the electrical pulses is configured to a value of τ_{pulse}= 200 ps. The OFC is provided with coherence by means of optical injection at λ_{inj}= 1549.57 nm with an injection power of P_{inj}= 70.8 μW (-11.5 dBm), measured at the output of the master laser. Moreover, an EDFA is placed at the input of the optical spectrum analyzer, and the current of the amplifier is maintained at the same value for both experiments.

Fig. A.7 (a) shows the optical spectrum of the single-pulsed GS comb, measured with the high-resolution optical spectrum analyzer. The optical frequency comb obtained under the described operation conditions exhibits a bandwidth at 10 dB of Δf_{10dB}= 86.4 GHz and an average optical power after amplification, calculated considering the tones comprised within Δf_{10dB}, of -38.60 dBm (∼138 μW).

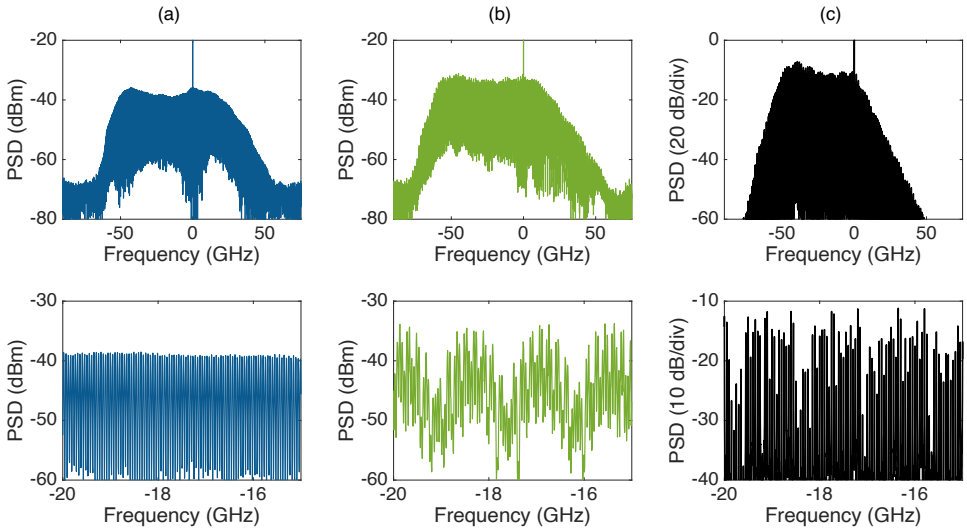

Figure A.7: (a) Experimental 50-MHz GS OFC obtained under single-pulsed electrical excitation measured with a 10-MHz resolution optical spectrum analyzer. (b) Experimental 50-MHz GS OFC obtained under multi-pulsed electrical excitation with a sequence containing 5 pulses per period. (c) Optical simulation of a 50-MHz GS OFC obtained by using the same gain-switching multi-pulsed electrical signal.

The optical spectrum obtained when employing multi-pulsed excitation is shown in Fig. A.7 (b). The excitation signal is selected from the previously described spectral flatness optimization algorithm. The OFC features a Δf_{10dB} of 85 GHz and an average optical power (after amplification in the same conditions) within this spectral width of -36.62 dBm (∼219 μW). Nevertheless, despite the selected gain-switching signal is

the one that yields the optimum spectral flatness (considering 500 iterations of the optimization algorithm), a ripple in the comb envelope can be clearly distinguished (see zoomed view in panel (b), bottom). This ripple negatively impacts the calculation of average optical power, leading to a much smaller increase in power than expected (approximately 1.6 times the single-pulsed value).

Additionally, an optical simulation has been carried out using the same multi-pulsed signal. The gain-switching signal switches the discrete-mode laser from below to above threshold, between I_{off}= 4.6 mA and I_{off}= 44.6 mA. As in the experiments, the electrical pulses have a duration of 200 ps. Regarding optical injection, it is performed at the blue side of the frequency spectrum using a detuning value of 35 GHz. The injected power is 0.5 mW. The optical spectrum obtained from the simulation is included in Fig. A.7 (c). Although less defined than in the experimental realization, a ripple showing the same periodicity as in the experiments modulates the comb envelope.

Finally, other types of gain-switching signals, such as maximum length sequences, were also investigated during this thesis. Fig. A.8 presents two experimental GS combs generated by gain-switching a commercial discrete-mode laser using an MLS. Panel (a) shows the result obtained for a binary sequence with a binary rate of 10 Gb/s and a length of 31 bits (2^5-1), yielding a comb repetition rate of approximately 322.6 MHz. Panel (b) shows the result obtained for an MLS with the same data rate of 10 Gb/s but with a length of 127 bits (2^7-1), resulting in a comb repetition rate of ∼78.74 MHz.

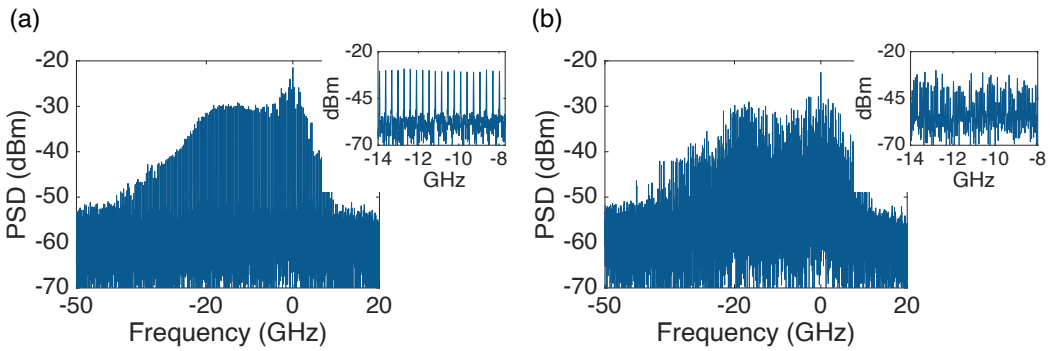

Figure A.8: Experimental results of OFCs generated under pulsed gain switching of a discrete-mode laser using MLSs. (a) GS comb obtained with a repetition rate of ∼322.6 MHz. (b) GS comb featuring a repetition rate of ∼78.74 MHz.

In summary, the combs resulting from these approaches did not exhibit the desired spectral quality, particularly in terms of spectral flatness. However, while they may not be suitable for absorption spectroscopy, they could be useful for applications that do not require flat combs, such as dual-comb applications where the information can be retrieved from the spectral phase of the comb lines. The continuation of this research line, involving gain switching with advanced modulation signals, could therefore be of interest for developing low-repetition-rate combs suitable for these applications. In the case of pseudo-random modulation, a more in-depth analysis should be conducted, including both optical and electrical simulations.

List of publications

Contributions included in the thesis

Journal articles

C. Quevedo-Galán, V. Durán, A. Rosado, A. Pérez-Serrano, J. M. G. Tijero, and I. Esquivias, "Gain-switched semiconductor lasers with pulsed excitation and optical injection for dual-comb spectroscopy," *Optics Express*, vol. 28, no. 22, pp. 33307–33317, 2020. DOI: 10.1364/OE.404398.

C. Quevedo-Galán, A. Pérez-Serrano, I. E. López-Delgado, J. M. G. Tijero, and I. Esquivias, "Dual-Comb Spectrometer Based on Gain-Switched Semiconductor Lasers and a Low-Cost Software-Defined Radio," *IEEE Access*, vol. 9, pp. 92367–92373, 2021. DOI: 10.1109/ACCESS.2021.3091872.

I. Rebolledo-Salgado, C. Quevedo-Galán, Ó.B. Helgason, A. Lööf, Z. Ye, F. Lei, J. Schröder, M. Zelan, and V. Torres-Company, "Platicon dynamics in photonic molecules," *Communications Physics*, vol. 6, no. 1, p. 303, 2023. DOI: 10.1038/s42005-023-01424-5.

C. Quevedo-Galán, A. Rosado, A. Pérez-Serrano, J. M. G. Tijero, and I. Esquivias, "Dual-Comb Spectroscopy With Enhanced Resolution by Pseudorandom Phase Modulation of Gain-Switched Optical Pulses," *Journal of Lightwave Technology*, vol. 42, no. 10, pp. 3954–3962, 2024. DOI: 10.1109/JLT.2024.3368363.

International conferences[1]

C. Quevedo-Galán$^{\diamond}$, A. Rosado, V. Durán, A. Pérez-Serrano, J. M. G. Tijero, and I. Esquivias, "100-MHz dual-comb spectroscopy by pulsed gain-switching of externally injected semiconductor lasers," in *Frontiers in Optics/Laser Science*, Washington DC (USA), September 2020, Paper LM5F.2 [Oral]. DOI: 10.1364/LS.2020.LM5F.2

C. Quevedo-Galán$^{\diamond}$, A. Rosado, V. Durán, A. Pérez-Serrano, J. M. G. Tijero, and I. Esquivias, "Dual-comb spectroscopy application of a 100 MHz line spacing optical frequency comb generated by gain-switching a laser diode," in *European Semiconductor Laser Workshop*, Eindhoven (Netherlands), December 2020 [Oral].

[1]The author who presented the contribution is indicated with $^{\diamond}$.

C. Quevedo-Galán$^{\diamond}$, P. López-Querol, A. Pérez-Serrano, J. M. G. Tijero, and I. Esquivias, "Gain-switched optical frequency combs with comb spacing down to 5 MHz," in *European Semiconductor Laser Workshop*, Paris (France), September 2021 [Oral].

P. López-Querol, C. Quevedo-Galán, A. Pérez-Serrano, J. M. G. Tijero$^{\diamond}$, and I. Esquivias, "Low repetition rate optical frequency combs generated by pulsed gain-switching of semiconductor lasers," in *27th International Semiconductor Laser Conference (ISLC)*, Potsdam (Germany), October 2021 [Poster]. DOI: 10.1109/ISLC51662.2021.9615720.

C. Quevedo-Galán$^{\diamond}$, P. López-Querol, E. Sentre-Arribas, A. Pérez-Serrano, J. M. G. Tijero, and I. Esquivias, "Dual-Comb Ranging Using Low-Repetition-Rate Gain-Switched Semiconductor Lasers," in *Frontiers in Optics/Laser Science*, Rochester, New York (USA), October 2022, Paper JW5B.18 [Poster]. DOI: 10.1364/FIO.2022.JW5B.18.

C. Quevedo-Galán$^{\diamond}$, A. Rosado, A. Pérez-Serrano, J. M. G. Tijero, and I. Esquivias, "Ultra-high-resolution dual-comb spectrometer based on densified gain-switching optical frequency combs," in *CLEO*, San José, California (USA), May 2023, Paper SM3O.4 [Oral]. DOI: 10.1364/CLEO_SI.2023.SM3O.4.

C. Quevedo-Galán$^{\diamond}$, A. Rosado, P. López-Querol, A. Pérez-Serrano, J. M. G. Tijero, and I. Esquivias, "Dual-comb interferometer based on densified gain-switched laser diodes for high-resolution sensing applications," in *CLEO/Europe-EQEC*, Munich (Germany), June 2023, Paper cb74 [Oral]. DOI: 10.1109/CLEO/Europe-EQEC57999.2023.10231545.

National conferences

I. E. López-Delgado$^{\diamond}$, C. Quevedo-Galán, A. Pérez-Serrano, J. M. G. Tijero, and I. Esquivias, "Dual-Comb spectroscopy system based on gain-switched semiconductor lasers, software-defined radios, and step-recovery diodes," in *XII Reunión Española de Optoelectrónica OPTOEL'21*, Virtual, July 2021 [Poster].

P. López-Querol$^{\diamond}$, C. Quevedo-Galán, A. Pérez-Serrano, J. M. G. Tijero, and I. Esquivias, "Experimental analysis of low repetition rate optical frequency combs generated by pulsed gain-switching of optically injected laser diodes," in *XII Reunión Española de Optoelectrónica OPTOEL'21*, Virtual, July 2021 [Poster].

C. Quevedo-Galán$^{\diamond}$, A. Rosado, L. Monroy, P. López-Querol, A. Pérez-Serrano, J. M. G. Tijero, and I. Esquivias, "Ultra-high resolution dual comb spectroscopy based on gain-switching optical frequency combs," in *XIII Reunión Española de Optoelectrónica OPTOEL'23*, Sevilla (Spain), June 2023 [Poster].

Other contributions not included in the thesis

Journal articles

A. Pérez-Serrano, C. Quevedo-Galán, V. R. Aguilera-Sánchez, J. M. G. Tijero, and I. Esquivias, "Differential Absorption Lidar Transmitter Based on an Indium Phosphide Photonic Integrated Circuit for Carbon Dioxide Sensing," *IEEE Journal of Selected Topics in Quantum Electronics*, vol. 28, no. 5, pp. 1–8, 2022. DOI: 10.1109/JSTQE.2022.3156183.

P. López-Querol, C. Quevedo-Galán, A. Pérez-Serrano, J. M. G. Tijero, and I. Esquivias, "Generation of optical frequency combs by Q-switching integrated multi-section semiconductor lasers," *Optics Express*, vol. 31, no. 20, pp. 33475–33485, 2023. DOI: 10.1364/OE.498426

L. Monroy, C. Quevedo-Galán, A. Pérez-Serrano, J.M.G. Tijero, I. Esquivias, "Low-cost dual-comb spectrometer for CO2 monitoring based on gain-switched semiconductor lasers," *Results in Physics*, vol. 58, p. 107516, 2024. DOI: 10.1016/j.rinp.2024.107516.

International and national conferences

A. Pérez-Serrano$^{\diamond}$, C. Quevedo-Galán, V. R. Aguilera-Sánchez, P. Castera, J. M. G. Tijero, and I. Esquivias, "Differential Absorption Lidar Transmitter based on a Photonic Integrated Circuit for Carbon Dioxide Sensing," in *Frontiers in Optics/Laser Science*, Washington DC (USA), November 2021, Paper FM1B.4 [Oral]. DOI: 10.1364/FIO.2021.FM1B.4.

A. Pérez-Serrano$^{\diamond}$, C. Quevedo-Galán, V. R. Aguilera-Sánchez, J. M. G. Tijero, and I. Esquivias, "Carbon Dioxide Sensing with a Photonic Integrated Differential Absorption LiDAR Transmitter," in *23rd European Conference on Integrated Optics*, Milan (Italy), May 2022 [Oral].

P. López-Querol$^{\diamond}$, C. Quevedo-Galán, A. Soria-Gómez, I. Pintor, J. M. G. Tijero, I. Esquivias, and A. Pérez-Serrano, "Photonic Integrated Circuits at CEMDATIC-UPM," in *XIII Reunión Española de Optoelectrónica OPTOEL'23*, Sevilla (Spain), June 2023 [Poster].

S. del Río-Martín$^{\diamond}$, C. Quevedo-Galán, P. López-Querol, and I. Esquivias, "Photonic Microwave Phase Shifter based on an I/Q modulator," in *XIII Reunión Española de Optoelectrónica OPTOEL'23*, Sevilla (Spain), June 2023 [Poster].

D. Domínguez-Castillejo$^{\diamond}$, C. Quevedo-Galán, P. López-Querol, and A. Pérez-Serrano, "Pseudo Random Phase Modulation Coherent LIDAR," in *XIII Reunión Española de Optoelectrónica OPTOEL'23*, Sevilla (Spain), June 2023 [Poster].

P. López-Querol$^{\diamond}$, C. Quevedo-Galán, A. Pérez-Serrano, J. M. G. Tijero, and I. Esquivias, "Q-switched semiconductor lasers as sources for optical frequency comb generation," in *CLEO/Europe-EQEC*, Munich (Germany), June 2023, Paper cbp15 [Poster].

L. Monroy$^{\diamond}$, C. Quevedo-Galán, A. Pérez-Serrano, J. M. G. Tijero, and Ignacio Esquivias, "L-band dual-comb based on gain-switched lasers for CO2 monitoring," in *European Optical Society Annual Meeting (EOSAM)*, Dijon (France), September 2023 [Oral]. DOI: 10.1051/epjconf/202328707010.

Bibliography

[1] P. M. Anandarajah, K. Shi, J. O'Carroll, A. Kaszubowska, R. Phelan, L. P. Barry, A. D. Ellis, P. Perry, D. Reid, B. Kelly, and J. O'Gorman, "Phase shift keyed systems based on a gain switched laser transmitter", *Optics Express*, vol. 17, no. 15, pp. 12 668–12 677, 2009. DOI: 10.1364/OE.17.012668.

[2] I. Coddington, W. C. Swann, and N. R. Newbury, "Coherent multiheterodyne spectroscopy using stabilized optical frequency combs", *Physical Review Letters*, vol. 100, no. 1, p. 13 902, 2008. DOI: 10.1103/PhysRevLett.100.013902.

[3] B. Jerez, P. Martín-Mateos, E. Prior, C. de Dios, and P. Acedo, "Dual optical frequency comb architecture with capabilities from visible to mid-infrared", *Optics Express*, vol. 24, no. 13, pp. 14 986–14 994, 2016. DOI: 10.1364/OE.24.014986.

[4] B. Jerez, P. Martín-Mateos, E. Prior, C. de Dios, and P. Acedo, "Gain-switching injection-locked dual optical frequency combs: Characterization and optimization", *Optics Letters*, vol. 41, no. 18, pp. 4293–4296, 2016. DOI: 10.1364/OL.41.004293.

[5] T. Udem, R. Holzwarth, and T. W. Hänsch, "Optical frequency metrology", *Nature*, vol. 416, no. 6877, pp. 233–237, 2002. DOI: 10.1038/416233a.

[6] N. Dimarcq, M. Gertsvolf, G. Mileti, *et al.*, "Roadmap towards the redefinition of the second", *Metrologia*, vol. 61, no. 1, p. 012 001, 2024. DOI: 10.1088/1681-7575/ad17d2.

[7] T. Fortier and E. Baumann, "20 years of developments in optical frequency comb technology and applications", *Communications Physics*, vol. 2, no. 1, p. 153, 2019. DOI: 10.1038/s42005-019-0249-y.

[8] J. L. Hall, "Nobel lecture: Defining and measuring optical frequencies", *Reviews of Modern Physics*, vol. 78, no. 4, pp. 1279–1295, 2006. DOI: 10.1103/RevModPhys.78.1279.

[9] J. N. Eckstein, A. I. Ferguson, and T. W. Hänsch, "High-resolution two-photon spectroscopy with picosecond light pulses", *Physical Review Letters*, vol. 40, no. 13, pp. 847–850, 1978. DOI: 10.1103/PhysRevLett.40.847.

[10] T. Udem, J. Reichert, R. Holzwarth, and T. W. Hänsch, "Accurate measurement of large optical frequency differences with a mode-locked laser", *Optics Letters*, vol. 24, no. 13, pp. 881–883, 1999. DOI: 10.1364/OL.24.000881.

[11] T. Udem, J. Reichert, R. Holzwarth, and T. W. Hänsch, "Absolute optical frequency measurement of the cesium D_1 line with a mode-locked laser", *Physical Review Letters*, vol. 82, no. 13, pp. 3568–3571, 1999. DOI: 10.1103/PhysRevLett.82.3568.

[12] J. K. Ranka, R. S. Windeler, and A. J. Stentz, "Visible continuum generation in air–silica microstructure optical fibers with anomalous dispersion at 800 nm", *Optics Letters*, vol. 25, no. 1, pp. 25–27, 2000. DOI: 10.1364/OL.25.000025.

[13] S. A. Diddams, D. J. Jones, J. Ye, S. T. Cundiff, J. L. Hall, J. K. Ranka, R. S. Windeler, R. Holzwarth, T. Udem, and T. W. Hänsch, "Direct link between microwave and optical frequencies with a 300 THz femtosecond laser comb", *Physical Review Letters*, vol. 84, no. 22, pp. 5102–5105, 2000. DOI: 10.1103/PhysRevLett.84.5102.

[14] D. J. Jones, S. A. Diddams, J. K. Ranka, A. Stentz, R. S. Windeler, J. L. Hall, and S. T. Cundiff, "Carrier-envelope phase control of femtosecond mode-locked lasers and direct optical frequency synthesis", *Science*, vol. 288, no. 5466, pp. 635–639, 2000. DOI: 10.1126/science.288.5466.635.

[15] R. Holzwarth, T. Udem, T. W. Hänsch, J. C. Knight, W. J. Wadsworth, and P. S. J. Russell, "Optical frequency synthesizer for precision spectroscopy", *Physical Review Letters*, vol. 85, no. 11, pp. 2264–2267, 2000. DOI: 10.1103/PhysRevLett.85.2264.

[16] A. Hermans, K. V. Gasse, and B. Kuyken, "On-chip optical comb sources", *APL Photonics*, vol. 7, no. 10, p. 100 901, 2022. DOI: 10.1063/5.0105164.

[17] E. Russell, B. Corbett, and F. C. G. Gunning, "Gain-switched dual frequency comb at 2 μm", *Optics Express*, vol. 30, no. 4, pp. 5213–5221, 2022. DOI: 10.1364/OE.446171.

[18] M. H. P. Pfeiffer, C. Herkommer, J. Liu, H. Guo, M. Karpov, E. Lucas, M. Zervas, and T. J. Kippenberg, "Octave-spanning dissipative Kerr soliton frequency combs in Si_3N_4 microresonators", *Optica*, vol. 4, no. 7, pp. 684–691, 2017. DOI: 10.1364/OPTICA.4.000684.

[19] H. Ito, H. Yokoyama, S. Murata, and H. Inaba, "Picosecond optical pulse generation from an R.F. modulated AlGaAs D.H. diode laser", *Electronics Letters*, vol. 15, no. 23, pp. 738–740, 1979. DOI: 10.1049/el:19790528.

[20] C. Lin, P. Liu, T. Damen, D. Eilenberger, and R. Hartman, "Simple picosecond pulse generation scheme for injection lasers", *Electronics Letters*, vol. 16, no. 15, pp. 600–602, 1980. DOI: 10.1049/el:19800416.

[21] K. Y. Lau, "Gain switching of semiconductor injection lasers", *Applied Physics Letters*, vol. 52, no. 4, pp. 257–259, 1988. DOI: 10.1063/1.99486.

[22] L. A. Coldren, S. W. Corzine, and M. Mashanovitch, *Diode Lasers and Photonic Integrated Circuits*, 2nd ed. John Wiley & Sons, 2012.

[23] P. P. Vasil'ev, I. H. White, and J. Gowar, "Fast phenomena in semiconductor lasers", *Reports on Progress in Physics*, vol. 63, no. 12, p. 1997, 2000. DOI: 10.1088/0034-4885/63/12/203.

[24] A. Rosado, A. Pérez-Serrano, J. M. G. Tijero, A. V. Gutierrez, L. Pesquera, and I. Esquivias, "Numerical and experimental analysis of optical frequency comb generation in gain-switched semiconductor lasers", *IEEE Journal of Quantum Electronics*, vol. 55, no. 6, pp. 1–12, 2019. DOI: 10.1109/JQE.2019.2943482.

[25] C. Henry, "Theory of the linewidth of semiconductor lasers", *IEEE Journal of Quantum Electronics*, vol. 18, no. 2, pp. 259–264, 1982. DOI: 10.1109/JQE.1982.1071522.

[26] S. Mohrdiek, H. Burkhard, F. Steinhagen, H. Hillmer, R. Losch, W. Schlapp, and R. Gobel, "10-Gb/s standard fiber transmission using directly modulated 1.55-μm quantum-well DFB lasers", *IEEE Photonics Technology Letters*, vol. 7, no. 11, pp. 1357–1359, 1995. DOI: 10.1109/68.473497.

[27] K. Petermann, *Laser Diode Modulation and Noise*, 1st ed. Springer Dordrecht, 1991.

[28] L. Bjerkan, A. Royset, L. Hafskjaer, and D. Myhre, "Measurement of laser parameters for simulation of high-speed fiberoptic systems", *Journal of Lightwave Technology*, vol. 14, no. 5, pp. 839–850, 1996. DOI: 10.1109/50.495166.

[29] A. Consoli, I. Esquivias, F. J. Hernández, J. Mulet, and S. Balle, "Characterization of gain-switched pulses from 1.55-μm VCSEL", *IEEE Photonics Technology Letters*, vol. 22, no. 11, pp. 772–774, 2010. DOI: 10.1109/LPT.2010.2045648.

[30] D.-S. Seo, D. Y. Kim, and H.-F. Liu, "Timing jitter reduction of gain-switched DFB laser by external injection-seeding", *Electronics Letters*, vol. 32, no. 1, pp. 44–45, 1996. DOI: 10.1049/el:19960019.

[31] P. Gunning, J. Lucek, D. Moodie, K. Smith, R. Davey, S. Chernikov, M. Guy, J. Taylor, and A. Siddiqui, "Gain switched DFB laser diode pulse source using continuous wave light injection for jitter suppression and an electroabsorption

modulator for pedestal suppression", *Electronics Letters*, vol. 32, no. 11, pp. 1010–1011, 1996. DOI: 10.1049/el:19960649.

[32] C. Guignard, P. M. Anandarajah, A. Clarke, L. P. Barry, O. Vaudel, and P. Besnard, "Experimental investigation of the impact of optical injection on vital parameters of a gain-switched pulse source", *Optics Communications*, vol. 277, no. 1, pp. 150–155, 2007. DOI: 10.1016/j.optcom.2007.04.058.

[33] S. P. Ó. Dúill, R. Zhou, P. M. Anandarajah, and L. P. Barry, "Analytical approach to assess the impact of pulse-to-pulse phase coherence of optical frequency combs", *IEEE Journal of Quantum Electronics*, vol. 51, no. 11, pp. 1–8, 2015. DOI: 10.1109/JQE.2015.2485228.

[34] A. Rosado, A. Pérez-Serrano, J. M. G. Tijero, Á. Valle, L. Pesquera, and I. Esquivias, "Experimental study of optical frequency comb generation in gain-switched semiconductor lasers", *Optics & Laser Technology*, vol. 108, pp. 542–550, 2018. DOI: 10.1016/j.optlastec.2018.07.038.

[35] A. Rosado, A. Pérez-Serrano, J. M. G. Tijero, Á. Valle, L. Pesquera, and I. Esquivias, "Enhanced optical frequency comb generation by pulsed gain-switching of optically injected semiconductor lasers", *Optics Express*, vol. 27, no. 6, pp. 9155–9163, 2019. DOI: 10.1364/OE.27.009155.

[36] P. M. Anandarajah, S. P. Ó. Dúill, R. Zhou, and L. P. Barry, "Enhanced optical comb generation by gain-switching a single-mode semiconductor laser close to its relaxation oscillation frequency", *IEEE Journal of Selected Topics in Quantum Electronics*, vol. 21, no. 6, pp. 592–600, 2015. DOI: 10.1109/JSTQE.2015.2456751.

[37] P. M. Anandarajah, R. Maher, Y. Q. Xu, S. Latkowski, J. O'Carroll, S. G. Murdoch, R. Phelan, J. O'Gorman, and L. P. Barry, "Generation of coherent multicarrier signals by gain switching of discrete mode lasers", *IEEE Photonics Journal*, vol. 3, no. 1, pp. 112–122, 2011. DOI: 10.1109/JPHOT.2011.2105861.

[38] H. Shams, T. Shao, M. J. Fice, P. M. Anandarajah, C. C. Renaud, F. V. Dijk, L. P. Barry, and A. J. Seeds, "100 Gb/s multicarrier THz wireless transmission system with high frequency stability based on a gain-switched laser comb source", *IEEE Photonics Journal*, vol. 7, no. 3, pp. 1–11, 2015. DOI: 10.1109/JPHOT.2015.2438437.

[39] J. Pfeifle, V. Vujicic, R. T. Watts, P. C. Schindler, C. Weimann, R. Zhou, W. Freude, L. P. Barry, and C. Koos, "Flexible terabit/s Nyquist-WDM superchannels using a gain-switched comb source", *Optics Express*, vol. 23, no. 2, pp. 724–738, 2015. DOI: 10.1364/OE.23.000724.

[40] E. P. Martin, T. Shao, V. Vujicic, P. M. Anandarajah, C. Browning, R. Llorente, and L. P. Barry, "25-Gb/s OFDM 60-GHz radio over fiber system based on a gain switched laser", *Journal of Lightwave Technology*, vol. 33, no. 8, pp. 1635–1643, 2015. DOI: 10.1109/JLT.2015.2391994.

[41] P. M. Anandarajah, R. Zhou, R. Maher, D. Lavery, M. Paskov, B. Thomsen, S. Savory, and L. P. Barry, "Gain-switched multicarrier transmitter in a long-reach UDWDM PON with a digital coherent receiver", *Optics Letters*, vol. 38, no. 22, pp. 4797–4800, 2013. DOI: 10.1364/OL.38.004797.

[42] J. N. Kemal, J. Pfeifle, P. Marin-Palomo, M. D. G. Pascual, S. Wolf, F. Smyth, W. Freude, and C. Koos, "Multi-wavelength coherent transmission using an optical frequency comb as a local oscillator", *Optics Express*, vol. 24, no. 22, pp. 25 432–25 445, 2016. DOI: 10.1364/OE.24.025432.

[43] Á. R. Criado, C. de Dios, G. H. Döhler, S. Preu, S. Malzer, S. Bauerschmidt, H. Lu, A. C. Gossard, and P. Acedo, "Ultra-narrow linewidth CW sub-THz generation using GS based OFCG and n-i-pn-i-p superlattice photomixers", *Electronics Letters*, vol. 48, no. 22, pp. 1425–1426, 2012. DOI: 10.1049/el.2012.3158.

[44] Á. R. Criado, C. de Dios, E. Prior, G. H. Döhler, S. Preu, S. Malzer, H. Lu, A. C. Gossard, and P. Acedo, "Continuous-wave sub-THz photonic generation with ultra-narrow linewidth, ultra-high resolution, full frequency range coverage and high long-term frequency stability", *IEEE Transactions on Terahertz Science and Technology*, vol. 3, no. 4, pp. 461–471, 2013. DOI: 10.1109/T{THz}.2013.2260374.

[45] Á. R. C. Serrano, C. de Dios Fernandez, E. P. Cano, M. Ortsiefer, P. Meissner, and P. Acedo, "VCSEL-based optical frequency combs: Toward efficient single-device comb generation", *IEEE Photonics Technology Letters*, vol. 25, no. 20, pp. 1981–1984, 2013. DOI: 10.1109/LPT.2013.2280700.

[46] E. Prior, C. D. Dios, M. Ortsiefer, P. Meissner, and P. Acedo, "Understanding VCSEL-based gain switching optical frequency combs: Experimental study of polarization dynamics", *Journal of Lightwave Technology*, vol. 33, no. 22, pp. 4572–4579, 2015. DOI: 10.1109/JLT.2015.2476956.

[47] E. Prior, C. de Dios, R. Criado, M. Ortsiefer, P. Meissner, and P. Acedo, "Dynamics of dual-polarization VCSEL-based optical frequency combs under optical injection locking", *Optics Letters*, vol. 41, no. 17, pp. 4083–4086, 2016. DOI: 10.1364/OL.41.004083.

[48] A. Quirce, C. de Dios, A. Valle, and P. Acedo, "VCSEL-based optical frequency combs expansion induced by polarized optical injection", *IEEE Journal of Selected Topics in Quantum Electronics*, vol. 25, no. 6, pp. 1–9, 2019. DOI: 10.1109/JSTQE.2018.2888560.

[49] R. Zhou, S. Latkowski, J. O'Carroll, R. Phelan, L. P. Barry, and P. Anandarajah, "40nm wavelength tunable gain-switched optical comb source", *Optics Express*, vol. 19, no. 26, pp. 415–420, 2011. DOI: 10.1364/OE.19.00B415.

[50] E. Prior, C. de Dios, Á. R. Criado, M. Ortsiefer, P. Meissner, and P. Acedo, "Expansion of VCSEL-based optical frequency combs in the sub-THz span: Comparison of non-linear techniques", *Journal of Lightwave Technology*, vol. 34, no. 17, pp. 4135–4142, 2016. DOI: 10.1109/JLT.2016.2594129.

[51] P. D. Lakshmijayasimha, P. M. Anandarajah, P. Landais, and A. Kaszubowska-Anandarajah, "Optical frequency comb expansion using mutually injection-locked gain-switched lasers", *Applied Sciences*, vol. 11, no. 15, p. 7108, 2021. DOI: 10.3390/app11157108.

[52] P. D. Lakshmijayasimha, A. Kaszubowska-Anandarajah, E. P. Martin, P. Landais, and P. M. Anandarajah, "Expansion and phase correlation of a wavelength tunable gain-switched optical frequency comb", *Optics Express*, vol. 27, no. 12, pp. 16 560–16 570, 2019. DOI: 10.1364/OE.27.016560.

[53] P. D. Lakshmijayasimha, A. Kaszubowska-Anandarajah, M. Srivastava, E. P. Martin, and P. M. Anandarajah, "Generation of a wideband OFC by the correlation of multiple modes of a gain-switched Fabry Pérot laser", *Journal of Lightwave Technology*, vol. 41, no. 15, pp. 5084–5090, 2023. DOI: 10.1109/JLT.2023.3284912.

[54] K. Tong, H. Li, L. Yuan, J. Li, and Z. Du, "Experimental investigation of the dependence of compact optical frequency comb generated by direct modulation of semiconductor laser on the modulation waveform and mode", *Optics & Laser Technology*, vol. 155, p. 108 434, 2022. DOI: 10.1016/j.optlastec.2022.108434.

[55] P. Kaur, A. Boes, G. Ren, T. G. Nguyen, G. Roelkens, and A. Mitchell, "Hybrid and heterogeneous photonic integration", *APL Photonics*, vol. 6, no. 6, p. 061 102, 2021. DOI: 10.1063/5.0052700.

[56] J. K. Alexander, P. E. Morrissey, H. Yang, M. Yang, P. J. Marraccini, B. Corbett, and F. H. Peters, "Monolithically integrated low linewidth comb source using gain switched slotted Fabry-Perot lasers", *Optics Express*, vol. 24, no. 8, pp. 7960–7965, 2016. DOI: 10.1364/OE.24.007960.

[57] M. D. G. Pascual, V. Vujicic, J. Braddell, F. Smyth, P. M. Anandarajah, and L. P. Barry, "InP photonic integrated externally injected gain switched optical frequency comb", *Optics Letters*, vol. 42, no. 3, pp. 555–558, 2017. DOI: 10.1364/OL.42.000555.

[58] M. D. G. Pascual, V. Vujicic, J. Braddell, F. Smyth, P. Anandarajah, and L. Barry, "Photonic integrated gain switched optical frequency comb for spectrally

efficient optical transmission systems", *IEEE Photonics Journal*, vol. 9, no. 3, pp. 1–8, 2017. DOI: 10.1109/JPHOT.2017.2678478.

[59] M. Srivastava, S. T. Ahmad, A. Sharma, P. D. Lakshmijayasimha, M. D. G. Pascual, F. Smyth, P. M. Anandarajah, and A. Kaszubowska-Anandarajah, "Monolithically integrated optical frequency comb generator based on mutually injection locked gain switched lasers", *IEEE Journal of Selected Topics in Quantum Electronics*, vol. 29, no. 5, pp. 1–8, 2023. DOI: 10.1109/JSTQE.2023.3305829.

[60] S. Shao, J. Li, H. Chen, S. Yang, and M. Chen, "Gain-switched optical frequency comb source using a hybrid integrated self-injection locking DFB laser", *IEEE Photonics Journal*, vol. 14, no. 1, pp. 1–6, 2022. DOI: 10.1109/JPHOT.2022.3141424.

[61] A. M. Weiner, *Ultrafast Optics*, 1st ed. John Wiley & Sons, 2009.

[62] K. V. Gasse, S. Uvin, V. Moskalenko, S. Latkowski, G. Roelkens, E. Bente, and B. Kuyken, "Recent advances in the photonic integration of mode-locked laser diodes", *IEEE Photonics Technology Letters*, vol. 31, no. 23, pp. 1870–1873, 2019. DOI: 10.1109/LPT.2019.2945973.

[63] A. Yadav, N. B. Chichkov, E. A. Avrutin, A. Gorodetsky, and E. U. Rafailov, "Edge emitting mode-locked quantum dot lasers", *Progress in Quantum Electronics*, vol. 87, p. 100 451, 2023. DOI: 10.1016/j.pquantelec.2022.100451.

[64] V. Vujicic, C. Calò, R. Watts, F. Lelarge, C. Browning, K. Merghem, A. Martinez, A. Ramdane, and L. P. Barry, "Quantum dash mode-locked lasers for data centre applications", *IEEE Journal of Selected Topics in Quantum Electronics*, vol. 21, no. 6, pp. 53–60, 2015. DOI: 10.1109/JSTQE.2015.2487884.

[65] P. Marin-Palomo, J. N. Kemal, P. Trocha, S. Wolf, K. Merghem, F. Lelarge, A. Ramdane, W. Freude, S. Randel, and C. Koos, "Comb-based WDM transmission at 10 Tbit/s using a DC-driven quantum-dash mode-locked laser diode", *Optics Express*, vol. 27, no. 22, pp. 31 110–31 129, 2019. DOI: 10.1364/OE.27.031110.

[66] ITU-T, "Recommendation ITU-T G.694.1. Spectral grids for WDM applications: DWDM frequency grid", International Telecommunication Union, Tech. Rep., 2020.

[67] P. Trocha, J. N. Kemal, Q. Gaimard, G. Aubin, F. Lelarge, A. Ramdane, W. Freude, S. Randel, and C. Koos, "Ultra-fast optical ranging using quantum-dash mode-locked laser diodes", *Scientific Reports*, vol. 12, no. 1, p. 1076, 2022. DOI: 10.1038/s41598-021-04368-4.

[68] T. Sakamoto, T. Kawanishi, and M. Izutsu, "Asymptotic formalism for ultraflat optical frequency comb generation using a Mach-Zehnder modulator", *Optics Letters*, vol. 32, no. 11, pp. 1515–1517, 2007. DOI: 10.1364/OL.32.001515.

[69] M. Fujiwara, M. Teshima, J. Kani, H. Suzuki, N. Takachio, and K. Iwatsuki, "Optical carrier supply module using flattened optical multicarrier generation based on sinusoidal amplitude and phase hybrid modulation", *Journal of Lightwave Technology*, vol. 21, no. 11, pp. 2705–2714, 2003. DOI: 10.1109/JLT.2003.819147.

[70] Y. Dou, H. Zhang, and M. Yao, "Generation of flat optical-frequency comb using cascaded intensity and phase modulators", *IEEE Photonics Technology Letters*, vol. 24, no. 9, pp. 727–729, 2012. DOI: 10.1109/LPT.2012.2187330.

[71] R. Wu, V. R. Supradeepa, C. M. Long, D. E. Leaird, and A. M. Weiner, "Generation of very flat optical frequency combs from continuous-wave lasers using cascaded intensity and phase modulators driven by tailored radio frequency waveforms", *Optics Letters*, vol. 35, no. 19, pp. 3234–3236, 2010. DOI: 10.1364/OL.35.003234.

[72] V. Torres-Company, J. Lancis, and P. Andrés, "Lossless equalization of frequency combs", *Optics Letters*, vol. 33, no. 16, pp. 1822–1824, 2008. DOI: 10.1364/OL.33.001822.

[73] A. Parriaux, K. Hammani, and G. Millot, "Electro-optic frequency combs", *Advances in Optics and Photonics*, vol. 12, no. 1, pp. 223–287, 2020. DOI: 10.1364/AOP.382052.

[74] V. Torres-Company and A. M. Weiner, "Optical frequency comb technology for ultra-broadband radio-frequency photonics", *Laser & Photonics Reviews*, vol. 8, no. 3, pp. 368–393, 2014. DOI: 10.1002/lpor.201300126.

[75] A. Ishizawa, T. Nishikawa, A. Mizutori, H. Takara, H. Nakano, T. Sogawa, A. Takada, and M. Koga, "Generation of 120-fs laser pulses at 1-GHz repetition rate derived from continuous wave laser diode", *Optics Express*, vol. 19, no. 23, pp. 22 402–22 409, 2011. DOI: 10.1364/OE.19.022402.

[76] T. Yang, J. Dong, S. Liao, D. Huang, and X. Zhang, "Comparison analysis of optical frequency comb generation with nonlinear effects in highly nonlinear fibers", *Optics Express*, vol. 21, no. 7, pp. 8508–8520, 2013. DOI: 10.1364/OE.21.008508.

[77] D. R. Carlson, D. D. Hickstein, W. Zhang, A. J. Metcalf, F. Quinlan, S. A. Diddams, and S. B. Papp, "Ultrafast electro-optic light with subcycle control", *Science*, vol. 361, no. 6409, pp. 1358–1363, 2018. DOI: 10.1126/science.aat6451.

[78] V. Durán, S. Tainta, and V. Torres-Company, "Ultrafast electrooptic dual-comb interferometry", *Optics Express*, vol. 23, no. 23, pp. 30 557–30 569, 2015. DOI: 10.1364/OE.23.030557.

[79] Y. Bao, X. Yi, Z. Li, Q. Chen, J. Li, X. Fan, and X. Zhang, "A digitally generated ultrafine optical frequency comb for spectral measurements with 0.01-

pm resolution and 0.7-μ s response time", *Light: Science & Applications*, vol. 4, no. 6, p. e300, 2015. DOI: 10.1038/lsa.2015.73.

[80] M. Soriano-Amat, H. F. Martins, V. Durán, L. Costa, S. Martin-Lopez, M. Gonzalez-Herraez, and M. R. Fernández-Ruiz, "Time-expanded phase-sensitive optical time-domain reflectometry", *Light: Science & Applications*, vol. 10, no. 1, p. 51, 2021. DOI: 10.1038/s41377-021-00490-0.

[81] B. Xue, Z. Wang, H. Zhang, K. Zhang, Y. Chen, M. He, B. Lin, and H. Wu, "Absolute distance measurement by self-heterodyne EO comb interferometry", *IEEE Photonics Technology Letters*, vol. 30, no. 9, pp. 861–864, 2018. DOI: 10.1109/LPT.2018.2820710.

[82] N. Andriolli, T. Cassese, M. Chiesa, C. de Dios, and G. Contestabile, "Photonic integrated fully tunable comb generator cascading optical modulators", *Journal of Lightwave Technology*, vol. 36, no. 23, pp. 5685–5689, 2018. DOI: 10.1109/JLT.2018.2877020.

[83] M. Xu, M. He, Y. Zhu, S. Yu, and X. Cai, "Flat optical frequency comb generator based on integrated lithium niobate modulators", *Journal of Lightwave Technology*, vol. 40, no. 2, pp. 339–345, 2022. DOI: 10.1109/JLT.2021.3100254.

[84] M. Yu, D. B. III, R. Cheng, C. Reimer, P. Kharel, L. He, L. Shao, D. Zhu, Y. Hu, H. R. Grant, L. Johansson, Y. Okawachi, A. L. Gaeta, M. Zhang, and M. Lončar, "Integrated femtosecond pulse generator on thin-film lithium niobate", *Nature*, vol. 612, no. 7939, pp. 252–258, 2022. DOI: 10.1038/s41586-022-05345-1.

[85] K. Zhang, W. Sun, Y. Chen, H. Feng, Y. Zhang, Z. Chen, and C. Wang, "A power-efficient integrated lithium niobate electro-optic comb generator", *Communications Physics*, vol. 6, no. 1, p. 17, 2023. DOI: 10.1038/s42005-023-01137-9.

[86] M. Zhang, B. Buscaino, C. Wang, A. Shams-Ansari, C. Reimer, R. Zhu, J. M. Kahn, and M. Lončar, "Broadband electro-optic frequency comb generation in a lithium niobate microring resonator", *Nature*, vol. 568, no. 7752, pp. 373–377, 2019. DOI: 10.1038/s41586-019-1008-7.

[87] R. Zhuang, K. Ni, G. Wu, T. Hao, L. Lu, Y. Li, and Q. Zhou, "Electro-optic frequency combs: Theory, characteristics, and applications", *Laser & Photonics Reviews*, vol. 17, no. 6, p. 2 200 353, 2023. DOI: 10.1002/lpor.202200353.

[88] A. Pasquazi, M. Peccianti, L. Razzari, D. J. Moss, S. Coen, M. Erkintalo, Y. K. Chembo, T. Hansson, S. Wabnitz, P. Del'Haye, X. Xue, A. M. Weiner, and R. Morandotti, "Micro-combs: A novel generation of optical sources", *Physics Reports*, vol. 729, pp. 1–81, 2018. DOI: 10.1016/j.physrep.2017.08.004.

[89] G. Agrawal, *Nonlinear Fiber Optics*, 6th ed. Elsevier Science, 2019.

[90] T. Herr, "Solitons and dynamics of frequency comb formation in optical microresonators", Ph.D. dissertation, EPFL, Lausanne, 2013. DOI: 10.5075/epfl-thesis-5877.

[91] P. Del'Haye, A. Schliesser, O. Arcizet, T. Wilken, R. Holzwarth, and T. J. Kippenberg, "Optical frequency comb generation from a monolithic microresonator", *Nature*, vol. 450, no. 7173, pp. 1214–1217, 2007. DOI: 10.1038/nature06401.

[92] K. Saha, Y. Okawachi, B. Shim, J. S. Levy, R. Salem, A. R. Johnson, M. A. Foster, M. R. E. Lamont, M. Lipson, and A. L. Gaeta, "Modelocking and femtosecond pulse generation in chip-based frequency combs", *Optics Express*, vol. 21, no. 1, pp. 1335–1343, 2013. DOI: 10.1364/OE.21.001335.

[93] T. Herr, V. Brasch, J. D. Jost, C. Y. Wang, N. M. Kondratiev, M. L. Gorodetsky, and T. J. Kippenberg, "Temporal solitons in optical microresonators", *Nature Photonics*, vol. 8, no. 2, pp. 145–152, 2014. DOI: 10.1038/nphoton.2013.343.

[94] L. A. Lugiato and R. Lefever, "Spatial dissipative structures in passive optical systems", *Physical Review Letters*, vol. 58, no. 21, pp. 2209–2211, 1987. DOI: 10.1103/PhysRevLett.58.2209.

[95] X. Xue, Y. Xuan, Y. Liu, P.-H. Wang, S. Chen, J. Wang, D. E. Leaird, M. Qi, and A. M. Weiner, "Mode-locked dark pulse Kerr combs in normal-dispersion microresonators", *Nature Photonics*, vol. 9, no. 9, pp. 594–600, 2015. DOI: 10.1038/nphoton.2015.137.

[96] X. Xue, M. Qi, and A. M. Weiner, "Normal-dispersion microresonator Kerr frequency combs", *Nanophotonics*, vol. 5, no. 2, pp. 244–262, 2016. DOI: 10.1515/nanoph-2016-0016.

[97] V. E. Lobanov, G. Lihachev, T. J. Kippenberg, and M. L. Gorodetsky, "Frequency combs and platicons in optical microresonators with normal GVD", *Optics Express*, vol. 23, no. 6, pp. 7713–7721, 2015. DOI: 10.1364/OE.23.007713.

[98] X. Xue, P.-H. Wang, Y. Xuan, M. Qi, and A. M. Weiner, "Microresonator Kerr frequency combs with high conversion efficiency", *Laser & Photonics Reviews*, vol. 11, no. 1, p. 1 600 276, 2017. DOI: 10.1002/lpor.201600276.

[99] X. Xue, Y. Xuan, P.-H. Wang, Y. Liu, D. E. Leaird, M. Qi, and A. M. Weiner, "Normal-dispersion microcombs enabled by controllable mode interactions", *Laser & Photonics Reviews*, vol. 9, no. 4, pp. L23–L28, 2015. DOI: 10.1002/lpor.201500107.

[100] Ó. B. Helgason, M. Girardi, Z. Ye, F. Lei, J. Schröder, and V. Torres-Company, "Surpassing the nonlinear conversion efficiency of soliton microcombs", *Nature Photonics*, vol. 17, no. 11, pp. 992–999, 2023. DOI: 10.1038/s41566-023-01280-3.

[101] W. Wang, L. Wang, and W. Zhang, "Advances in soliton microcomb generation", *Advanced Photonics*, vol. 2, no. 3, p. 034 001, 2020. DOI: 10.1117/1.AP.2.3.034001.

[102] C. Wang, M. Zhang, M. Yu, R. Zhu, H. Hu, and M. Loncar, "Monolithic lithium niobate photonic circuits for Kerr frequency comb generation and modulation", *Nature Communications*, vol. 10, no. 1, p. 978, 2019. DOI: 10.1038/s41467-019-08969-6.

[103] T. J. Kippenberg, A. L. Gaeta, M. Lipson, and M. L. Gorodetsky, "Dissipative Kerr solitons in optical microresonators", *Science*, vol. 361, no. 6402, p. eaan8083, 2018. DOI: 10.1126/science.aan8083.

[104] V. Brasch, E. Lucas, J. D. Jost, M. Geiselmann, and T. J. Kippenberg, "Self-referenced photonic chip soliton Kerr frequency comb", *Light: Science & Applications*, vol. 6, no. 1, pp. e16202–e16202, 2017. DOI: 10.1038/lsa.2016.202.

[105] P. Marin-Palomo, J. N. Kemal, M. Karpov, A. Kordts, J. Pfeifle, M. H. P. Pfeiffer, P. Trocha, S. Wolf, V. Brasch, M. H. Anderson, R. Rosenberger, K. Vijayan, W. Freude, T. J. Kippenberg, and C. Koos, "Microresonator-based solitons for massively parallel coherent optical communications", *Nature*, vol. 546, no. 7657, pp. 274–279, 2017. DOI: 10.1038/nature22387.

[106] M.-G. Suh, X. Yi, Y.-H. Lai, S. Leifer, I. S. Grudinin, G. Vasisht, E. C. Martin, M. P. Fitzgerald, G. Doppmann, J. Wang, D. Mawet, S. B. Papp, S. A. Diddams, C. Beichman, and K. Vahala, "Searching for exoplanets using a microresonator astrocomb", *Nature Photonics*, vol. 13, no. 1, pp. 25–30, 2019. DOI: 10.1038/s41566-018-0312-3.

[107] P. Griffiths, J. De Haseth, and J. Winefordner, *Fourier Transform Infrared Spectrometry*, 2nd ed. Wiley, 2007.

[108] N. Picqué and T. W. Hänsch, "Frequency comb spectroscopy", *Nature Photonics*, vol. 13, no. 3, pp. 146–157, 2019. DOI: 10.1038/s41566-018-0347-5.

[109] S.-J. Lee, B. Widiyatmoko, M. Kourogi, and M. Ohtsu, "Ultrahigh scanning speed optical coherence tomography using optical frequency comb generators", *Japanese Journal of Applied Physics*, vol. 40, no. 8B, p. L878, 2001. DOI: 10.1143/JJAP.40.L878.

[110] S. Schiller, "Spectrometry with frequency combs", *Optics Letters*, vol. 27, no. 9, pp. 766–768, 2002. DOI: 10.1364/OL.27.000766.

[111] I. Coddington, N. Newbury, and W. Swann, "Dual-comb spectroscopy", *Optica*, vol. 3, no. 4, pp. 414–426, 2016. DOI: 10.1364/OPTICA.3.000414.

[112] C. N. Banwell and E. McCash, *Fundamentals of Molecular Spectroscopy*, 4th ed. McGraw-Hill, 1994.

[113] I. Gordon, L. Rothman, R. Hargreaves, *et al.*, "The HITRAN2020 molecular spectroscopic database", *Journal of Quantitative Spectroscopy and Radiative Transfer*, vol. 277, p. 107 949, 2022. DOI: 10.1016/j.jqsrt.2021.107949.

[114] R. V. Kochanov, I. E. Gordon, L. S. Rothman, P. Wcisło, C. Hill, and J. S. Wilzewski, "HITRAN application programming interface (HAPI): A comprehensive approach to working with spectroscopic data", *Journal of Quantitative Spectroscopy and Radiative Transfer*, vol. 177, pp. 15–30, 2016. DOI: 10.1016/j.jqsrt.2016.03.005.

[115] J. Roy, J.-D. Deschênes, S. Potvin, and J. Genest, "Continuous real-time correction and averaging for frequency comb interferometry", *Optics Express*, vol. 20, no. 20, pp. 21 932–21 939, 2012. DOI: 10.1364/OE.20.021932.

[116] T. Ideguchi, A. Poisson, G. Guelachvili, N. Picqué, and T. W. Hänsch, "Adaptive real-time dual-comb spectroscopy", *Nature Communications*, vol. 5, no. 1, p. 3375, 2014. DOI: 10.1038/ncomms4375.

[117] N. B. Hébert, V. Michaud-Belleau, J.-D. Deschênes, and J. Genest, "Self-correction limits in dual-comb interferometry", *IEEE Journal of Quantum Electronics*, vol. 55, no. 4, pp. 1–11, 2019. DOI: 10.1109/JQE.2019.2918935.

[118] E. P. Martin, S. Chandran, A. Rosado, E. P. Soderholm, J. K. Alexander, F. H. Peters, A. A. Ruth, and P. M. Anandarajah, "Mutually injection locked gain switched optical frequency combs for dual comb spectroscopy of H2S", in *Conference on Lasers and Electro-Optics*, Optica Publishing Group, 2020, AM4K.2. DOI: 10.1364/CLEO_AT.2020.AM4K.2.

[119] E. P. Martin, S. T. Ahmad, S. Chandran, A. Rosado, A. A. Ruth, and P. M. Anandarajah, "Stability characterisation and application of mutually injection locked gain switched optical frequency combs for dual comb spectroscopy", *Journal of Lightwave Technology*, vol. 41, no. 13, pp. 4516–4521, 2023. DOI: 10.1109/JLT.2023.3255550.

[120] E. Russell, A. A. Ruth, B. Corbett, and F. C. G. Gunning, "Tunable dual optical frequency comb at 2 μm for CO_2 sensing", *Optics Express*, vol. 31, no. 4, pp. 6304–6313, 2023. DOI: 10.1364/OE.477295.

[121] L. Monroy, C. Quevedo-Galán, A. Pérez-Serrano, J. M. G. Tijero, and I. Esquivias, "Low-cost dual-comb spectrometer for CO_2 monitoring based on gain-switched semiconductor lasers", *Results in Physics*, vol. 58, p. 107 516, 2024. DOI: 10.1016/j.rinp.2024.107516.

[122] J. K. Alexander, L. Caro, M. Dernaika, S. P. Duggan, H. Yang, S. Chandran, E. P. Martin, A. A. Ruth, P. M. Anandarajah, and F. H. Peters, "Integrated dual optical frequency comb source", *Optics Express*, vol. 28, no. 11, pp. 16 900–16 906, 2020. DOI: 10.1364/OE.384706.

[123] Z. Chen, M. Yan, T. W. Hänsch, and N. Picqué, "A phase-stable dual-comb interferometer", *Nature Communications*, vol. 9, no. 1, p. 3035, 2018. DOI: 10.1038/s41467-018-05509-6.

[124] G. Ycas, F. R. Giorgetta, E. Baumann, I. Coddington, D. Herman, S. A. Diddams, and N. R. Newbury, "High-coherence mid-infrared dual-comb spectroscopy spanning 2.6 to 5.2 μm", *Nature Photonics*, vol. 12, no. 4, pp. 202–208, 2018. DOI: 10.1038/s41566-018-0114-7.

[125] S. M. Link, D. J. H. C. Maas, D. Waldburger, and U. Keller, "Dual-comb spectroscopy of water vapor with a free-running semiconductor disk laser", *Science*, vol. 356, no. 6343, pp. 1164–1168, 2017. DOI: 10.1126/science.aam7424.

[126] A. Dutt, C. Joshi, X. Ji, J. Cardenas, Y. Okawachi, K. Luke, A. L. Gaeta, and M. Lipson, "On-chip dual-comb source for spectroscopy", *Science Advances*, vol. 4, no. 3, e1701858, 2024. DOI: 10.1126/sciadv.1701858.

[127] P. Martín-Mateos, B. Jerez, and P. Acedo, "Dual electro-optic optical frequency combs for multiheterodyne molecular dispersion spectroscopy", *Optics Express*, vol. 23, no. 16, p. 21 149, 2015. DOI: 10.1364/oe.23.021149.

[128] G. Millot, S. Pitois, M. Yan, T. Hovhannisyan, A. Bendahmane, T. W. Hänsch, and N. Picqué, "Frequency-agile dual-comb spectroscopy", *Nature Photonics*, vol. 10, no. 1, pp. 27–30, 2016. DOI: 10.1038/nphoton.2015.250.

[129] D. A. Long, A. J. Fleisher, K. O. Douglass, S. E. Maxwell, K. Bielska, J. T. Hodges, and D. F. Plusquellic, "Multiheterodyne spectroscopy with optical frequency combs generated from a continuous-wave laser", *Optics Letters*, vol. 39, no. 9, pp. 2688–2690, 2014. DOI: 10.1364/OL.39.002688.

[130] M. Yan, P.-L. Luo, K. Iwakuni, G. Millot, T. W. Hänsch, and N. Picqué, "Mid-infrared dual-comb spectroscopy with electro-optic modulators", *Light: Science & Applications*, vol. 6, no. 10, e17076–e17076, 2017. DOI: 10.1038/lsa.2017.76.

[131] M. Soriano-Amat, M. A. Soto, V. Duran, H. F. Martins, S. Martin-Lopez, M. Gonzalez-Herraez, and M. R. Fernández-Ruiz, "Common-path dual-comb spectroscopy using a single electro-optic modulator", *Journal of Lightwave Technology*, vol. 38, no. 18, pp. 5107–5115, 2020. DOI: 10.1109/JLT.2020.2998372.

[132] I. Coddington, W. C. Swann, L. Nenadovic, and N. R. Newbury, "Rapid and precise absolute distance measurements at long range", *Nature Photonics*, vol. 3, no. 6, pp. 351–356, 2009. DOI: 10.1038/nphoton.2009.94.

[133] P. Trocha, M. Karpov, D. Ganin, M. H. P. Pfeiffer, A. Kordts, S. Wolf, J. Krockenberger, P. Marin-Palomo, C. Weimann, S. Randel, W. Freude, T. J. Kippenberg, and C. Koos, "Ultrafast optical ranging using microresonator soliton frequency combs", *Science*, vol. 359, no. 6378, pp. 887–891, 2018. DOI: 10.1126/science.aao3924.

[134] M.-G. Suh and K. J. Vahala, "Soliton microcomb range measurement", *Science*, vol. 359, no. 6378, pp. 884–887, 2018. DOI: 10.1126/science.aao1968.

[135] K. Hei, K. Anandarajah, E. P. Martin, G. Shi, P. M. Anandarajah, and N. Bhattacharya, "Absolute distance measurement with a gain-switched dual optical frequency comb", *Optics Express*, vol. 29, no. 6, pp. 8108–8116, 2021. DOI: 10.1364/OE.413478.

[136] E. L. Teleanu, V. Durán, and V. Torres-Company, "Electro-optic dual-comb interferometer for high-speed vibrometry", *Optics Express*, vol. 25, no. 14, pp. 16 427–16 436, 2017. DOI: 10.1364/OE.25.016427.

[137] B. Martin, P. Feneyrou, D. Dolfi, and A. Martin, "Performance and limitations of dual-comb based ranging systems", *Optics Express*, vol. 30, no. 3, pp. 4005–4016, 2022. DOI: 10.1364/OE.446146.

[138] Z. Zhu and G. Wu, "Dual-comb ranging", *Engineering*, vol. 4, no. 6, pp. 772–778, 2018. DOI: 10.1016/j.eng.2018.10.002.

[139] N. Kuse, A. Ozawa, and Y. Kobayashi, "Static FBG strain sensor with high resolution and large dynamic range by dual-comb spectroscopy", *Optics Express*, vol. 21, no. 9, pp. 11 141–11 149, 2013. DOI: 10.1364/OE.21.011141.

[140] T. Minamikawa, Y.-D. Hsieh, K. Shibuya, E. Hase, Y. Kaneoka, S. Okubo, H. Inaba, Y. Mizutani, H. Yamamoto, T. Iwata, and T. Yasui, "Dual-comb spectroscopic ellipsometry", *Nature Communications*, vol. 8, no. 1, p. 610, 2017. DOI: 10.1038/s41467-017-00709-y.

[141] P. Martín-Mateos, F. U. Khan, and O. E. Bonilla-Manrique, "Direct hyperspectral dual-comb imaging", *Optica*, vol. 7, no. 3, pp. 199–202, 2020. DOI: 10.1364/OPTICA.382887.

[142] E. Vicentini, Z. Wang, K. V. Gasse, T. W. Hänsch, and N. Picqué, "Dual-comb hyperspectral digital holography", *Nature Photonics*, vol. 15, no. 12, pp. 890–894, 2021. DOI: 10.1038/s41566-021-00892-x.

[143] P. J. Marchand, J. Riemensberger, J. C. Skehan, J.-J. Ho, M. H. P. Pfeiffer, J. Liu, C. Hauger, T. Lasser, and T. J. Kippenberg, "Soliton microcomb based spectral domain optical coherence tomography", *Nature Communications*, vol. 12, no. 1, p. 427, 2021. DOI: 10.1038/s41467-020-20404-9.

[144] J. T. Friedlein, E. Baumann, K. A. Briggman, G. M. Colacion, F. R. Giorgetta, A. M. Goldfain, D. I. Herman, E. V. Hoenig, J. Hwang, N. R. Newbury, E. F. Perez, C. S. Yung, I. Coddington, and K. C. Cossel, "Dual-comb photoacoustic spectroscopy", *Nature Communications*, vol. 11, no. 1, p. 3152, 2020. DOI: 10.1038/s41467-020-16917-y.

[145] Q. Wang, Z. Wang, H. Zhang, S. Jiang, Y. Wang, W. Jin, and W. Ren, "Dual-comb photothermal spectroscopy", *Nature Communications*, vol. 13, no. 1, p. 2181, 2022. DOI: 10.1038/s41467-022-29865-6.

[146] C. Quevedo-Galán, V. Durán, A. Rosado, A. Pérez-Serrano, J. M. G. Tijero, and I. Esquivias, "Gain-switched semiconductor lasers with pulsed excitation and optical injection for dual-comb spectroscopy", *Optics Express*, vol. 28, no. 22, pp. 33 307–33 317, 2020. DOI: 10.1364/OE.404398.

[147] C. Quevedo-Galán, A. Pérez-Serrano, I. E. López-Delgado, J. M. G. Tijero, and I. Esquivias, "Dual-comb spectrometer based on gain-switched semiconductor lasers and a low-cost software-defined radio", *IEEE Access*, vol. 9, pp. 92 367–92 373, 2021. DOI: 10.1109/ACCESS.2021.3091872.

[148] V. Durán, P. A. Andrekson, and V. Torres-Company, "Electro-optic dual-comb interferometry over 40 nm bandwidth", *Optics Letters*, vol. 41, no. 18, pp. 4190–4193, 2016. DOI: 10.1364/OL.41.004190.

[149] A. J. Fleisher, D. A. Long, Z. D. Reed, J. T. Hodges, and D. F. Plusquellic, "Coherent cavity-enhanced dual-comb spectroscopy", *Optics Express*, vol. 24, no. 10, pp. 10 424–10 434, 2016. DOI: 10.1364/OE.24.010424.

[150] V. Durán, C. Schnébelin, and H. G. de Chatellus, "Coherent multi-heterodyne spectroscopy using acousto-optic frequency combs", *Optics Express*, vol. 26, no. 11, pp. 13 800–13 809, 2018. DOI: 10.1364/OE.26.013800.

[151] S. Gilbert, W. Swann, and C. Wang, *Hydrogen cyanide $H^{13}C^{14}N$ absorption reference for 1530 nm to 1565 nm wavelength calibration - SRM 2519a*, 2005. DOI: 10.6028/NIST.SP.260-137.

[152] A. Rosado, E. P. Martin, A. Pérez-Serrano, J. M. G. Tijero, I. Esquivias, and P. M. Anandarajah, "Optical frequency comb generation via pulsed gain-switching in externally-injected semiconductor lasers using step-recovery diodes", *Optics & Laser Technology*, vol. 131, p. 106 392, 2020. DOI: 10.1016/j.optlastec.2020.106392.

[153] C. A. Michal, "A low-cost multi-channel software-defined radio-based nmr spectrometer and ultra-affordable digital pulse programmer", *Concepts in Magnetic Resonance Part B: Magnetic Resonance Engineering*, vol. 48B, no. 3, p. e21401, 2018. DOI: 10.1002/cmr.b.21401.

[154] A. Doll, "Pulsed and continuous-wave magnetic resonance spectroscopy using a low-cost software-defined radio", *AIP Advances*, vol. 9, no. 11, p. 115 110, 2019. DOI: 10.1063/1.5127746.

[155] L. M. Riobó, F. E. Veiras, M. T. Garea, and P. A. Sorichetti, "Software-defined optoelectronics: Space and frequency diversity in heterodyne interferometry", *IEEE Sensors Journal*, vol. 18, no. 14, pp. 5753–5760, 2018. DOI: 10.1109/JSEN.2018.2842143.

[156] M. Čížek, V. Hucl, J. Hrabina, R. Šmíd, B. Mikel, J. Lazar, and O. Číp, "Two-stage system based on a software-defined radio for stabilizing of optical frequency combs in long-term experiments", *Sensors*, vol. 14, no. 1, pp. 1757–1770, 2014. DOI: 10.3390/s140101757.

[157] RTL-SDR.COM Blog, www.rtl-sdr.com, Accessed: 2024-04-17.

[158] R. W. Stewart, K. W. Barlee, D. S. W. Atkinson, and L. H. Crockett, *Software Defined Radio using MATLAB & Simulink and the RTL-SDR*. Strathclyde Academic Media, 2015.

[159] V. Duran, L. Djevarhidjian, and H. G. de Chatellus, "Bidirectional frequency-shifting loop for dual-comb spectroscopy", *Optics Letters*, vol. 44, no. 15, pp. 3789–3792, 2019. DOI: 10.1364/OL.44.003789.

[160] N. B. Hébert, V. Michaud-Belleau, S. Magnan-Saucier, J.-D. Deschênes, and J. Genest, "Dual-comb spectroscopy with a phase-modulated probe comb for sub-MHz spectral sampling", *Optics Letters*, vol. 41, no. 10, pp. 2282–2285, 2016. DOI: 10.1364/OL.41.002282.

[161] A. Rosado, M. R. Fernández-Ruiz, P. Corredera, J. M. G. Tijero, and I. Esquivías, "High-density and broad band optical frequency combs generated by pseudo-random phase modulation of optically injected gain-switched semiconductor lasers", *Optics & Laser Technology*, vol. 163, p. 109 312, 2023. DOI: 10.1016/j.optlastec.2023.109312.

[162] C. Quevedo-Galán, A. Rosado, A. Pérez-Serrano, J. M. G. Tijero, and I. Esquivias, "Dual-comb spectroscopy with enhanced resolution by pseudorandom phase modulation of gain-switched optical pulses", *Journal of Lightwave Technology*, vol. 42, no. 10, pp. 3954–3962, 2024. DOI: 10.1109/JLT.2024.3368363.

[163] N. Takeuchi, N. Sugimoto, H. Baba, and K. Sakurai, "Random modulation CW lidar", *Applied Optics*, vol. 22, no. 9, pp. 1382–1386, 1983. DOI: 10.1364/AO.22.001382.

[164] S. Donati, *Electro-Optical Instrumentation: Sensing and Measuring with Lasers*, 1st ed. Pearson Education, 2004.

[165] P. McManamon, *Field guide to Lidar*, 1st ed. SPIE Press, 2015.

[166] B. Behroozpour, P. A. M. Sandborn, M. C. Wu, and B. E. Boser, "Lidar system architectures and circuits", *IEEE Communications Magazine*, vol. 55, no. 10, pp. 135–142, 2017. DOI: 10.1109/MCOM.2017.1700030.

[167] W. C. Swann and N. R. Newbury, "Frequency-resolved coherent lidar using a femtosecond fiber laser", *Optics Letters*, vol. 31, no. 6, pp. 826–828, 2006. DOI: 10.1364/OL.31.000826.

[168] I. Rebolledo-Salgado, C. Quevedo-Galán, Ó. B. Helgason, A. Lööf, Z. Ye, F. Lei, J. Schröder, M. Zelan, and V. Torres-Company, "Platicon dynamics in photonic molecules", *Communications Physics*, vol. 6, no. 1, p. 303, 2023. DOI: 10.1038/s42005-023-01424-5.

[169] Ó. B. Helgason, F. R. Arteaga-Sierra, Z. Ye, K. Twayana, P. A. Andrekson, M. Karlsson, J. Schröder, and V. Torres-Company, "Dissipative solitons in photonic molecules", *Nature Photonics*, vol. 15, no. 4, pp. 305–310, 2021. DOI: 10.1038/s41566-020-00757-9.

[170] J. Kang, P. Feng, B. Li, C. Zhang, X. Wei, E. Y. Lam, K. K. Tsia, and K. K. Y. Wong, "Video-rate centimeter-range optical coherence tomography based on dual optical frequency combs by electro-optic modulators", *Optics Express*, vol. 26, no. 19, pp. 24 928–24 939, 2018. DOI: 10.1364/OE.26.024928.